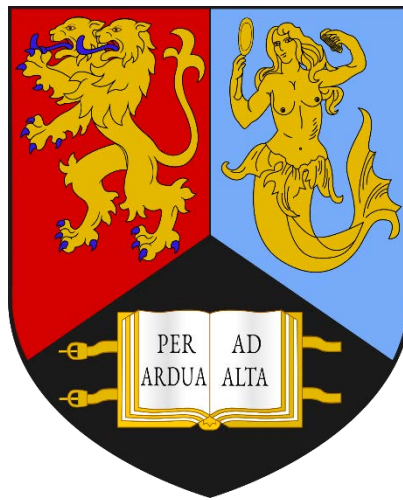


**COMBINED NUMERICAL AND MORPHOLOGICAL STUDY
OF THE HEART: DEVELOPMENT OF A SCALABLE
MITRAL VALVE MORPHOMETRIC MODEL AND
ASSESSMENT OF MODELLING CRITERIA FOR THE
RIGHT ATRIUM**

by

DIANA MARTA CRUZ DE OLIVEIRA

A thesis submitted to the University of Birmingham for the degree of
DOCTOR OF PHILOSOPHY



Department of Mechanical Engineering
School of Engineering
College of Engineering and Physical Sciences
University of Birmingham
October 2021

UNIVERSITY OF
BIRMINGHAM

University of Birmingham Research Archive

e-theses repository

This unpublished thesis/dissertation is copyright of the author and/or third parties. The intellectual property rights of the author or third parties in respect of this work are as defined by The Copyright Designs and Patents Act 1988 or as modified by any successor legislation.

Any use made of information contained in this thesis/dissertation must be in accordance with that legislation and must be properly acknowledged. Further distribution or reproduction in any format is prohibited without the permission of the copyright holder.

ABSTRACT

Frameworks for the computational modelling of heart components are continuously evolving, either to create models in a faster manner, or to represent its components more accurately. The mitral valve on the left side of the heart, for example, has a very complex geometry, and shape alterations induced by surgical procedures affect the long-term restoration of function. While several frameworks that recreate mitral valve shape from patient-specific images have been developed, allowing for the development of computational simulations of pre- and post-repaired cases, they are not flexible enough to yield a variety of models. On the other hand, accurate computational models of the right side of the heart are lacking, and since the right heart is used as a platform for clinical treatments such as haemodialysis, the development and validation of a computational model representing its function is necessary.

The overall aim of this thesis was to develop computational modelling frameworks for two components of the heart: the mitral valve on the left side, and the right atrium on the right side.

A mathematical evaluation of mitral valve morphometry through correlation analysis and evaluation of prediction equations for its shape was performed by using imaging datasets obtained in collaboration with clinicians and from the literature. This information led to the development of a computational toolbox enabling the quick generation of anatomically accurate and clinically useful parametric models of the mitral valve. This toolbox, implemented in MATLAB, generates the mitral valve geometry and respective mesh, and assigns boundary conditions and material properties, necessary for finite element analysis.

A sensitivity analysis of boundary conditions was performed to determine their influence on mitral valve biomechanics, with the chosen conditions being incorporated in the tool. A

healthy valve geometry was generated and analysed, and the respective computational predictions for valve physiology were validated against data in the literature. Moreover, two patient-specific mitral valve models including geometric alterations associated with disease were generated and analysed. Mitral valve function was compromised in both models, as given by the presence of regurgitating areas, elevated stress on the leaflets and unbalanced subvalvular apparatus forces. These results showcase the importance of a healthy mitral valve shape for adequate function; further, they demonstrate the potential of the computational toolbox, which allows for the automatic finite element analysis of the mitral valve in a variety of clinical cases, useful to study the biomechanics of patient-specific shapes.

In addition, a physiological blood flow model of the right atrium was developed and validated against data in the literature. This model was used as a simulation platform to evaluate the performance of four catheter designs for haemodialysis: while the symmetric tip had the best haemodynamic results, associated with low recirculation of flow and shear stress values, the step tip designs yielded the worst haemodynamic outcomes. The presence of side holes at the tip led to a decrease in recirculating flow, associated with improved catheter performance. The present simulation platform therefore enables the assessment of the performance of several catheter designs before their release on the market.

The work presented in this thesis bridges engineering and medicine through the development of two computational frameworks with primary clinical objectives: a computational tool for the evaluation of mitral valve biomechanics for a variety of geometries and assessment of current and novel mitral interventions; and a right atrium simulation platform which potentially highlights haemodialysis catheter design features requiring optimisation for optimal performance.

ACKNOWLEDGEMENTS

I want to start by expressing my heartfelt gratitude towards my supervisors, Daniel Espino and Duncan Shepherd, for this amazing opportunity. From the start of my PhD project until the very end, they have been nothing but supporting and encouraging. They have provided continuous guidance, crucial for the successful completion of my PhD research, while allowing me to explore my own ideas and create my path in academia. For making this an exciting and rewarding journey, and for helping me become a better-rounded researcher over the last four years, I am extremely grateful.

I would also like to thank all my collaborators who have provided guidance and support during my PhD and helped me succeed. First, a big thanks to Keith Buchan and Dana Dawson for their continuous clinical input during my PhD and for the access to medical images at Aberdeen Royal Infirmary, used in this work. Thanks to Luca Deorsola, Jonathan Mynard and Vijay Rajagopal, for their sincere interest and clinical advice regarding my PhD research. Finally, I wish to thank Kimal Plc and especially Adam Sheward for a fruitful and exciting collaboration which opened doors for the use of engineering resources towards the optimisation of haemodialysis catheters.

I am grateful to the University of Birmingham for funding my PhD with a School of Engineering scholarship, fundamental for the development of this research. Thanks so much for all the additional opportunities available within the University: to the Birmingham Environment for Academic Research (BEAR), which allowed me to store all my simulations and results and run complex jobs in a faster and efficient way; to the Library Services and the University Graduate School for all the researcher development and social sessions; to the

School of Engineering for organising several outreach activities in which I was involved and which made me passionate about public engagement.

I am thankful to my former supervisors from Instituto Superior Técnico, Portugal, Adélia Sequeira and Jorge Tiago, for their constant words of encouragement even after my Master's, and for helping me develop my passion for cardiovascular modelling.

I am grateful to my friends and colleagues at the University of Birmingham, with which I shared this journey over the last four years, and who have made this experience much more enjoyable. A big thanks to Khadijat, Weiqi, Sanj, Joe, David, and all those from the Biomedical Engineering Lab for the companionship, support and peer-to-peer feedback sessions. To my friends all over the world, thank you so much for your invaluable support and care throughout these years. A special thanks to Ana, Júlia, Gabriel, Rita, André, Magda, Joana and Phoe.

At last, I want to thank my family for their love and support, and especially my parents for their advice and continuous words of comfort, and for giving me the wings to fly and to follow my dreams. I also wish to thank Karn for his continuous patience and motivation during my PhD, and for being there by my side every day.

“No matter what anybody tells you, words and ideas can change the world.”

Dead Poets Society

STATEMENT OF CONTRIBUTIONS

This thesis presents novel research from three peer-reviewed scientific publications for which I am the first author. Below are the publications, the type of license associated and a statement of contributions for all co-authors.

OLIVEIRA, D., SRINIVASAN, J., ESPINO, D., BUCHAN, K., DAWSON, D. & SHEPHERD, D. 2020. Geometric description for the anatomy of the mitral valve: A review. *J Anat*, 237, 209-224, doi: 10.1111/joa.13196.

This manuscript has been published as an open access article, associated with the Creative Commons Attribution (CC-BY) License, allowing for its reproduction and alteration. Material from this publication has therefore been reproduced in Chapters 2 and 3 of this thesis.

I designed the study and created the initial draft of the manuscript, gathered morphometric mitral valve information from the literature, performed statistical analysis with published data, acquired mitral valve anatomic data and performed the respective data analysis. All co-authors were involved in the design of the study and have critically revised the manuscript. JS acquired mitral valve anatomic data. DD provided clinical guidance and recommended which clinical database and sample of patients to use for data analysis. KB provided clinical guidance, determined relevant morphometric aspects of the mitral valve (including anatomic arrangements from a surgical point of view) and provided advice on image sketches for the manuscript. DE and DS provided guidance on the organisation and presentation of information and data.

DE OLIVEIRA, D. C., ESPINO, D. M., DEORSOLA, L., MYNARD, J. P., RAJAGOPAL, V., BUCHAN, K., DAWSON, D. & SHEPHERD, D. E. T. 2021a. A toolbox for generating scalable mitral valve morphometric models. *Comput Biol Med*, 135, doi: 10.1016/j.combiomed.2021.104628.

This manuscript has been published as a subscription article. According to Elsevier's copyright policies, and as first author of the manuscript, I have the right to re-use this work within my thesis. Material from this publication has therefore been included in Chapter 4 of this thesis.

I developed the software which constitutes the mitral valve toolbox, validated the morphometric equations employed in the generation of an average model and created the initial draft of the manuscript. All co-authors have critically revised the manuscript. DE and DS provided supervisory guidance. LD provided clinical guidance and shared morphometric equations for mitral valve shape which they obtained from imaging data. JM and VR provided data for a patient-specific left ventricular shape, employed in the toolbox. KB and DD provided clinical guidance regarding key aspects of mitral valve shape and the functionality of the toolbox from a clinical perspective.

DE OLIVEIRA, D. C., OWEN, D. G., QIAN, S., GREEN, N. C., ESPINO, D. M. & SHEPHERD, D. E. T. 2021b. Computational fluid dynamics of the right atrium: Assessment of modelling criteria for the evaluation of dialysis catheters. *PLoS One*, 16, doi: 10.1371/journal.pone.0247438

This manuscript has been published as open access, associated with the Creative Commons Attribution (CC BY) License, allowing for its reproduction and alteration. Material from this publication has therefore been reproduced in Chapter 6 of this thesis.

I designed the study, developed all computational models, curated the data, performed formal analysis and visualisation of results, validated the results and wrote the original draft of the manuscript. All co-authors were involved in the design of the study and have critically revised the manuscript. Moreover, all authors except DS contributed towards the development of methodology necessary to create the computational modelling framework. DGO developed scripts for boundary conditions and helped validate the results. SQ assisted in the retrieval of relevant results and generation of images for the manuscript. NG and DE acquired the funding, administered and supervised the project and helped validate the results. DS supervised the project and helped validate the results.

Other scientific manuscripts which have been peer-reviewed and published or accepted for publication during this PhD, and for which I am first author or co-author, include:

DE OLIVEIRA, D. M. C., ABDULLAH, N., GREEN, N. C. & ESPINO, D. M. 2020. Biomechanical Assessment of Bicuspid Aortic Valve Phenotypes: A Fluid-Structure Interaction Modelling Approach. *Cardiovasc Eng Technol*, 11(4), 431-447, doi: 10.1007/s13239-020-00469-9

OWEN, D. G., DE OLIVEIRA, D. C., QIAN, S., GREEN, N. C., SHEPHERD, D. E. T. & ESPINO, D. M. 2020. Impact of side-hole geometry on the performance of hemodialysis catheter tips: A computational fluid dynamics assessment. *PLoS One*, 15, doi: 10.1371/journal.pone.0236946

OWEN, D. G., DE OLIVEIRA, D. C., NEALE, E. K., SHEPHERD, D. E. T. & ESPINO, D. M. 2021. Numerical modelling of blood rheology and platelet activation through a stenosed left coronary artery bifurcation. Accepted for publication in *PLoS One*.

International and national conference presentations include:

DE OLIVEIRA, D. C., ESPINO, D. M., BUCHAN, K. G. & SHEPHERD, D. E. T. 2019. Computational modelling of variability of mitral valve morphometry. BioMedEng 2019 Conference, Imperial College London, UK (Poster)

DE OLIVEIRA, D. C., ESPINO, D. M., BUCHAN, K. G. & SHEPHERD, D. E. T. 2018. Mitral valve morphology and its implication in disease. 8th Biennial Heart Valve Biology and Tissue Engineering Meeting, The Royal Society of Medicine, London, UK (Poster)

TABLE OF CONTENTS

CHAPTER 1 INTRODUCTION.....	1
1.1. Thesis overview	5
CHAPTER 2 BACKGROUND.....	7
2.1. Introduction	7
2.2. Heart anatomy and physiology	8
2.3. Mitral valve anatomy and physiology	10
2.3.1. Annulus.....	10
2.3.2. Leaflets	11
2.3.3. Chordae tendineae	12
2.3.4. Papillary muscles.....	14
2.3.5. Mathematical analysis of mitral valve geometry.....	15
2.4. Biomechanical properties of the mitral valve.....	19
2.4.1. Leaflets	19
2.4.2. Chordae tendineae	21
2.5. Mitral valve disease	22
2.5.1. Pathophysiology of MR: Carpentier's functional classification.....	22
2.5.2. Changes in mitral valve geometry during disease	24
2.5.3. Treatments for MV disease.....	27

Usual approaches and drawbacks	27
Necessity for tailored surgical approaches	28
2.6. Computational modelling methodologies for the mitral valve	30
2.6.1. Overview	30
2.6.2. The Finite Element Method	31
Mesh discretisation	31
Brief introduction to the FE method	33
2.7. Previous computational models of the mitral valve	36
2.7.1. Numerical approaches	36
2.7.2. Computational analyses	39
2.8. Connection between the right atrium and chronic kidney disease	40
2.8.1. Right atrial haemodynamics	40
2.8.2. Chronic kidney disease and association with cardiovascular disease	41
2.8.3. Treatment for chronic kidney disease	41
2.9. Modelling haemodialysis catheter blood flow	45
2.9.1. Characteristics of blood flow and governing equations	45
2.9.2. Brief introduction to the Finite Volume method	47
2.10. Summary	48

CHAPTER 3 MATHEMATICAL CHARACTERISATION OF MITRAL VALVE MORPHOMETRY	49
3.1. Introduction	49
3.2. Morphometric data collections and measurements	52
3.2.1. Datasets from literature	52
3.2.2. Patient-specific dataset (PSD)	56
3.2.3. Chordae orientation dataset	59
3.3. Mitral valve morphometry and the Golden Ratio	60
3.4. Correlation analyses and validation of prediction equations	62
3.4.1. Correlation analyses methodology	62
3.4.2. Mathematical representation of collagen arches	65
3.5. Results	65
3.5.1. Analysis of datasets from Warraich, Duplessis and PSD	65
3.5.2. Correlation analyses accuracy	68
Comparison with other datasets	68
Comparison with literature	71
3.5.3. Accuracy of prediction equations based on the Golden Ratio	75
Annulus	76
Leaflet lengths	76
Leaflet areas	77
3.5.4. Analysis of chordae insertions as a guide for collagen orientation	83

3.6. Discussion.....	85
3.6.1. Main study findings	85
3.6.2. Accuracy of prediction equations	87
3.6.3. Challenges of obtaining morphometric data for the mitral valve.....	89
3.7. Conclusions	90
CHAPTER 4 THE MITRAL VALVE TOOLBOX.....	91
4.1. Introduction	91
4.2. Mitral valve toolbox	93
4.2.1. Generic features	93
4.2.2. Geometrical model.....	96
Pre-processing and assumptions	96
Annular parameterization	98
Leaflet parameterization	99
Papillary muscle parameterization.....	100
Chordae generation.....	105
4.2.3 Model generation: average vs patient-specific geometries.....	106
4.3. FE model pre-processing and computational performance of toolbox.....	107
4.3.1 Generation of final model.....	107
4.3.2 Mesh evaluation.....	109
4.4. GUI workflow and examples of generated models	112

4.5. Initial assessment of prediction equations for paediatric patients	117
4.6. Discussion.....	120
4.6.1. Overview	120
4.6.2. Computational approach for the average MV model and current challenges	120
4.6.3. Comparison with other state-of-the-art methodologies	122
4.7. Conclusions	124
CHAPTER 5 PRE-PROCESSING OF A MITRAL VALVE MODEL FOR FINITE-ELEMENT ANALYSIS.....	125
5.1. Introduction	125
5.2. LS-DYNA simulations and automatic FE pre-processing from MATLAB.....	128
5.2.1. Mesh and shell element definitions	128
Shell definitions for an orthotropic material.....	130
Shell definitions for a hyperelastic material	132
5.2.2. Material properties.....	134
Leaflets: orthotropic material properties	135
Leaflets: hyperelastic material properties.....	136
Subvalvular apparatus.....	140
Transition elements	141
5.2.3. Boundary and loading conditions.....	142
Annular displacement.....	142

PM displacement	145
Pressure loading.....	146
Contact properties.....	147
5.2.4. Control properties and database outputs.....	148
5.3. Cases simulated and analysis.....	151
5.3.1. Solver settings and parameters evaluated.....	151
5.3.2. Mitral valve average model validation	152
Geometry description and generation.....	152
Valve closure dynamics.....	153
Leaflet stresses.....	156
Papillary muscles and chordae forces.....	157
5.3.3. Sensitivity study of material properties	159
5.3.4. Sensitivity study of boundary conditions and PM shape.....	161
5.3.5. Different patient scenarios.....	165
Geometry description and generation.....	165
Valve closure dynamics.....	166
Leaflet stresses.....	167
Papillary muscles and chordae forces.....	168
5.4. Discussion.....	170
5.4.1. Overview and main findings	170

5.4.2. MV predicted biomechanics is sensitive to boundary conditions and material responses.....	171
5.4.3. Potential applications.....	174
5.5. Summary.....	175
CHAPTER 6 COMPUTATIONAL FLUID DYNAMICS OF THE RIGHT ATRIUM: ASSESSMENT OF MODELLING CRITERIA FOR THE EVALUATION OF DIALYSIS CATHETERS.....	174
6.1. Introduction	177
6.2. Right atrium and dialysis catheter models.....	179
6.3. CFD models.....	182
6.3.1. Boundary conditions.....	183
Right atrium model.....	183
Catheter models	184
6.3.2. Flow governing equations and material properties	185
6.3.3. Computational settings	187
Meshing	187
Domain independence analysis	191
Time convergence analysis.....	191
Solving settings	192
6.4. Haemodynamics	193

6.5. CFD results	195
6.5.1. Right atrium model validation	196
6.5.2. Catheter models	202
Alterations in RA haemodynamics	198
Catheter performance	202
6.6. Discussion	210
6.6.1. Main study findings	210
6.6.2. Catheter insertion affects vorticity and WSS predictions in the RA	211
6.6.3. Different catheter designs and placements yield different performance	212
6.7. Conclusions	214
CHAPTER 7 SYNTHESIS	216
7.1. Overall discussion	216
7.2. Opportunities for future research	220
7.3. Overall conclusions	223
REFERENCES	225
APPENDIX A DESCRIPTION OF MATERIAL PROPERTIES	257
APPENDIX B SURFACE CONTACT FORMULATION	260
APPENDIX C CHORDAE TENDINEAE TENSIONS RETRIEVED FROM THE LITERATURE	261

APPENDIX D FINITE VOLUME METHOD FUNDAMENTALS	262
APPENDIX E MULTIPHASE FLOW FORMULATIONS.....	264

LIST OF FIGURES

Figure 2.1: a) Heart anatomy diagram displaying the right (blue) and left (red) sides, with the four chambers and respective valves (reproduced from pixabay under CC BY-SA 3.0: https://creativecommons.org/licenses/by-sa/3.0/deed.en); b) Example of physiological ventricular and atrial pressures over one cardiac cycle, with timings for heart valve opening and closing indicated. Notes: AV, aortic valve; PV, pulmonary valve; MV, mitral valve; TV, tricuspid valve.	9
Figure 2.2: Schematic of mitral valve anatomy, fitted within the left heart and including all anatomical components. Reproduced with permission from (Otto, 2001), Copyright Massachusetts Medical Society.	10
Figure 2.3: MV annulus a) viewed from within the left atrium and b) from above, with key anatomical landmarks and dimensions represented. Notes: LT, left trigone; RT, right trigone; d_{IT} , distance between trigones; d_{AP} , anteroposterior diameter; d_{CW} , commissural width; h_{AH} , annular height.	11
Figure 2.4: Human mitral valve leaflet shape and main areas of different tissue characterisation. Notes: C, clear zone; R, rough zone; B, basal zone.	12
Figure 2.5: Ex vivo example of chordae tendineae arising from both PMs and branching before inserting into the AL and PL (adapted from pixabay under CC BY-SA 4.0: https://creativecommons.org/licenses/by-sa/4.0/). Notes: AL, anterior leaflet; PL, posterior leaflet; PM, papillary muscle.	13
Figure 2.6: Circle representing the annulus, according to Okamoto et al. (2007), with relevant dimensions highlighted. Notes: LT, left trigone; RT, right trigone; AL-PM diameter, anterolateral-posteromedial diameter; CW, commissural width; IT distance, inter-trigonal distance; θ_{Tg} , trigonal angle; θ_{Com} , commissural angle.	15
Figure 2.7: Coaptation triangle, where the hypotenuses can be considered as a simplified representation of the anterior and posterior leaflets. The tenting height divides the base of the triangle (AP diameter) into two segments – the anterior and the posterior cords. Notes: α_A , anterior leaflet angle; α_P , posterior leaflet angle.	17
Figure 2.8: Microstructure of the central region of the AL, showcasing the main four tissue layers. The relative thickness of each layer is showcased, with collagen and elastin fibers being coloured in red and green, respectively. The referential indicates the circumferential (C) and radial (R) directions of the fibers. Notes: V, ventricularis; F, fibrosa; S, spongiosa; A, atrialis (reproduced with permission from (Zhang et al., 2016)).	21

Figure 2.9: Carpentier’s classification for the aetiology of MV dysfunction. Reproduced from (El Sabbagh et al., 2018), with permission.....	24
Figure 2.10: Examples of novel treatment devices for the MV, including (a) an asymmetrical annuloplasty ring mimicking annular saddle shape (Copyright 2018 Medtronic) and (b) the MitraClip (Abbott Vascular, Santa Clara, CA, USA), with its insertion into the mitral leaflets schematised (reproduced under CC BY-SA 3.0: https://creativecommons.org/licenses/by-sa/3.0/deed.en).	30
Figure 2.11: Types of FE elements and respective order.	32
Figure 2.12: Shell through the thickness integration points for different layer representations.	33
Figure 2.13: Framework proposed by Mansi et al. for the generation of MV models from medical imaging, and creation of the final MV model ready for FE simulations. Patient-specific images of the MV are used to capture its structure and its apparatus is estimated from anatomical landmarks, giving rise to a mapped parameterisation of the leaflet surfaces. Chordae tendineae are then defined based on PM tip location and assumptions for distribution, giving rise to the complete MV model.	37
Figure 2.14: Leaflet stress distributions [MPa] obtained by Errthum et al. when simulating repair with MitraClip in different spatial configurations (Errthum et al., 2021).	40
Figure 2.15: Schematic of the dialysis process, including the main stages for filtering blood with a dialysis machine. Here, the insertion of a HD catheter into the RA from a vein in the neck is also displayed, with the external limbs of the catheter connecting to the dialysis machine (reproduced from Wikimedia Commons under CC BY-SA 3.0 and 4.0).	42
Figure 2.16: Examples of commercially available central venous catheter tips, adapted from (Vesely and Ravenscroft, 2016). a) Step-tip catheter Titan™ (Medcomp. Harleysville, PA) and b) Split-tip catheter Ash Split® (Medcomp. Harleysville, PA).	44
Figure 2.17: Example of finite volume mesh discretisation.	47
Figure 3.1: Outline of this chapter. Imaging datasets from Warraich et al. and Duplessis et al. were selected for the mathematical analysis of the mitral valve. Moreover, new mitral valve images based on (1) clinical databases from Aberdeen Royal Infirmary and (2) mitral leaflet samples were included for analysis, as well as morphometric equations from the literature based on the Golden Proportion. Linear/nonlinear regression analysis was performed for the measurements from the selected datasets. Predicted dimensions from obtained fits and morphometric equations were assessed by comparing against mean data from previous studies, and fittings resulting from the correlation analysis were also compared against other datasets,	

when possible. Notes: AH and h_{AH} , annular height; AP and d_{AP} , anteroposterior diameter; d_{CW} , commissural width; NPA, non-planarity angle. 51

Figure 3.2: Mitral annular dimensions (in bold) measured by Warraich et al. (Warraich et al., 2012). Notes: LT, left trigone; RT, right trigone; d_{AP} , anteroposterior diameter; d_{AL-PM} , anterolateral-posteromedial diameter (diameter at the middle of the annular circumference); h_{AH} , annular height; d_{CW} , commissural width (distance from commissure to commissure); NPA, non-planarity angle; A_{ann} , annular area. 53

Figure 3.3: Mitral leaflet dimensions (in bold) measured by Duplessis et al. (Duplessis and Marchand, 1964). Notes: A_C , annular circumference; A_{AC} , anterior annular circumference; P_{AC} , posterior annular circumference; L_{FE} , leaflet free edge length; A_h , anterior leaflet height; P_{mh} , posterior leaflet middle scallop height; A_{la} , anterior leaflet area; P_{la} , posterior leaflet area. ... 55

Figure 3.4: Mitral dimensions (in bold) evaluated using the PSD available at Aberdeen Royal Infirmary. Notes: A_C , annular circumference; A_{AC} , anterior annular circumference; P_{AC} , posterior annular circumference; LT, left trigone; RT, right trigone; d_{AP} , anteroposterior diameter; d_{AL-PM} , anterolateral-posteromedial diameter; A_{ann} , annular area; T_h , tenting height; T_a , tenting area; d_{PM} , inter-papillary muscle distance; $d_{PM-apex}$, distance between left ventricular apex and the central point of the inter-papillary muscle distance. 57

Figure 3.5: Photographs of a) anterior and b) posterior MV leaflet samples, including annulus, leaflets, chordae tendineae and part of the PMs (courtesy of Mr. Keith Buchan, Consultant Cardiac Surgeon, Aberdeen Royal Infirmary). 60

Figure 3.6: Correlation analysis process exemplified for two MV parameters. a) Correlation of clinical data (in this case, h_{AH}/d_{AP} vs NPA) and set of prediction equations generated from linear and nonlinear regression models (y = value of NPA; x = value of h_{AH}/d_{AP}); b) Prediction equation curves are displayed for a range of physical dimensions within a grey “window”, allowing to assess the physical meaning of each equation within the expected ranges; c) Values of NPA predicted using linear and polynomial equations are superimposed on clinical data to allow the selection of the best equation. Residual plots are evaluated for linear and polynomial fits, showing that there is not great difference between predictions arising from these fits. ... 64

Figure 3.7: Prediction variability for polynomial fittings above the 3rd degree for the A_C and P_{AC} variables from the dataset from Duplessis et al. (Duplessis and Marchand, 1964): high curvature changes are present in these polynomials (a), as well as unrealistic prediction of dimensions (b). 68

Figure 3.8: Fitting equations D1 and D2 obtained from the Duplessis dataset and with coefficients included in Table 3.6 are tested using data from the PSD: a) PSD original vs predicted data is displayed; b) Box plots representing the relative difference (%) between data from the PSD dataset and that obtained employing fitting equations. 70

Figure 3.9: Fitting equations PSD1 and PSD3 obtained from the PSD and with coefficients included in Table 3.7 are tested using data from the Duplessis dataset: a) Duplessis original vs predicted data is displayed; b) Box plots representing the relative difference (%) between data from the Duplessis dataset and that obtained employing fitting equations. 71

Figure 3.10: Box plots representing the relative difference (%) between original dimensional MV data and that obtained employing fitting equations from the correlation analysis results for the Warraich dataset: a) W1 and W2, b) W3 and W4 and c) W5. 73

Figure 3.11: Box plots representing the relative difference (%) between original dimensional MV data and that obtained employing fitting equations from the correlation analysis results for the PSD dataset: a) PSD1, b) PSD2 and c) PDS3. Concerning the box plot from b), only two data points were available in the literature for analysis..... 73

Figure 3.12: Box plots representing the relative difference (%) between original dimensional MV data and that obtained employing fitting equations from the correlation analysis results for the Duplessis dataset: a) D1, b) D2, c) D3, d) D4, e) D5 and D6, f) D7 and D8 and g) D9 and D10. 74

Figure 3.13: Comparison between predictions for mean healthy and diseased clinical data using equation W5 (from the Warraich dataset): a) The linear fit is plotted against raw clinical data and b) Box plots representing the relative difference (%) between clinical data and that obtained employing equation W5. 75

Figure 3.14: Predictions for commissural width (a) and annular height (b) as a function of the anteroposterior diameter, as given by the Golden Ratio (colored shades representing up to 20% deviation from the average value) and by adult and paediatric clinical data (represented by black – adult - and dark green – paediatric - standard deviation bars) (Pouch et al., 2014; Jassar et al., 2014; Lee et al., 2013; Mihaila et al., 2014; Jolley et al., 2017; Munin et al., 2014). A direct regression analysis is shown for commissural width (c) and annular height (d), with the orange fitting line representing the one-to-one fit between predicted and patient data and the blue line representing the patient data best linear fit. 79

Figure 3.15: Predictions for anterior (a) and posterior (b) leaflet lengths as a function of the anteroposterior diameter, as given by the Golden Ratio (colored shades representing up to 20% deviation from the average value) and by adult in vivo data (Deorsola and Bellone, 2019; Munin et al., 2014). Black and green points represent unique patient data for the studies from Deorsola et al. (2019) (Deorsola and Bellone, 2019) and Nomura et al. (Nomura et al., 2019), respectively. A direct regression analysis is shown for anterior (c) and posterior (d) leaflet lengths, with the orange fitting line representing the one-to-one fit between predicted and patient data and the blue line representing the patient data best linear fit. 80

Figure 3.16: Predictions for the anterior leaflet surface area as a function of the anteroposterior diameter for ratios of 1.48 (a) and 1.64 (b), as given by the Golden Ratio (colored shades

representing up to 20% deviation from the average value), by adult and paediatric clinical data (represented by black – adult - and dark green – paediatric - standard deviation bars) (Lee et al., 2013; Mihaila, 2013; Mihaila et al., 2014; Jolley et al., 2017; Munin et al., 2014; Kim et al., 2019). A direct regression analysis is shown for ratios of 1.48 (c) and 1.64 (d), with the orange fitting line representing the one-to-one fit between predicted and patient data and the blue line representing the patient data best linear fit. 81

Figure 3.17: Predictions for the posterior leaflet surface area as a function of the anteroposterior diameter for ratios of 1.48 (a) and 1.64 (b), as given by the Golden Ratio (colored shades representing up to 20% deviation from the average value), by adult and paediatric clinical data (represented by black – adult - and dark green – paediatric - standard deviation bars) (Lee et al., 2013; Mihaila, 2013; Mihaila et al., 2014; Jolley et al., 2017; Munin et al., 2014; Kim et al., 2019). A direct regression analysis is shown for ratios of 1.48 (c) and 1.64 (d), with the orange fitting line representing the one-to-one fit between predicted and patient data and the blue line representing the patient data best linear fit. 82

Figure 3.18: Photographs of a) AL and b) PL samples, with selected collagen arches highlighted with solid coloured lines (courtesy of Mr. Keith Buchan, Aberdeen Royal Infirmary). Arches were numbered as demonstrated for the posterior leaflet (from lowest to greatest height). 83

Figure 3.19: Regression analysis on a) AL and b) PL arch height from arch fittings and original raw data. 85

Figure 4.1: Workflow of the MV toolbox, from the generation of the morphometric model to the FE simulation result: (a) The inputs are a baseline mitral annular 3D profile and MV dimensions, either obtained from mathematical formulations or from patient-specific medical images; (b) The model is parameterized, with the annulus, leaflets and PM (papillary muscles) being independently scaled; (c) A surface model mesh is created for the leaflets and points identifying each PM are stored. The user can choose to output these as an .stl file for the mesh and a text file for PM coordinates; (d) The meshed model is pre-processed: chordae tendineae are added, material properties, boundary and contact conditions are defined; (e) The .k input file is created and run in LS-DYNA. 95

Figure 4.2: Input parameters requested in the toolbox to parameterize the annular boundary, where the MV annulus is a) viewed from within the left atrium and b) from above. The 3D axis denote the orientation for each image. Notes: LT, left trigone; RT, right trigone; d_{AP} , anteroposterior distance; d_{CW} , commissural distance; h_{AH} , annular height. 97

Figure 4.3: Saddle-horn height (H) representation in a lateral view of the mitral annulus. 97

Figure 4.4: Input parameters requested in the toolbox to parameterize the leaflets. 99

Figure 4.5: The lateral half of the MV is represented, with boundaries defined during the parameterization process of the leaflets. Notes: AAC, anterior annular circumference; PAC, posterior annular circumference.	100
Figure 4.6: a) Distances between PM tips and corresponding points of mitral annulus, as characterized by the literature (Sakai et al., 1999; Yamaura, 2008). 0, 2, 10, 4 and 8 o'clock represent: anterior annular midpoint; right trigone; left trigone; division between middle and posteromedial commissural scallops; division between middle and anterolateral commissural scallops, respectively (Yamaura, 2008); b) 3D shape representing chordae origins in the PMs (axial view); c) Different origin points correspond to different points of insertion into the leaflets. Notes: ALPM, anterolateral PM; PMPM, posteromedial PM; PL, posterior leaflet; AL, anterior leaflet.	101
Figure 4.7: GUI options for the definition of PM displacement in a dysfunctional case. Notes: PM, papillary muscle; ALPM, anterolateral papillary muscle; PMPM, posteromedial papillary muscle; LV, left ventricle.	103
Figure 4.8: MATLAB process of PM displacement due to LV dilation: a) A LV 3D model reconstructed from MRI imaging is employed as a template, which can be scaled according to input dimensions for width and length (b)); c) A 2D cross-section representation of PM displacement due to LV dilation is displayed, including positions for PMPM and ALPM before and after LV scaling. In a scenario where LV anterior dilation occurs, the position of the anterior PM base is altered accordingly, leading to ALPM displacement. Notes: PM, papillary muscle; ALPM, anterolateral papillary muscle; PMPM, posteromedial papillary muscle; LV, left ventricle.	104
Figure 4.9: a) Single PM tip (left) and b) 3D PM shape (right) chordae tendineae distributions, with the number of chordae generated being in agreement with data from the literature.	105
Figure 4.10: Example of distances from the PMPM tip to annular landmarks obtained with AP diameters associated with a healthy adult shape, as well as inter-PM distances. Given the symmetry assumed along the long axis meridian of the AL for the average model, distances from the ALPM tip to annular landmarks are equal. Notes: inter-PM, inter-PM distance. ...	107
Figure 4.11: Transition elements on the free margin (brown quadrilateral shell elements)...	108
Figure 4.12: Mesh quality metrics for MV models generated with different AP diameters (20, 25 and 30 mm).	111
Figure 4.13: Mesh convergence test performed in LS-DYNA.	112
Figure 4.14: MV toolbox workflow of GUI options.	113
Figure 4.15: Average MV models generated with different AP diameters (20 and 30 mm). ...	113

Figure 4.16: Mitral valve geometry obtained with CW varying between 25 and 35 mm.	114
Figure 4.17: Mitral valve geometry obtained with the ring concavity varying from 0 (D-shaped annulus) to 0.2 (pronounced concavity).	115
Figure 4.18: Mitral valve AL and PL geometries obtained for with different middle leaflet heights.....	115
Figure 4.19: Mitral valve AL and PL geometries obtained for varying leaflet areas.....	116
Figure 4.20: Patient-specific input of PM position, with PMPM displacement represented.	117
Figure 4.21: AP diameter [mm] as a function of the BSA [mm ²], using prediction equations from different sources (Daubeney et al., 1999; Lopez et al., 2017; Jolley et al., 2017; Pettersen et al., 2008). An AP diameter > 30 mm may be associated with the onset of MV annular dilation.	120
Figure 4.22: Sample 3D MV model with all components included, ready for computational simulations.....	123
Figure 5.1: After the MV geometry generation and meshing (Chapter 4), the model is pre-processed for FE simulations, including the definition of boundary conditions, material properties and necessary control settings. Using these definitions, an average (healthy) model of the MV was generated and its computational predictions validated against the literature. Moreover, the sensitivity of computational results to different boundary conditions, material properties and PM shapes was analysed. Finally, two patient-specific cases were generated and solved.....	127
Figure 5.2: Aspect ratio of mesh elements for (a) the original MV model in a full-diastolic open state and (b) for a deformed MV model at peak systole.....	129
Figure 5.3: Maximum principal stress [MPa] displayed on the atrial side of the MV leaflets for 1 integration point through the thickness and 3 integration points through the thickness, respectively, at peak systole.	131
Figure 5.4: Warping angle displayed for both the AL and PL with NIP of 1 and 3, respectively, at peak systole.....	131
Figure 5.5: Shell representations for orthotropic and hyperelastic materials in LS-DYNA. a) The shell is characterised by a total thickness T for the orthotropic material, while b) for an hyperelastic material a composite approach is used, employing two shell layers (layer 1: fibrosa; layer 2: atrialis and ventricularis) of different thicknesses and defined with hyperelastic material properties is used, with t_1 and t_2 being the layer thicknesses.	133

Figure 5.6: Comparison of the numerical (FE) results against experimental data (average calculated from individual specimens) for the a) anterior leaflet and the b) posterior leaflet under equibiaxial loading, with $K = 10$ MPa.	138
Figure 5.7: Part of the AL model with fibers embedded. The primary layer represents collagen fibers oriented preferentially in a circumferential orientation (fiber angle: 0°), while the secondary layer provides support in the radial direction (fiber angle: 35°).	139
Figure 5.8: Non-linear stress-strain behaviour of marginal and strut chordae tendineae for a strain range of 0-10 %, obtained from Kunzelman and Cochran (Kunzelman and Cochran, 1990) and adapted based on information from Liao and Veseley (Liao and Vesely, 2003). .	141
Figure 5.9: Annular displacements for cases 2 (a) and 3 (b and c). a) The magnitude of the annular displacement towards its centroid and through a cardiac cycle is displayed for case 2, with the annulus reaching a maximum displacement of 1.5 mm at peak systole; b) In case 3, all annular portions contract at the same time, but the magnitude of the annular displacement through a cardiac cycle is adapted to represent different stages of contraction, with the maximum displacement occurring at early systole; c) The three-dimensional annulus and its spatial displacement from mid-diastole to peak systole is showcased for case 3, with different annular coordinates being associated with varying displacements.	144
Figure 5.10: Temporal changes in PM displacement for the whole cardiac cycle.	146
Figure 5.11: Transvalvular pressure load curves adapted from (Herring and Paterson, 2018) and applied as boundary conditions to the atrial and ventricular surfaces of the MV leaflets.	146
Figure 5.12: Internal and hourglass energies [N mm] over time [s] for four main hourglass control formulations. HG1 and HG3 are viscosity-based controls, HG4 is a stiffness-based control and HG8 is applied to fully integrated shell elements.	149
Figure 5.13: Cross-sections used for the evaluation of several results. a) Three cross-sectional planes are used for the calculation of results (C1, middle section; C2, PMPM section; C3, ALPM section); b) C1 (middle section) is used to evaluate results related to MV coaptation (C_L , coaptation length; B_h , posterior billowing height). Notes: PL, posterior leaflet; AL, anterior leaflet.	152
Figure 5.14: Time evolution of the average MV shape (atrial view) as predicted by the FE model at four different time instances of the cardiac cycle	154
Figure 5.15: MV leaflet contact distributions.....	155
Figure 5.16: Leaflet stress distributions at peak systole and maximum and minimum stress values obtained at relevant cross-sections.	156
Figure 5.17: Time-dependent PMPM reaction forces.	157

Figure 5.18: Forces carried by different groups of chordae at peak systole. Black coloured data represents the predictions of the present model, while blue and red correspond to estimations from experimental (Jimenez et al., 2005; Nielsen et al., 2003; Paulsen et al., 2020; Paulsen et al., 2019) and computational (Prot et al., 2009; Stevanella et al., 2009; Wang and Sun, 2013) studies, respectively.....	159
Figure 5.19: Distribution of circumferential and radial strains on mitral leaflets at peak systole for orthotropic and hyperelastic material models.	160
Figure 5.20: Effects of three annular boundary conditions on the leaflet coaptation profile (middle cross-section) and resultant displacement at peak systole. PL z-displacements are also displayed for each case. Coaptation lengths are 1.703 mm, 4.484 mm and 4.924 mm for cases 1, 2 and 3, respectively.	162
Figure 5.21: Leaflets' maximum principal stresses distribution at peak systole for four different model conditions.	162
Figure 5.22: MV peak systolic closure for patient-specific shapes PS1 and PS2, (a) showcasing regurgitant areas and (b) displaying the middle coaptation cross-sectional profile and resultant displacement.	167
Figure 5.23: Leaflet stress distributions at peak systole for the simulated patient-specific geometries incorporating annular flattening and leaflet enlargement (PS1) and PMPM displacement due to LV dilation PS2).....	168
Figure 5.24: Time-dependent PM reaction forces for PS1 and PS2 valves in comparison with the prediction for the average healthy model. While the PM reaction forces for the PS1 valve are increased in comparison with the healthy model, the PS2 valve demonstrates an imbalance of PM forces, caused by PMPM displacement.....	169
Figure 6.1: Outline of this chapter. CFD modelling was performed, first with the RA model, then with catheter models virtually placed in the RA. The RA model was validated (1) through a numerical approach, and (2) by comparing its haemodynamic predictions with the literature. After validation, the catheter models were developed, considering four different tip designs and diverse placements within the RA. Appropriate conditions were chosen for the model and relevant metrics were defined to evaluate tip performance. Lastly, the obtained results were compared amongst catheters and against literature.	179
Figure 6.2: RA computational domain. Notes: IVC, inferior vena cava; SVC, superior vena cava; TV, tricuspid valve.....	180
Figure 6.3: Catheter tip designs A, B, C and D, with arterial and venous lumens indicated. Note: Catheters A and B were set in reverse mode (for C and D designs, forward and reverse mode lead to the same model configuration).	181

Figure 6.4: RA computational domain with example catheter inserted and set of boundary conditions defined.	182
Figure 6.5: Diagrammatic overview of all computational models developed (with names written in bold). Acute refers to temporary catheter placement and chronic to permanent catheter placement, this is of relevance to the clinical use of the catheters.	182
Figure 6.6: Time-dependent pressure, with diastolic and systolic periods represented, imposed at the inlets (adapted from Cohen et al. 1986).....	184
Figure 6.7: Time-dependent vorticity and WSS profiles, predicted with Newtonian and Non-Newtonian blood models.	186
Figure 6.8: Mesh convergence results for (a) RA model and (b) catheter model.	189
Figure 6.9: Mesh element quality, varying from 0 to 1, assessed across all catheter models. The average number of elements for each quality range is displayed, with error bars showing the standard deviation from average values.	190
Figure 6.10: Meshed model, with a closer look at the SVC boundary. Boundary layers can be observed near the right atrial wall. A greater number of mesh elements was used to represent the catheter, in comparison with the RA.	190
Figure 6.11: Relative percentage error for (a) velocity and (b) pressure measurements.....	192
Figure 6.12: Example of volume definition to be placed at the tip.	194
Figure 6.13: Quantitative results for volume-averaged velocity (left), volume-averaged vorticity (middle) and area-averaged WSS (right) at five time instances of the cardiac cycle.	198
Figure 6.14: Time evolution of spatially averaged WSS and volume-averaged vorticity.	198
Figure 6.15: Time evolution of right atrial flow patterns: streamline fields representing velocity magnitudes are displayed at five different time instances ($t = 0.1$ s, 0.25 s, 0.4 s, 0.55 s, 0.7 s).	199
Figure 6.16: Time evolution of right atrial flow patterns: isosurfaces representing helicity (h) are displayed at five different time instances ($t = 0.1$ s, 0.25 s, 0.4 s, 0.55 s, 0.7 s), as well as the percentage of RA volume occupied by $h < 0$ and $h > 0$	201
Figure 6.17: Blood flow rate profiles over one cardiac cycle at SVC, IVC and TV boundaries.	202

Figure 6.18: Time evolution of right atrial flow patterns after catheter insertion (symmetric design – D2): streamline fields representing velocity magnitudes are displayed at five time instances.	203
Figure 6.19: Volume-averaged vorticity profile through the cardiac cycle for all models. (a) All designs are compared with the RA; (b) A and D tip placement changes do not greatly influence overall vorticity quantifications.	203
Figure 6.20: Time-averaged WSS [Pa] for the whole RA domain is displayed for all models.	205
Figure 6.21: Time-averaged volume fraction of filtered blood (recirculation phase) within the RA for all catheter models. Higher volume fractions indicate larger quantities of filtered blood at one location over one cardiac cycle, while lower volume fractions indicate lower quantities of filtered blood at one location over one cardiac cycle.	207
Figure 6.22: Volume-averaged shear stress profile through the cardiac cycle for all catheter venous lumen tips. (a) All designs are present; (b) A and D tip placement changes impact on tip shear stress.	209
Figure 6.23: Isosurface regions near the catheter tip where blood shear stress is 10 Pa for all models at the beginning of systole ($t = 0.25$ s).	209

LIST OF TABLES

Table 2.1: Classification of chordae tendineae and their role in MV function (Espino <i>et al.</i> , 2005; Timek <i>et al.</i> , 2001; Nielsen <i>et al.</i> , 2003; Sedransk <i>et al.</i> , 2002; Wilcox <i>et al.</i> , 2014; Lam <i>et al.</i> , 1970; Faletra and Narula, 2017).	14
Table 3.1: Mitral annular dimensions collected by Warraich <i>et al.</i> (Warraich <i>et al.</i> , 2012). ...	54
Table 3.2: Mitral annular and leaflet dimensions collected by Duplessis <i>et al.</i> (Duplessis and Marchand, 1964).....	55
Table 3.3: Dimensions at end-systole from new imaging data obtained at Aberdeen Royal Infirmary. Notes: Missing measurements at the subvalvular apparatus for patients 4 and 13 are due to poor image quality.	58
Table 3.4: Regression models employed for correlation analysis.	63
Table 3.5: Correlation analysis results from the Warraich <i>et al.</i> (Warraich <i>et al.</i> , 2012) dataset. Equation coefficients and statistical measures for goodness of fit (R^2 , p-value and residual SD) are displayed for linear and best fitting nonlinear model.	66
Table 3.6: Correlation analysis results from the Duplessis <i>et al.</i> (Duplessis and Marchand, 1964) dataset. Equation coefficients and statistical measures for goodness of fit (R^2 , p-value and residual SD) are displayed for linear and best fitting nonlinear model.	66
Table 3.7: Correlation analysis results from the PSD. Equation coefficients and statistical measures for goodness of fit (R^2 , p-value and residual SD) are displayed for linear and best fitting nonlinear model.	67
Table 3.8: Mean relative difference between Golden Proportion predictions and original mid-systolic data from the literature, as well as estimated diastolic literature data for AL and PL areas, assuming total to closed leaflet surface area ratios of 1.48 and 1.64.	78
Table 3.9: Correlation analysis results for 2D anterior leaflet collagen arch data. Equation coefficients and statistical measures for goodness of fit (R^2 and p-value) are displayed for best fitting nonlinear model. Since the best fitting model is a 2nd order polynomial, the height of the quadratic curve (i.e. the collagen arch), as well as its counterpart from raw data, are also included.	84
Table 3.10: Correlation analysis results for 2D posterior leaflet collagen arch data. Equation coefficients and statistical measures for goodness of fit (R^2 and p-value) are displayed for best fitting nonlinear model. Since the best fitting model is a 2nd order polynomial, the height of the	

quadratic curve (i.e. the collagen arch), as well as its counterpart from raw data, are also included.	84
Table 3.11: Correlation analysis results for the height of collagen arches (obtained from fitting and from original data). Equation coefficients and statistical measures for goodness of fit (R ² and p-value) are displayed for best fitting model.	85
Table 4.1: Dimensions used to parameterise the MV geometry.	98
Table 5.1: Shell definitions. Notes: NIP, number of integration points.	130
Table 5.2: Material parameters employed in simulations with the linear orthotropic model, where x- and y- refer to circumferential and radial directions, respectively. Notes: E _c , circumferential Young's modulus; E _r , radial Young's modulus; E _o , out-of-plane Young's modulus; G _{cr} , circumferential/radial shear modulus; G _{ro} , out-of-plane shear modulus; G _{oc} , out-of-plane shear modulus; ν _{cr} , in-plane Poisson's ratio.	136
Table 5.3: Displacement conditions and shell layer thickness ratios applied in simulated biaxial tensile test. Notes: D, displacement.	138
Table 5.4: Material properties determined by (Wenk et al., 2012) by fitting the stress equations for a 2-layer composite to experimental data from (May-Newman and Yin, 1998) and final hyperelastic material properties employed in FE simulations reported in this chapter. Notes: C _{3,1} , for example, represents the C ₃ material constant in the first layer.	140
Table 5.5: Percentage changes in annular dimensions from mid-diastole to systole caused by different prescribed displacement cases. The values presented for Case 2 reflect changes from mid-diastole to peak systole, while those for Case 3 demonstrate the maximum changes obtained from mid-diastole to early-systole, compared against healthy ranges from the literature (Topilsky <i>et al.</i> , 2013; Tang <i>et al.</i> , 2019; Levack <i>et al.</i> , 2012).	145
Table 5.6: Contact formulation options for the MV, prescribed in the toolbox.	147
Table 5.7: Control options included for FE simulations.	150
Table 5.8: MV average model dimensions.	153
Table 5.9: Chordae tendineae elongation, tension and load proportion (mean ± standard deviation) at peak systole.	158
Table 5.10: Chordae tendineae tension and load proportion at peak systole under varying boundary conditions and PM shapes. Conditions simulated correspond to (A) fixed annulus and PM (single PM tip), (B) moving annulus and fixed PM (single PM tip), (C) moving annulus and PM (single PM tip) and (D) moving annulus and PM (3D PM shape).	164

Table 5.11: MV patient-specific model dimensions.....	165
Table 5.12: Chordae tendineae tension and load proportion at peak systole for patient-specific cases.....	170
Table 6.1: Catheter dimensions. Notes: Fr, French gauge (1 Fr = 0.33 mm).	181
Table 6.2: Gauge pressure values applied at catheter outlets and respective flow rates achieved.	184
Table 6.3: Rheological model definitions and parameters (adapted from Cho <i>et al.</i> 1991 and Johnston <i>et al.</i> 2004).	185
Table 6.4: Reynolds number study performed for the RA model.	186
Table 6.5: CFD set-up.	187
Table 6.6: Mesh settings and quality assessment.	191
Table 6.7: Tip volume dimensions.	194
Table 6.8: Parameter definitions for evaluation of haemodynamics.	195
Table 6.9: Haemodynamic predictions for all models.	196

LIST OF ABBREVIATIONS

2D	2-dimensional
3D	3-dimensional
A _{AC}	Anterior annular circumference
AH	Annular height
AHCWR	Annular height to commissural width ratio
AL	Anterior leaflet
ALPM	Anterolateral papillary muscle
AL-PM	Anterolateral-posteromedial
AP	Anteroposterior
BC	Boundary condition
BSA	Body surface area
BT	Belytschko-Lin-Tsay
CAD	Computer aided design
CFD	Computational fluid dynamics
CKD	Chronic kidney disease
CVD	Cardiovascular diseases
CW	Commissural width
EROA	Effective regurgitant orifice area
FE	Finite element
FSI	Fluid-structure interaction
GUI	Graphic user interface

HD	Haemodialysis
IVC	Inferior vena cava
LV	Left ventricle
MR	Mitral regurgitation
MV	Mitral valve
NIP	Number of integration points
NPA	Non-planarity angle
P _{AC}	Posterior annular circumference
PL	Posterior leaflet
PM	Papillary muscle
PMPM	Posteromedial papillary muscle
PSD	Patient-specific dataset
RA	Right atrium
STL	Stereolithography
SVC	Superior vena cava
TAWSS	Time-averaged wall shear stress
TV	Tricuspid valve
WSS	Wall shear stress

CHAPTER 1

INTRODUCTION

Cardiovascular diseases (CVD) are the leading cause of global mortality, accounting for approximately 32 % of all deaths worldwide (IHME, 2019; Roth *et al.*, 2020). In addition to increased morbidity, the healthcare costs involved in treating patients with CVD are substantial: in the UK, these are estimated at £9 billion each year (Roth *et al.*, 2020). CVD is an umbrella name for multiple conditions, including those that affect the heart and heart valves. One of these is the mitral valve (MV), located in the left heart and quite complex in shape and function (McCarthy *et al.*, 2010). When the structural integrity of the MV is compromised, due to increasing age or other factors, valvular dysfunction occurs: anatomical changes can affect mitral performance, inducing backflow (or regurgitation) and resulting in suboptimal ventricular filling and ejection (Al-Atabi *et al.*, 2012; Castillo *et al.*, 2011). MV disease, especially calcification (increased accumulation of calcium on the mitral leaflets), is also strongly associated with the prevalence and incidence of chronic kidney disease, a condition in which the kidneys become faulty and do not filter blood correctly, affecting approximately 15 % of adults in the UK (NHS, 2016).

The only way to stop the progression of MV dysfunction is to have surgery that restores it to its native, healthy shape. Given the complexity of its structure, surgical approaches to improve the durability of repairs are permanently evolving. Indeed, MV repair is associated with excellent long-term survival rates and restoration of function (Lazam *et al.*, 2017). However, in several cases, surgery itself alters the shape of the MV, inducing alterations in its biomechanics (Kong *et al.*, 2020; Errthum *et al.*, 2021). This can lead to residual valvular dysfunction, and

reoperation of the MV. There is limited knowledge linking long-term changes in mitral shape and function. Given the anatomical complexity of the MV, cardiologists and cardiac surgeons would benefit from greater understanding of each patient's MV shape and performance during diagnostic and surgical planning.

On the other hand, treatment for chronic kidney disease would also potentially reduce the risk of calcification for the MV and associated dysfunction. This condition is usually treated through haemodialysis with the use of central venous catheters, devices which filter blood externally and which are inserted in the right heart (specifically the right atrium) (Smith and Nolan, 2013). Various catheter designs are available in the market, with the goal to optimise their performance (Knuttninen *et al.*, 2009). Nevertheless, haemodialysis catheters are associated with diverse issues, including the inability to aspirate blood and the presence of low flow rates.

Echocardiography is the clinical tool of choice for MV assessment and surgical planning (Weiner *et al.*, 2012), as well as insertion procedures of haemodialysis catheters in the right heart. While 2-dimensional (2D) and 3-dimensional (3D) modalities provide detailed morphologic and functional data of the MV (Lee *et al.*, 2013; Jolley *et al.*, 2017), Doppler echocardiography is used to evaluate hemodynamics (Grigioni *et al.*, 2015). However, global measures currently used are unable to capture high/abnormal stresses induced on the valve leaflets post-surgery. These can lead to post-surgical failure or impairment of valvular function (Al-Atabi *et al.*, 2012) by inducing leaflet remodelling and thickening (Kruithof *et al.*, 2020). Moreover, such global measures are not sufficient to determine whether a haemodialysis catheter is performing adequately, and further metrics are necessary for this effect.

Computational models provide a viable alternative for surgical planning of the MV and of the insertion of catheters for haemodialysis, as they are able to predict stress distributions and blood flow characteristics. This could potentially improve MV surgical planning by enabling a virtual

evaluation of pre- and post-operative scenarios in order to find a surgical procedure ideal for a patient, and which would preserve their native valve geometry and associated biomechanics (Al-Atabi et al., 2012; Kruithof et al., 2020).

Previous computational models of the MV have indeed predicted mitral transvalvular flow and leaflet stresses in disease/post-repair cases, usually employing accurate geometries obtained from patient-specific medical imaging (Kong *et al.*, 2020; Pham *et al.*, 2017; Mansi *et al.*, 2012). The accuracy of these geometries is an important factor which determines the reliability of the computer model of predicting MV physiology. However, (1) these geometries correspond to the valve shape at the time of surgery, not accounting for a subject's growth, for example, and (2) the time required to set-up/solve the associated models has been a major barrier for translation into clinical practice (Shinbane and Saxon, 2018). While several frameworks allow to obtain MV geometries from medical images and solve the associated models (Mansi *et al.*, 2012; Mansi *et al.*, 2011; Zhang *et al.*, 2017), they are only applicable to a unique set of medical images at the time. This means that they do not offer the flexibility to generate a number of models covering the anatomical variability inter- and -intra-patients, or representing the growth of a patient and that of their own valve. There is, therefore, the absence in existing studies of a framework which incorporates a realistic shape of the MV and allows to create a scalable, parametric model of this valve.

On the other hand, computational studies have assessed catheter performance by providing an insight into how to optimise their designs (Clark *et al.*, 2015; Clark *et al.*, 2012). These studies have mostly used idealised geometries for catheter insertion, neglecting the realistic environment in which these devices are actually inserted inside the human body. Practically no literature is available on the computational modelling of the right heart and, therefore, there is a need for a proper assessment of modelling criteria for these. Using a validated model of the

right atrium as a simulation platform to evaluate haemodialysis catheter performance would allow for a more accurate assessment of important haemodynamic characteristics, including blood flow patterns, recirculation, among others.

The aim of this thesis was to perform a combined morphometric and computational study of components from both the left and right sides of the heart: regarding the left side of the heart, the aim was to produce a framework allowing the quick creation of anatomically accurate parametric models of the MV, to subsequently be used in numerical simulations of MV function; regarding the right side of the heart, the aim was to develop a blood flow model of the right atrium, validated against the literature, to be used as a simulation platform for the evaluation of several designs of haemodialysis catheters.

To fulfil this aim, three main objectives were pursued:

- ❖ To evaluate MV morphometry and mathematical representations of its shape through regression analysis of key dimensions and assessment of the accuracy in predictions from mathematical equations obtained;
- ❖ To generate a computational framework incorporating a realistic MV shape and able to quickly generate a scalable, parametric MV model, including all steps from geometry generation to the preparation for finite element simulations;
- ❖ To develop a blood flow simulation platform for the right atrium, allowing for the evaluation of the performance of different haemodialysis catheter designs.

1.1. Thesis overview

This thesis is divided into seven chapters:

- ❖ The present introduction (Chapter 1) outlines the motivations for the work presented in this thesis, as well as respective aims and objectives;
- ❖ In Chapter 2, the background required to understand the work presented in subsequent chapters is described. This includes a description of the anatomy and physiology of the MV and right atrium, as well as the biomechanical properties of the MV. The connection between MV geometry and function is outlined, including pathways to disease. Moreover, the use of the right atrium as a treatment platform for chronic kidney disease is explained. The concepts of computational modelling for the MV and the right atrium are elucidated, and previous studies on these topics are assessed;
- ❖ Chapter 3 includes the evaluation of MV morphometry for healthy and diseased cases through the analysis of mathematical correlations and empirical equations found in the literature, as well as obtained from medical images. This chapter includes correlation analyses between key dimensions, and an assessment of their employability as prediction equations through application to other *in vivo* and *ex vivo* datasets;
- ❖ Chapter 4 details the development of a parametric and scalable geometrical model of the MV, using a MATLAB-based toolbox able to quickly generate a variety of MV shapes. In this chapter, the workflow of the toolbox is described, including user options, key dimensions needed to parameterise the MV, and examples of generated shapes;
- ❖ Chapter 5 describes the automatized pre-processing of the MV model for finite element simulations, implemented within the MATLAB framework detailed in Chapter 4. All boundary conditions, material properties and control options are explained, and the biomechanics

associated with a healthy MV geometry being validated against the literature. Moreover, the analysis of two patient-specific MV models is included;

❖ In Chapter 6, the development of a physiological model of the right atrium employing computational fluid dynamics is described, as well as its validation against data in the literature. Moreover, the use of this novel simulation platform to evaluate the performance of four catheter designs is detailed, leading to insight on design features which need optimisation in future devices;

❖ Lastly, Chapter 7 summarises the main findings of this thesis and provides an overall discussion, including scope for future work and conclusions.

CHAPTER 2

BACKGROUND

2.1. Introduction

The development of accurate computational models which can be used to (1) represent the physiological of a cardiovascular component such as the MV or (2) evaluate the design of biomedical devices, such as haemodialysis catheters, requires the analysis of the current state-of-the-art. This chapter first introduces the anatomy and physiology of the heart (section 2.2) and is then divided into two main sections, focusing on topics related to each side of the heart:

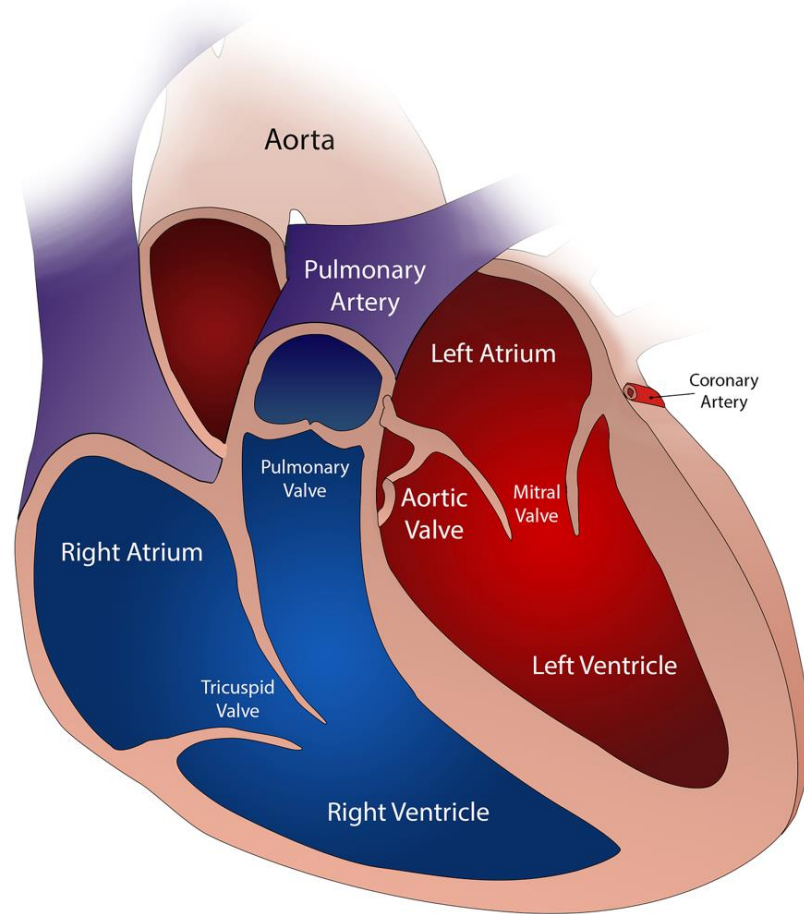
- ❖ Regarding the left side of the heart (sections 2.3-2.7), focus is given to the MV, and a description of its anatomy and the mathematical analysis of its geometry is performed. The biomechanical properties of the MV, and their connection with its function, are described. Further, the pathophysiology of MV disease is outlined, including how changes in its geometry are associate with the onset of dysfunction and how surgical treatments aim to restore that geometry in order to improve performance. The finite element (FE) method is introduced as a powerful tool to study MV function in healthy, diseased and repaired cases, providing an overview of the models previously developed;
- ❖ The use of the right side of the heart as a location for treatment of chronic kidney disease is explained (sections 2.8-2.9). An introduction to chronic kidney disease and its relationship with MV disease is performed. Further, the use of haemodialysis catheters inserted on the right side of the heart to treat chronic kidney disease is outlined, as well as associated malfunctions and pathways for upcoming research.

2.2. Heart anatomy and physiology

The heart, located in the centre of the chest in the thoracic cavity, functions as a mechanical cycling pump, pumping blood throughout the circulatory system (Tortora and Derrickson, 2014). The healthy heart beats around 60 to 90 times per minute (Mason *et al.*, 2007), yielding a typical cardiac cycle period of 0.675 to 1 s. The right and left sides of the heart are associated with different functions: while the right (venous) side received deoxygenated blood from the circulatory system and sends it to the lungs, the left (arterial) side pumps oxygenated blood from the lungs throughout the body (Goodman, 2004). The anatomy of both right and left hearts is different, with the left side having four times more muscle than the right side. This causes a change in the pressure environment: the arterial side pumps blood at higher pressures (69 and 114 mmHg for diastole and systole, respectively) and throughout the whole body (Reference Values for Arterial Stiffness, 2010), while the venous side, with a thinner muscle layer, pumps blood at lower pressures (8 to 10 mmHg) and through shorter distances (Goodman, 2004; Gelman, 2008).

Both sides of the heart are separated into upper and lower chambers, represented in Figure 2.1a). The atria (upper chambers) fill with venous blood during diastole and direct it to the ventricles (lower chambers). At systole, the ventricles contract and pump blood away from the heart (Goodman, 2004; Tortora and Derrickson, 2014). The four heart valves open and close to control the passage of blood flow between the chambers and out of the heart, preventing backflow during systole (Goodman, 2004). This function creates pressure gradients across the valves which aid propelling blood flow in the correct direction and generating the correct pressure environments in each chamber (Figure 2.1b).

a)



b)

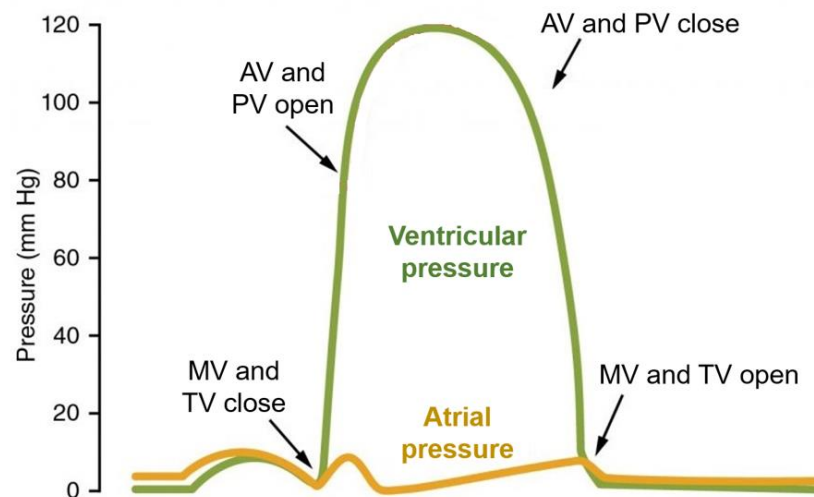


Figure 2.1: a) Heart anatomy diagram displaying the right (blue) and left (red) sides, with the four chambers and respective valves (reproduced from pixabay under CC BY-SA 3.0: <https://creativecommons.org/licenses/by-sa/3.0/deed.en>); b) Example of physiological ventricular and atrial pressures over one cardiac cycle, with timings for heart valve opening and closing indicated. Notes: AV, aortic valve; PV, pulmonary valve; MV, mitral valve; TV, tricuspid valve.

2.3. Mitral valve anatomy and physiology

The MV lies between the left atrium and left ventricle (LV). It has a complex geometry comprising the mitral annulus, the anterior (AL) and posterior (PL) leaflets and the subvalvular apparatus (Figure 2.2). The latter is formed by the chordae tendineae and the papillary muscles (PM), which are inserted into the LV wall (McCarthy *et al.*, 2010; Dal-Bianco and Levine, 2013; Topilsky, 2020). These structures work in synchrony towards its effective mechanics to enable closing and opening through the cardiac cycle (McCarthy *et al.*, 2010).

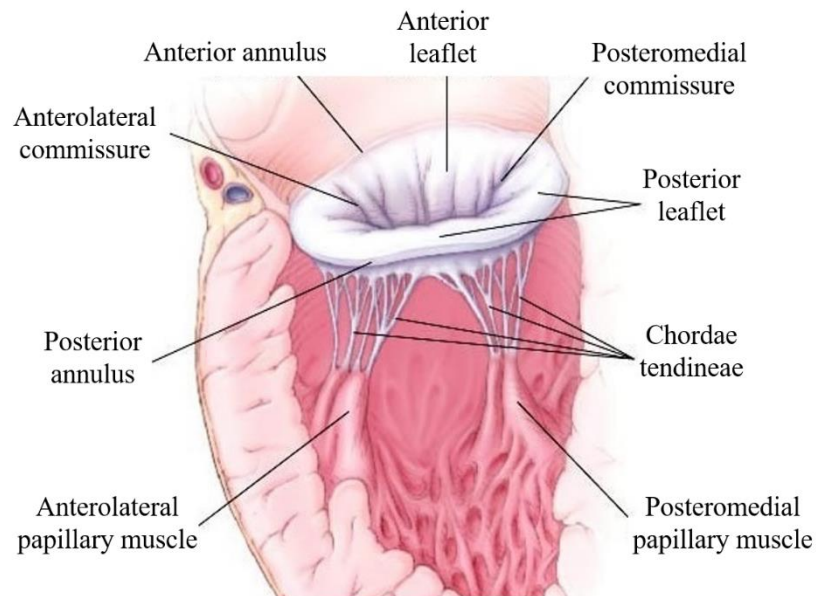


Figure 2.2: Schematic of mitral valve anatomy, fitted within the left heart and including all anatomical components. Reproduced with permission from (Otto, 2001), Copyright Massachusetts Medical Society.

2.3.1. Annulus

The annulus is a ring of fibrous tissue circumscribing the perimeter of the MV orifice and its base, anchoring it within the left heart (Dal-Bianco and Levine, 2013) and sharing a fibrous continuity with the aortic valve (Veronesi *et al.*, 2009; Ranganathan *et al.*, 1970). This adjacent section defines the anterior portion of the mitral annulus, limited by the left and right fibrous

trigones; the posterior part of the annulus is distal to the trigones and includes the lower points of its saddle shape (Dal-Bianco and Levine, 2013; Pouch *et al.*, 2014; Jassar *et al.*, 2014). Its shape and associated diameters vary during the cardiac cycle (Jiang *et al.*, 2014; Tang *et al.*, 2019; Topilsky *et al.*, 2013), making it a dynamic structure: in diastole the annulus has a more circular shape, while in systole its non-planarity is more enhanced in synchrony with valve closure/leaflet coaptation, reducing mechanical stress during systole (Garbi and Monaghan, 2015; Al-Atabi *et al.*, 2012; Dal-Bianco and Levine, 2013). A schematic representation of the annulus is presented in Figure 2.3, including key dimensions.

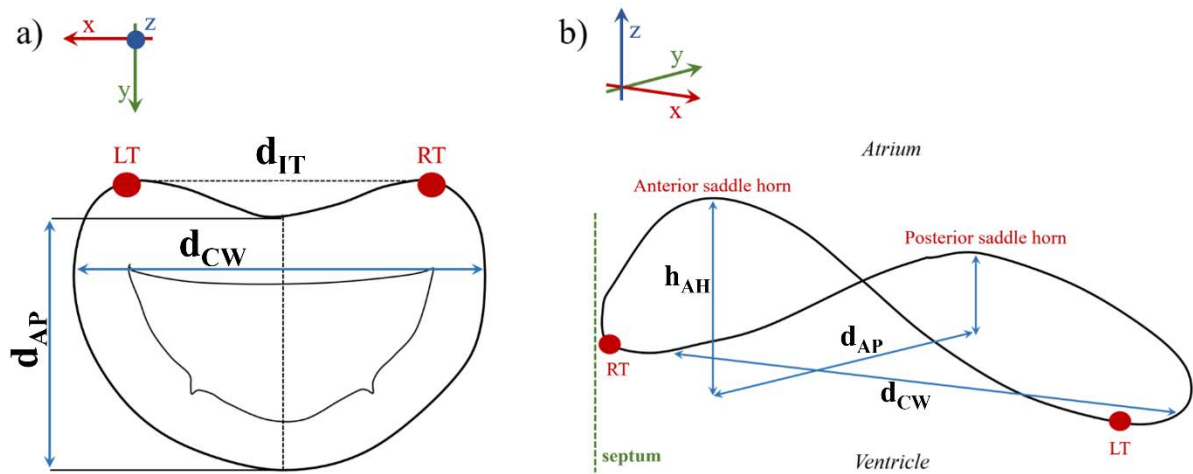


Figure 2.3: MV annulus a) viewed from within the left atrium and b) from above, with key anatomical landmarks and dimensions represented. Notes: LT, left trigone; RT, right trigone; d_{IT} , distance between trigones; d_{AP} , anteroposterior diameter; d_{CW} , commissural width; h_{AH} , annular height.

2.3.2. Leaflets

The leaflets of the MV are a continuous band of tissue extending from the annulus. According to their geometrical form and anatomical connection to the annulus, the leaflets are divided into anterior, posterior and commissural parts (Dal-Bianco and Levine, 2013; McCarthy *et al.*, 2010). The PL has a semilunar shape and a relatively short radial length in comparison with the

AL, being composed of three minor semi-oval scallops: a central one opposite to the anterior leaflet, and two other, to each side (Ranganathan *et al.*, 1970; Dal-Bianco and Levine, 2013; Carpentier *et al.*, 1995). The AL, on the other hand, is dome-shaped, longer and thicker (Ranganathan *et al.*, 1970; Dal-Bianco and Levine, 2013).

Tissue characteristics of both leaflets also change accordingly to region, as stated by previous human mitral valve studies and as displayed in Figure 2.4: while the central portion is thinner and smoother (clear zone), towards the free edges the tissue becomes thicker and rougher (rough zone) (Al-Atabi *et al.*, 2012; Dal-Bianco and Levine, 2013; McCarthy *et al.*, 2010): this is the main area of chordae tendineae attachment and usually extends 6 to 8 mm from the free edges of the leaflets (Lam *et al.*, 1970; Dal-Bianco and Levine, 2013). In systole, the leaflets coapt along the rough zone (or zone of apposition), closing the valve (Ranganathan *et al.*, 1970); in diastole, the leaflets separate and the valve opens (McCarthy *et al.*, 2010). The PL also possesses a chordae attachment area near the annulus, named the basal zone (Lam *et al.*, 1970).

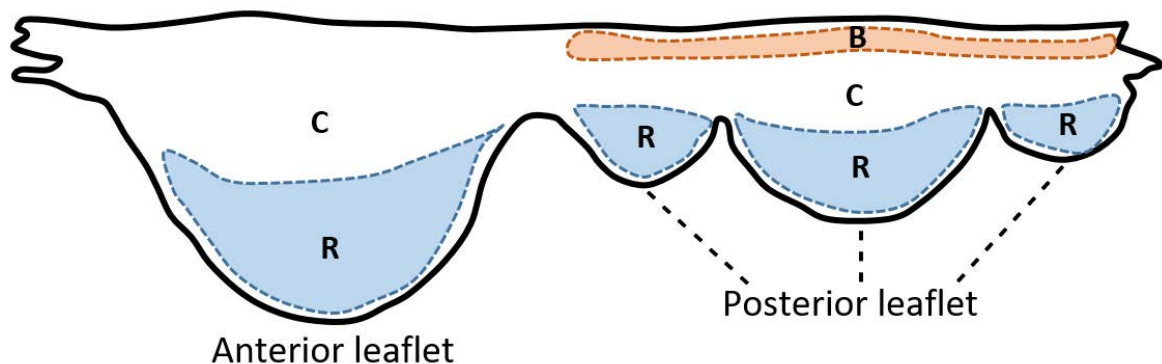


Figure 2.4: Human mitral valve leaflet shape and main areas of different tissue characterisation. Notes: C, clear zone; R, rough zone; B, basal zone.

2.3.3. Chordae tendineae

The chordae are chord-like structures that arise from the tip of either of the two PMs and insert into the leaflets (Lam *et al.*, 1970; Al-Atabi *et al.*, 2012), as displayed in Figure 2.5. They are

characterized according to their point of attachment and size: in a human MV, the marginal chordae are thinnest and attach to the free edge of the leaflets; basal chordae are thicker and more extensible, inserting between the free edges and the leaflet's attachment to the annulus (rough zone). There are two thick basal chords (strut chordae) that arise from the tip of each PM and insert into the anterior leaflet: these are the largest and thickest of all chordae, carrying also the highest tension (Al-Atabi *et al.*, 2012; Lam *et al.*, 1970; Dal-Bianco and Levine, 2013; Lomholt *et al.*, 2002; Wilcox *et al.*, 2014). Their insertion region into the anterior leaflet experiences varying stretch during the cardiac cycle, which demonstrates a transfer of forces from the leaflets to the chordae and vice versa and aids in valve function (Padala *et al.*, 2010). There are also tertiary chordae, which originate at the LV wall and connect to the basal region of the PL (Al-Atabi *et al.*, 2012; McCarthy *et al.*, 2010). According to porcine and ovine studies, different types of chordae are associated with different functions, as presented in Table 2.1.

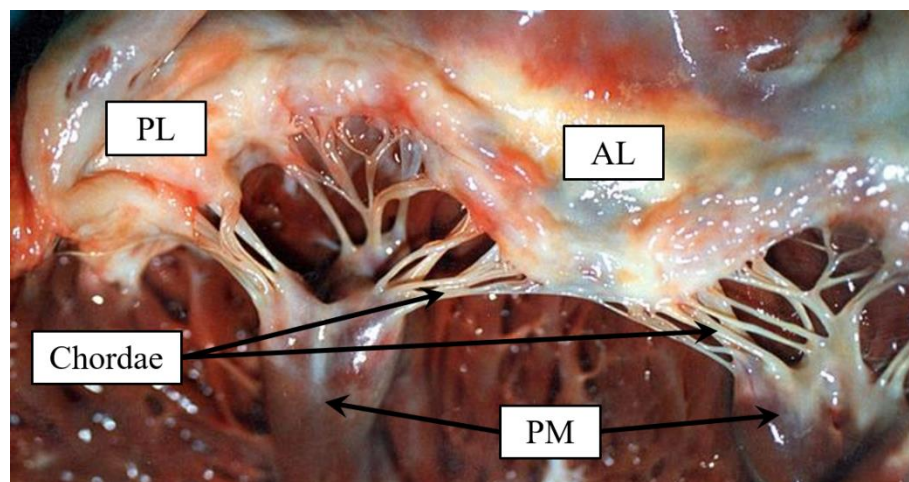


Figure 2.5: Ex vivo example of chordae tendineae arising from both PMs and branching before inserting into the AL and PL (adapted from pixabay under CC BY-SA 4.0: <https://creativecommons.org/licenses/by-sa/4.0/>). Notes: AL, anterior leaflet; PL, posterior leaflet; PM, papillary muscle.

Table 2.1: Classification of chordae tendineae and their role in MV function (Espino *et al.*, 2005; Timek *et al.*, 2001; Nielsen *et al.*, 2003; Sedransk *et al.*, 2002; Wilcox *et al.*, 2014; Lam *et al.*, 1970; Faletra and Narula, 2017).

Type	Leaflet attachment	Function
Marginal (primary: includes commissural and cleft chordae)	Free edge	Leaflet coaptation during systole
Basal (secondary)	Rough zone	Support and transfer loads to leaflets
Strut (secondary)	Ventricular portion of AL	Carry high loads to protect marginal chordae from failure
Tertiary	Ventricular portion of PL	To limit PL motion

2.3.4. Papillary muscles

The two PMs are known as anterolateral and posteromedial, relative to the anterior and lateral body orientations and indicating the anatomical parts of the LV wall into which they insert. Similarly to the mitral annulus, they are dynamic structures that move through the cardiac cycle, to ensure appropriate MV coaptation. Moreover, PM and annular motion are intrinsically connected: during early systole, the PMs displace closer to the annulus, contracting throughout middle and late systole, shortening their own length and increasing the distance between the PM tips and the annulus (Topilsky *et al.*, 2013; Topilsky, 2020).

The human PMs exhibit great morphological variability. Although two in number (Al-Atabi *et al.*, 2012), there are usually groups of muscles adjoining, reaching a total number as high as five and attaching to the LV wall either at its middle, upper or lower sections (Saha and Roy, 2018). Moreover, their shape is diversified, resembling either a cone (conical shape), having a truncated shape, or being bifurcated or trifurcated (Saha and Roy, 2018). Further, the number of chordae tendineae that attach to the PM, as well as their insertion distribution, is a source of variability. These features contribute to PM morphological heterogeneity, either in shape or attachment site.

2.3.5. Mathematical analysis of mitral valve geometry

Medical imaging modalities have been used to obtain dimensions of the MV in healthy (Sonne *et al.*, 2009; Mihaila *et al.*, 2014; Jolley *et al.*, 2017; Pouch *et al.*, 2014) and diseased (Lee *et al.*, 2013; Mihaila, 2013; Jassar *et al.*, 2014; Calleja *et al.*, 2015) geometries, including dimensions related to the subvalvular apparatus, such as PM distances to annulus and chordae tendineae lengths (Delgado *et al.*, 2009; Obase *et al.*, 2016; Obase *et al.*, 2015). Given the dynamic variability of the MV, further studies have published quantitative measurements throughout the whole cardiac cycle (Topilsky *et al.*, 2013; Jiang *et al.*, 2014; Tang *et al.*, 2019).

While most of these studies just report key MV dimensions, some attempt to find mathematical correlations between measurements. For instance, Okamoto *et al.* performed an anatomical study with excised human hearts where they examined MV geometry by assuming the mitral annulus as a circle and the anterior (A_{AC}) and posterior (P_{AC}) annular circumferences as arc lengths, as displayed in Figure 2.6.

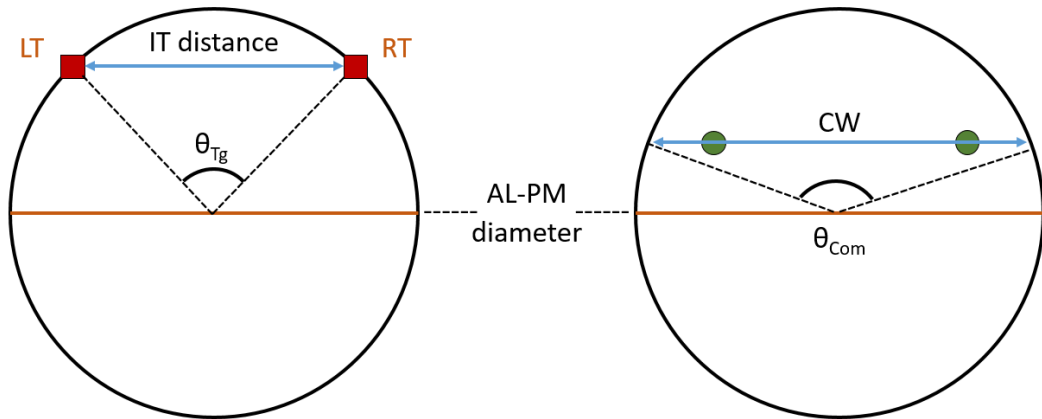


Figure 2.6: Circle representing the annulus, according to Okamoto *et al.* (2007), with relevant dimensions highlighted. Notes: LT, left trigone; RT, right trigone; AL-PM diameter, anterolateral-posteromedial diameter; CW, commissural width; IT distance, inter-trigonal distance; θ_{Tg} , trigonal angle; θ_{Com} , commissural angle.

This work underlined positive linear relationships between these dimensions and a dimensionless Z-value representing the annular diameter (or AL-PM distance), as given by equations 2.1 ($R^2 = 0.66$, p-value < 0.01) and 2.2 ($R^2 = 0.91$, p-value < 0.01) (Okamoto *et al.*, 2007):

$$A_{AC} = 25 + 0.42d_{AL-PM}, \quad (2.1)$$

where d_{AL-PM} represents the AL-PM distance, with both variables in mm,

$$P_{AC} = 44 + 1.2d_{AL-PM}, \quad (2.2)$$

where both variables are in mm. Further, the authors of this study have mathematically defined the A_{AC} , P_{AC} and the inter-trigonal distance, assuming the annulus divided into anterior and posterior portions by the left and right trigones or commissures, as displayed in Figure 2.6 and defined by equations 2.3-2.5:

$$d_{IT} = 2 \cdot d_{AL-PM} \cdot \sin\left(\frac{\theta_{Tg}}{2}\right), \quad (2.3)$$

$$A_{AC} = \pi \cdot d_{AL-PM} \cdot \theta_{Tg} \cdot \theta_{Com}, \quad (2.4)$$

$$P_{AC} = \pi \cdot d_{AL-PM} \cdot (360 - \theta_{Tg} \cdot \theta_{Com})/360, \quad (2.5)$$

where d_{IT} is the inter-trigonal distance, θ_{Tg} is the angle between left and right trigones and θ_{Com} is the angle between commissures at the annular plane (Okamoto *et al.*, 2007).

Another author has discussed that the coaptation triangle (2D triangle formed by the anteroposterior (AP) diameter, anterior and posterior leaflets when the leaflets coapt, represented in Figure 2.7, including tenting height, tenting area, and leaflet angles, also play an important role in the evaluation of human MV geometry and function (Deorsola and Bellone, 2018; Delgado *et al.*, 2009; Silbiger, 2011; Ciarka *et al.*, 2010). Deorsola *et al.* hypothesized that the coaptation triangle of healthy valves could be based on the Golden Ratio, a ratio observed in Nature which derives from sectioning a certain segment in two different parts (Deorsola and Bellone, 2018). Such ratios yield an irrational number (rounded to 0.618 or 1.618) known as the Golden Ratio. This study states that the value of 0.618 can be obtained through the ratio between the anterior cord and the AP diameter, between the posterior and the anterior cords and between the tenting height and the posterior cord.

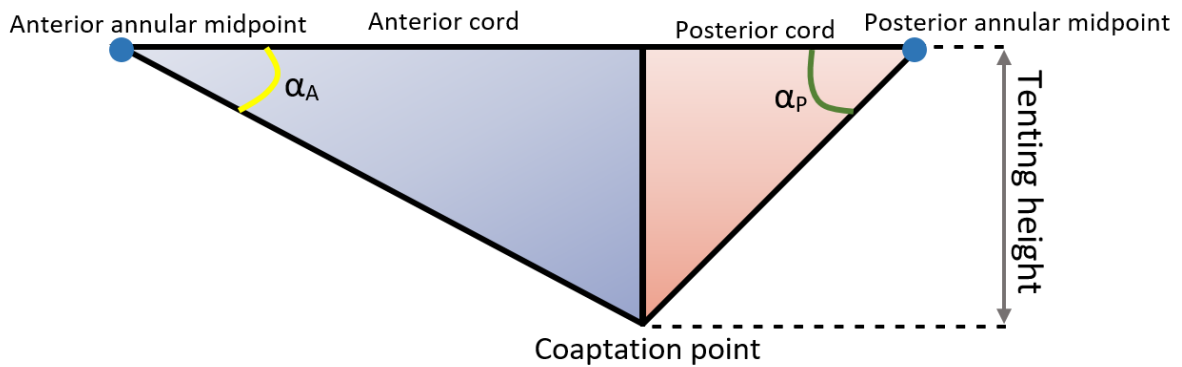


Figure 2.7: Coaptation triangle, where the hypotenuses can be considered as a simplified representation of the anterior and posterior leaflets. The tenting height divides the base of the triangle (AP diameter) into two segments – the anterior and the posterior cords. Notes: α_A , anterior leaflet angle; α_P , posterior leaflet angle.

Indeed, Deorsola *et al.* found strong correlations between the original coaptation triangle and the Golden (or mathematical) one at early systole ($0.353 \leq R^2 \leq 0.966$). Moreover, good linear relationships were found between the AP diameter and the anterior cord (equation 2.6, $R^2 = 0.97$, p-value < 0.01) and between anterior and posterior cords (equation 2.7, $R^2 = 0.82$, p-value < 0.01):

$$A_{\text{cord}} = 1.391 + 0.580d_{\text{AP}}, \quad (2.6)$$

where d_{AP} (AP diameter) and A_{cord} (anterior cord) are in mm,

$$P_{\text{cord}} = -1.279 + 0.667 \cdot A_{\text{cord}}, \quad (2.7)$$

where the A_{cord} and P_{cord} (posterior cord) are in mm. Unfortunately, only the early systolic frame of the cardiac cycle was evaluated, and it is unclear whether the correlations found would be maintained throughout the cardiac cycle (Deorsola and Bellone, 2018). In a more recent study performed by the same authors at a diastolic frame, correlations were found between the AP diameter and AL (equation 2.8, $R^2 = 0.94$, p-value = 0.01) and PL (equation 2.9, $R^2 = 0.94$, p-value = 0.01) lengths, as well as between the AL and PL lengths (equation 2.10, $R^2 = 0.98$, p-value = 0.01):

$$A_h = 3.2061 + 0.9764d_{\text{AP}}, \quad (2.8)$$

$$P_{\text{mh}} = -1.4546 + 0.6731A_h, \quad (2.9)$$

$$P_{mh} = 0.5344 + 0.6626d_{AP}, \quad (2.10)$$

where A_h and P_{mh} are the middle anterior and posterior leaflet heights, respectively.

The results obtained by Deorsola *et al.* and Okamoto *et al.* demonstrate how different components of MV geometry can be mathematically defined, and how several MV dimensions are mathematically correlated (Deorsola and Bellone, 2018; Deorsola and Bellone, 2019; Okamoto *et al.*, 2007). These preliminary observations demonstrate that there is additional scope to determine more correlations between additional dimensions, in order to potentially define a unique mathematical model representing the overall shape of the MV.

2.4. Biomechanical properties of the mitral valve

2.4.1. Leaflets

The mitral leaflets consist of four histological layers with different biomechanical properties which allow them to withstand high tensile forces, stretch and recoil (Sacks *et al.*, 2009): the atrialis (facing the left atrium), the spongiosa (middle layer), the fibrosa and the ventricularis (on the ventricular surface). The atrialis is a thin layer composed mainly of a network of aligned elastin and collagen fibres, potentially associated with leaflet remodelling in the onset and progression of pathology (Dal-Bianco *et al.*, 2009). Comprising the majority of the free edge, the spongiosa layer consists of a loose connective tissue matrix rich in proteoglycans and glycosaminoglycans, along with elastic fibres and loosely organised collagen. Due to this composition, it has been hypothesized that this layer protects the leaflets during closure and opening of the valve (McCarthy *et al.*, 2010), and especially as they experience shearing, but

further studies are required to fully understand its role (Sacks and Yoganathan, 2007). Beneath the spongiosa is the fibrosa, a major load-bearing layer during MV closure which forms the central structural collagenous core of each leaflet. This is the thickest layer of the MV (Gumpangseth *et al.*, 2020), being composed of a dense network of crimped and predominantly circumferentially aligned collagen fibres which provide the tissue reinforced stiffening during loading (Kramer *et al.*, 2019). Finally, the ventricularis is the thinnest layer, covered by a continuous sheet of endothelial cells folded with elastin and collagen fibres. It contributes to the formation of chordae tendineae, as these structures insert on the ventricular side of the leaflet (McCarthy *et al.*, 2010). Since both the atrialis and ventricularis layers have a similar histological composition, both facilitate leaflet movement and restoration to the valve's unloaded geometry after closure (Kramer *et al.*, 2019).

The biomechanical response of the mitral leaflets when subjected to loading is non-linear and anisotropic, as obtained by experimental tension tests performed on leaflet tissue samples (May-Newman and Yin, 1998). This non-linear behaviour is a result of collagen fiber distribution and its mechanical response, associated with different stiffnesses in fiber/cross-fiber directions (Rausch *et al.*, 2013). These mechanical responses greatly vary between the AL and PL, since the structural composition of their tissue layers differs. Given that the AL withstands higher loads than the PL, its predominant layer is the fibrosa, as represented in Figure 2.8; on the opposite, the PL is thinner and more flexible (Kunzelman *et al.*, 1993b). Regardless, the tissue histology of both leaflets is altered with age (Gumpangseth *et al.*, 2020) or due to pathological states (Dal-Bianco *et al.*, 2009). Gumpangseth *et al.* observed increasing elastin and collagen fibers with advancing age, with the presence of elastic fiber fragmentation and irregular and denser fiber networks. In cases of MV structural degeneration, thickened leaflet tissue with irregular regions of collagen and microstructural alterations in the fibrosa layer has been found

(Hadian *et al.*, 2007). On the other hand, it has been observed that the subjection of the leaflets to abnormal stress can induce interstitial cell activation and proliferation, potentially associated with an adaptation mechanism which can lead to leaflet enlargement during pathological conditions (Dal-Bianco *et al.*, 2009). These indicate that changes in the leaflet tissue microstructure can alter the biomechanical properties of the MV, leading to dysfunction.

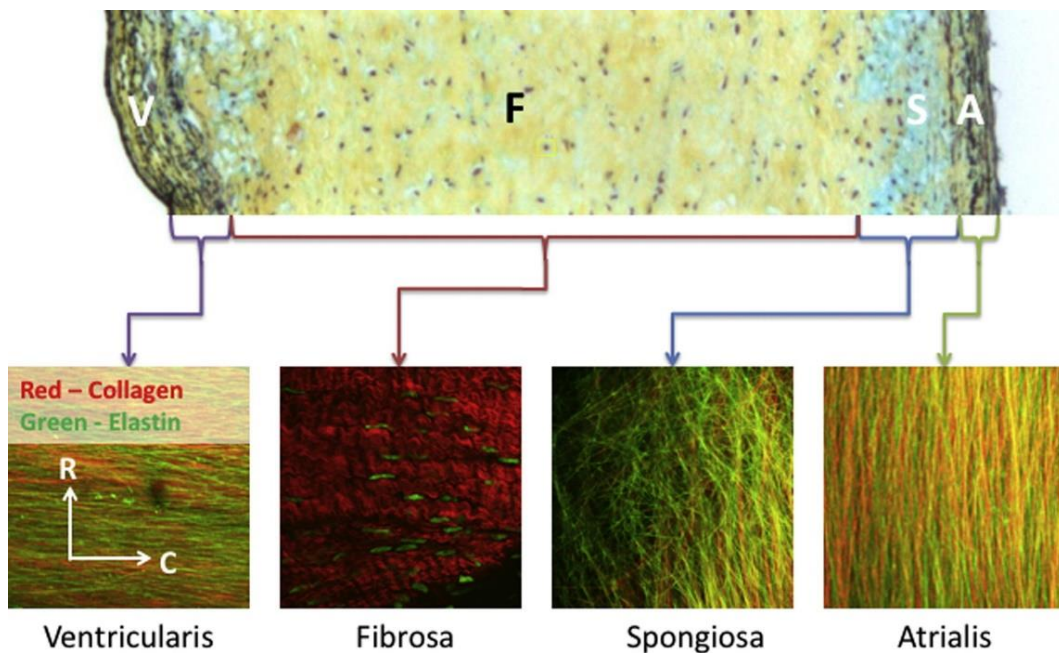


Figure 2.8: Microstructure of the central region of the AL, showcasing the main four tissue layers. The relative thickness of each layer is showcased, with collagen and elastin fibers being coloured in red and green, respectively. The referential indicates the circumferential (C) and radial (R) directions of the fibers. Notes: V, ventricularis; F, fibrosa; S, spongiosa; A, atrialis (reproduced with permission from (Zhang *et al.*, 2016)).

2.4.2. Chordae tendineae

The chordae tendineae are fibrous chords composed of collagen and elastin, similarly to the MV leaflets. The collagen fibers are densely organised in the innermost core of the chordae, aligned with the longitudinal direction of the chordae itself (Zuo *et al.*, 2016; Millington-Sanders *et al.*, 1998). When relaxed, these collagen fibers are arranged in an undulating pattern,

and straighten when the PM contracts and chordae stretch, helping reduce the stress created with PM contraction (Millington-Sanders *et al.*, 1998). This behaviour gives rise to a non-linear biomechanical response (Kunzelman and Cochran, 1990) which varies according to the type of chordae: while marginal chordae have the highest collagen density associated with limited extensibility which prevents leaflet edge inversion and flail, secondary chordae have more elastin, being less stiff (Obadia *et al.*, 1997).

Similarly to the leaflets, the histology and associated biomechanical response of the chordae alters with pathological loading conditions or with increasing age. For example, the cross-sectional area of the collagen network in the chordae reduces with increasing age, potentially leading to stretching and rupture of the chordae (Millington-Sanders *et al.*, 1998).

2.5. Mitral valve disease

The physiological-functioning of all components of the MV (and the LV), as well as their ability to adapt to altered stress state imposed by the passage of blood flow, rely on their biomechanical properties and structural integrity (Al-Atabi *et al.*, 2012; Topilsky, 2020). The presence of abnormal function of any of the MV components can ultimately lead to mitral regurgitation (MR), a condition on which the leaflets do not coapt correctly, causing backflow from the LV into the left atrium (Al-Atabi *et al.*, 2012). This affects MV performance, resulting in suboptimal ventricular filling or ejection.

2.5.1. Pathophysiology of MR: Carpentier's functional classification

One of the most commonly used classifications of MR was designed by Alain Carpentier (Carpentier, 1983), sometimes referred to as the “pathophysiologic triad” (Carpentier *et al.*, 1980). It divides MV dysfunctions in three categories, all of which yield lesions that lead to

clinical mitral regurgitation (Figure 2.9). These categories are based on the position of leaflet margins with respect to the mitral annulus plane, with primary MR being a consequence of MV apparatus disease and secondary MR offsetting from LV pathologies such as myocardial infarction (Castillo *et al.*, 2011; Carpentier, 1983; Stone *et al.*, 2015; Al-Atabi *et al.*, 2012; El Sabbagh *et al.*, 2018). Type I refers to normal leaflet motion and is associated with annular dilation and leaflet perforation. Type II characterizes excessive leaflet motion which commonly leads to leaflet prolapse (leaflet bulging towards the left atrium) and is usually derived from elongation or rupture of the chordae tendineae and/or the PM. Type III relates to restricted leaflet motion, either diastolic and systolic (Type IIIa) or just systolic (Type IIIb). The first type (IIIa) is associated with leaflet and/or chordae thickening due to inflammatory or congenital diseases, including rheumatic MV disease. Additionally, calcium can deposit on the annulus or the leaflets (calcification), making these thicker and less flexible. In type IIIb, the PM is displaced away from the mitral annulus due to LV enlargement, causing systolic tethering of the mitral leaflets and preventing their motion. Further information on this classification and the associated lesions can be found elsewhere (Castillo *et al.*, 2011; Carpentier, 1983; Stone *et al.*, 2015; Al-Atabi *et al.*, 2012).

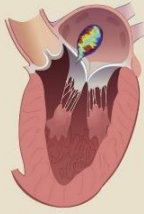
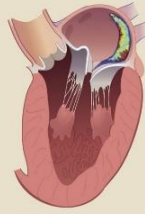
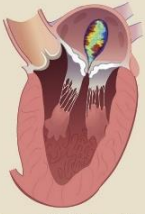
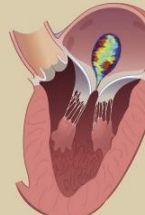
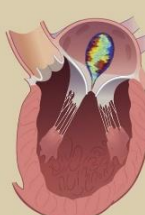
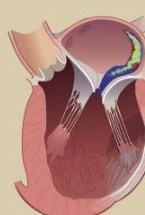
	Carpentier Type I	Carpentier Type II	Carpentier Type IIIa	Carpentier Type IIIb
	(normal leaflet motion and position)	(excess leaflet motion)	(restricted leaflet motion in systole and diastole)	(restricted leaflet motion in systole)
PRIMARY MR	 <p>Leaflet Perforation Cleft</p>	 <p>Mitral Valve Prolapse</p>	 <p>Rheumatic Valve Disease Mitral Annular Calcification Drug Induced MR</p>	
SECONDARY MR	 <p>Atrial MR</p>  <p>Nonischemic Cardiomyopathy</p>			 <p>Ischemic Cardiomyopathy</p>

Figure 2.9: Carpentier's classification for the aetiology of MV dysfunction. Reproduced from (El Sabbagh *et al.*, 2018), with permission.

2.5.2. Changes in mitral valve geometry during disease

Changes in MV shape are intrinsically connected with disease onset and progression. For example, changes in annular dimensions have been associated with different dysfunction scenarios. The increase in annular size associated with annular dilation compromises leaflet coaptation length (Silbiger, 2011). On the other hand, a previous *in vitro* study based on porcine MV showed that increasing annular area values were associated with a decrease in the pressures needed to cause MV failure (Espino *et al.*, 2007). The link between the effective regurgitant orifice area (EROA) and MV geometry serves as a validation of the role played by abnormalities in shape in dysfunctional cases. Concerning the human MV, increases in EROA, linked to greater severity of regurgitation, have been associated with increasing annular circumference and area at end-systole, although such associations were poorly correlated ($R^2 = 0.38$, $R^2 = 0.48$, respectively, with $p\text{-value} < 0.01$) (Cong *et al.*, 2018). Lee *et al.* (2013) have

also seen an inverse correlation between EROA and the annular height to commissural width ratio (AHCWR), showing loss of MV saddle shape with increasing regurgitation ($R^2 = 0.44$, p-value < 0.01) (Lee *et al.*, 2013). Other clinical studies have also correlated an increase in EROA with greater non-coaptation distance between leaflets (maximal distance between both leaflet edges) at end-systole, as given by equation 2.11 ($R^2 = 0.68$, p-value < 0.01) (Senechal *et al.*, 2012).

$$\lambda = 0.066 \cdot e^{(0.325 \cdot \mu)}, \quad (2.11)$$

where μ represents the non-coaptation distance (in mm) and λ represents the EROA (in cm^2).

Clinical studies also show that the MV annular flattening present in disease is associated with loss of nonplanarity (Silbiger, 2011; Lee *et al.*, 2013), quantified by increased non-planarity angles (NPAs) (Mihaila, 2013), and greater billowing. Indeed, a correlation between lower AHCWR and higher values of billow volume ($R^2 = 0.66$, p-value < 0.01) has been obtained at end-systole:

$$BV = 10.000 - 0.792 \cdot \varepsilon + 0.016 \cdot \varepsilon^2, \quad (2.12)$$

where BV represents the billow volume (ml) and ε represents the AHCWR (as a percentage) (Lee *et al.*, 2013).

Morphometric changes in the subvalvular apparatus also affect MV function. Clinical studies have shown that the PMs suffer displacement in an attempt to attenuate the regurgitation effects (Lee *et al.*, 2013; Silbiger, 2011); this is translated into increased inter-PM distance (Obase *et al.*, 2016; Kim *et al.*, 2014), which has been well correlated with increased regurgitant volume

in patients with severe functional ischemic mitral regurgitation, as mathematically described by the equation below for end-systolic data ($R^2 = 0.84$, $p\text{-value} < 0.01$):

$$RV = -36.440 + 1.434 \cdot v, \quad (2.13)$$

where RV represents the regurgitant volume (in ml) and v represents the inter-PM distance (in mm) (Jensen *et al.*, 2010). Moreover, an increase in left ventricular dimensions causes apical displacement of the PM, leading to increased annulo-papillary lengths and chordae tendineae elongation (Obase *et al.*, 2016). Previous clinical studies have connected PM displacement with the severity of mitral regurgitation: increased apical displacement of the posteromedial PM (PMPM) was associated with greater regurgitant volume (Jensen *et al.*, 2010) and augmented tethering distance, characteristic of PM displacement, was correlated with increasing mitral regurgitation fraction (equation 2.14, R^2 stated as 0.64, $p\text{-value} < 0.01$) (Uemura *et al.*, 2005):

$$M_{RF} = -60.990 + 3.583 \cdot TD, \quad (2.14)$$

where TD represents the PMPM tethering distance (in mm/m²) and M_{RF} represents the mitral regurgitation fraction (as a percentage). Another clinical study found independent associations between apical displacement of the PMPM and posterior displacement of the ALPM with increasing tenting area, related to loss of systolic annular function and regurgitation (Yiu *et al.*, 2000). However, the obtained data was too dispersed to yield strong correlations amongst these parameters.

As detailed above, MV geometry and function are interlinked, with geometrical alterations in any component of this valve leading to dysfunction. Further studies focusing on the influence

of MV shape in the onset of disease are, therefore, critical to understand the interplay between the two, and potentially determine which dimensional changes affect MV function the most.

2.5.3. Treatments for MV disease

Several surgical approaches are available for MV dysfunction, depending on its aetiology and pathophysiology (El Sabbagh *et al.*, 2018; Al-Atabi *et al.*, 2012). These can include the incorporation of biocompatible materials within the MV structure, the use of repair methods or even the replacement of the MV with a mechanical valve.

Usual approaches and drawbacks

MV repair procedures have been greatly improved over the last decades, leading to lower mortality rates, greater long-term survival and quality of life in comparison with MV replacement (Lazam *et al.*, 2017). A conventional approach to treat a dilated annulus, for instance, is annuloplasty, in which a ring is inserted into the annulus to restore its shape (Carpentier, 1983). In the case of leaflet perforation, leaflet resection is performed in addition to annuloplasty, removing the perforated segment (Bashore *et al.*, 2006). If the leaflets are thickened, surgery focuses on re-opening fused commissures and restoring normal chordal length, usually achieved with valve replacement (Feindel *et al.*, 2003; Bonow *et al.*, 2008).

If the cause of MV dysfunction is in the subvalvular apparatus, adjunctive procedures to annuloplasty are usually necessary to mitigate MR (Al-Atabi *et al.*, 2012; Silbiger, 2011). If the chordae are affected (e.g. chordal rupture), other procedures are usually considered. Chordal replacement consists of replacing the affected chordae using synthetic materials (e.g. expanded polytetrafluoroethylene sutures); however, given the increased stiffness in replacement materials in comparison with native chordae, this approach may reduce leaflet mobility, and the

artificial chordae can suffer elongation and calcification, leading to native chordae rupture (Tabata *et al.*, 2014; Colli *et al.*, 2015). In chordal transposition, a healthy chord from another region of the MV is used to replace a damaged chord, correcting leaflet prolapse. This approach also has drawbacks, with a recurrence rate of 13% of mild MR in the long-term (Sousa Uva *et al.*, 1993). Edge-to-edge repair, or Alfieri stitch (Alfieri *et al.*, 2001), consists of suturing the prolapsing leaflet against the non-prolapsing leaflet, creating a double-orifice MV. This technique reduces the orifice area allowing for the passage of blood flow, which causes an increase in diastolic pressure gradients and associated leaflet stresses (Nielsen *et al.*, 2001).

Patients with secondary MR and LV systolic dysfunction are subjected to different treatments, including a coronary artery bypass graft or percutaneous coronary intervention to aid relieve LV dysfunction. MV replacement is usually preferred to repair in these patients, since repair has high recurrence rates of MR (58.8 % vs 3.8 % in a trial reported by Harmel *et al.*) and is associated with worse quality of life and heart failure (Harmel *et al.*, 2018). Further details on surgical planning for MR and different types of surgical approaches can be found elsewhere (El Sabbagh *et al.*, 2018; Maganti *et al.*, 2010).

Necessity for tailored surgical approaches

Given the drawbacks associated with usual treatment approaches, it is imperative to improve repair techniques and optimise biomaterial designs for MV surgery (Fedak *et al.*, 2008; Al-Atabi *et al.*, 2012). In fact, alterations of the valvular geometry after surgery lead to changes in blood flow patterns and valve closure, ultimately disrupting normal flow through the left ventricle (Xu *et al.*, 2021). High/abnormal stresses induced on the valve leaflets have been found post-repair, potentially indicating post-surgical failure or impairment of MV function (Kong *et al.*, 2020). Therefore, the success of MV surgical approaches depends on the

restoration of normal fluid dynamics, usually involving correction of valve biomechanics (Al-Atabi *et al.*, 2012). As an example of design optimisation, novel annuloplasty ring designs for the MV which mimic the native annular saddle-shape (Doll *et al.*, 2019) and optimise load bearing by the annulus (Ncho *et al.*, 2020) have been recently developed (example on Figure 2.10a). On the other hand, catheter-based (percutaneous) surgical approaches which minimise MV structural changes and are minimally invasive have been recently developed. One of these is the “edge-to-edge” MitraClip device (Abbott Vascular, Santa Clara, California), which mimics the Alfieri stitch and clips the free edges of the AL and PL (Figure 2.10b). Clinical trials have assessed the long-term benefits of MitraClip therapy (Obadia *et al.*, 2018; Stone *et al.*, 2018), with patients with heart failure and moderate-to-severe secondary MR benefiting the most from this approach (Stone *et al.*, 2018). This technique is therefore currently employed in patients at high risk for conventional surgery, and it is still crucial to clearly identify criteria to be met for the use of this type of repair (Pibarot *et al.*, 2019). Percutaneous approaches have also been used for MV and chordae replacement; however, these techniques must be further developed before a percutaneous MV is widely available for clinical use (El Sabbagh *et al.*, 2018). For this, additional methods to provide further insight into the long-term performance of these novel surgical techniques are necessary.

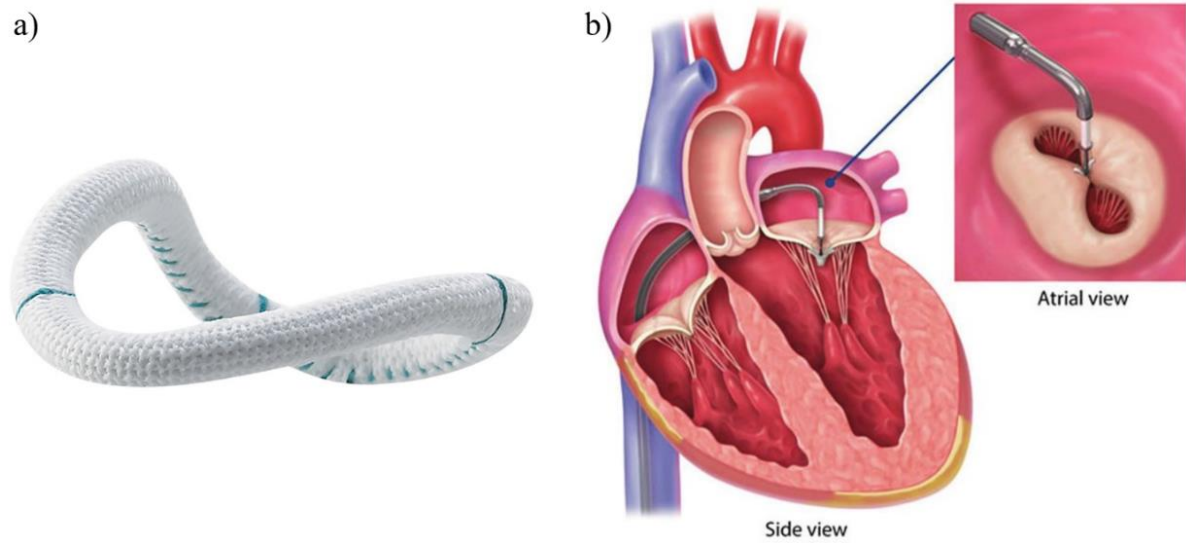


Figure 2.10: Examples of novel treatment devices for the MV, including (a) an asymmetrical annuloplasty ring mimicking annular saddle shape (Copyright 2018 Medtronic) and (b) the MitraClip (Abbott Vascular, Santa Clara, CA, USA), with its insertion into the mitral leaflets schematised (reproduced under CC BY-SA 3.0: <https://creativecommons.org/licenses/by-sa/3.0/deed.en>).

2.6. Computational modelling methodologies for the mitral valve

2.6.1. Overview

The use of computational models to study the biomechanics of the human body, and especially the behaviour of the cardiovascular system, is becoming increasingly widespread (Niederer *et al.*, 2019; Owen *et al.*, 2018). Computational models based on a variety of numerical techniques can be used to simulate complex problems in biomechanics ranging from structural analysis to fluid mechanics (Viceconti *et al.*, 2005), and even the interaction between structural deformation and fluid motion. Such models use a detailed set of mathematical descriptions that govern the behaviour of a system of interest. For example, the physiological function of the MV can be described by a structural-only model, able to virtually simulate MV closure and provide detailed deformation and stress patterns (Stevanella *et al.*, 2009; Votta *et al.*, 2008; Rim *et al.*, 2013), relevant to understand MV performance in diseased states (Pham *et al.*, 2017;

Choi *et al.*, 2016). Fluid flow numerical approaches, on the other hand, can be used to study blood flow behaviour (Morris *et al.*, 2016). Moreover, models representing the interaction between blood flow and structural deformation can provide detailed information on the behaviour of transvalvular blood flow in the case of the MV, in addition to deformation and stress patterns of the mitral leaflets (Gao *et al.*, 2017a; Hassani *et al.*, 2019; Adham Esfahani *et al.*, 2019). These are, however, more computationally intensive than structural-only models. In this thesis, a structural-only model employing the FE method is developed and used to simulate MV function (Chapters 4 and 5).

2.6.2. The Finite Element Method

Mesh discretisation

To obtain the numerical solution of a specific computational model, its geometry (or domain) must be discretised into smaller finite geometric/topological elements. These correspond to a computational mesh in which the governing mathematical equations are solved. Central to the implementation of the FE method is, therefore, the mesh generation, which can be based on several types of elements in 1D, 2D or 3D, as displayed in Figure 2.11. Regardless of type or shape, the numerical solutions are calculated at the nodes of the element. In first order elements, these are obtained at the vertex of the geometry, while in increasing order elements they are calculated at several points on the edges of an element. 2D and 3D elements are classified according to their geometrical surface: the most common are triangular and quadrilateral elements for a 2D representation or tetrahedral and hexahedral for a 3D one.






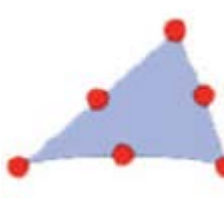
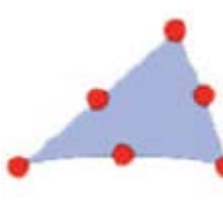
Element order	3D elements	2D elements		1D elements
	Solid	Shell	Plate	Beam
First order				
Second order				

Figure 2.11: Types of FE elements and respective order.

Shell elements are associated with geometries in which one dimension (thickness) is significantly smaller than the other dimensions. Different shell types are associated with different thickness-to-span ratios: thick shells have a ratio between $1/8$ and $1/20$ and thin shells between $1/20$ and $1/100,000$, for example. Shell elements are, therefore, ideal to model MV leaflet tissue, since its thickness is much smaller (ratio $< 1/20$) than other leading dimensions (Kunzelman *et al.*, 1997), with this is the type of element being employed throughout thesis to represent the MV surface. These elements define the geometry at a reference surface (usually the mid-surface of the geometry) and the thickness of the body is defined through a unique parameter. They are characterised by transverse shear and membrane and bending deformation, with the latter defining the bending stiffness of the elements. If the stiffness of an element must be calculated during the computational analysis, numerical integration is used to calculate the stresses and strains independently at section points through the shell thickness called integration points. In the case of a membrane implementation, one integration point is assumed, neglecting bending stiffness; to increase the bending stiffness, or to characterise different layers within

one shell element, the number of integration points through the shell thickness can be increased accordingly (Figure 2.12).

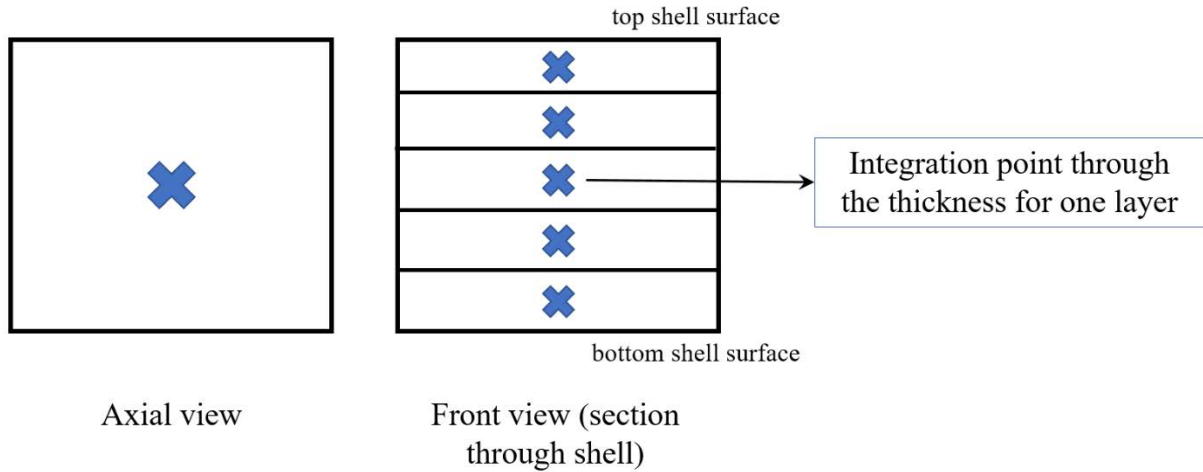


Figure 2.12: Shell through the thickness integration points for different layer representations.

Brief introduction to the FE method

In the case of a structural-only numerical problem with specific loading and boundary conditions, the goal of the FE method is to determine a set of nodal displacements (unknown variables) which minimise the total potential energy of the model (i.e. state of equilibrium). For a node of a FE element, the fundamental equation is defined by:

$$[\mathbf{K}] \cdot [\mathbf{U}] = [\mathbf{F}] \quad (2.15)$$

where $[\mathbf{K}]$ is the stiffness matrix, $[\mathbf{F}]$ is the force vector acting at the node and $[\mathbf{U}]$ is the unknown vector of nodal displacements. The stiffness matrix $[\mathbf{K}]$ depends on the material properties applied to the model. In the case of a plane stress solid (e.g. shell element), external

forces are applied on the x-y plane, and stresses in the z-direction are null. This means that the stress (σ) and strain (ϵ) vectorial components can be written as in equations 2.16 and 2.17:

$$\sigma = \begin{Bmatrix} \sigma_{xx} \\ \sigma_{yy} \\ \sigma_{xy} \end{Bmatrix} \quad (2.16)$$

$$\epsilon = \begin{Bmatrix} \epsilon_{xx} \\ \epsilon_{yy} \\ \epsilon_{xy} \end{Bmatrix} \quad (2.17)$$

Strain-displacement relationships are also given as:

$$\epsilon_{xx} = \frac{\partial u}{\partial x}; \quad \epsilon_{yy} = \frac{\partial v}{\partial y}; \quad \gamma_{xy} = \frac{\partial u}{\partial x} + \frac{\partial v}{\partial y} \quad (2.18)$$

where the strains ϵ_{xx} and ϵ_{yy} are evaluated as the displacements u and v with respect to their initial positions x and y and the shear strain γ is the sum of the strains in both directions. The strain-displacement relation can also be written as:

$$\epsilon = [L][U] = \begin{bmatrix} \partial/\partial x & 0 \\ 0 & \partial/\partial y \\ \partial/\partial y & \partial/\partial x \end{bmatrix} \begin{Bmatrix} u \\ v \end{Bmatrix}, \quad (2.19)$$

where $[L]$ is the differential operator matrix.

According to Hooke's law, the stress-strain relationship is given by:

$$\boldsymbol{\sigma} = [\mathbf{K}]\boldsymbol{\epsilon}, \quad (2.20)$$

where the stiffness matrix $[\mathbf{K}]$ is composed of material constants to be determined. For plane stress, isotropic materials, $[\mathbf{K}]$ becomes:

$$[\mathbf{K}] = \frac{E}{1-\nu^2} \begin{bmatrix} 1 & \nu & 0 \\ \nu & 1 & 0 \\ 0 & 0 & (1-\nu)/2 \end{bmatrix}, \quad (2.21)$$

where $[\mathbf{K}]$ depends on the Young's modulus (E) and Poisson's ratio (ν). The shear modulus G is a function of E and ν , resulting in:

$$G = \frac{E}{2(1+\nu)}. \quad (2.22)$$

The dynamic equilibrium equations which satisfy the displacement continuity between the nodes of an element, can be defined as a matrix:

$$[\mathbf{L}]^T \boldsymbol{\sigma} + \mathbf{f}_b = \rho[\ddot{\mathbf{U}}], \quad (2.23)$$

where \mathbf{f}_b is the external force vector (including x and y force components). More details on the FE method fundamentals and the different numerical approaches available to obtain the solution to this system (e.g. explicit vs implicit approach) can be found elsewhere (Liu and Quek, 2014).

2.7. Previous computational models of the mitral valve

Computational modelling of the MV has focused on two different fronts:

- ❖ To develop frameworks able to more accurately represent the complex MV anatomy and function in timescales compatible with clinical translation;
- ❖ To study MV physiology, including dysfunctional cases and surgical procedures.

2.7.1. Numerical approaches

The complexity of frameworks to simulate MV function has increased over the last decades. During the first years of MV modelling, structural-only FE approaches were used to simulate valve function (Kunzelman *et al.*, 1993a; Salgo *et al.*, 2002). These first models employed parametric shapes of the MV, based on literature data, and were used to study leaflet stress distributions associated with healthy geometries. Since then, FE models of the MV have greatly evolved: studies have focused on improving the geometries used, material properties chosen and boundary conditions imposed, given that computational predictions are highly sensitive to these factors. For instance, MV geometries including PM tips with diverse representations (Prot *et al.*, 2010; Votta *et al.*, 2008) and chordae distributions based on imaging data (Wang and Sun, 2013) have been developed. Indeed, patient-specific models based on MV geometries and functional information obtained from medical images have been developed and faster and improved algorithms have been created to capture the structure of the MV (Einstein *et al.*, 2010; Ionasec *et al.*, 2010; Mansi *et al.*, 2012), as exemplified in Figure 2.13.

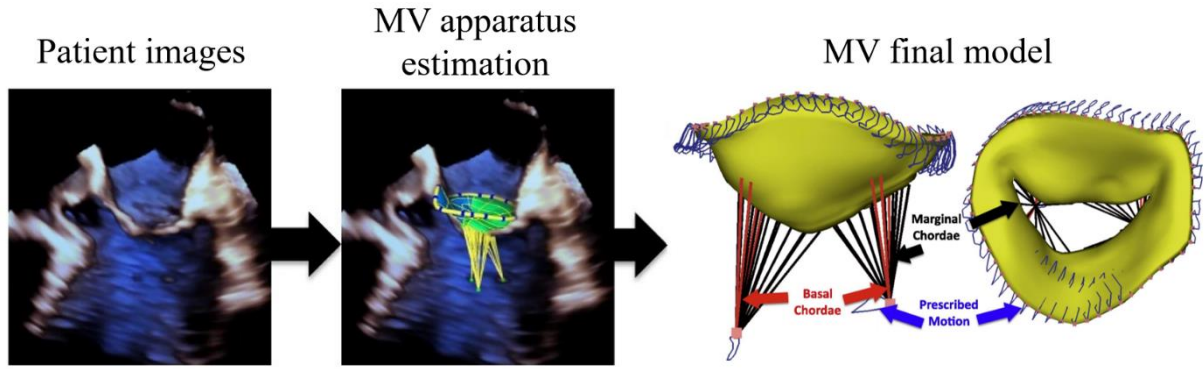


Figure 2.13: Framework proposed by Mansi *et al.* for the generation of MV models from medical imaging, and creation of the final MV model ready for FE simulations. Patient-specific images of the MV are used to capture its structure and its apparatus is estimated from anatomical landmarks, giving rise to a mapped parameterisation of the leaflet surfaces. Chordae tendineae are then defined based on PM tip location and assumptions for distribution, giving rise to the complete MV model.

Medical images such as 3D transesophageal echocardiography (Ge *et al.*, 2014; Mansi *et al.*, 2012; Rim *et al.*, 2013; Zhang *et al.*, 2017), multislice computed tomography (Wang and Sun, 2013) or cardiac magnetic resonance (Stevanella *et al.*, 2011) have been used for the creation of patient-specific MV models; In addition, and given the coupling of the MV with the LV, several FE models have also obtained the LV geometry from medical images and incorporated the entire structure for computational analysis (Ge *et al.*, 2014; Wenk *et al.*, 2010).

Structural-only models of the MV do not incorporate fluid dynamics and its interaction with the valve. To account for this interaction, fluid-structure interaction (FSI) approaches, characterised by a coupling between the equations describing fluid mechanics and those describing solid mechanics (Formaggia *et al.*, 2009). The first FSI approach to study MV behaviour appeared less than 15 years ago, employing an idealised 3D MV model (Kunzelman *et al.*, 2007). Since then, more sophisticated FSI frameworks with increasing complexity have been developed, incorporating patient-specific structures: models with patient-specific MV and LV were developed (Gao *et al.*, 2017a; Mao *et al.*, 2017; Khodaei *et al.*, 2017; Caballero *et al.*,

2020; Caballero *et al.*, 2018), and sub-valvular geometrical data acquired from an ovine model gave rise to comprehensive FSI analyses of PM and chordae performance (Toma *et al.*, 2017; Toma *et al.*, 2016). Regardless, FSI approaches are computationally more expensive than FE methods, given the increase in complexity in multiphysics modelling. For this reason, FE analysis is still a widely used numerical approach for the study of MV function (Aguilera *et al.*, 2021; Kong *et al.*, 2018; Kong *et al.*, 2020).

The validity of computational models for the MV is usually performed through comparisons of computational predictions with *in vitro* or *ex vivo* experiments (Toma *et al.*, 2016; Lee *et al.*, 2015), as well as clinical imaging. For example, computationally predicted MV geometries at peak closure can be compared against their ground truth from medical images (Wang and Sun, 2013; Mansi *et al.*, 2012; Zhang *et al.*, 2017). The comparison of computational results against other computational studies arises as an alternative when no other data is available. Further experimental and computational benchmark data for MV models is required, since in several cases clinical data available is usually limited (and of poor resolution), material properties and boundary conditions are unknown and models are over-simplified (Gao *et al.*, 2017b).

In addition, in order to obtain generalised results, patient-specific models and frameworks cannot be employed. A framework able to automatically generate scalable models which can be quickly created to represent a variety of scenarios associated with clinical cases is still missing in the current literature. Nonetheless, current computational models of the MV are able to: (1) evaluate MV biomechanics; (2) assess the effect of novel surgical techniques on MV function; (3) inform personalised clinical planning by allowing the simulation of several treatments in a patient-specific geometry.

2.7.2. Computational analyses

Computational analyses of the MV have either focused on normal physiological function (Gao *et al.*, 2017a; Votta *et al.*, 2008; Wang and Sun, 2013), dysfunctional cases (Choi *et al.*, 2016; Rim *et al.*, 2013; Wenk *et al.*, 2010; Aguilera *et al.*, 2021) and surgical procedures (Ge *et al.*, 2014; Rim *et al.*, 2015; Caballero *et al.*, 2020; Kong *et al.*, 2020). Metrics such as leaflet stress distributions, chordae tendineae tensions, PM reaction forces and blood flow velocity magnitudes are usually obtained to assess MV function. Computational predictions for dysfunctional MVs (altered geometries) have been associated with larger peak systolic stress distributions across the mitral leaflets (Rim *et al.*, 2014; Stevanella *et al.*, 2011), a decrease in the coaptation area (Choi *et al.*, 2016; Aguilera *et al.*, 2021) and much higher PM and chordae forces (Stevanella *et al.*, 2011) in comparison with healthy valves. On the other hand, the virtual simulation of leaflet resection and annuloplasty to treat MR in diseased geometries has shown a decrease in leaflet stress distributions and an increase in the contact area between leaflets (Rim *et al.*, 2015; Kong *et al.*, 2018). The virtual implantation of MitraClip has also provided relevant information on its performance: an improved geometrical configuration with increased leaflet coaptation was obtained, but increasing leaflet peak stress after MitraClip implantation (Figure 2.14) could be a factor in triggering leaflet remodelling (Kong *et al.*, 2020; Errthum *et al.*, 2021). Similarly, the implantation of neochordae in MV models led to a decrease in MR, but increased neochordae tension and PL peak stress in specific configurations, revealing that the location of neochordae implantation affects MV biomechanics (Caballero *et al.*, 2020). Computational models of the MV are, therefore, powerful tools to understand the effect of altered geometries and the impact of surgical procedures in its biomechanics.

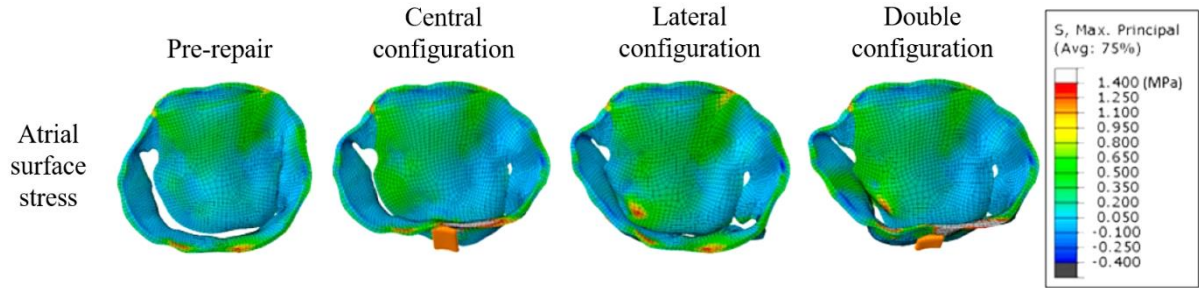


Figure 2.14: Leaflet stress distributions [MPa] obtained by Errthum *et al.* when simulating repair with MitraClip in different spatial configurations (Errthum *et al.*, 2021).

2.8. Connection between the right atrium and chronic kidney disease

2.8.1. Right atrial haemodynamics

While left heart function has been extensively explored through clinical, *in vitro* and *in silico* studies, the right side has been mostly neglected (Gulan *et al.*, 2017). For instance, despite the availability of detailed information of the morphology and function of the right heart in the literature (Rudski *et al.*, 2010), only a few *in vivo* and *in vitro* studies have provided insight on the nature of its complex haemodynamics (Gulan *et al.*, 2017; Wehrum *et al.*, 2018; Parikh *et al.*, 2017; Hirtler *et al.*, 2016). The right atrium (RA), for example, can be compared to a haemodynamic chamber with flow patterns depending on the position of the superior (SVC) and inferior (IVC) vena cavae, which bring blood back to this chamber. Right atrial flow has been described as heterogeneous (Parikh *et al.*, 2017), characterised by the formation of vortex rings in clockwise or counter-clockwise directions and helical flow due to the mixing of flow patterns brought by the SVC and IVC (Parikh *et al.*, 2017; Gulan *et al.*, 2017). Moreover, different characteristics of flow including altered vorticity or low WSS have been associated with the potential impairment of function due to right ventricular dilation or even atrial thrombus formation (Hirtler *et al.*, 2016; Gulan *et al.*, 2017). Further evaluations of right atrial haemodynamics are therefore required, especially when medical devices are inserted into the

right heart long-term. Such an example is the insertion of central venous catheters, used as a support treatment for chronic kidney disease (CKD) (Smith and Nolan, 2013).

2.8.2. Chronic kidney disease and association with cardiovascular disease

The kidneys filter blood by removing waste and extra fluid. In the presence of chronic kidney disease (CKD), a long-term, systemic pathology, there is a gradual or complete loss of kidney function (Jha *et al.*, 2013). The identification and staging of CKD relies on the measurement of glomerular filtration rate, with decreasing rates (< 90 mL/min) being consecutively associated with worsened kidney function (KDIGO CKD Work Group, 2013).

CKD has been highly associated with the incidence of CVD (Stevens *et al.*, 2007; Go *et al.*, 2004; Thompson *et al.*, 2015), with cardiovascular mortality accounting for 40-50 % of all deaths in patients with advanced CKD and end-stage kidney disease (Thompson *et al.*, 2015; Webster *et al.*, 2017). CKD has been associated with enhanced calcifications of coronary arteries (Goodman *et al.*, 2000) and heart valves (Abd Alamir *et al.*, 2015), stenosis, and even myocardial infarction (KDIGO CKD Work Group, 2013), likely due to dysregulation of inflammatory processes, hormones and electrolytes in these patients. There is, therefore, a strong connection between the prevalence and incidence of CKD and MV disease (Baumgartner *et al.*, 2017). While severe CKD affects the long-term outcome of MV repair as given by increased mortality rates (Shah *et al.*, 2019), improvement of kidney function has been observed after MV replacement (Doshi *et al.*, 2018).

2.8.3. Treatment for chronic kidney disease

Haemodialysis is used clinically during CKD to support blood filtering. During this process, haemodialysis catheters (HD) are used to retrieve blood from the body, filter it externally, and

transport it back to the heart. Central venous catheters, a specific type of HD catheters, are typically inserted into a large vein in the neck or the chest, extending through the SVC and into the RA (Smith and Nolan, 2013). This is schematised in Figure 2.15, which also shows how these catheters connect to an external dialysis machine. This process is extensively used among patients awaiting permanent access placement or maturation (Malas *et al.*, 2015). A retrospective study indicated that, in 2011, more than 80 % of patients starting haemodialysis in the United States did so through a catheter, where 27 % of those undergoing frequent dialysis (long-term cases) had a catheter fitted (Malas *et al.*, 2015; Collins *et al.*, 2012).

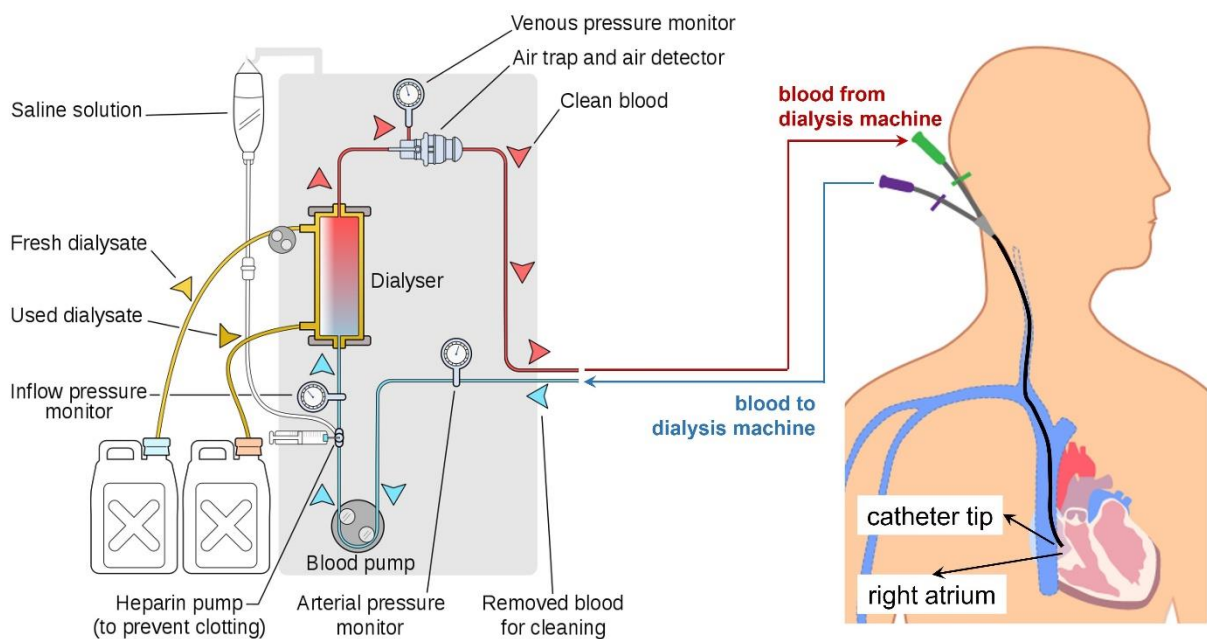


Figure 2.15: Schematic of the dialysis process, including the main stages for filtering blood with a dialysis machine. Here, the insertion of a HD catheter into the RA from a vein in the neck is also displayed, with the external limbs of the catheter connecting to the dialysis machine (reproduced from Wikimedia Commons under CC BY-SA 3.0 and 4.0).

A catheter design is usually based on a circular tube (with a 5 mm diameter) made of silicone rubber or polyurethane (Schults *et al.*, 2019) which has two separate lumens: the venous lumen

brings filtered blood towards the heart while the arterial lumen carries unfiltered blood away from the heart. Moreover, they can work in standard or reverse mode, where the latter refers to a switch in venous and arterial lumens. Several HD catheter tip designs are commercially available, with the goal to maximise catheter performance. These are differentiated in symmetric, split and step tips, with diverse features such as the presence or not of side holes (Figure 2.9) (Knutтинен *et al.*, 2009). Regardless of the design or the working mode, these catheters must comply with specific requirements for optimal performance, including:

- ❖ The catheter flow rate must be 300 ml/min or greater, and catheter dysfunction is associated with any flow rate below this value (Depner, 2001);
- ❖ The amount of filtered blood returning to the catheter (re-filtration), or flow recirculation, has to be minimised (ideally < 1-2 %) (Hwang *et al.*, 2012);
- ❖ The formation of biofilm/thrombus at the tip needs to be prevented to avoid infection, with catheter surface coatings or anticoagulants being used to prevent this (Mathew *et al.*, 2019);
- ❖ An adequate site of tip placement within the RA needs to be accounted for, as this affects the appropriate mixing of filtered blood within the RA, directly related to the efficiency of haemodialysis (Vascular Access Work Group, 2006).

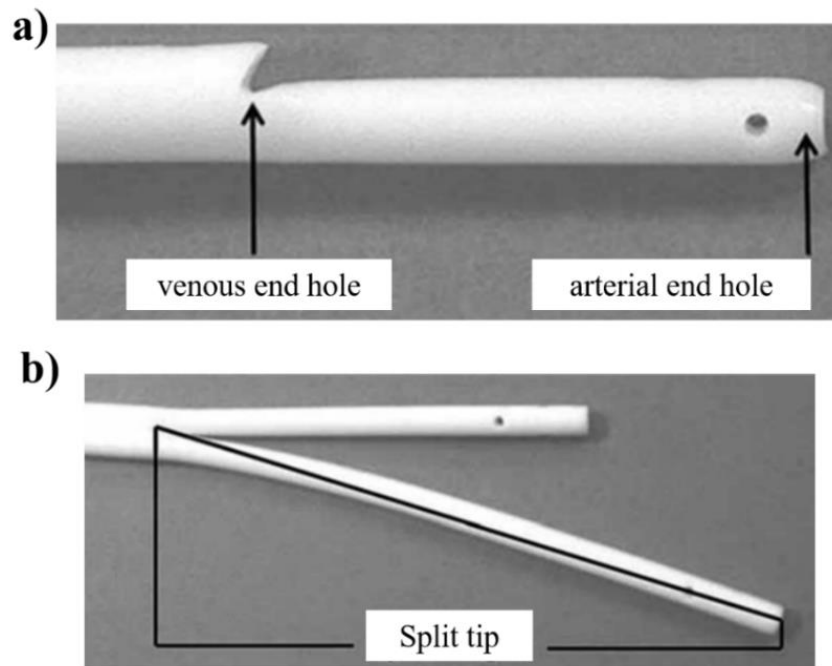


Figure 2.16: Examples of commercially available central venous catheter tips, adapted from (Vesely and Ravenscroft, 2016). a) Step-tip catheter Titan™ (Medcomp. Harleysville, PA) and b) Split-tip catheter Ash Split® (Medcomp. Harleysville, PA).

HD catheters have complications such as high rates of infection and dysfunction compared with other forms of dialysis, associated with increased rates of morbidity and mortality in these patients (Dhingra *et al.*, 2001; Lok and Foley, 2013). Indeed, the presence of inappropriate blood flow rates during the HD process causes approximately one-third of catheter removals (Vascular Access Work Group, 2006). Other possible complications include catheter lumen occlusion, for which contribute high blood shear rates and the activation of platelets (Casa *et al.*, 2015). To avoid such complications, several studies have been conducted to evaluate the performance of different catheter designs. Multiple randomised trials have shown that varying tip designs affect catheter performance (Knuttinen *et al.*, 2009; Kakkos *et al.*, 2008; Tal, 2005): the step tip (represented in Figure 2.16a) is known to have elevated recirculation percentages (filtration of blood already filtered) in reverse mode, associated with poor performance, while

a symmetric tip catheter is usually associated with lower recirculating flow. This symmetric design is often considered the best design available at present. However, since multiple requirements must be considered for adequate performance, an optimal catheter design is yet to be identified. Moreover, and given the complex haemodynamic environment in which these catheters are inserted (i.e. the RA), further studies accounting for RA haemodynamics need to be conducted.

There is, therefore, scope to use blood flow computational models for a much more comprehensive evaluation of fluid behaviour through a catheter design which is inserted in the RA. For example, when such models are applied to study blood flow patterns present in different HD catheter designs, additional metrics of interest such as recirculation of flow and shear stress can be obtained to quantify performance (Clark *et al.*, 2015; Owen *et al.*, 2020a; Mareels *et al.*, 2004). However, only a few computational studies have focused on assessing RA haemodynamics (Rigatelli *et al.*, 2018; Mareels *et al.*, 2004), with only one CFD study using a realistic RA geometry to study the performance of a single catheter design (Mareels *et al.*, 2004). The development of a simulation platform employing a physiological model of the RA for the evaluation of HD catheter designs is, therefore, lacking in the current literature.

2.9. Modelling haemodialysis catheter blood flow

2.9.1. Characteristics of blood flow and governing equations

Blood is a complex fluid, composed by the suspension of multiple particles, including red blood cells and platelets, in plasma. Red blood cells are the main determinant in the mechanical properties of blood, being able to adapt to variable flow shear rates; they tend to aggregate at low shear rates, and deform and align with the blood flow field at high ones. This means that

blood viscosity (or resistance to deformation by shear stress) is not constant, varying with shear rates and turning blood into a non-Newtonian fluid. Non-Newtonian behaviour is, nonetheless, stronger in smaller vessels due the comparability of sizes of blood cells against those of the vessel (Formaggia *et al.*, 2009). If blood is assumed to have constant density, its mass is conserved, and the flow entering and exiting an infinitesimal volume remains constant. This continuity of mass can be described by equation 2.24:

$$\nabla \cdot \mathbf{u} = 0, \quad (2.24)$$

where \mathbf{u} is the velocity vector and ∇ is the differential operator. Equation 2.24 states that the divergence of the velocity vector field does not change in magnitude along the flow of the vector field. Moreover, the forces acting on the fluid must remain in equilibrium and therefore the linear momentum must be conserved for the flow entering and exiting an infinitesimal volume. When body forces and external forces are neglected, this conservation of momentum, or Navier-Stokes equation, can be described by equation 2.25:

$$\rho \left\{ \frac{\partial \mathbf{u}}{\partial t} + (\mathbf{u} \cdot \nabla) \mathbf{u} \right\} + \nabla p - \mu \nabla^2 \mathbf{u} = 0, \quad (2.25)$$

where ρ is the density of the fluid, p is the static pressure and μ is the fluid viscosity (ANSYS, 2013). In a non-Newtonian model, the viscosity μ becomes a function of the strain rate, associated varying viscosity models available in the literature as described elsewhere (Owen *et al.*, 2020b).

2.9.2. Brief introduction to the Finite Volume method

The Finite Volume Method is often used in computational fluid dynamics (CFD) for the analysis of fluid flows. Similarly to the FE method, the geometry is discretised into cells, with each cell having a centroid (P), as indicated in Figure 2.17, where unknown flow variables such as velocity and pressure are calculated and stored (cell-centred approach). The Navier-Stokes equations are discretised within each cell and integrated over this volume. These integrals are solved by balancing fluxes across the faces (or boundaries) of each volume, with the flux being calculated at its centroid. The cell centroids of a current and neighbouring cell are then interpolated to obtain the unknown centred velocity values. More details on the fundamentals of the Finite Volume method can be found in Appendix D and further information on the different interpolation approaches available to obtain the solution to this system can be found elsewhere (Rapp, 2017).

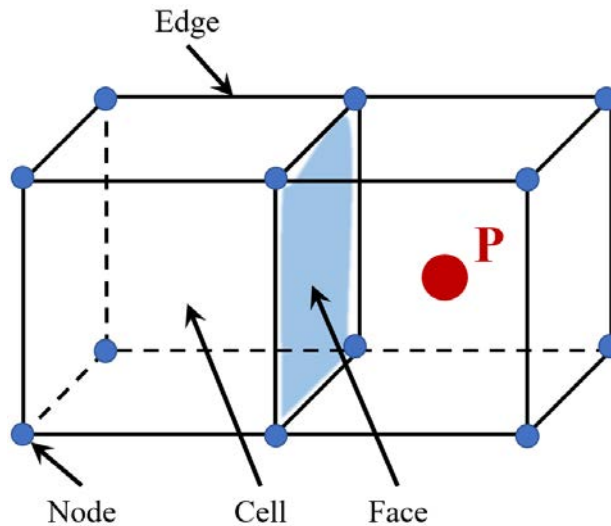


Figure 2.17: Example of finite volume mesh discretisation.

2.10. Summary

In this chapter, an introduction of the background required for the following chapters has been performed. The main topics include: an assessment of the anatomy of the heart and the MV, with the MV geometry being evaluated in terms of mathematical associations between dimensions; an analysis of MV pathophysiology, as well as its link to geometrical alterations; the use of computational modelling to study the cardiovascular system, including the frameworks currently available to generate computational models of the MV; the haemodynamics of the RA, and how this chamber is used as a platform to treat chronic kidney disease through the insertion of HD central venous catheters; and an introduction to the fundamental numerical tools and governing equations employed in computational methods for the MV and blood flow modelling for HD catheters. These topics are expanded in subsequent chapters, and the three main research questions explored in this work are:

- ❖ Can the morphometric information currently available for the MV be used to create a unified mathematical model defining its shape?
- ❖ Can the computational technology currently available be used to develop a framework which generates clinically useful parametric models of the MV?
- ❖ Can a more realistic blood flow model of the RA be developed and employed to assess a variety of HD catheter designs?

The next chapter targets the first research question by presenting a mathematical evaluation of MV morphometry. This evaluation is performed through correlation analysis between key dimensions and evaluation of prediction equations from the literature, with the accuracy in predictions from the obtained fits being assessed.

CHAPTER 3

MATHEMATICAL CHARACTERISATION OF MITRAL VALVE MORPHOMETRY

3.1. Introduction

The complex shape of the MV is key to many aspects of its function and disease, as identified by clinical (Lee *et al.*, 2013; Jassar *et al.*, 2014), *in silico* (Kunzelman *et al.*, 2007; Stevanella *et al.*, 2011) and *in vitro* studies (Espino *et al.*, 2007; Bloodworth *et al.*, 2017). As mentioned in Chapter 2, computational modelling has been vastly used to gain further insight on MV dysfunction or surgical procedures, mostly employing geometries obtained from medical imaging (Mansi *et al.*, 2012; Zhang *et al.*, 2017). Parametric and scalable models have also been used to study its function (Choi *et al.*, 2016; Alleau *et al.*, 2019). These are built from average leading dimensions usually obtained in the literature or from direct *ex vivo* measurements.

The development of parametric and scalable models therefore relies on quantitative studies of MV shape, and correlation analyses between key dimensions. A large number of MV anatomical datasets is required for the generation of reliable parametric models, both allowing for the inclusion of anatomical variability and including all necessary dimensions to represent the complete shape of the valve. This is challenging, because although many sources of MV anatomy quantification exist, such studies usually report mean dimensions, being often incomplete and focusing on different parts of the MV shape. This means that not all the dimensions which characterise MV morphometry are stated in a unique study; furthermore,

dimensions for each patient are typically not reported, which would be valuable to perform correlation analyses.

In addition, very few studies have attempted to perform correlation analyses between MV dimensions. Warraich *et al.* and Duplessis *et al.* have published MV datasets (Warraich *et al.*, 2012; Duplessis and Marchand, 1964), which, despite the small number of subjects, allow for new correlation analyses to be performed, while Deorsola *et al.* have attempted to correlate different dimensions of the MV geometry (Deorsola and Bellone, 2019; Deorsola and Bellone, 2018). There is then potential to develop novel correlation studies based on the datasets available, as well as evaluate previous correlations from the literature and their respective prediction equations. Moreover, the accuracy of such correlation analyses must be further validated against available data from the literature and dimensions obtained from the scans of new individuals.

The aim of this chapter is to mathematically evaluate MV morphometry, which was performed through: (1) correlation analysis between key dimensions; (2) application of regression models to characterise chordae collagen arches; (3) evaluation of prediction equations available in the literature. Datasets present in the literature, as well as a new dataset obtained from clinical images at Aberdeen Royal Infirmary, were used for correlation analyses. The validity of all prediction equations was assessed by comparing dimension predictions against other datasets and average literature data. The effect of predicting dimensions using linear and nonlinear empirical data fits was also investigated, *in vivo* and *ex vivo*, for healthy and diseased cases. The workflow of this chapter is displayed in Figure 3.1.

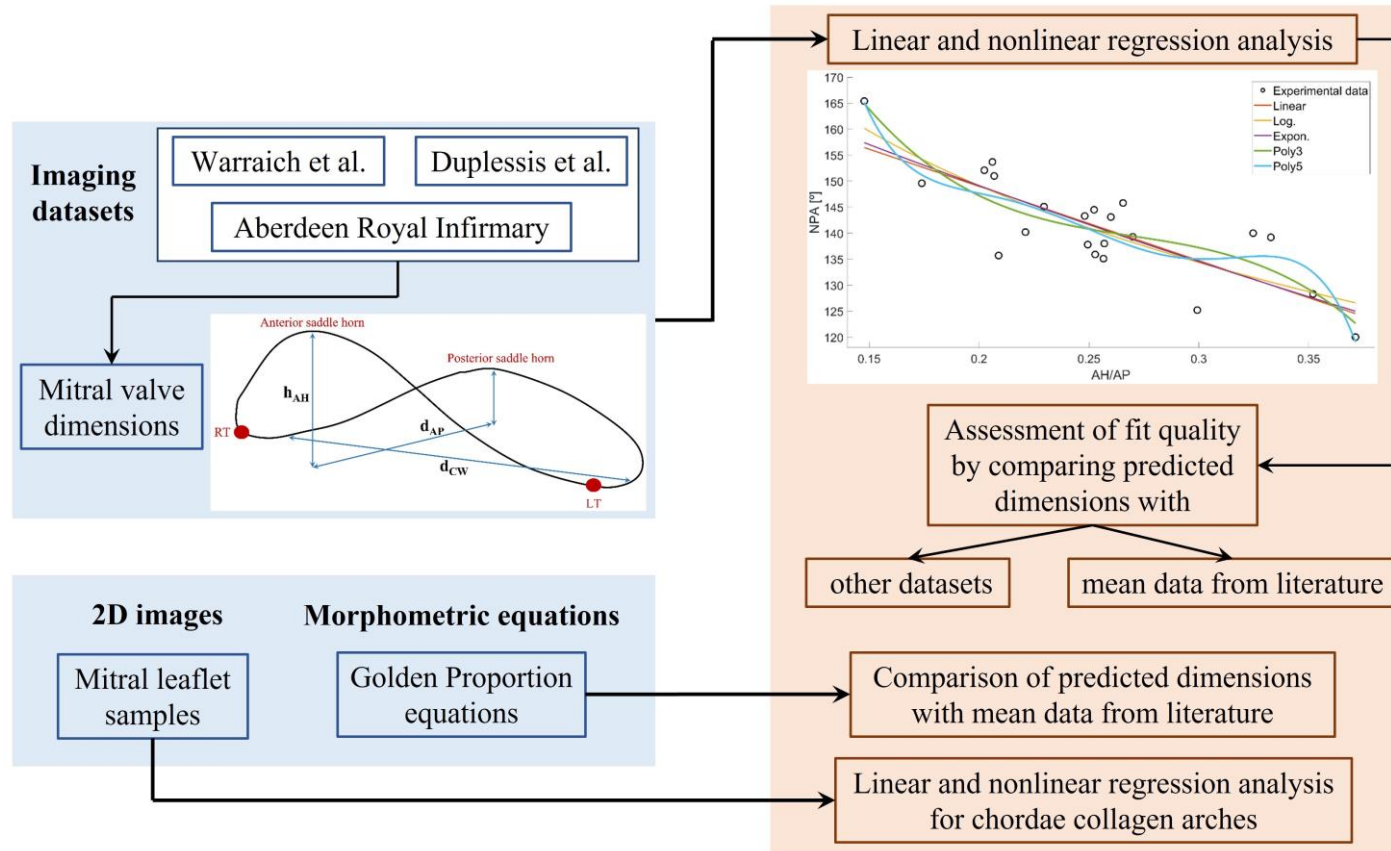


Figure 3.1: Outline of this chapter. Imaging datasets from Warraich et al. and Duplessis et al. were selected for the mathematical analysis of the mitral valve. Moreover, new mitral valve images based on (1) clinical databases from Aberdeen Royal Infirmary and (2) mitral leaflet samples were included for analysis, as well as morphometric equations from the literature based on the Golden Proportion. Linear/nonlinear regression analysis was performed for the measurements from the selected datasets. Predicted dimensions from obtained fits and morphometric equations were assessed by comparing against mean data from previous studies, and fittings resulting from the correlation analysis were also compared against other datasets, when possible. Notes: AH and h_{AH} , annular height; AP and d_{AP} , anteroposterior diameter; d_{CW} , commissural width; NPA, non-planarity angle.

3.2. Morphometric data collections and measurements

In this section, the morphometric MV datasets collected by Warraich *et al.* (Warraich *et al.*, 2012) and Duplessis *et al.* (Duplessis and Marchand, 1964) have been analysed. To create a more complete MV more morphometric dataset, new measurements have been collected from medical images available at Aberdeen Royal Infirmary. These have then been used to verify the predictions for patient-specific use, as well as disclose possible correlations amongst dimensions. Moreover, to analyse dimensions characteristic of chordae tendineae insertion patterns into the leaflets, measurements regarding collagen fibre distributions stemming from the chordae were performed at Aberdeen Royal Infirmary.

3.2.1. Datasets from literature

Warraich *et al.* (2012) have based their study on intraoperative 3D transesophageal echocardiography scans of patients undergoing surgery for mitral regurgitation. Mitral annular geometry was the focus of the study and the authors sought to demonstrate that the AHCWR could be used as a proxy for annular nonplanarity by finding a mathematical correlation between this ratio and the NPA. Measurements were obtained from 23 patients, with dimensions (Figure 3.2) being provided as raw data and in terms of mean values and standard deviations, as reported in Table 3.1.

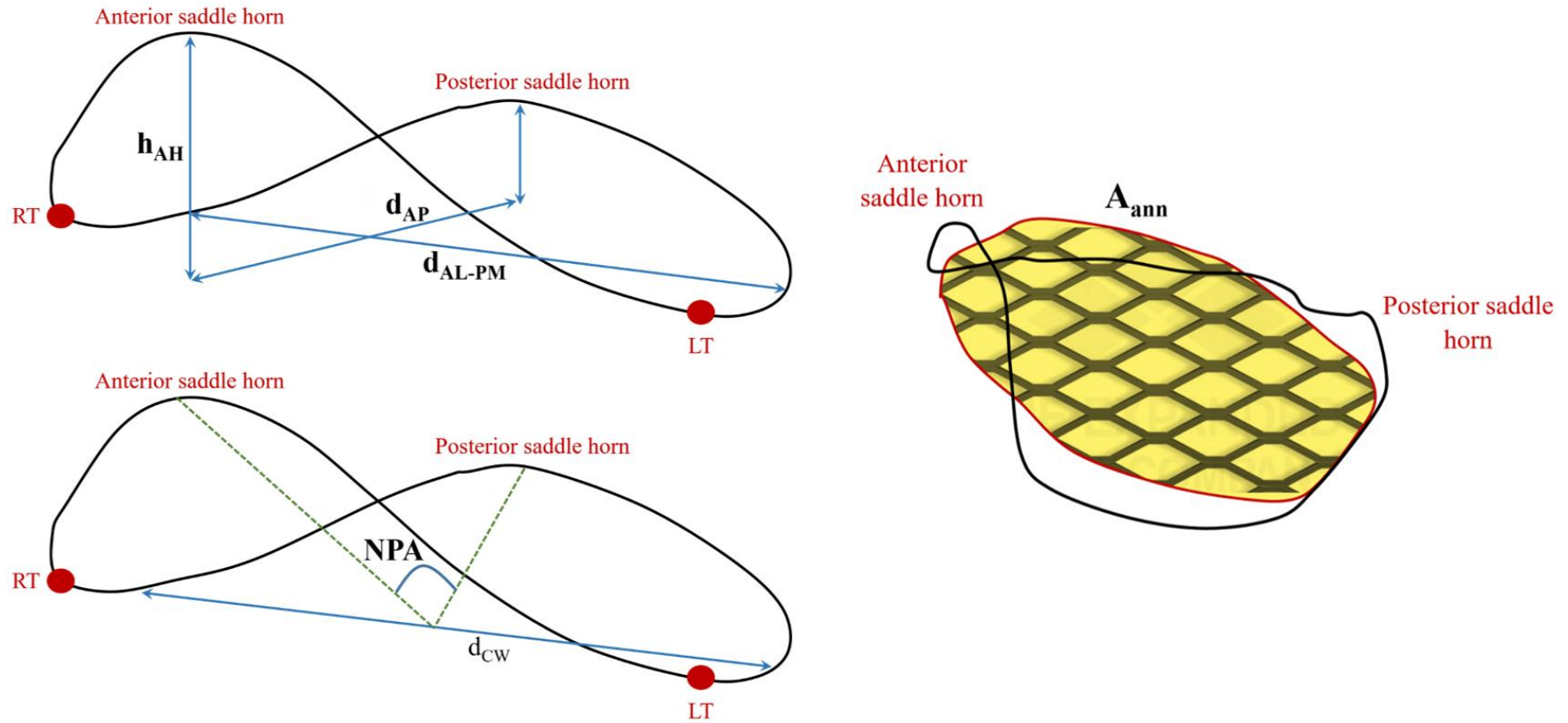


Figure 3.2: Mitral annular dimensions (in bold) measured by Warraich et al. (Warraich et al., 2012). Notes: LT, left trigone; RT, right trigone; d_{AP} , anteroposterior diameter; d_{AL-PM} , anterolateral-posteromedial diameter (diameter at the middle of the annular circumference); h_{AH} , annular height; d_{CW} , commissural width (distance from commissure to commissure); NPA, non-planarity angle; A_{ann} , annular area.

Table 3.1: Mitral annular dimensions collected by Warraich *et al.* (Warraich *et al.*, 2012).

Patient	d _{AP} (mm)	d _{AL-PM} (mm)	h _{AH} (mm)	h _{AH} /d _{AP}	h _{AH} /d _{AL-PM}	NPA (°)	A _{ann} (mm ²)
1	40.2	41.5	8.316	0.2068657	0.2003855	151	1220
2	36.6	43.5	9.08	0.2480874	0.2087356	143.3	1460
3	32.9	44.1	10.948	0.332766	0.248254	139.2	1060
4	39.19	41.23	10.405	0.2655014	0.2523648	145.8	1360
5	41.04	42.95	9.074	0.2211014	0.2112689	140.2	1480
6	41.9	40.75	12.54	0.299284	0.3077301	125.2	1460
7	48.71	44.18	11.18	0.2295217	0.2530557	145.1	1520
8	44.05	52.29	8.916	0.2024064	0.1705106	152.1	1740
9	29.78	37.38	7.5142	0.2523237	0.2010219	144.5	870
10	40.06	46.37	10.415	0.259985	0.2246064	143.1	1520
11	37.82	42.17	9.704	0.2565838	0.2301162	135.1	1310
12	43.09	49.55	7.495	0.1739383	0.1512614	149.6	1540
13	35.32	37.59	9.076	0.2569649	0.2414472	138	1050
14	52.72	55.85	14.23	0.2699165	0.2547896	139.3	1425
15	53.72	51.11	11.07	0.2060685	0.2165917	153.7	2200
17	33.16	38.69	11.67	0.35193	0.3016283	128.3	1080
18	42.63	48.69	6.299	0.1477598	0.1293695	165.4	1620
19	33.71	39.29	10.945	0.3246811	0.2785696	140	1050
20	41.05	44.68	15.24	0.3712546	0.3410922	120	1430
21	43.49	47.1	9.084	0.2088756	0.1928662	135.7	1810
22	38.34	34.3	9.564	0.2494523	0.2788338	137.8	1060
23	39.47	39.72	9.979	0.2528249	0.2512336	135.9	1360
Mean ± STD	40.4 ± 6	43.8 ± 5	10.1 ± 2	0.25 ± 0.1	0.23 ± 0.1	141.3 ± 10	1390 ± 300

Duplessis *et al.* performed an anatomical study of MV morphometry, focusing on the difference in measurements between anterior and posterior leaflets (including annular circumferences, middle leaflet height and leaflet surface area). Ten fresh human hearts were dissected and the complete MV structure (leaflets with annulus, chordae and PMs) was removed, with the valve being flattened and preserved with diglycerol stearate for evaluation. Measurements (Figure 3.3) were performed with point dividers and a metric ruler, being provided as raw data and in terms of mean values, as reported in Table 3.2.

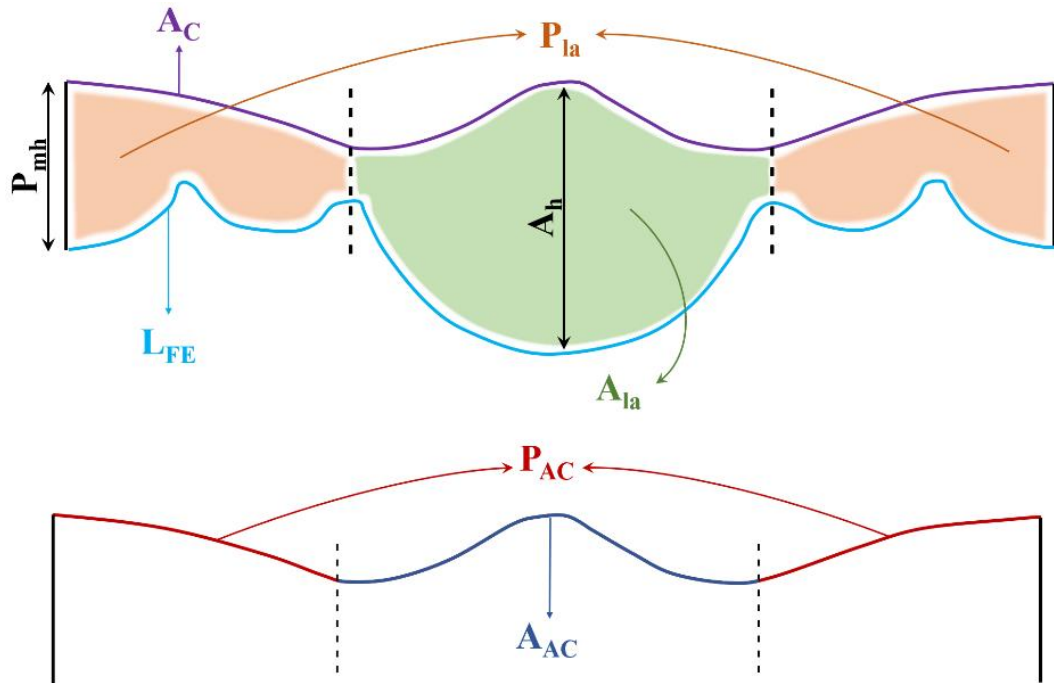


Figure 3.3: Mitral leaflet dimensions (in bold) measured by Duplessis et al. (Duplessis and Marchand, 1964). Notes: A_c , annular circumference; A_{AC} , anterior annular circumference; P_{AC} , posterior annular circumference; L_{FE} , leaflet free edge length; A_h , anterior leaflet height; P_{mh} , posterior leaflet middle scallop height; A_{la} , anterior leaflet area; P_{la} , posterior leaflet area.

Table 3.2: Mitral annular and leaflet dimensions collected by Duplessis et al. (Duplessis and Marchand, 1964).

Specimen	A_{AC} (mm)	P_{AC} (mm)	A_c (mm)	L_{FE} (mm)	A_h (mm)	P_{mh} (mm)	A_{la} (mm²)	P_{la} (mm²)
1	39	72	111	105	28	18	520	530
2	30	64	94	85	22	10	400	450
3	39	67	106	95	26	14	550	480
4	32	64	96	85	32	12	450	480
5	29	69	98	84	25	13	430	460
6	31	54	85	80	24	12	440	450
7	34	51	85	79	25	13	450	420
8	41	87	128	117	29	14	590	650
9	45	79	124	93	30	15	560	580
10	32	60	92	83	26	13	500	500
Mean	35.2	66.7	101.9	90.6	26.7	13.4	489	500

3.2.2. Patient-specific dataset (PSD)

Transthoracic 2D echocardiogram images available at Aberdeen Royal Infirmary were analysed. All images were obtained as part of a previous ethically approved research study entitled “Exercise Capacity in Adults” with REC reference 13/NS/0034 and IRAS ID 127501. The control imaging database corresponded to healthy adult volunteers, with normal cardiac anatomy and function. From this database, 15 patients with an anatomically and functionally normal MV were selected (mixed population, between 40 and 60 years of age) of which one was excluded due to low quality of the images. Therefore, in total, 14 imaging scans were evaluated. Parasternal long and short axes standard views were employed, and a frame allowing for the identification and measurement of the different MV dimensions was identified – the mid-systolic frame. To minimise measuring errors, the analysis of each echocardiographic imaging data was performed together with an experienced sonographer. All measurements were evaluated using EchoPAC (v 113, General Electric Healthcare), a software for offline analysis and post-processing of ultrasound images available at Aberdeen Royal Infirmary. Since mitral leaflet surface areas can only be obtained from 3D imaging data, these measurements were not obtained in this analysis. Moreover, the imaging views available for evaluation of the MV shape did not allow for accurate measurements of leaflet lengths, which were therefore excluded. Focus was then given to the morphometric quantification of the mitral annulus, with additional measurements on leaflet tenting and PM distances being obtained. A schematic of the dimensions evaluated is given in Figure 3.4 and all measurements obtained from the patient-specific dataset (PSD) are reported in Table 3.3.

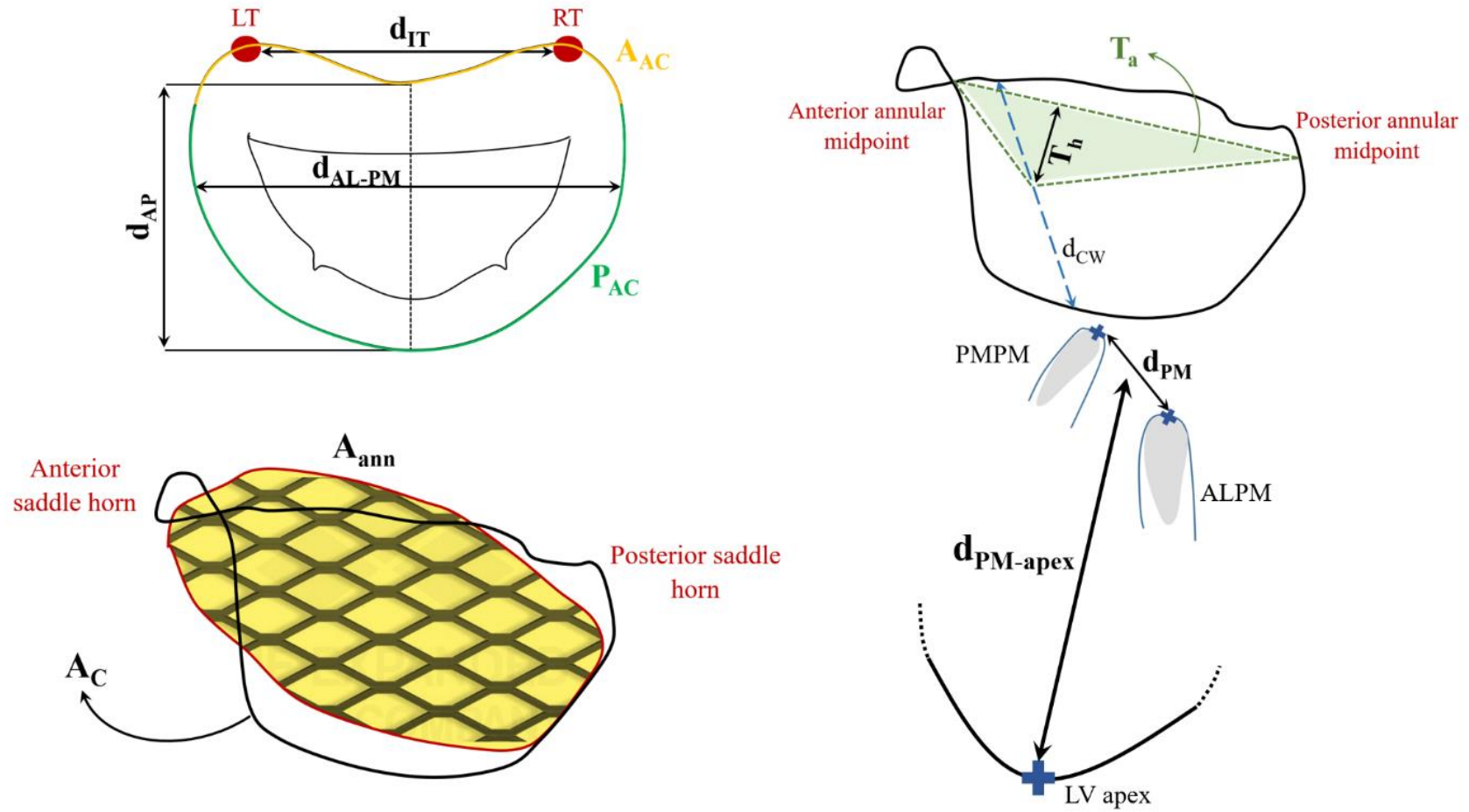


Figure 3.4: Mitral dimensions (in bold) evaluated using the PSD available at Aberdeen Royal Infirmary. Notes: AC, annular circumference; AAC, anterior annular circumference; PAC, posterior annular circumference; LT, left trigone; RT, right trigone; d_{AP} , anteroposterior diameter; d_{AL-PM} , anterolateral-posteromedial diameter; A_{ann} , annular area; T_h , tenting height; T_a , tenting area; d_{PM} , inter-papillary muscle distance; $d_{PM-apex}$, distance between left ventricular apex and the central point of the inter-papillary muscle distance.

Table 3.3: Dimensions at end-systole from new imaging data obtained at Aberdeen Royal Infirmary. Notes: Missing measurements at the subvalvular apparatus for patients 4 and 13 are due to poor image quality.

	Annulus							Leaflet related		Subvalvular apparatus	
Patient	d _{AP} (mm)	d _{AL-PM} (mm)	A _C (mm)	A _{AC} (mm)	P _{AC} (mm)	A _{ann} (mm ²)	d _{IT} (mm)	T _h (mm)	T _a (mm ²)	d _{PM} (mm)	d _{PM-apex} (mm)
1	28	29	97	40	45	490	31	10	140	5	40
2	36	38	93	48	51	510	43	12	290	10	37
3	27	37	94	47	48	530	35	9	170	5	37
4	31	46	105	51	56	500	43	10	210	-	30
5	29	35	86	43	44	460	37	9	210	6	30
6	29	44	104	48	48	600	39	13	300	6	33
7	30	41	85	38	40	400	36	9	250	8	34
8	34	46	104	45	52	550	44	8	160	6	35
9	26	51	105	51	56	680	48	9	220	3	30
10	34	37	89	43	46	520	38	13	280	6	32
11	35	42	101	46	47	610	36	9	250	7	40
12	30	37	86	46	46	460	39	9	200	5	39
13	34	48	111	48	61	790	42	10	310	-	42
14	38	36	90	42	48	530	31	10	350	7	45
Mean ± STD	31.5 ± 3.52	4.5 ± 5.78	96.43 ± 8.27	45.43 ± 3.72	49.14 ± 5.36	545 ± 95.75	39 ± 4.7	10 ± 1.54	238.57 ± 59.74	6.17 ± 1.75	36 ± 4.61

3.2.3. Chordae orientation dataset

Both the MV leaflet and chordae tendineae are mostly composed of collagen fibers (Ross *et al.*, 2021). Despite having several tissue layers with different microstructures, chordae have an inner, central collagen core with a high level of collagen content (Ritchie *et al.*, 2005), with straight collagen fibers (Ross *et al.*, 2021). Moreover, these highly aligned collagen fibres transition into more complex collagen fibre architectures at the area of chordae insertion into the leaflets. Previous studies have found that the direction of collagen fibres in the leaflets from healthy MVs are relatively continuous with the fibres in chordae tendineae (Hadian *et al.*, 2007; Ross *et al.*, 2021).

Based on this previous research, chordae orientation has been used as a proxy to approximate collagen alignment in this study. Two AL and PL samples (displayed in Figure 3.5) were processed as a part of separate studies (Zajec, 2020; Collas, 2021). They were dissected from porcine hearts (Wetlab Ltd., United Kingdom) and fixed using a 10% formalin solution and stained with Van Gieson stain (Sigma-Aldrich, Merck KGaA, Germany). The 2D photographs from both samples were analysed using Fiji software, an ImageJ image processing package (Schindelin *et al.*, 2012), to approximate representative collagen fibre alignments from chordae orientation. Six and four arches in the AL and PL, respectively, were identified by a cardiothoracic surgeon from Aberdeen Royal Infirmary and selected for image post-processing. PM tip location was assumed as the origin of Y-coordinate and the respective inter-PM distances were used to calibrate the data to be obtained. X-Y coordinate data representing the arches was then obtained and recorded, and regression analysis was performed on this data.

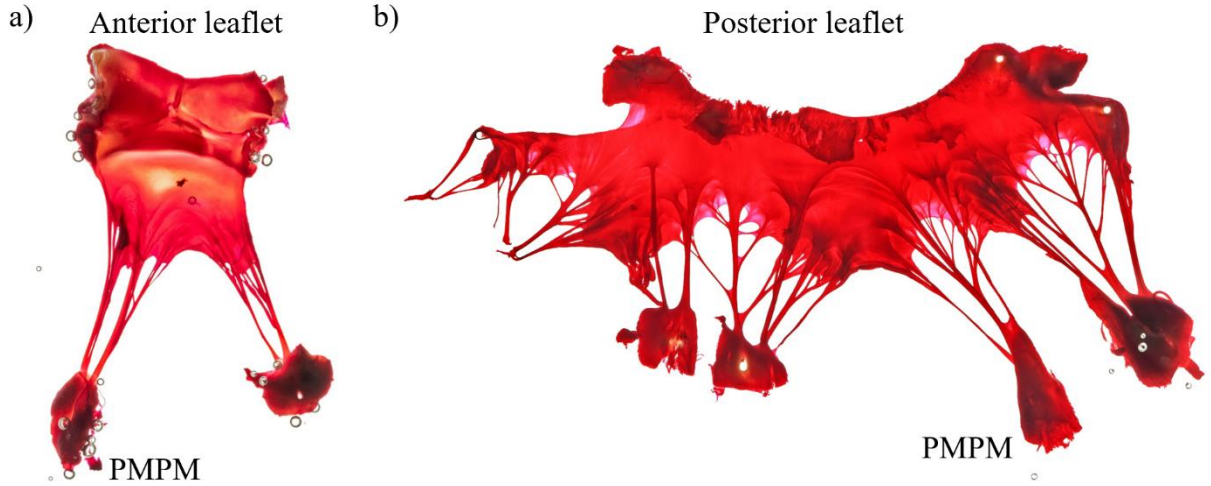


Figure 3.5: Photographs of a) anterior and b) posterior MV leaflet samples, including annulus, leaflets, chordae tendineae and part of the PMs (courtesy of Mr. Keith Buchan, Consultant Cardiac Surgeon, Aberdeen Royal Infirmary).

3.3. Mitral valve morphometry and the Golden Ratio

Recently, the Golden Ratio has been used to mathematically describe average MV morphometry (annulus and leaflets, specifically) (Deorsola and Bellone, 2018; Deorsola and Bellone, 2019). This ratio has been observed in nature (Iosa *et al.*, 2013; Ferring and Panherz, 2008; Henein *et al.*, 2011) and mathematical equations based on it have been derived in function of one predictor variable, the AP diameter. The mitral annulus is described by the AP diameter, CW and AH, and the leaflets are described by the anterior leaflet height, the posterior leaflet middle and commissural scallop heights, and the anterior and posterior leaflet surface areas. MV annulus and leaflets can be described by a unique set of mathematical equations (hereby named prediction equations). The annulus can be defined by:

$$d_{CW} = 1.236d_{AP}, \quad (3.1)$$

$$h_{AH} = 0.236d_{AP}, \quad (3.2)$$

where d_{CW} is the commissural width (CW), h_{AH} is the annular height (AH, which is assumed equal to the tenting height, in agreement with the findings from Deorsola and Bellone) and d_{AP} is the anteroposterior diameter. Assuming the annular boundary as a circumference, the annular radius is equal to half of the CW. As for leaflet heights (or lengths), the anterior leaflet height is defined equal to the AP diameter and the posterior leaflet heights are defined as:

$$P_{mh} = r = 0.618d_{AP}, \quad (3.3)$$

$$P_{ch} = 0.618^2 d_{AP}, \quad (3.4)$$

where r is the annular radius, P_{mh} and P_{ch} are the posterior leaflet middle and commissural scallop heights, respectively. The leaflets are mathematically defined as half-ellipses:

$$A_a = \pi \frac{[4.236r^2]}{4} = 0.4045\pi d_{AP}^2, \quad (3.5)$$

$$P_a = \pi \frac{[2.854r^2]}{4} = 0.2725\pi d_{AP}^2, \quad (3.6)$$

where A_a and P_a are the anterior and posterior leaflet surface areas, respectively.

3.4. Correlation analyses and validation of prediction equations

3.4.1. Correlation analyses methodology

Concerning the datasets described in sections 3.2.1 and 3.2.2, and to find associations between measurements, regression analysis was performed using Minitab 19 (Minitab, State College, Pennsylvania, USA) and MATLAB (MATLAB®, R2019b, 9.7.0.1247435, The MathWorks Inc., Natick, MA, USA). A similar approach to that of Kunkel *et al.* (Kunkel *et al.*, 2010), who performed correlation analyses for dimensions characterising the human vertebrae, was employed. The main assumption behind this analysis was that all valve dimensions assessed were considered as: (1) a variable that can be predicted; (2) a possible predictor variable. This process involved three steps described below.

Firstly, least-squares estimation was used to find equations describing the relationship between two valve parameters at a time, with each data point representing the value associated with one patient. This involved fitting different linear and non-linear regression models to the data, using the order presented in Table 3.4 (C_1 , C_2 and C_3 are generic equation coefficients), and evaluating the correlation coefficient R^2 . An example of this fitting process is represented in Figure 3.6a. This fitting process continued until the next fitting model did not significantly increase R^2 and was not associated with an ill-conditioned Jacobian (related to overfitting or fitting a model that is too complex for the data). $R^2 < 0.5$, $0.5 < R^2 < 0.8$ and $R^2 > 0.8$ were interpreted as poor, moderate and good correlations, respectively.

In the second step, an analysis of variance at a 95% confidence interval was performed to select an equation from the generated set, based on quality of fit and on the physical meaning of the prediction equations. This meant that the values generated by each equation were compared to the clinical range and the SD from literature data for validity. For instance, Figure 3.6b

exemplifies the obtained fits for a wide range of values of x (h_{AH}/d_{AP}) and y (NPA), with the additional grey “window” representing extreme values present in clinical data from the literature. It can be observed that the obtained regression fits behave differently as x and y approach extreme values. Given this, high values of R^2 associated with a p -value < 0.01 (significant regression), together with sensible 95% prediction intervals and consistent with the clinical ranges, indicated the equation with best-fitting that could provide the best approximation to the data. When R^2 proved similar amongst predictions (relative difference $< 3\%$), the simplest fit was chosen. Lastly, the selected best fitting was further evaluated by superimposing on experimental data (as represented in Figure 3.6c) and examining regression residual plots and residual standard deviations (as displayed in Figure 3.6d), which were assumed appropriate if the prediction led to a random arrangement of residuals.

Table 3.4: Regression models employed for correlation analysis.

Regression model	Equation form
Linear	$y = C_1 + C_2x$
Logarithmic	$y = C_1 + C_2 \ln x$
Exponential	$y = C_1 e^{C_2x}$
Polynomial	$y = C_1 + C_2x + C_3x^2 + \dots$

To assess the accuracy of the best-fitting equations found using the methods described in the previous section, these were employed as prediction equations using (1) experimental data from the other datasets described in sections 3.2.1 and 3.2.2, when available, and (2) mean clinical data from a range of literature sources. Moreover, the prediction equations obtained based on the Golden Ratio were also assessed for accuracy in a similar fashion, being compared against the data available.

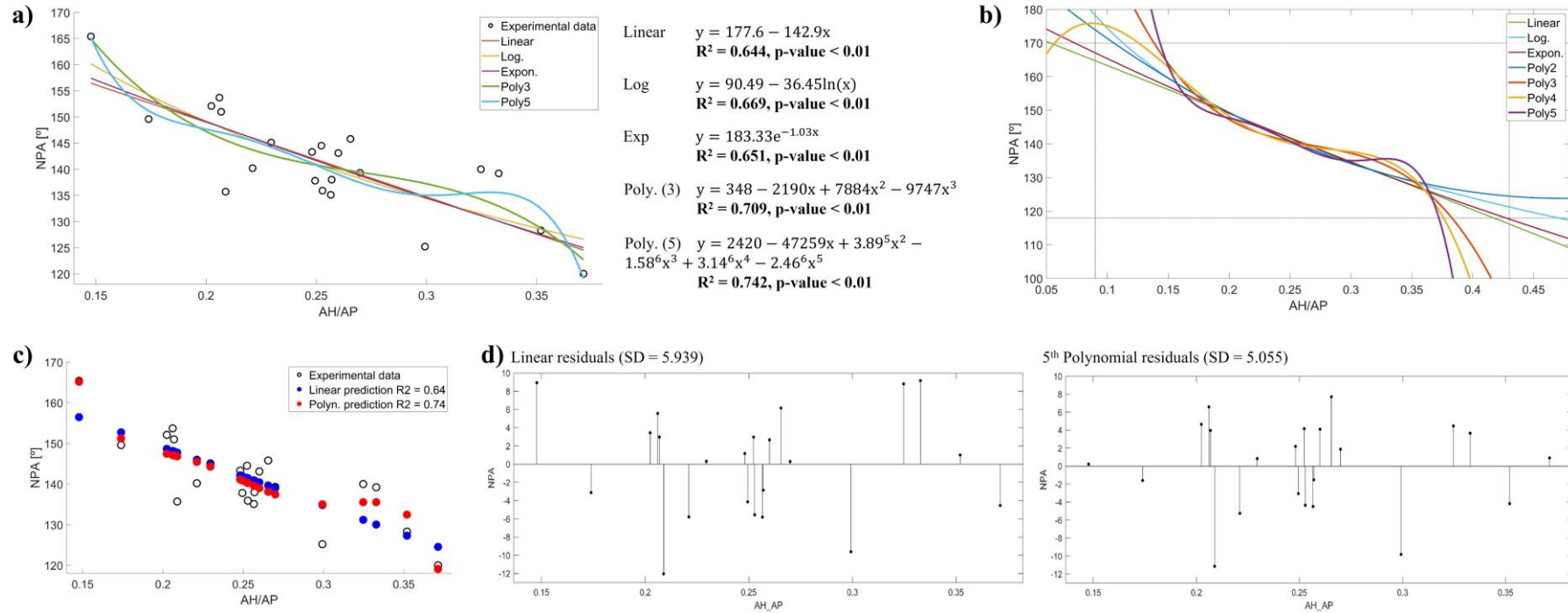


Figure 3.6: Correlation analysis process exemplified for two MV parameters. a) Correlation of clinical data (in this case, h_{AH}/d_{AP} vs NPA) and set of prediction equations generated from linear and nonlinear regression models (y = value of NPA; x = value of h_{AH}/d_{AP}); b) Prediction equation curves are displayed for a range of physical dimensions within a grey “window”, allowing to assess the physical meaning of each equation within the expected ranges; c) Values of NPA predicted using linear and polynomial equations are superimposed on clinical data to allow the selection of the best equation. Residual plots are evaluated for linear and polynomial fits, showing that there is not great difference between predictions arising from these fits.

3.4.2. Mathematical representation of collagen arches

Linear and non-linear regression analyses were performed to the X-Y data characterising collagen arches, using the order presented in Table 3.4, and evaluating the correlation coefficient R^2 . Similar criteria for the R^2 value and fitting processes as in section 3.4.1 were employed, including an analysis of variance at a 95% confidence interval to select an equation from the generated set, based on quality of fit. An analysis of the equations obtained, and their physical meaning was then performed by attempting to establish a relationship dictating arch heights.

3.5. Results

3.5.1. Analysis of datasets from Warraich, Duplessis and PSD

MV dimensions which generated prediction equations with a $R^2 \geq 0.6$ and p-value < 0.01 , as well as estimated coefficients, are reported in Tables 3.5, 3.6 and 3.7. All datasets evaluated yielded specific correlations amongst MV dimensions, with moderate to high R^2 (ranging between 0.607 and 0.931). In general, there were no large differences for the correlations obtained when comparing linear, exponential and logarithmic regressions with each other. This explains the elevated presence of linear fittings in the resulting correlation analysis.

Table 3.5: Correlation analysis results from the Warraich et al. (Warraich et al., 2012) dataset. Equation coefficients and statistical measures for goodness of fit (R^2 , p-value and residual SD) are displayed for linear and best fitting nonlinear model.

Equation Number	Dimensions		Regression model	C ₁	C ₂	C ₃	C ₄	C ₅	C ₆	R ²	p-value	Residual SD
	x	y										
W1	h _{AH} /d _{AP}	h _{AH} /d _{AL-PM}	Linear	0.02955	0.8045					0.781	< 0.01	0.0239
W2			3 rd Polyn.	-0.43141	6.1149	-19.573	23.148			0.807	< 0.01	0.0224
W3	h _{AH} /d _{AP}	NPA	Linear	177.6	-142.9					0.644	< 0.01	5.9391
W4			5 th Polyn.	2422.2	-47259	388730	-1576300	3140600	-2458800	0.742	< 0.01	5.0545
W5	d _{AP}	A _{ann}	Linear	-2.5885	0.4086					0.652	< 0.01	1.7929

Table 3.6: Correlation analysis results from the Duplessis et al. (Duplessis and Marchand, 1964) dataset. Equation coefficients and statistical measures for goodness of fit (R^2 , p-value and residual SD) are displayed for linear and best fitting nonlinear model.

Equation number	Dimensions		Regression model	C ₁	C ₂	C ₃	R ²	p-value	Residual SD
	x	y							
D1	A _C	A _{AC}	Linear	4.1366	0.3048		0.723	< 0.01	2.8483
D2	A _C	P _{AC}	Linear	-4.1366	0.6952		0.931	< 0.01	2.85
D3	A _C	A _{la}	Linear	127.3	3.549		0.700	< 0.01	35.0485
D4	A _C	P _{la}	Linear	65.749	4.2615		0.854	< 0.01	26.5709
D5	A _{AC}	A _{la}	Linear	114.83	10.63		0.807	< 0.01	28.098
D6			2 nd Polyn.	-474.66	43.558	-0.4501	0.832	< 0.01	26.2087
D7	P _{AC}	P _{la}	Linear	113.3	5.798		0.821	< 0.01	29.4851
D8			Exp.	227.02	0.0117		0.852	< 0.01	26.8196
D9	A _{la}	P _{la}	Linear	53.285	0.9135		0.706	< 0.01	37.7332
D10			Exp.	199.47	0.0019		0.729	< 0.01	36.2103
D11	A _C	L _{FE}	Linear	18.824	0.7044		0.759	< 0.01	5.9895
D12	P _{AC}	L _{FE}	Linear	26.301	0.9640		0.738	< 0.01	6.2496
D13	A _{la}	L _{FE}	Linear	17.084	0.1503		0.622	< 0.01	7.5027
D14			Exp.	39.285	0.0017		0.643	< 0.01	7.2895
D15	P _{la}	L _{FE}	Linear	14.797	0.1516		0.748	< 0.01	6.1309

Table 3.7: Correlation analysis results from the PSD. Equation coefficients and statistical measures for goodness of fit (R^2 , p-value and residual SD) are displayed for linear and best fitting nonlinear model.

Equation number	Dimensions		Regression model	C_1	C_2	R^2	p-value	Residual SD
	x	y						
PSD1	P_{AC}	A_{AC}	Linear	18.865	0.54054	0.607	< 0.01	2.4187
PSD2	d_{AL-PM}	d_{IT}	Linear	12.119	0.65668	0.644	< 0.01	2.925
PSD3	A_C	P_{AC}	Linear	-2.1361	0.53178	0.674	< 0.01	3.174

When evaluating the physical meaning of the different prediction equations, it was observed that, even though polynomials of increasing degree (3rd onwards) had higher R^2 values, they were characterised by high changes in their curvatures, which affected prediction of dimensions within a reasonable range. An example of this is the correlation analysis performed between the dimensions A_C and P_{AC} from Duplessis *et al.* (Duplessis and Marchand, 1964), displayed in Figure 3.7. Two models of best fit were taken into account: the linear regression ($R^2 = 0.931$, p-value < 0.01) and a 3rd degree polynomial ($R^2 = 0.976$, p-value < 0.01). Both equations were tested with randomly generated values for the A_C based on the standard-deviation from literature data and compared against the values obtained from a proportion found in the literature ($P_{AC} = 3/5A_C$). Despite having a higher R^2 than the linear equation, a 3rd degree polynomial equation greatly overestimates the P_{AC} for A_C values above 130 mm (when the annulus dilates), yielding non-physiological dimensions (Figure 3.7b). This factor can strongly affect the estimation of MV dimensions. A similar case can be made for h_{AH}/d_{AP} vs NPA (present in Figure 3.6), where polynomials above 3rd degree yield wrong predictions as the fitting goes into a range potentially associated with diseased configurations.

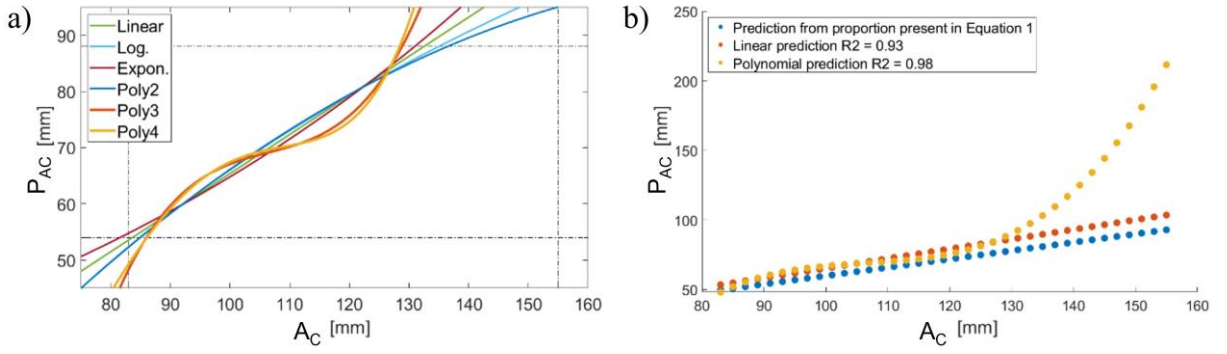


Figure 3.7: Prediction variability for polynomial fittings above the 3rd degree for the A_C and P_{AC} variables from the dataset from Duplessis et al. (Duplessis and Marchand, 1964): high curvature changes are present in these polynomials (a), as well as unrealistic prediction of dimensions (b).

In the following sections, an analysis of the accuracy of prediction equations found through correlations (3.5.2) and based on the Golden Ratio (3.5.3) is presented.

3.5.2. Correlation analyses accuracy

For comparison of dimensions obtained with the correlations against both available data from a different dataset and mean clinical/anatomical literature data, relative error values (E) were evaluated using equation 3.7:

$$E = 100 \times \frac{d_T - d_C}{d_T}, \quad (3.7)$$

where d_T are the true measurements available (either from another dataset or from mean literature data) and d_C are the dimensions obtained with the correlation analyses.

Comparison with other datasets

From the correlation analyses, only three dimensions are common amongst datasets and are associated with fitting equations which can be tested employing data from other datasets: A_C ,

A_{AC} and P_{AC} . Equations D1 and D2 were therefore tested with data from the PSD (Figure 3.8), while equations PSD1 and PSD3 were tested with data from the Duplessis dataset (Figure 3.9), respectively. For all cases, predicted values were associated with high errors. Percentage differences evaluated confirm this, being within the ranges 15.7 – 34% (D1), 18.7 – 42% (D2), 36.6 - 93.7% (PSD1) and 15.6 - 27.6% (PSD3). The equations obtained with the Duplessis dataset, despite having elevated R^2 (D1: $R^2 = 0.72$; D2: $R^2 = 0.93$), are unable to accurately predict dimensions from the PSD, either underestimating (D1) or overestimating (D2) these dimensions. Similarly, the equations obtained with the PSD are unable to accurately predict dimensions from the Duplessis dataset, overestimating (PSD1) and underestimating (PSD3) these. This can, however, be explained by lower R^2 (PSD1: $R^2 = 0.61$; PSD3: $R^2 = 0.67$), which indicates a lesser ability to predict dimensions from different datasets. Alternatively, the use of fittings obtained with *ex vivo* to predict *in vivo* data (and vice-versa) can potentially affect the prediction of dimensions. The potential of prediction by these equations should be further assessed using datasets with equivalent data, which would allow to derive more conclusions regarding their employability as prediction equations.

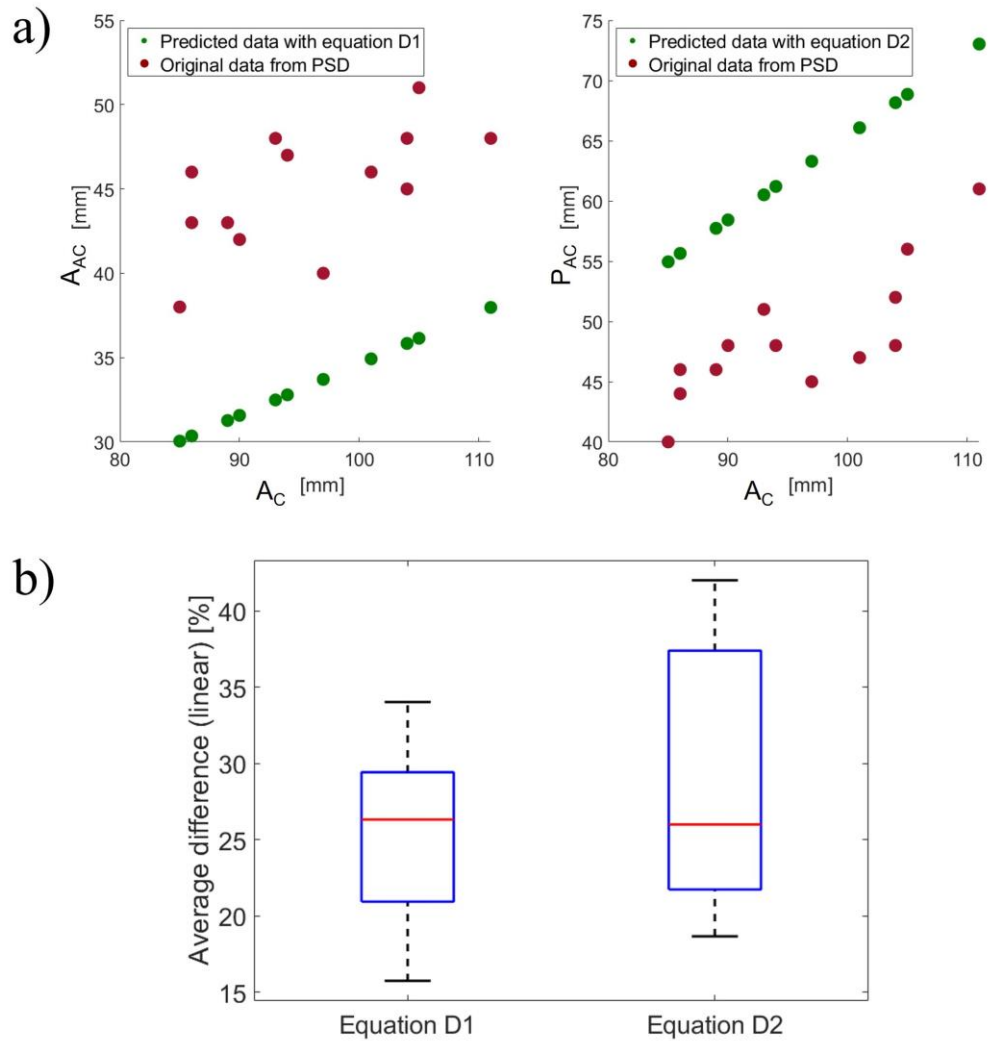


Figure 3.8: Fitting equations D1 and D2 obtained from the Duplessis dataset and with coefficients included in Table 3.6 are tested using data from the PSD: a) PSD original vs predicted data is displayed; b) Box plots representing the relative difference (%) between data from the PSD dataset and that obtained employing fitting equations.

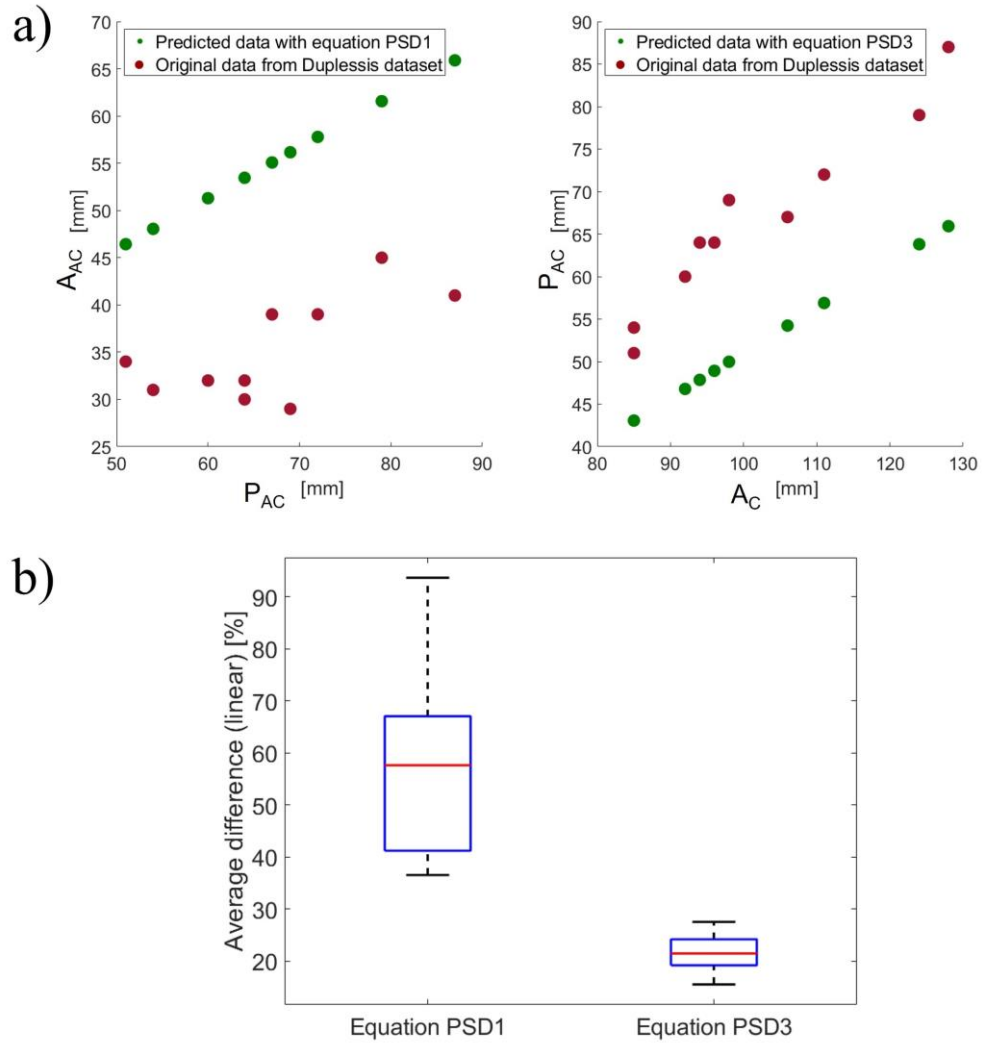


Figure 3.9: Fitting equations PSD1 and PSD3 obtained from the PSD and with coefficients included in Table 3.7 are tested using data from the Duplessis dataset: a) Duplessis original vs predicted data is displayed; b) Box plots representing the relative difference (%) between data from the Duplessis dataset and that obtained employing fitting equations.

Comparison with literature

This analysis was performed to assess differences between: 1) predictions from linear and nonlinear fitting equations; predictions concerning *in vivo* and *ex vivo* data; predictions concerning healthy and diseased data. Box plots were created to represent the relative error values obtained using equation 3.7, and are depicted in Figures 3.10, 3.11 and 3.12 for prediction equations from the Warraich dataset, PSD and Duplessis dataset, respectively.

Moreover, the predictions from equation W5 (from the Warraich dataset) were evaluated accounting for healthy and diseased data, separately (Figure 3.13). Equations D12 – D15 were excluded from this analysis due to the lack of literature sample data including both variables.

The accuracy in predictions from linear and nonlinear fittings varies according to the equation and dimensions considered. Despite having a lower R^2 , linear predictions by equation W1 are associated with a smaller median relative error and a less disperse average difference (75th percentile < 5%) than the polynomial predictions by equation W2 (75th percentile < 10%). On the other hand, the polynomial fitting predictions do not greatly differ from linear predictions as demonstrated for equations W4/W5 (75th percentile < 5%) and equations D5/D6 (75th percentile < 15%). Concerning the Duplessis dataset equations, exponential fittings are either better (Figure 3.12 f)) or worse (Figure 3.12 g)) predictors than the linear fitting for the same dimensions; regardless, relative average differences do not greatly change between both regression models, especially for equations D7/D8 (75th percentile < 10 and 8%, respectively) and D9/10 when tested with *in vivo* data only (75th percentile < 45%).

Some fitting models, despite representing moderate to good correlations with $R^2 > 0.6$, yielded disperse relative errors with a high median when applied to literature data. This is the case for two of the prediction equations from the PSD (PSD1: 75th percentile < 40%; PSD2: 75th percentile < 60%) and all of the prediction equations from the Duplessis dataset when applied to *ex vivo* data (D3: 75th percentile < 70%; D4: 75th percentile < 330%; D9: 75th percentile < 200%; D10: 75th percentile < 250%). In fact, prediction equations consistently fitted *in vivo* data better than *ex vivo* data (as observed in Figures 3.12 c), d) and g)). This may indicate that the fittings based on the Duplessis dataset, despite being originated from fitting *ex vivo* data, yield *in vivo* dimensional predictions associated with smaller and less disperse relative errors than if applied to *ex vivo* data.

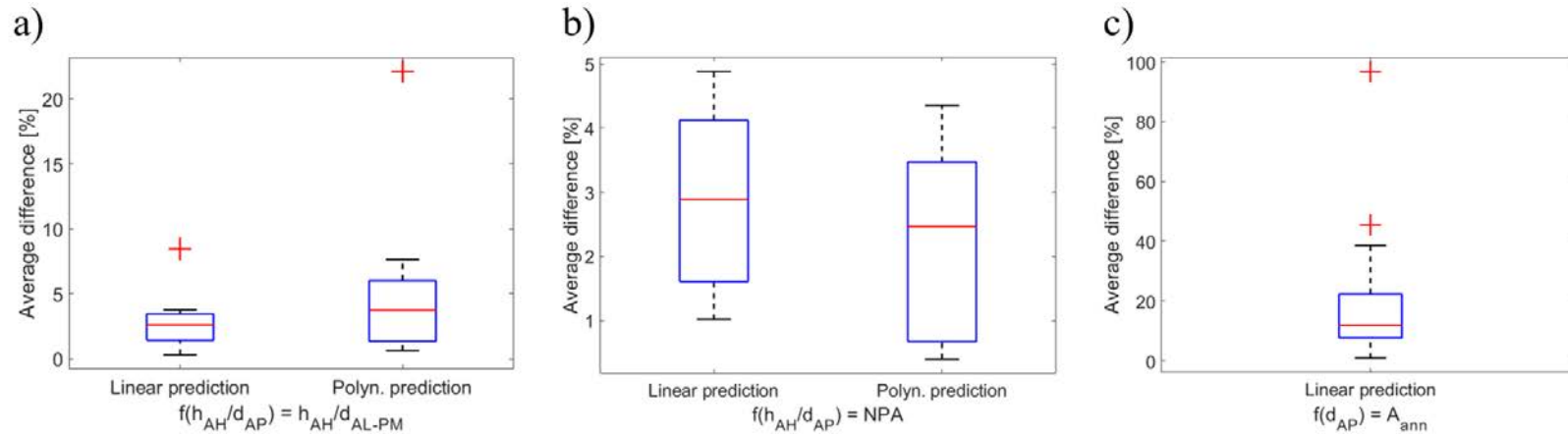


Figure 3.10: Box plots representing the relative difference (%) between original dimensional MV data and that obtained employing fitting equations from the correlation analysis results for the Warraich dataset: a) W1 and W2, b) W3 and W4 and c) W5.

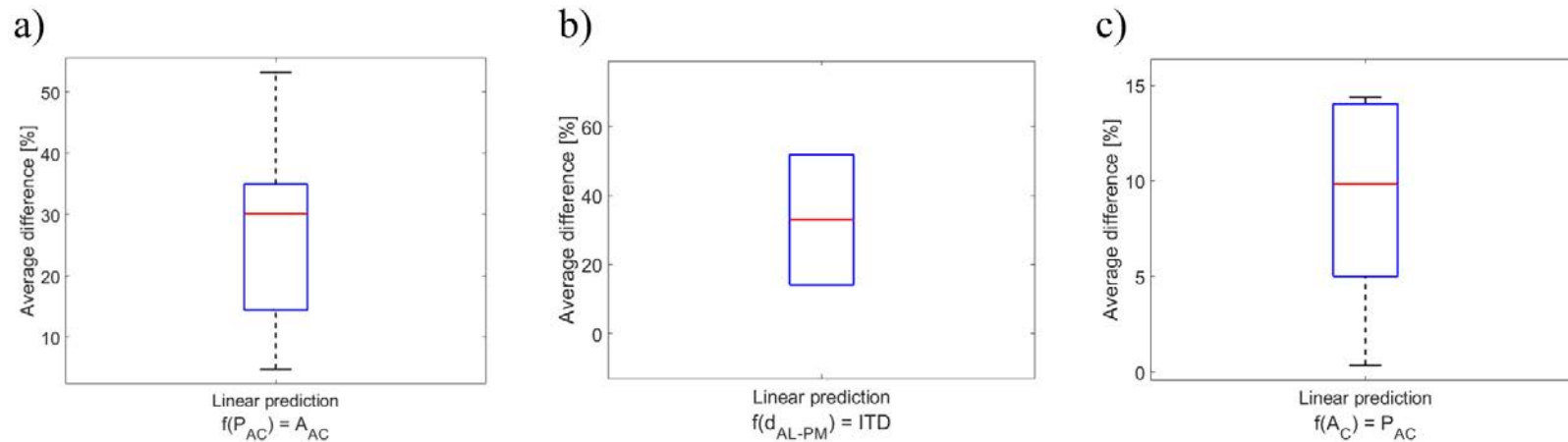


Figure 3.11: Box plots representing the relative difference (%) between original dimensional MV data and that obtained employing fitting equations from the correlation analysis results for the PSD dataset: a) PSD1, b) PSD2 and c) PDS3. Concerning the box plot from b), only two data points were available in the literature for analysis.

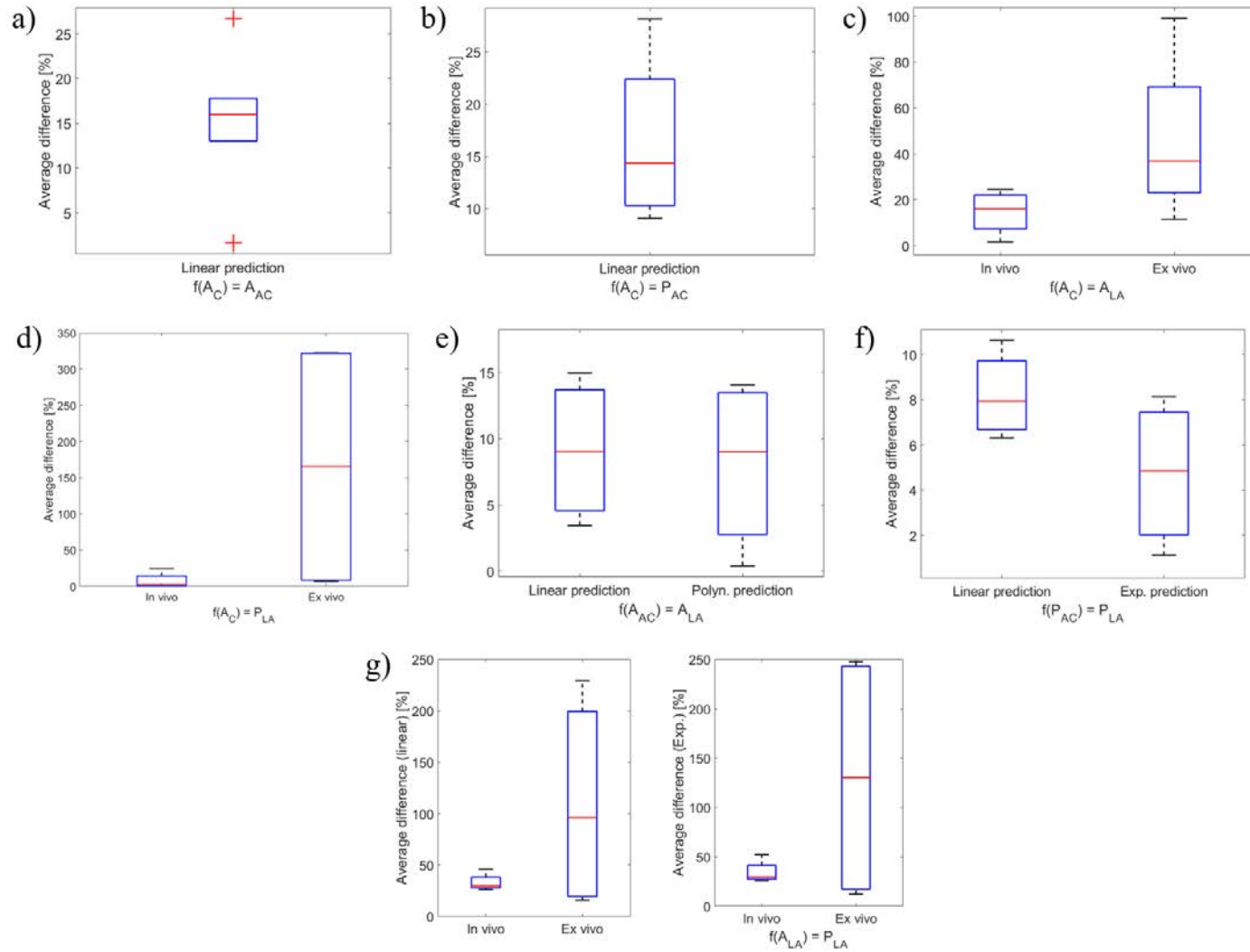


Figure 3.12: Box plots representing the relative difference (%) between original dimensional MV data and that obtained employing fitting equations from the correlation analysis results for the Duplessis dataset: a) D1, b) D2, c) D3, d) D4, e) D5 and D6, f) D7 and D8 and g) D9 and D10.

To assess differences between predictions for healthy and diseased data, equation W5 from the Warraich dataset was employed, since it was the only one where enough literature data was available for the two correlated dimensions (healthy: 10 data points; diseased: 11 data points). Interestingly, the predicted dimensions had a smaller relative error for diseased cases (75th percentile < 15%) than for healthy (75th percentile < 40%), as observed in Figure 3.13. However, it should be noted that the largest relative errors are associated with average measurements for smaller predictor dimensions ($AP \leq 25$ mm, with average relative errors $\geq 38\%$), which affects the statistical analysis performed. This may be indicative, nonetheless, that the prediction equations derived from this dataset (and perhaps the remaining datasets) do not accurately fit dimensional data obtained from a paediatric population.

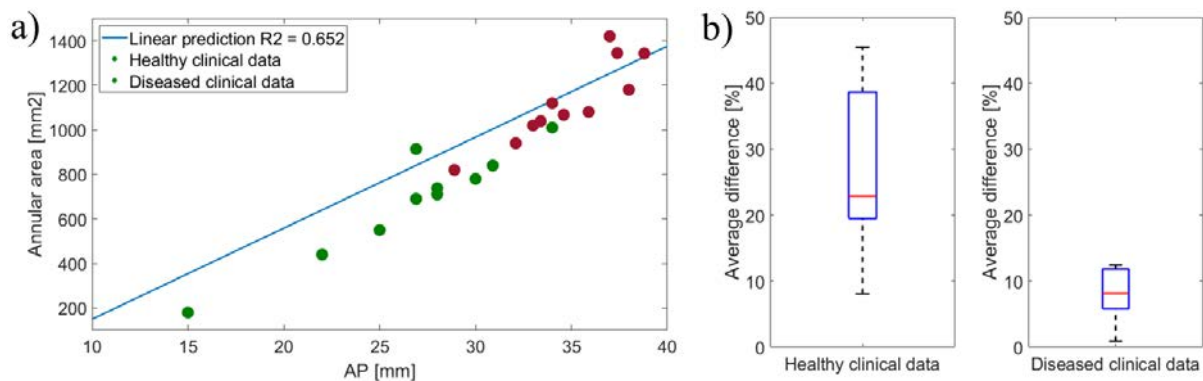


Figure 3.13: Comparison between predictions for mean healthy and diseased clinical data using equation W5 (from the Warraich dataset): a) The linear fit is plotted against raw clinical data and b) Box plots representing the relative difference (%) between clinical data and that obtained employing equation W5.

3.5.3. Accuracy of prediction equations based on the Golden Ratio

Since the Golden Ratio is associated with an average MV model, only literature data associated with healthy MVs was employed to assess the Golden Ratio prediction equations.

Annulus

Mid-diastolic data was employed for validation of the Golden Ratio predictions. For this, mid-systolic data was retrieved from adult and paediatric *in vivo* studies and converted to mid-diastolic values: variations of -9% and +3% were employed for AH and CW data, respectively, based on clinical findings (Tang *et al.*, 2019; Levack *et al.*, 2012; Maffessanti *et al.*, 2013). For end-systolic data, the same values were used. Predictions for CW and AH, as provided by clinical data and derived from the Golden Ratio, are present in Figures 3.14 a) and b), while goodness-of-fit is explored in Figure 3.14 c) and d). The Golden Ratio equations appear able to predict CW and AH values from the AP diameter, as given by R-squared values of 0.83 and 0.91, respectively. The average relative errors between predicted average values and clinical ones are $10.01 \pm 11.18\%$ and $5.68 \pm 19.82\%$ for the CW and AH, respectively. While the average relative error values are in an acceptable range, the standard deviation is greater than the respective average. This is due to the high variability in clinical data, which can have standard deviations as high as 13%, 16% and 37% from the average value for the AP diameter, CW and AH, respectively (Mihaila *et al.*, 2014). Despite this, the trend provided by the Golden Ratio agrees with the clinical data.

Leaflet lengths

As presented in Chapter 2, section 2.3.5, Deorsola *et al.* showed good correlations ($R^2 = 0.94$, p-value = 0.01) between the AP diameter and leaflet lengths (or heights) (Deorsola and Bellone, 2019). Further adult *in vivo* data was retrieved from the literature and compared with the predictions provided by the Golden Ratio, as observed in Figure 3.15. The Golden Ratio equations appear able to predict leaflet lengths from the AP diameter, with *in vivo* data falling within the predicted range and R-squared values being 0.89 and 0.69 for AL and PL leaflet lengths, respectively. Adult patient data from Deorsola *et al.* (2019) (Deorsola and Bellone,

2019) were used to estimate the mean relative errors between predicted values and clinical measures; these are 7.74% and 9.01% for AL and PL lengths, respectively.

Leaflet areas

The equations for leaflet areas, based on the Golden Proportion, yield total anterior and posterior leaflet areas; therefore, to assess their accuracy in obtaining leaflet surface areas, a comparison against mean total leaflet area values reported in the literature was performed. When total leaflet area values were available, corresponding to diastole, these were directly employed; however, most clinical studies report mean leaflet area values at mid-systole, a time frame where the leaflets are in full coaptation, with the coapting area not being included in the data. Therefore, to enable a comparison to be compatible between our predictions and literature, mean diastolic leaflet areas have been estimated from mean mid-systolic values.

For this estimation, the ratio between the diastolic total leaflet area and the closed mid-systolic leaflet area (minimal area that needs to be covered by the leaflets to occlude the mitral orifice) was employed as a scaling factor. This ratio ranges from 1.4 ± 0.1 (Beaudoin *et al.*, 2013a; Beaudoin *et al.*, 2013b) to 1.63 ± 0.17 (Kim *et al.*, 2019). Here, two ratios of 1.48 and 1.64 were employed to (1) obtain an estimation of the total leaflet areas from adult and paediatric mid-systolic data reported by clinical papers and (2) assess the effect of varying this ratio in the estimation of total leaflet area. An assessment of the average relative errors is presented in Table 3.8, and predictions for AL and PL surface areas, as provided in the literature and derived from the Golden Proportion, can be observed in Figures 3.16 and 3.17.

Table 3.8: Mean relative difference between Golden Proportion predictions and original mid-systolic data from the literature, as well as estimated diastolic literature data for AL and PL areas, assuming total to closed leaflet surface area ratios of 1.48 and 1.64.

	<i>In vivo</i> relative error [%]		
	Original literature data	Estimated diastolic data: Ratio = 1.48	Estimated diastolic data: Ratio = 1.64
AL area	84.06	35.61 ± 31.60	23.83 ± 28.65
PL area	73.21	24.39 ± 36.70	13.58 ± 33.25

Table 3.8 shows that the relative difference between Golden Proportion predictions and original mid-systolic data for leaflet areas is much greater than when comparing Golden Proportion predictions and estimated diastolic data. This further corroborates the fact that estimating diastolic leaflet surface areas is required to assess the validity of the Golden Proportion predictions. Moreover, the relative error estimated is sensitive to the ratio used, with the average *in vivo* relative error decreasing by more than 10% for both leaflets when the ratio is increased. This ratio greatly varies amongst the AL and PL, since the literature shows ratios of 1.32 ± 0.39 and 1.47 ± 0.50 for AL and PL areas, respectively, for an AP diameter of 14.3 ± 1.8 mm (Debonnaire *et al.*, 2015). In addition, the standard deviation for leaflet surface areas can be as high as 28% for the AL or 25% for the PL in a clinical sample (Mihaila, 2013), which can help justify the elevated variability in literature data and in the resulting error standard deviations present in Table 3.8.

Figures 3.16 and 3.17 show that the *in vivo* data follows the general trend presented by the Golden Proportion predictions for leaflet surface areas, given the assumed percentage of deviation. R-squared values improve with an increasing ratio (AL: 0.34 vs 0.70; PL: 0.15 vs 0.63), suggesting that the Golden Proportion better predicts leaflet surface areas with higher values. Given these factors, we deemed that a 15 % range for the Golden Proportion prediction of the leaflet areas is acceptable, and, in the toolbox, a value within that range will be employed for leaflet areas.

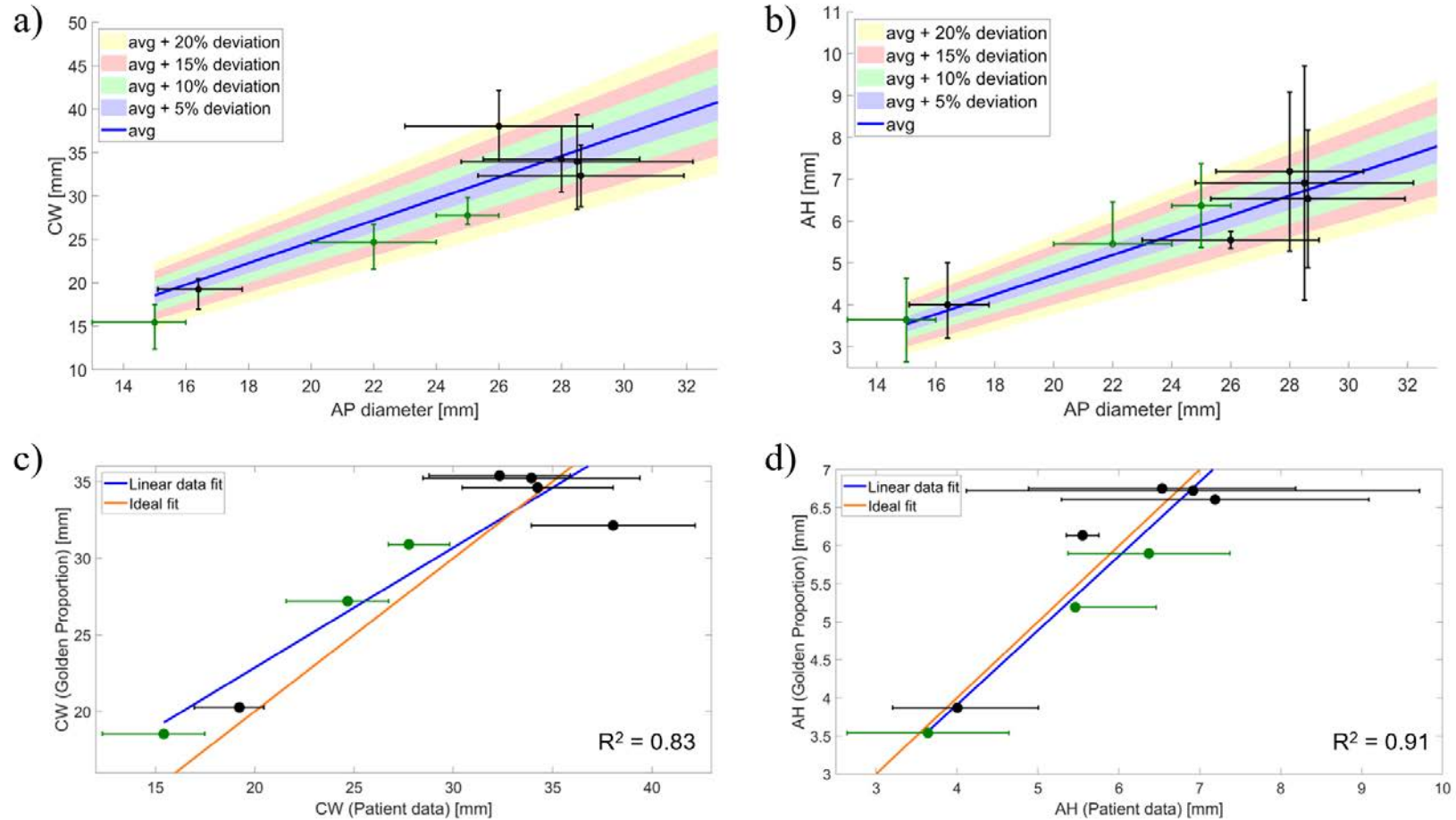


Figure 3.14: Predictions for commissural width (a) and annular height (b) as a function of the anteroposterior diameter, as given by the Golden Ratio (colored shades representing up to 20% deviation from the average value) and by adult and paediatric clinical data (represented by black – adult - and dark green – paediatric - standard deviation bars) (Pouch et al., 2014; Jassar et al., 2014; Lee et al., 2013; Mihaila et al., 2014; Jolley et al., 2017; Munin et al., 2014). A direct regression analysis is shown for commissural width (c) and annular height (d), with the orange fitting line representing the one-to-one fit between predicted and patient data and the blue line representing the patient data best linear fit.

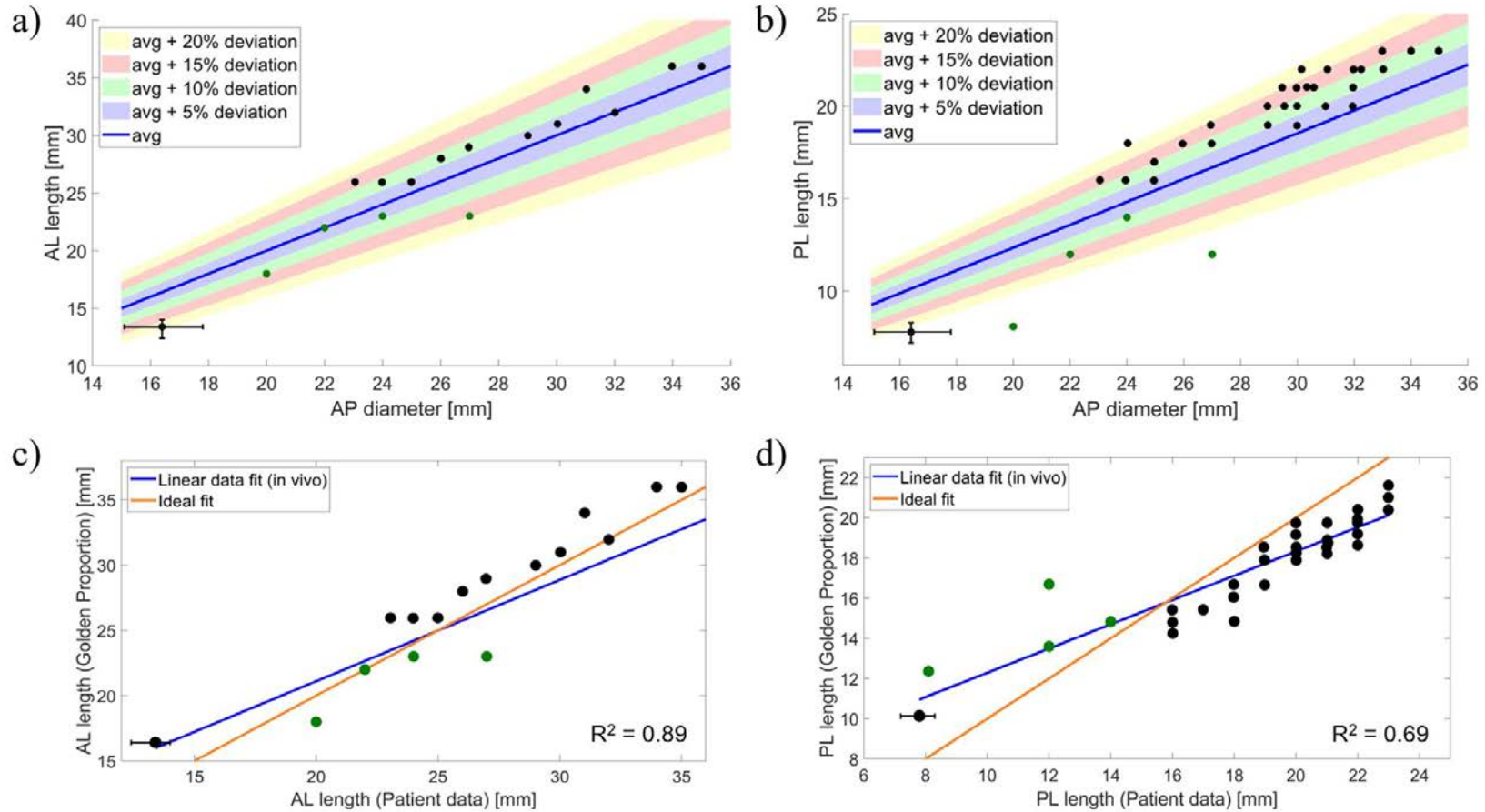


Figure 3.15: Predictions for anterior (a) and posterior (b) leaflet lengths as a function of the anteroposterior diameter, as given by the Golden Ratio (colored shades representing up to 20% deviation from the average value) and by adult in vivo data (Deorsola and Bellone, 2019; Munin et al., 2014). Black and green points represent unique patient data for the studies from Deorsola et al. (2019) (Deorsola and Bellone, 2019) and Nomura et al. (Nomura et al., 2019), respectively. A direct regression analysis is shown for anterior (c) and posterior (d) leaflet lengths, with the orange fitting line representing the one-to-one fit between predicted and patient data and the blue line representing the patient data best linear fit.

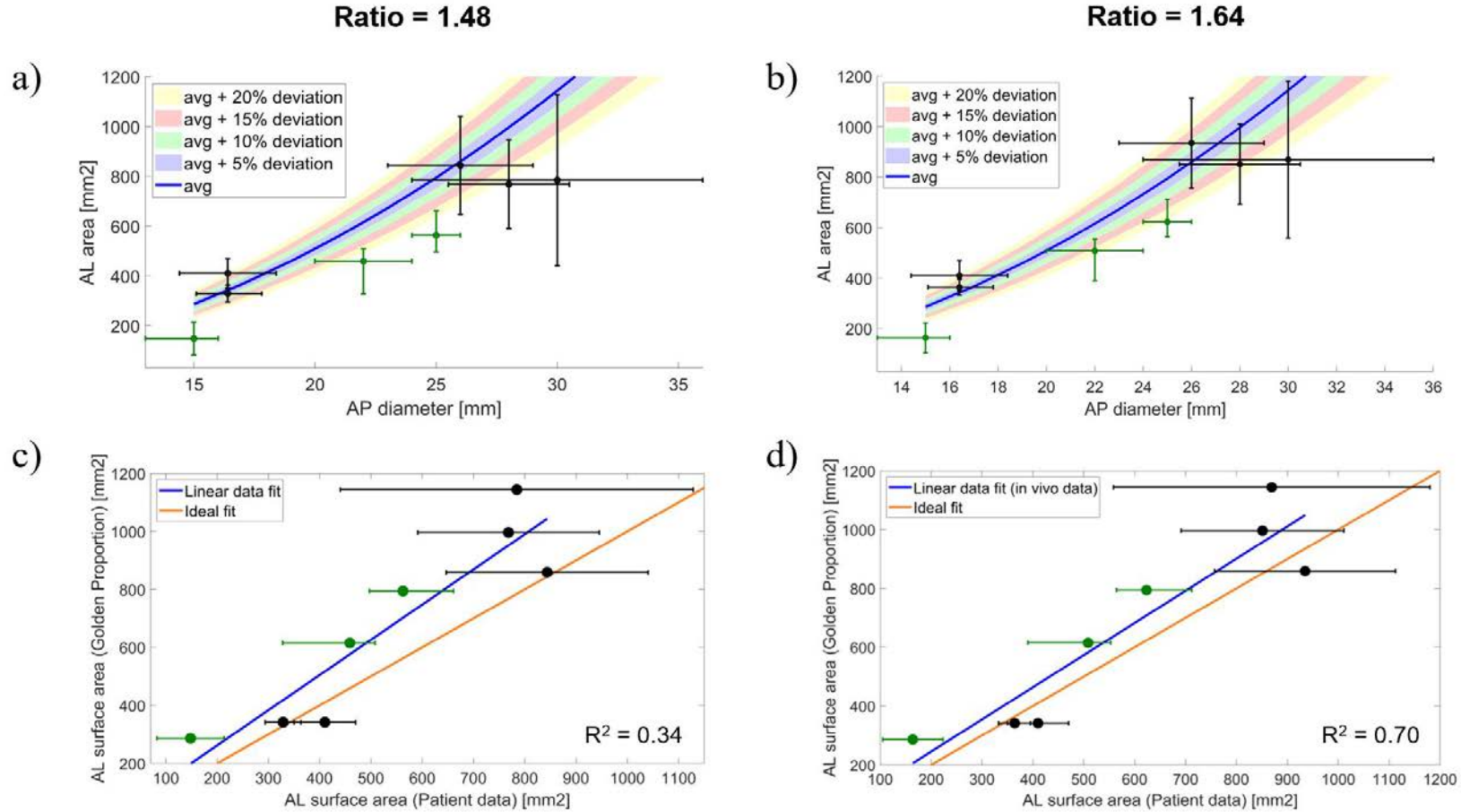


Figure 3.16: Predictions for the anterior leaflet surface area as a function of the anteroposterior diameter for ratios of 1.48 (a) and 1.64 (b), as given by the Golden Ratio (colored shades representing up to 20% deviation from the average value), by adult and paediatric clinical data (represented by black – adult – and dark green – paediatric – standard deviation bars) (Lee et al., 2013; Mihaila, 2013; Mihaila et al., 2014; Jolley et al., 2017; Munin et al., 2014; Kim et al., 2019). A direct regression analysis is shown for ratios of 1.48 (c) and 1.64 (d), with the orange fitting line representing the one-to-one fit between predicted and patient data and the blue line representing the patient data best linear fit.

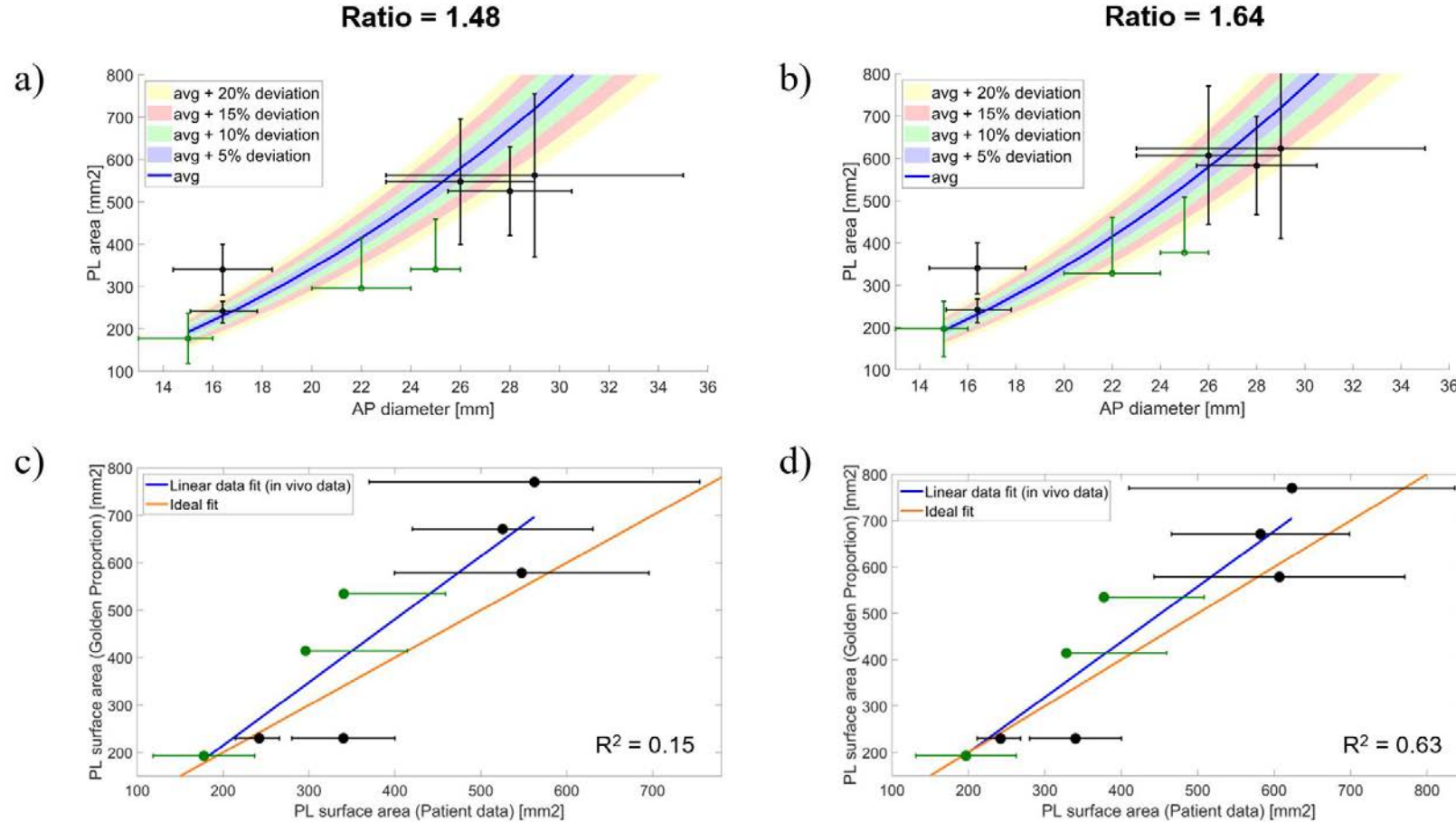


Figure 3.17: Predictions for the posterior leaflet surface area as a function of the anteroposterior diameter for ratios of 1.48 (a) and 1.64 (b), as given by the Golden Ratio (colored shades representing up to 20% deviation from the average value), by adult and paediatric clinical data (represented by black – adult - and dark green – paediatric - standard deviation bars) (Lee et al., 2013; Mihaila, 2013; Mihaila et al., 2014; Jolley et al., 2017; Munin et al., 2014; Kim et al., 2019). A direct regression analysis is shown for ratios of 1.48 (c) and 1.64 (d), with the orange fitting line representing the one-to-one fit between predicted and patient data and the blue line representing the patient data best linear fit.

3.5.4. Analysis of chordae insertions as a guide for collagen orientation

The collagen arches, determined from insertion patterns of chordae into the leaflets, are presented in Figure 3.18. The respective fitting models are reported in Tables 3.9 and 3.10. Second order polynomials (quadratic equations) yielded the best fits, as demonstrated by elevated R^2 values and p-values which were significant (< 0.01): R^2 ranged between 0.942 and 0.977 for AL arches and between 0.855 and 0.947 for PL arches, respectively. These fits represent parabolas, where the vertex corresponds to the highest point of each arch and the coordinates of the two points at the base represent each PM tip.

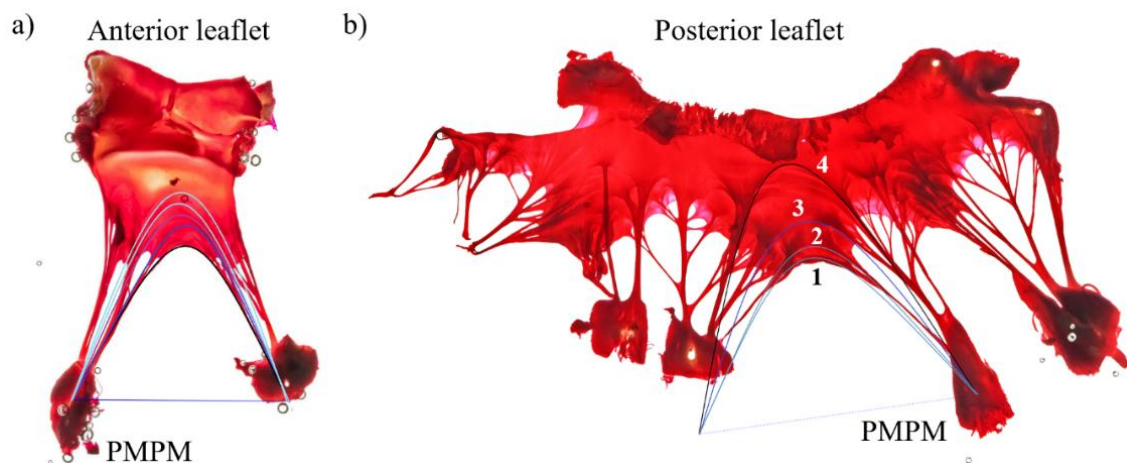


Figure 3.18: Photographs of a) AL and b) PL samples, with selected collagen arches highlighted with solid coloured lines (courtesy of Mr. Keith Buchan, Aberdeen Royal Infirmary). Arches were numbered as demonstrated for the posterior leaflet (from lowest to greatest height).

Since the arches are best described by quadratic equations, the height of each parabolic fitting has been found and compared against the arch height based on original raw data. Linear and non-linear regression analysis was performed on this data to determine if arch height progression can be mathematically characterised (Table 3.11). It was observed that arch height seems to follow a linear trend for the AL, while growing exponentially for the

PL (Figure 3.19). These results do need, however, to be further validated using data from a larger sample of MV specimens which preserve the valve's native shape (as the data evaluated here arises from the analysis of flattened specimens).

Table 3.9: Correlation analysis results for 2D anterior leaflet collagen arch data. Equation coefficients and statistical measures for goodness of fit (R^2 and p -value) are displayed for best fitting nonlinear model. Since the best fitting model is a 2nd order polynomial, the height of the quadratic curve (i.e. the collagen arch), as well as its counterpart from raw data, are also included.

AL arch number	Regression model	C ₁	C ₂	C ₃	R ²	p-value	Height parabolic fit	Height (original)
1	Polyn. 2	-0.6143	2.8087	-0.0819	0.977	< 0.01	23.4542	25.3667
2	Polyn. 2	-1.2224	3.0002	-0.0867	0.962	< 0.01	24.7284	28.08
3	Polyn. 2	-1.096	3.1416	-0.0914	0.96	< 0.01	25.8983	29.5187
4	Polyn. 2	-1.6251	3.3354	-0.0964	0.955	< 0.01	27.2389	30.333
5	Polyn. 2	-3.0229	3.5956	-0.1033	0.942	< 0.01	28.2715	31.7293
6	Polyn. 2	1.2164	3.6134	-0.1087	0.951	< 0.01	31.2538	33.2723

Table 3.10: Correlation analysis results for 2D posterior leaflet collagen arch data. Equation coefficients and statistical measures for goodness of fit (R^2 and p -value) are displayed for best fitting nonlinear model. Since the best fitting model is a 2nd order polynomial, the height of the quadratic curve (i.e. the collagen arch), as well as its counterpart from raw data, are also included.

PL arch number	Regression model	C ₁	C ₂	C ₃	R ²	p-value	Height parabolic fit	Height (original)
1	Polyn. 2	-1.5231	2.0941	-0.0699	0.943	< 0.01	14.1609	13.9553
2	Polyn. 2	-1.9541	2.2357	-0.0743	0.947	< 0.01	14.8736	15.6277
3	Polyn. 2	-1.6119	2.6039	-0.0849	0.935	< 0.01	18.3628	18.1783
4	Polyn. 2	-4.1456	3.3553	-0.1044	0.855	< 0.01	22.8107	24.3423

Table 3.11: Correlation analysis results for the height of collagen arches (obtained from fitting and from original data). Equation coefficients and statistical measures for goodness of fit (R^2 and p -value) are displayed for best fitting model.

Arch data	Regression model	C_1	C_2	R^2	p -value
AL (fit)	Linear	21.711	1.4562	0.964	< 0.01
AL (raw)	Linear	24.588	1.4654	0.971	< 0.01
PL (fit)	Exp.	11.126	0.17454	0.957	< 0.01
PL (raw)	Exp.	10.765	0.19627	0.954	< 0.01

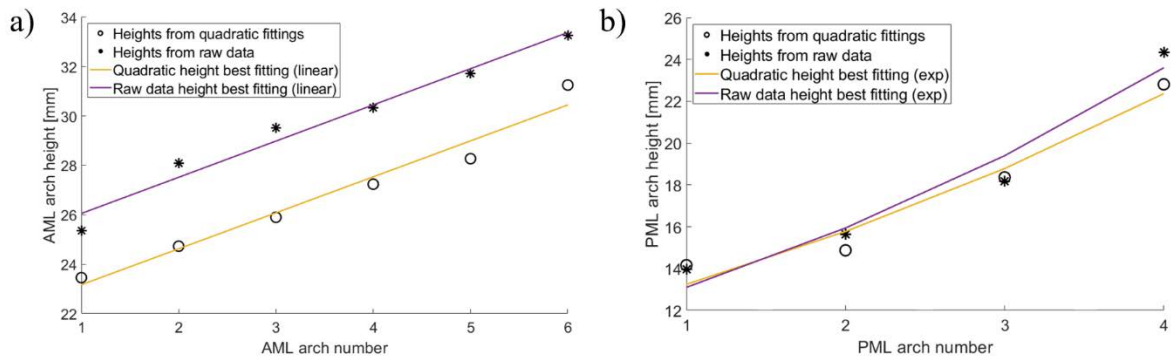


Figure 3.19: Regression analysis on a) AL and b) PL arch height from arch fittings and original raw data.

3.6. Discussion

3.6.1. Main study findings

Morphometric relationships characterising the MV structure have been evaluated through:

- 1) linear and nonlinear regression analysis of dimensions from datasets available in the literature and obtained for this study, and comparison of predicted dimensions against existing measurements; 2) determination of prediction equations based on the Golden Ratio and comparison of predicted dimensions against existing measurements; 3) an evaluation of mathematical descriptions for collagen arches arising from chordae tendineae. These

morphometric relationships are relevant for the development of accurate scalable MV models based on average dimensions (Chapter 4). This study suggests the following findings:

- ❖ Several MV morphometric correlations are present in the literature for the healthy and diseased geometry, with changes in MV shape being mathematically correlated with poorer functional outcomes;
- ❖ Moderate ($0.6 < R^2 < 0.8$) and good correlations ($R^2 > 0.8$) between MV dimensions have been found, based on datasets from the literature and one patient-specific dataset obtained at Aberdeen Royal Infirmary;
- ❖ Polynomials of increasing order (above 3rd) were poor predictors of MV dimensions, being characterised by high changes in their curvatures, which affected prediction of dimensions within a reasonable range, and yielding wrong predictions for data outside the range of values in which the fit was performed;
- ❖ The accuracy in predictions from linear and nonlinear fittings varied according to the equation and dimensions considered, with prediction equations being associated with a large range of relative errors (< 5% to > 250%) when predicting literature data;
- ❖ Predictions of average *in vivo* data were associated with lower relative errors than those of *ex vivo* data, despite employing equations derived from an *ex vivo* dataset;
- ❖ Prediction equations found through correlation analysis must be used with caution, as it remains unclear whether these can fit data from both healthy and diseased valves and can predict paediatric dimensions;

- ❖ Predicted literature dimensions employing equations based on the Golden Ratio show good agreement with the original data, with average relative errors < 10% for annular and leaflet length dimensions, and < 36 % for leaflet areas;
- ❖ Collagen arches approximated from chordae insertions into the leaflets are mathematically characterised by 2nd order polynomial fits and arch height follows linear and exponential growths for the AL and PL, respectively.

3.6.2. Accuracy of prediction equations

The correlation analysis performed yielded several prediction equations with moderate-good R^2 based on three different datasets. Interestingly, nonlinear fits of higher order (e.g. 3rd order polynomial and above) were associated with high changes in curvature, leading to either overestimation or underestimation of dimensions within the prediction range or yielding incorrect predictions for dimensions beyond the range in which the fit was found (associated with disease configurations). This means that the fit would only be valid either: (1) for a narrow range of values in which it was performed and not being applicable to a wider range or population; (2) within an average range representative of a healthy MV, without the presence of geometrical alterations associated with disease. In general 1st order polynomials (linear regression model) yielded more accurate predictions and were associated with a similar range of mean relative errors as nonlinear regression models when employed to predict mean literature data, despite having a lower R^2 .

All datasets evaluated included different MV dimensions, and comparable dimensions yielded correlations in one dataset, but not on the other (e.g. annular dimensions correlated on Duplessis dataset, but not on PSD). This may be due to the datasets originating from ex vivo measurements (Duplessis) and in vivo (PSD) data, which yield different estimates for

MV dimensions (as further explained in section 3.6.3). At the same time, the prediction equations obtained from the Duplessis dataset and employed to predict dimensions from the PSD (and vice-versa) were associated with elevated average relative errors ($> 25\%$ and $> 20\%$ for Duplessis and PSD equations, respectively); however, such fittings were successfully employed in the prediction of mean literature clinical data, with average relative errors usually below 20% . Nonetheless, it remains unclear whether fittings based on *ex vivo* data can be accurately used to predict *in vivo* data.

Based on both healthy and diseased clinical data from Warraich *et al.*, generated fittings accurately predicted mean literature data, with average relative errors mostly below 20% . Since these equations were used to predict both healthy and diseased data, this is indicative that such equations may be employed to generate healthy and diseased dimensions; nonetheless, it is not possible to extrapolate whether they are able to predict dimensions in all cases of disease, especially when MV geometry is altered to an extreme, which occurs during significant mitral regurgitation, for example (Lee *et al.*, 2013; Calleja *et al.*, 2015). Similarly, the equations found using the dataset from Duplessis *et al.* and the PSD are based on valves from healthy subjects, and it remains unclear whether they can be used to predict dimensions in MV dysfunctional geometries.

Prediction equations based on the Golden Ratio were able to accurately predict annular and leaflet dimensions. The use of such equations to calculate all MV morphometry from the AP diameter may seem dubious, especially given the high average relative errors of these predictions in comparison with average *in vivo* data as observed for the leaflet areas (Section 3.2.3). However, it is important to recall that very good correlations ($R^2 = 0.94$, $p\text{-value} = 0.01$) have been found between MV leaflet lengths and the AP diameter which agreed with the Golden Ratio (Deorsola and Bellone, 2018; Deorsola and Bellone, 2019) and that annular

dimensions from the literature have also shown agreement with Golden Ratio predictions (Section 3.6.3).

3.6.3. Challenges of obtaining morphometric data for the mitral valve

MV quantitative measurements can be obtained from clinical imaging (such as echocardiography) or through analysis of anatomical specimens, with both methods having their own limitations. While clinical imaging modalities provide morphometric information based on living MVs, the accuracy of measurements obtained from scans depends on the type of modality used, their spatial and temporal resolutions, and the operator expertise, which can introduce a bias on the obtained data. MV leaflet areas, for example, need to be inferred from 3D imaging parameterizations, which can be associated with inaccuracies. These challenges may have an impact on the obtained MV dimensions, contributing towards model uncertainty (Wu and Takeuchi, 2017). While MV anatomical specimens can be directly touched and measured, they are associated with changes in dimension due to elastic recoil of valve tissue. This is caused by the removal of blood pressure, blood flow and myocardial tension, which alters the physiological balance of forces in the valve, potentially leading to reduced leaflet dimensions which may not be directly comparable to those obtained *in vivo*.

Lastly, the data available in the literature is heterogeneous, as observed in multiple standard deviations from clinical measurements. For example, standard deviations can be as high as 13%, 16% and 37% from the average value for the AP diameter, CW and AH, respectively (Mihaila *et al.*, 2014), or as high as 28% and 25% for AL and PL areas, respectively (Mihaila, 2013). Therefore, both the variability in data and the range of accuracy of the

measurements present in both clinical and anatomical studies can help explain the elevated average relative errors associated with several of the results obtained in this study.

3.7. Conclusions

Currently, the MV dimensions available in the literature are mostly reported in terms of mean and standard deviations, with studies focusing on either the mitral annulus, mitral leaflets, or subvalvular apparatus. Focus is given to reporting average measurements in healthy and diseased cases, and even provide an overview of the dynamic variability of mitral anatomy during the cardiac cycle. This means that not all the dimensions which characterise MV morphometry are stated in a single study; moreover, dimensions for each patient are difficult to obtain in the literature, with just a few datasets available. However, the datasets evaluated in this study correspond to either *ex vivo* data (Duplessis and Marchand, 1964), or data available from both healthy and diseased cases (Warraich *et al.*, 2012). This means that, despite yielding prediction equations associated with elevated R^2 with statistical significance, such data and corresponding fittings need to be extended to the general population with caution. Further studies providing more complete datasets (at a patient-specific level) are required, to take into account the anatomical variability between patients. Critically, collecting measurements for both healthy and diseased MV morphometry including the annulus, leaflets and subvalvular apparatus, would be beneficial to underline and strengthen correlations between dimensions.

In the next chapter there is a focus on the development of a MV parametric and scalable model. For this, the prediction equations obtained from the Golden Prediction have been used, since they provide the most complete set of dimensions to describe average MV morphometry to date.

CHAPTER 4

THE MITRAL VALVE TOOLBOX

4.1. Introduction

The improvement of repair techniques and the development of improved designs for medical devices for the MV is a clinical need (Fedak *et al.*, 2008; Al-Atabi *et al.*, 2012), as described in Chapter 2. To target this, the evaluation of pre- and post-operative scenarios accounting for a subject's MV shape can be performed using computational models, having the potential to improve surgical planning, specifically patient-specific repair procedures (Kohli *et al.*, 2021; Walczak *et al.*, 2021). MV models available in the literature are based either on patient-specific geometries obtained from medical images or based on averaged dimensions. The accuracy of MV computational models is sensitive to valve geometry; while patient-specific models represent the MV geometry of an individual, the associated generation process can be time consuming and computationally expensive, especially when employing numerical mesh-based approaches (Zhang *et al.*, 2019). Moreover, deductions made from a patient-specific case cannot be generalized, since multiple patient-specific models are required for statistical power (Biau *et al.*, 2008).

To overcome these limitations, parametric models, whose geometrical features are described by dimensional constraints, can be used. Some parametric MV models lack the anatomical detail that is necessary to be of clinical value, with their geometries being too simplistic (Salgo *et al.*, 2002; Shen *et al.*, 2017; Domenichini and Pedrizzetti, 2015). Other studies have included more complete parametric geometries including chordae tendineae and PM tips (Choi *et al.*,

2016; Alleau *et al.*, 2019), while more advanced parameterization frameworks have been recently developed to generate patient-specific MV surface models from measurements obtained via medical imaging (Lichtenberg *et al.*, 2020; Pasta *et al.*, 2020). These advanced frameworks can generate high quality MV models within a reasonable time frame, however, they can only be applied to each specific patient individually, not offering the flexibility required to allow for the evaluation of how specific dimensions of MV geometry affects its function, for example.

Given the importance of MV shape on the long-term outcome of valvular surgical procedures, there is a need to develop a computational framework which allows to generate scalable and customisable MV geometries, either based on average morphometric relationships or from patient-specific dimensions. Accordingly, such a framework could capture the range of morphological features required to address the high variability seen in clinical cases, something not currently available in the literature.

The aim of this study was to develop a tool (entitled the MV toolbox) that enables the quick generation of anatomically accurate and clinically useful parametric models of the MV. The toolbox, implemented using MATLAB, can create a variety of geometric models for the MV which are based on user-inputted choices and are directly compatible with the LS-DYNA software, allowing for finite-element simulations. The parameters defining the shape of the MV are either determined directly from patient-specific dimensions or can be estimated from mathematical equations based on the Golden Ratio which recreate a healthy, average model (validated against clinical data, as described in Chapter 3). In this chapter, the capabilities of the MV toolbox are described, including: 1) the development of the full geometrical model, 2) the framework that generates a model ready to be used in computational modelling software, 3) the user-options available, and 4) examples of generated geometries.

4.2. Mitral valve toolbox

4.2.1. Generic features

A software toolbox that can generate the geometry of the MV as a computational model was developed and implemented in MATLAB (MATLAB®, R2019b, 9.7.0.1247435, The MathWorks Inc., Natick, MA, USA). The toolbox yields a diastolic (stress-free) MV geometry including the annulus, anterior and posterior leaflets, and a spatial representation for both PM. The model is built from a baseline mitral annular 3D profile adapted from literature (Pouch *et al.*, 2014) and a set of key MV dimensions, used as constraints to generate the annulus and leaflet shapes. Then, PM spatial position is generated based on distances to key annular landmarks and chordae tendineae are created assuming equal spacing along the MV free edge and generated based on PM and selected free edge node coordinates.

The workflow of the toolbox is shown in Figure 4.1. The main geometric features of the MV annular and leaflet shape employed to generate the model follow the mathematical proportions based on the Golden Ratio which have been described and validated in Chapter 3 (Deorsola and Bellone, 2018; Deorsola and Bellone, 2019), and PM positions and chordae tendineae distributions are based on *in vivo* and *ex vivo* findings (Yamaura, 2008; Obase *et al.*, 2016; Lam *et al.*, 1970). The model can be parameterized using two alternative procedures: (1) based on patient-specific dimensions obtained from patient data (e.g. medical image modalities) and directly inputted by the user or (2) using average dimensions derived from mathematical proportions relating MV anatomical segments based only on the anteroposterior (AP) diameter. Multiple graphic user interface (GUI) options are provided to better characterize the subvalvular apparatus: the user can choose a one tip point representation for the PM, where all chordae originate from, or a 3D origin scheme; moreover, PM displacement can be prescribed. Greater

detail on all GUI options is provided in Sections 4.2.2 and 4.4. The toolbox generates two different outputs: a MV geometrical model or a MV model for computational simulations (further detail on these options is presented below). Once the parameterization is completed, the MV leaflet surface mesh can be exported as a stereolithography (.stl) file, compatible with a range of modelling software (including computer-aided design and FE analysis software), and the 3D coordinates of the PM can be exported as a text file. On the other hand, if one chooses to create an input file for computational simulations, the chordae tendineae distributions are also added, completing the MV model. The input file for FE simulations is compatible with LS-DYNA 4.5.12 (LSTC, Livermore CA, USA) and employs the generated geometry. For this, the meshed model is pre-processed by defining material properties, boundary conditions and contact properties through MATLAB, with the LS-DYNA input file being exported as a key (.k) file.

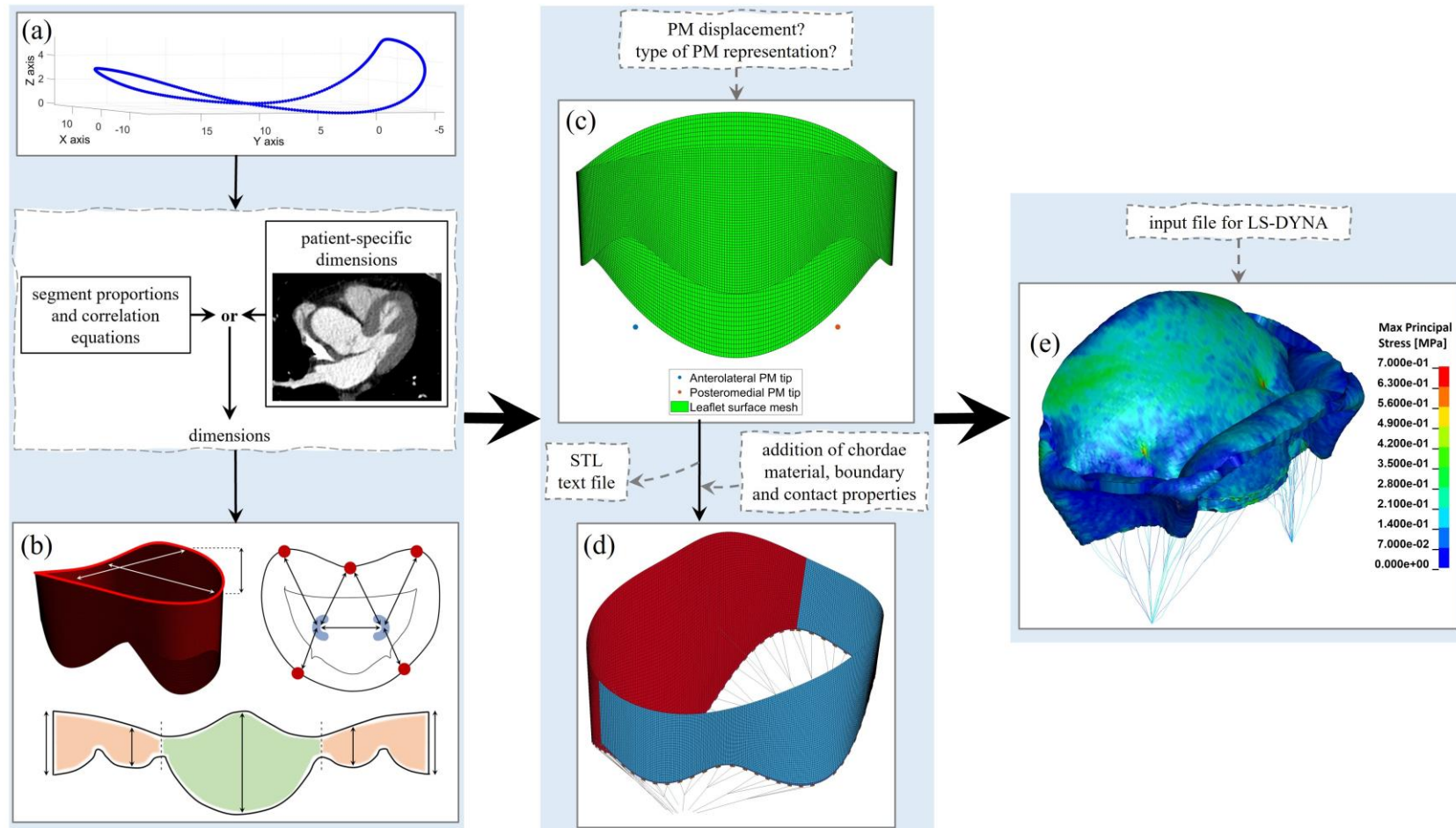


Figure 4.1: Workflow of the MV toolbox, from the generation of the morphometric model to the FE simulation result: (a) The inputs are a baseline mitral annular 3D profile and MV dimensions, either obtained from mathematical formulations or from patient-specific medical images; (b) The model is parameterized, with the annulus, leaflets and PM (papillary muscles) being independently scaled; (c) A surface model mesh is created for the leaflets and points identifying each PM are stored. The user can choose to output these as an .stl file for the mesh and a text file for PM coordinates; (d) The meshed model is pre-processed: chordae tendineae are added, material properties, boundary and contact conditions are defined; (e) The .k input file is created and run in LS-DYNA.

4.2.2. Geometrical model

Pre-processing and assumptions

MATLAB was used to define the annular saddle (Figure 4.2) based on a mean AHCWR rotational profile (proxy for annular nonplanarity) for a healthy adult obtained from Pouch *et al.* (2014) which was adapted to define annular height (over the z -coordinate, displayed in Figure 4.2) (Pouch *et al.*, 2014). Moreover, data from Jassar *et al.* (2014) was employed to change the annulus in the x - y plane (Figure 4.2) (Jassar *et al.*, 2014). The annular y and z -coordinates were further reshaped through an iterative process to match a diastolic profile, obtaining an approximately 7.6 mm saddle-horn height (represented in Figure 4.3), consistently with previous experimental findings (Dagum *et al.*, 2001). This annular boundary was used as a starting template from which to recreate the MV geometry (Figure 4.4a). The model incorporates the following assumptions, according to the GUI options chosen by the user:

1. The annular and leaflet shapes are assumed symmetric along the long axis meridian of the anterior MV leaflet, consistent with *ex vivo* findings (Ranganathan *et al.*, 1970; Krawczyk-Ozog *et al.*, 2017) and previous geometrical models (Choi *et al.*, 2016; Stevanella *et al.*, 2009). The PM tips are assumed symmetric; however, this symmetry can be removed if asymmetric PM displacement is prescribed;
2. If an average model is selected, a healthy MV leaflet shape is reproduced, since, in disease, the proportions characterizing annular and leaflet segments change (Deorsola and Bellone, 2019). However, if patient-specific data is inputted, the model shape is not constrained when generated, and it is possible to create either a healthy or diseased MV model according to the input.

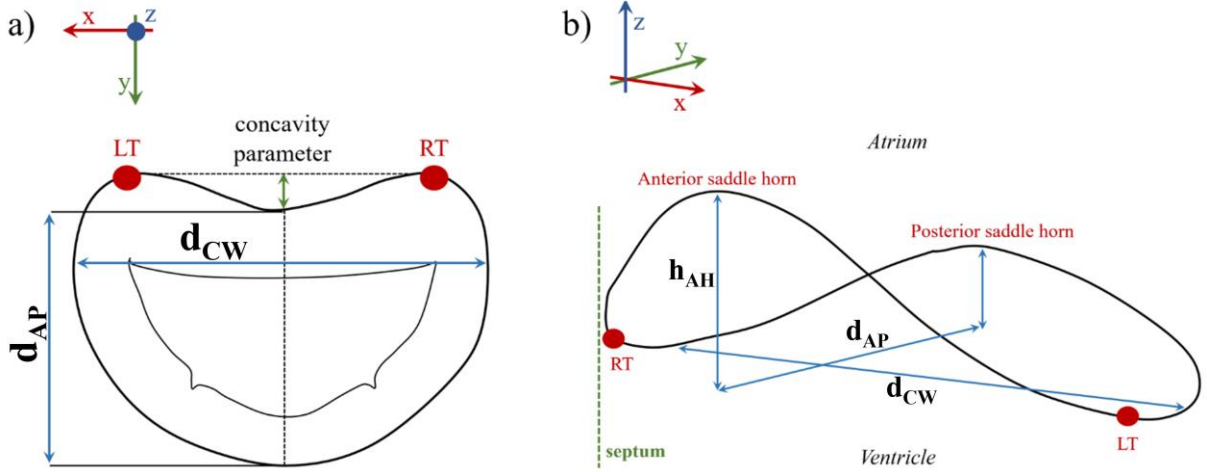


Figure 4.2: Input parameters requested in the toolbox to parameterize the annular boundary, where the MV annulus is a) viewed from within the left atrium and b) from above. The 3D axis denote the orientation for each image. Notes: LT, left trigone; RT, right trigone; d_{AP} , anteroposterior distance; d_{CW} , commissural distance; h_{AH} , annular height.

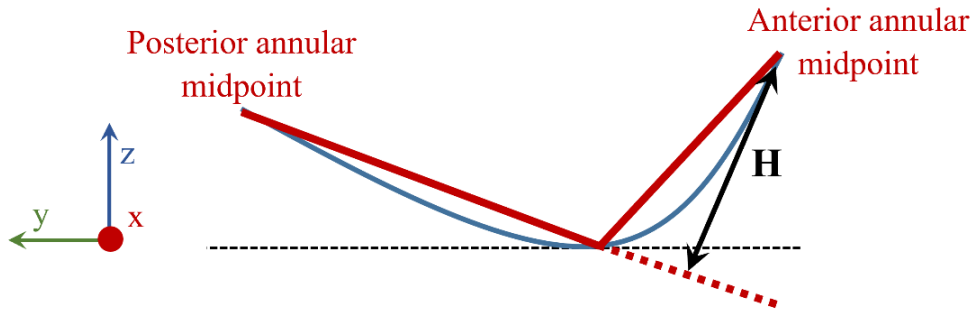


Figure 4.3: Saddle-horn height (H) representation in a lateral view of the mitral annulus.

The generation of a morphometric MV model focuses on 3 regions: first the annulus is parameterized, followed by the anterior and posterior leaflets, and lastly the PM tips. Table 4.1 includes the fundamental dimensions implemented in the toolbox which are required to generate the baseline MV model, further explained in the following sub-sections of Section 4.2.2.

Table 4.1: Dimensions used to parameterise the MV geometry.

MV part	Acronym	Dimension/measurement
Annulus	d_{AP}	Anteroposterior diameter
	d_{CW}	Commissural width
	h_{AH}	Annular height
	-	Ring concavity
Leaflets	A_h	Anterior leaflet height
	P_{mh}	Posterior leaflet middle scallop height
	P_{ch}	Posterior leaflet commissural scallop height
	A_a	Anterior leaflet surface area
	P_a	Posterior leaflet surface area
PM	$ALPM_0$	Distance from ALPM tip to anterior annular midpoint
	$ALPM_{10}$	Distance from ALPM tip to left trigone
	$ALPM_8$	Distance from ALPM tip to annular division between middle and anterolateral commissural scallops
	$PMPM_0$	Distance from PMPM tip to anterior annular midpoint
	$PMPM_2$	Distance from PMPM tip to right trigone
	$PMPM_4$	Distance from PMPM tip to annular division between middle and posteromedial commissural scallops

Annular parameterization

All dimensions required to parameterize the mitral annulus are included in Figure 4.2. The valve ring has a kidney bean shape, more evident in systole, and the anterior leaflet is centred on a slight depression in this ring (Degandt *et al.*, 2007; Misfeld and Sievers, 2007). Accounting for a previous mathematical study of the MV (Kaiser *et al.*, 2019), the valve ring concavity can be controlled given an input parameter that varies between 0 and 0.5; 0 corresponds to a D-shaped annulus, while 0.5 represents the maximum allowed concavity.

After defining the ring concavity, the annulus can be parameterized using three dimensions: the AP diameter, the CW and the AH. The best fitting polynomial curves were selected to manipulate the annular shape: first, they were used to scale the AP diameter and CW in the x - y plane; then, the AH was parameterized using polynomial curves to scale z coordinates. AH was defined as the vertical distance between the maximum and minimum annular heights (Jassar *et al.*, 2014; Pouch *et al.*, 2014), and, by default, characterised as the anterior saddle horn height.

By scaling this height, the posterior saddle horn height was appropriately scaled, maintaining the proportion between anterior and posterior saddle horn heights.

Leaflet parameterization

Given the assumed symmetry of the MV, the heights of the anterolateral and posteromedial commissural scallops were considered equal. The required MV dimensions to parameterize the leaflets are shown in Figure 4.4. The initial 3D free edge template was generated according to the inputted leaflet heights and baseline commissural heights (to be adapted during the implementation) reported by (Ranganathan *et al.*, 1970), which were interpolated.

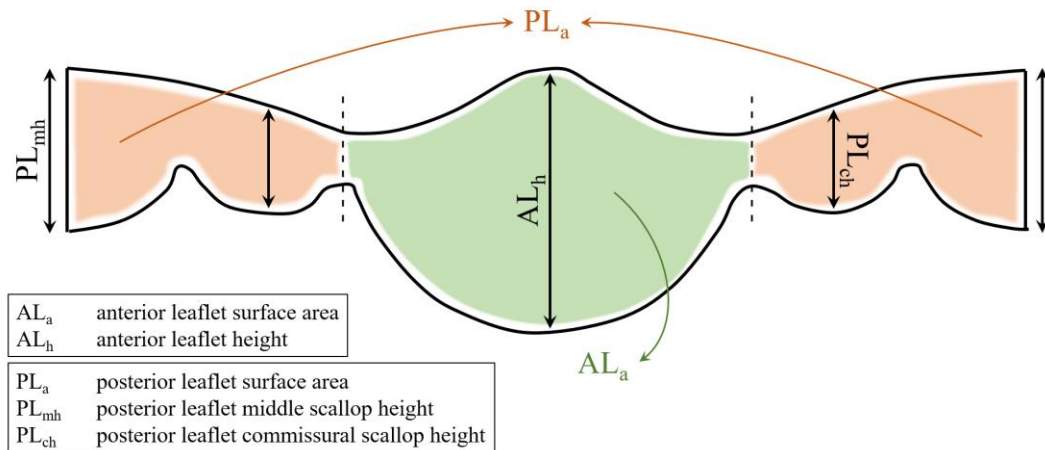


Figure 4.4: Input parameters requested in the toolbox to parameterize the leaflets.

To parameterize the leaflet surface areas, both annular and free edge boundaries were split into different portions representing the anterior leaflet and the posterior middle and commissural scallops. For this process, the annular boundary was first split considering anterior and posterior annular proportions (2/5 and 3/5 of the total annular circumference, respectively (Pouch *et al.*, 2014; Jassar *et al.*, 2014)). The annular split point has been set as the commissural point. In addition, the posterior leaflet middle scallop is usually broader than the other two scallops

(Ranganathan *et al.*, 1970; Krawczyk-Ozog *et al.*, 2017); therefore, to divide the posterior leaflet annular boundary between middle and commissural scallops and in agreement with a previous morphometry study (Deorsola and Bellone, 2019), the middle scallop was assumed equal to 9/20 of the total posterior leaflet circumference. In the implementation, the length of the commissural and cleft boundaries was then altered to obtain the desired leaflet areas. A representation of all leaflet boundaries employed is presented in Figure 4.5.

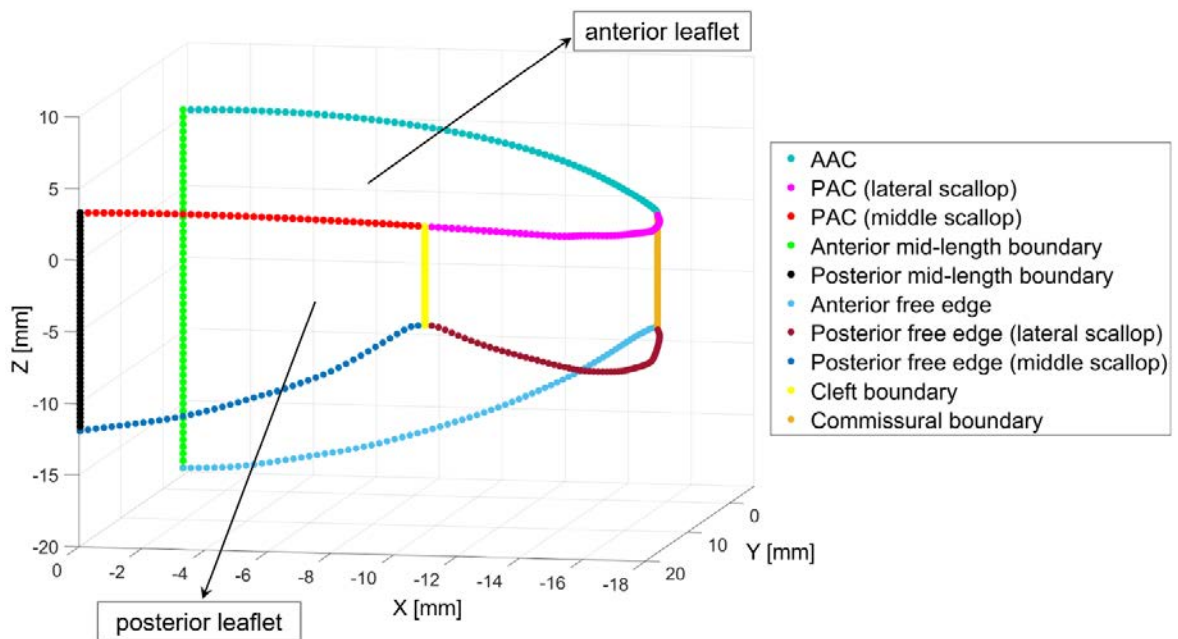


Figure 4.5: The lateral half of the MV is represented, with boundaries defined during the parameterization process of the leaflets. Notes: AAC, anterior annular circumference; PAC, posterior annular circumference.

Papillary muscle parameterization

The 3D spatial position of PM tips is parameterized according to distances between the tips and annular landmarks (o'clock points) (Yamaura, 2008; Sakai *et al.*, 1999). Figure 4.6a represents these annular points and the implemented distances. The user can decide whether to represent the PM as a single tip (where all chordae originate from), or as a 3D point cloud of chordae

origins in a C-shape (as given in an axial view), discretized in Figure 4.6b and 4.6c and based on *in vivo* and *ex vivo* findings (Obase *et al.*, 2016; Lam *et al.*, 1970) and previous computational studies (Stevanella *et al.*, 2011; Choi *et al.*, 2016). This point cloud consists of 13 origin points per PM, giving rise to 12 anterior leaflet free edge insertions, 12 posterior leaflet free edge insertions and 2 strut chordae insertions. In total, it equals 26 chordae, consistent with *in vivo* (Obase *et al.*, 2016) and *ex vivo* (Lam *et al.*, 1970) findings.

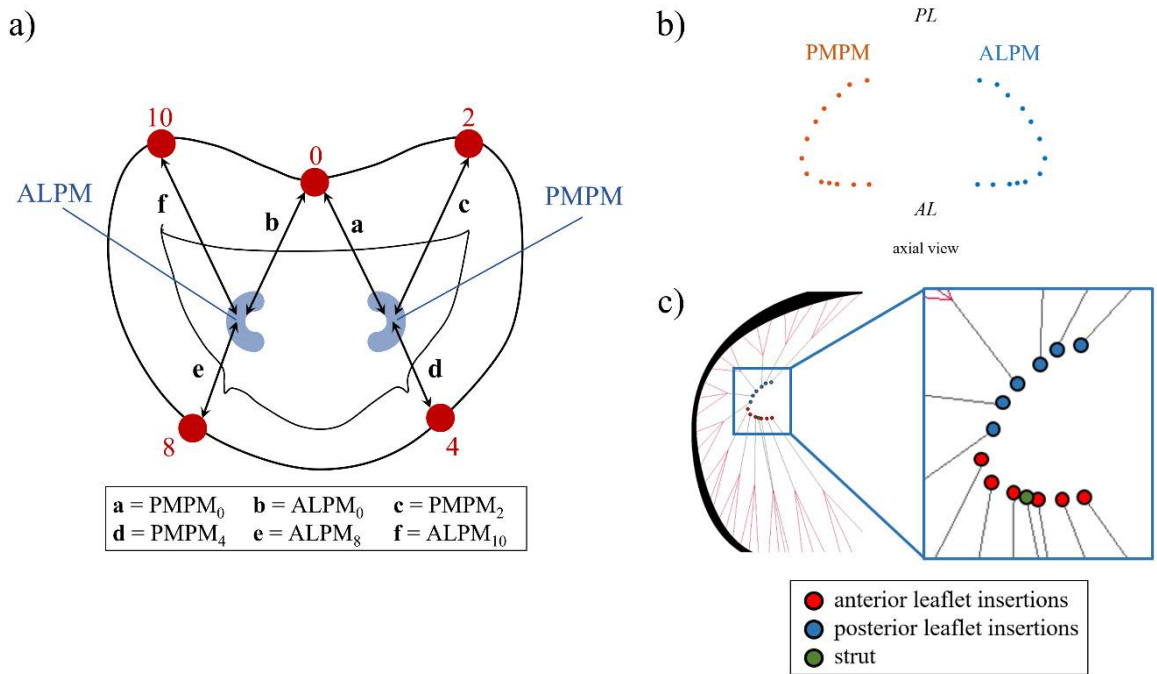


Figure 4.6: a) Distances between PM tips and corresponding points of mitral annulus, as characterized by the literature (Sakai *et al.*, 1999; Yamaura, 2008). 0, 2, 10, 4 and 8 o'clock represent: anterior annular midpoint; right trigone; left trigone; division between middle and posteromedial commissural scallops; division between middle and anterolateral commissural scallops, respectively (Yamaura, 2008); b) 3D shape representing chordae origins in the PMs (axial view); c) Different origin points correspond to different points of insertion into the leaflets. Notes: ALPM, anterolateral PM; PMPM, posteromedial PM; PL, posterior leaflet; AL, anterior leaflet.

The spatial position of PM tips can be further manipulated to represent dysfunction (Figure 4.7). The PMs can undergo medial/lateral (position change in x-y plane) and apical (change in

the z -coordinate) shifts, corresponding to malposition or change in position (Kim *et al.*, 2012). These relate to symmetric (same motion restriction for both leaflets) or asymmetric (prevalent restriction of one of the leaflets) tethering, represented by displacement of both PMs or either one of them (Kim *et al.*, 2012). Since these changes are associated with altered inter-PM distances (Kim *et al.*, 2014; Obase *et al.*, 2016), the user needs to provide the desired inter-PM distance as an input.

As the LV dilates, the PM also get displaced (Obase *et al.*, 2016). In the toolbox, the user can prescribe whether the LV dilates posteriorly, anteriorly, or on both sides. A .stl file of a 18 year old (female, weight 68 kg, body surface area 1.66 m²) adolescent LV model was reconstructed from a magnetic resonance imaging scan sequence obtained at the Murdoch Children's Research Institute (study approved by the Human Research Ethics Committee of the Royal Children's Hospital – HREC 33227). The left ventricle was scanned with a cine TrueFISP short axis stack sequence, using multiple breath-hold blocks, on a Siemens Aera magnetic resonance imaging machine at 1.5T (repetition time = 39.6 ms; echo time = 1.43; flip angle = 80 degrees; pixel spacing 1.33 × 1.33 mm; slice thickness = 7 mm; 25 frames over the cardiac cycle).

The reconstructed model was used as a template to approximate the inner geometry of the LV on which papillary muscles are placed. The template employed half of the model which was made symmetric along its height axis, and has been scaled to match adult dimensions from the literature (Di Donato *et al.*, 2006). Moreover, it was arranged in the 3D space to align its base with the MV annular plane, similar to previous computational studies (Park *et al.*, 2019; Domenichini and Pedrizzetti, 2015; Domenichini *et al.*, 2005). The geometry can then be parameterized based on the input width and length (Park *et al.*, 2019; Di Donato *et al.*, 2006; Domenichini and Pedrizzetti, 2015). The distance between the tip of each PM and its respective site of origin at the LV wall was assumed 26 mm, yielding a PM base within the middle third

of the wall (Saha and Roy, 2018). By parameterizing the LV geometry, the position of the PM base is also rearranged, and, if the respective distance between tip and base is greater than 8.8 mm (standard deviation for this distance (Saha and Roy, 2018)), the tip is displaced (as displayed in the schematic from Figure 4.8).

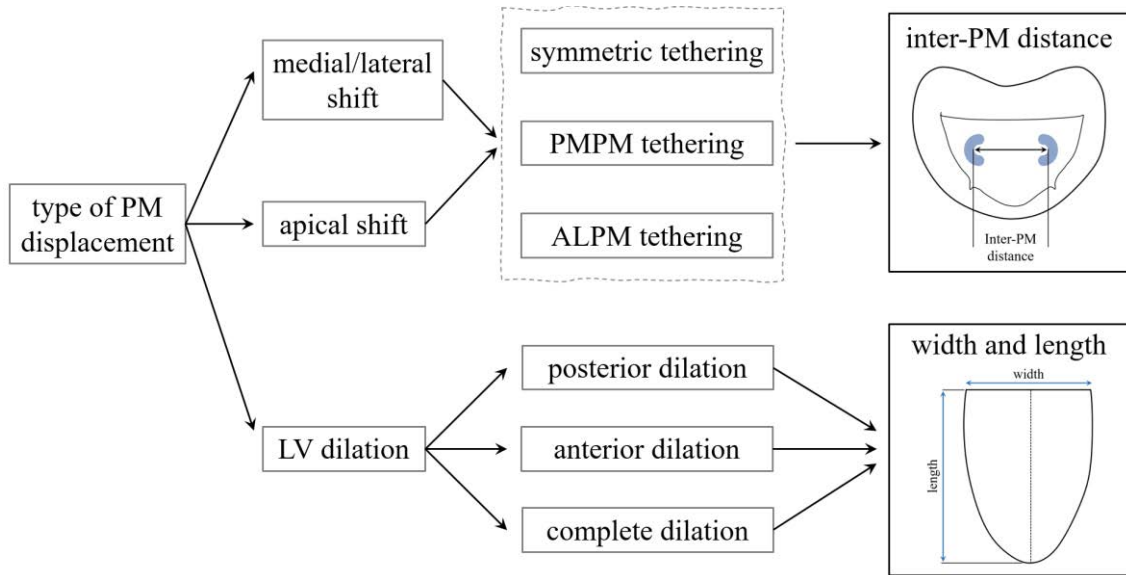


Figure 4.7: GUI options for the definition of PM displacement in a dysfunctional case. Notes: PM, papillary muscle; ALPM, anterolateral papillary muscle; PMPM, posteromedial papillary muscle; LV, left ventricle.

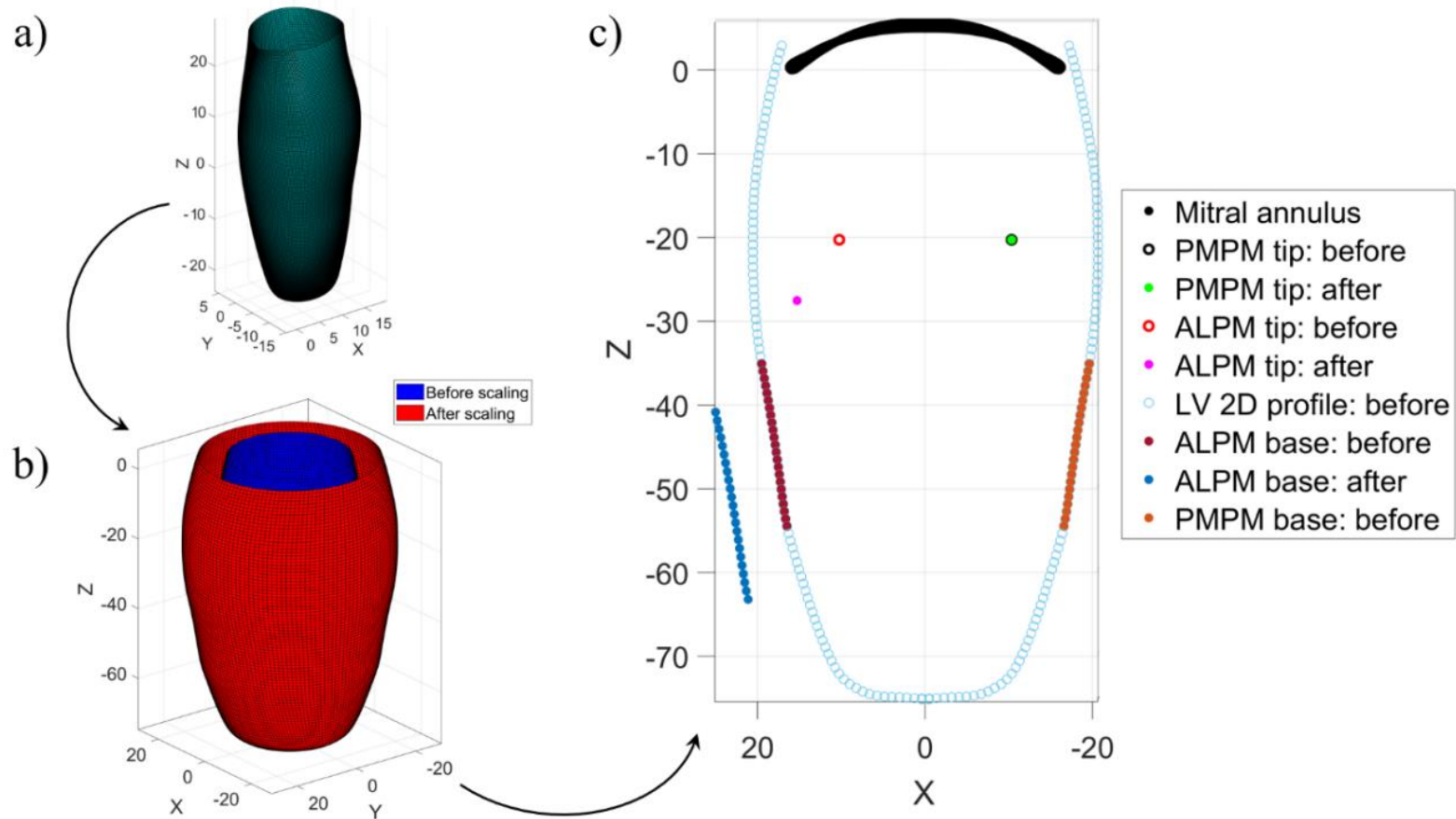


Figure 4.8: MATLAB process of PM displacement due to LV dilation: a) A LV 3D model reconstructed from MRI imaging is employed as a template, which can be scaled according to input dimensions for width and length (b)); c) A 2D cross-section representation of PM displacement due to LV dilation is displayed, including positions for PMPM and ALPM before and after LV scaling. In a scenario where LV anterior dilation occurs, the position of the anterior PM base is altered accordingly, leading to ALPM displacement. Notes: PM, papillary muscle; ALPM, anterolateral papillary muscle; PMPM, posteromedial papillary muscle; LV, left ventricle.

Chordae generation

All but the strut chordae are assumed to attach at the free edge (primary chordae) and secondary chordae are not included in the toolbox. The configuration of the chordae network was defined in order to allow proper coaptation of the leaflets under physiological conditions and to minimise numerical instabilities caused by mesh distortion. Primary chordae are equally spaced along the free margin and, based on the generated leaflet geometry, insertion points in the free edge are created according to the number of chordae branches to include: a split into three branches in the case of a single PM point and if the PM is represented with a 3D shape. Chordae are branched at a node midway between the PM origin node and the free margin. Finding this node involves:

- 1) Obtaining the midway point between the first and the third free margin nodes;
- 2) Obtaining the midway point between the midway point calculated in 1) and the PM origin node.

Examples of virtually created chordae tendineae with a single PM tip and a 3D PM shape are shown in Figure 4.9.

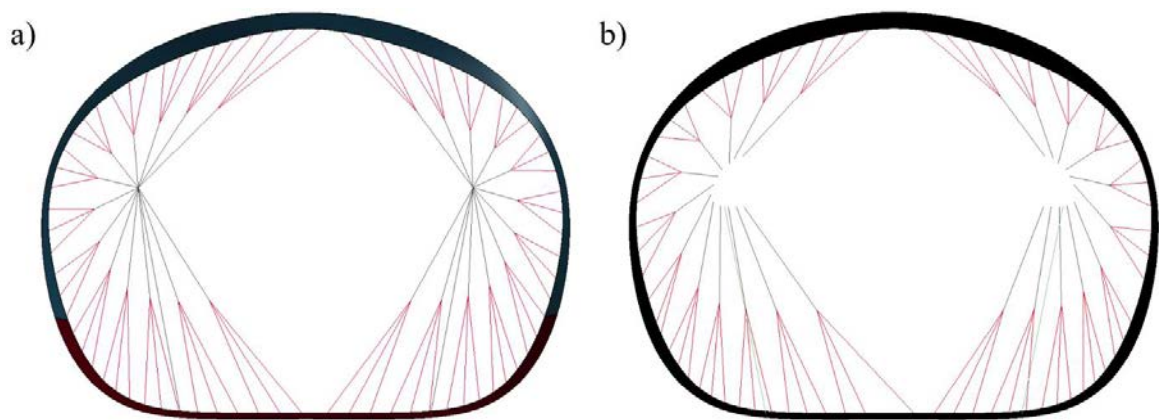


Figure 4.9: a) Single PM tip (left) and b) 3D PM shape (right) chordae tendineae distributions, with the number of chordae generated being in agreement with data from the literature.

4.2.3 Model generation: average vs patient-specific geometries

In the case of an average MV model, the MV toolbox includes a function enabling the automated generation of the full MV shape based on the AP diameter and mathematical equations obtained from the Golden Ratio (equations 3.1-3.6 from Chapter 3). Although the Golden Ratio yields a unifying mathematical model for an average, healthy MV geometry, equations describing average PM position are not available in the literature. A previous study suggests, however, that PM tip distance to annulus increases with increasing AL height (Rabbah *et al.*, 2013). Therefore, for the generation of an average MV model, the distances from PM tips to annular o'clock positions have been assumed proportional to the AP diameter, as given by equations 4.1-4.3:

$$ALPM_0 = PMPM_0 = 1.26d_{AP}, \quad (4.1)$$

$$ALPM_{10} = PMPM_2 = 1.08d_{AP}, \quad (4.2)$$

$$ALPM_8 = PMPM_4 = 0.96d_{AP}, \quad (4.3)$$

Coefficients of proportionality in equations 4.1-4.3 have been chosen to respect PM tip distances to annulus described in clinical studies (Yamaura, 2008; Topilsky *et al.*, 2013; Nomura *et al.*, 2019). A depiction of the distances generated with this approach is presented in Figure 4.10 for AP diameters associated with healthy MV shapes.

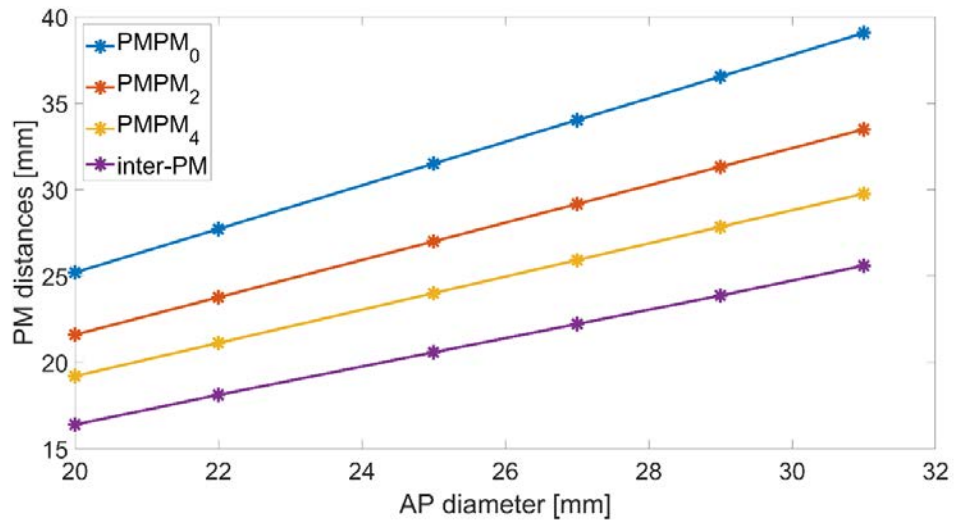


Figure 4.10: Example of distances from the PMPM tip to annular landmarks obtained with AP diameters associated with a healthy adult shape, as well as inter-PM distances. Given the symmetry assumed along the long axis meridian of the AL for the average model, distances from the ALPM tip to annular landmarks are equal. Notes: inter-PM, inter-PM distance.

If a patient-specific MV geometry is desired, all the dimensions present in Table 4.1 are required from the user to generate all MV components. The overall GUI workflow, including a summary of the choices available within the toolbox and information required from the user, is described in Section 4.4.

4.3. FE model pre-processing and computational performance of toolbox

4.3.1 Generation of final model

The final geometrical model created by the MV toolbox corresponds to point cloud boundaries representing the annulus and the free edge. Using functions from the GIBBON toolbox (Moerman, 2018), a surface mesh is created between these boundaries: if the user wishes to export the leaflet mesh as an .stl file, triangular shell elements are chosen; alternatively, if a

simulation input file is required, quadrilateral shell elements are selected (further information on the type of shell elements employed is included in Chapter 5 – section 5.2.1).

The pre-processing of the geometry to be used in a simulation input file is performed by adding transition elements on the leaflet free edge and creating the chordae tendineae. In LS-DYNA, chordae are discretized into 3D beam elements (two nodes per element), with a cable element formulation combined with cable material properties, in effect transforming these elements into elastic rods which have resistance under tension, but not under compression. To better represent the movement of the chordae tendineae, each chorda branch is discretized with 6 beam elements. Moreover, two transition quadrangular shell elements are defined at each leaflet insertion point, in continuity with the leaflet free edge shell elements. These transition elements, assumed to consist of a much stiffer material than the leaflet tissue, are where chordae insert, serving to avoid local mesh warping due to the transfer of concentrated loads from chordae tendineae to leaflets (Stevanella *et al.*, 2009). An example of the transition elements added to the model is displayed in Figure 4.11.

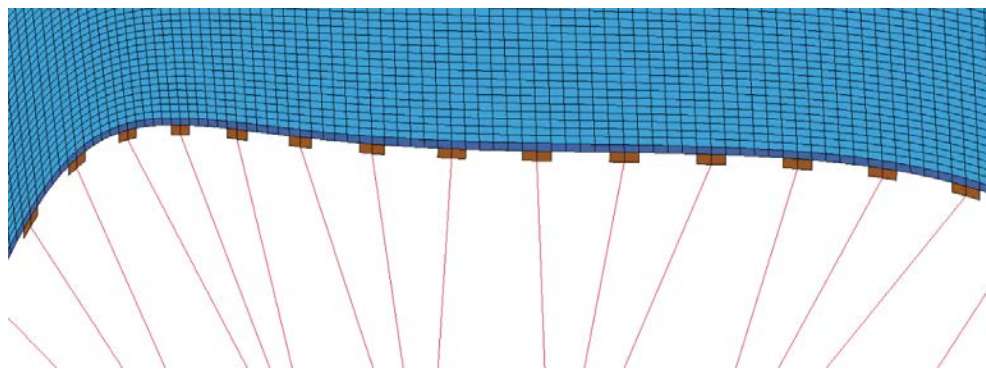


Figure 4.11: Transition elements on the free margin (brown quadrilateral shell elements).

4.3.2 Mesh evaluation

The leaflet computational mesh generated with MATLAB was assessed through a sensitivity analysis by (1) varying mesh size and (2) generating 3 models with different AP dimensions (20, 25 and 30 mm). For the first case, mesh refinement was achieved by progressively decreasing element size in MATLAB through increasing the sampling rate of annular and free edge boundaries from which the mesh is generated. Quality criteria included mesh element warping, aspect ratio and face angles, with the analysis being performed for the leaflet mesh elements, discarding transition elements. Consistent with previous studies (Shewchuk, 2002) and with the LS-DYNA meshing guide (Hallquist, 2006a), mesh quality was considered satisfactory when at least 95% of the elements had an aspect ratio less than 4, face angle less than 135° , and maximum warp angles of 5° . All generated meshes complied with these criteria. Figure 4.12 presents the mesh quality metrics for average MV geometries obtained with differing AP diameters. Variations on the geometrical dimensions have no greater effect on mesh quality: the aspect ratio and warp angle keep well below their maximum criteria (4 and 5°). For the model with an AP diameter of 30 mm, only 0.8% of the elements reach a maximum quad face angle of 140° , which meets the criteria of having at least 95% of the elements with a quad face angle below 140° .

An additional mesh convergence test was performed with LS-DYNA by simulating a structural-only closure of the full valve geometry (Figure 4.13). Physiological ventricular pressure was applied on the ventricular surface of the leaflets (Levick, 2010) and annular displacement was prescribed in order to achieve a 11% decrease in the AP diameter until full closure (Jiang *et al.*, 2014; Tang *et al.*, 2019). The PM tips were fully constrained in the 3D space. A penalty-based contact approach was set up for the leaflets, employing a single-surface contact formulation. The maximum value of the maximum principal stress on the anterior leaflet was obtained at the

peak pressure time instant. Mesh resolution was deemed acceptable when the predicted stress did not greatly change. The difference in stress between the model with the finest mesh and the others was computed and an error below 3% was deemed acceptable. A relative error below 3% appeared after 9000 shell elements (original boundary sampling of 250 points), as shown in Figure 4.13. Despite being below 3%, the relative error associated with the most refined mesh displayed in this figure (23,200 elements) is increased with respect to coarser meshes. This may be a result of a localised increase in the maximum value of the maximum principal stress, which does not reflect the overall quality of the mesh.

Given this, and according to the quality assessment performed, a mesh with boundary sampling of 400 and 23,200 elements was considered satisfactory for subsequent numerical simulations.

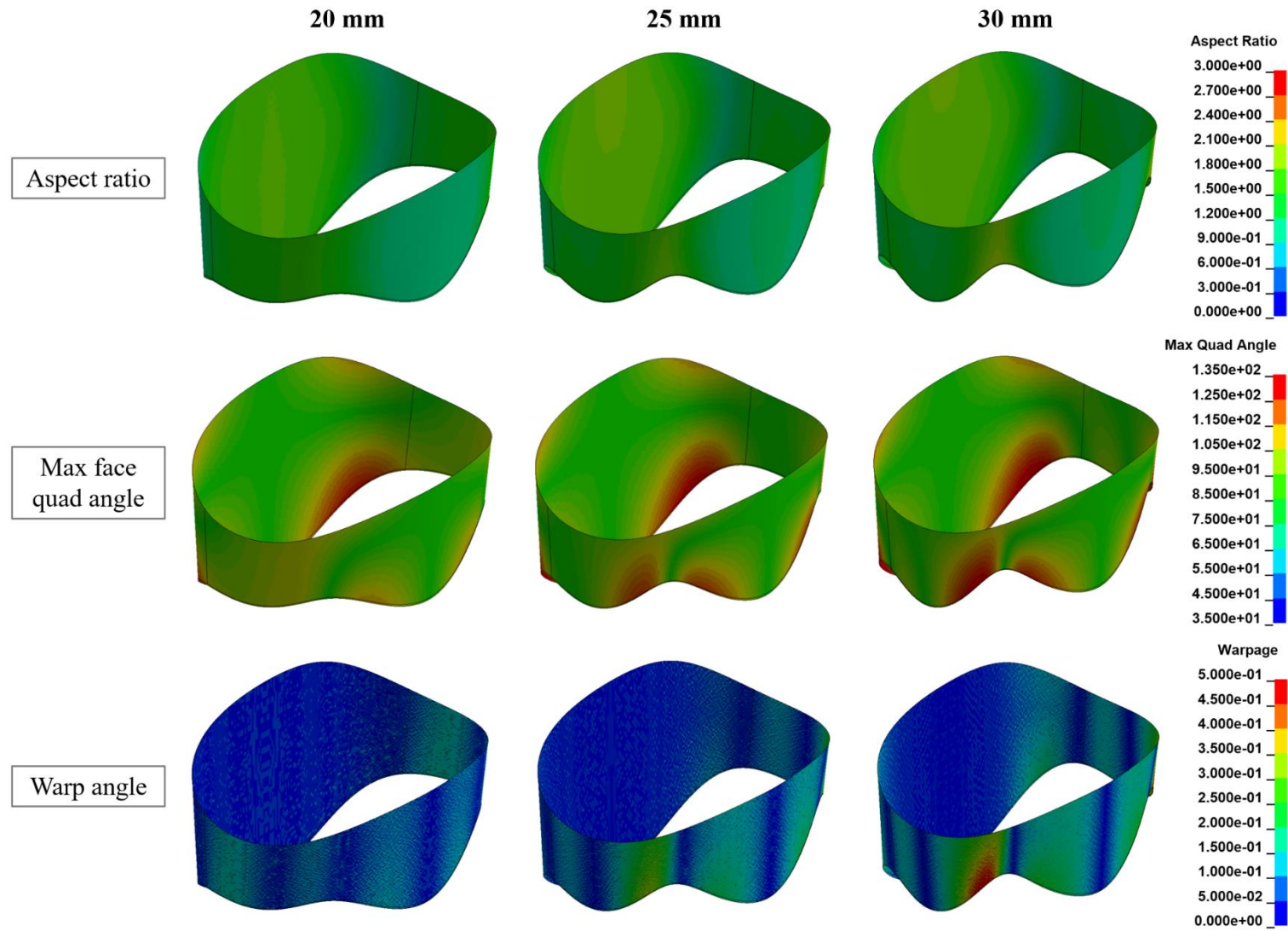


Figure 4.12: Mesh quality metrics for MV models generated with different AP diameters (20, 25 and 30 mm).

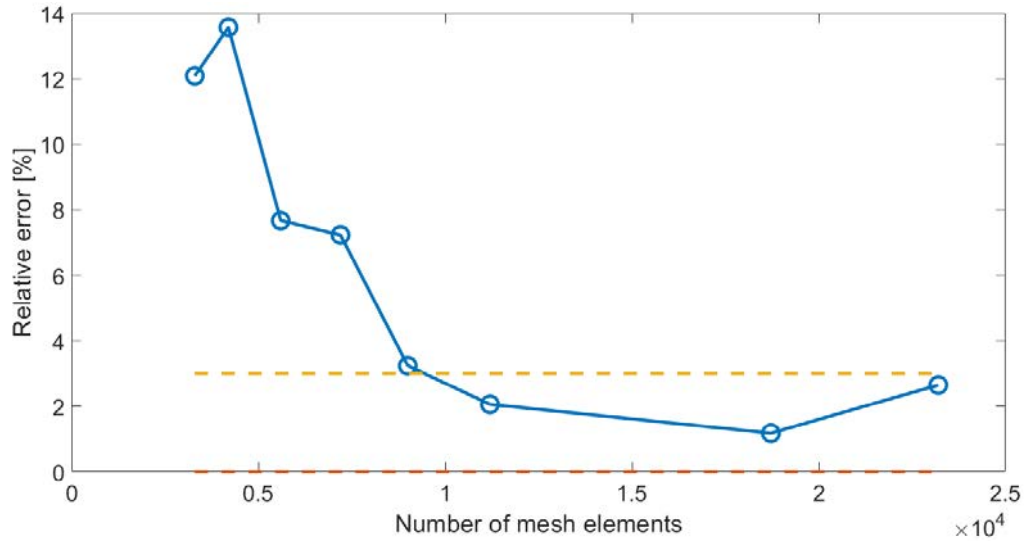


Figure 4.13: Mesh convergence test performed in LS-DYNA.

4.4. GUI workflow and examples of generated models

Figure 4.14 summarises the workflow of all GUI options available in the MV toolbox. First, the user chooses the type of geometry to generate (average or based on patient-specific dimensions). Based on this choice, either all measurements stated in Table 4.1 must be inputted for a patient-specific case, or just the AP diameter for an average model. The resulting mitral annular shape can be further reshaped by adding a ring concavity. After scaling the annular and leaflet geometries, the user can choose to incorporate PM displacement in the model, according to the options displayed in Figure 4.7. The full MV geometry can then be exported as an .stl file or employed in the definition of an input file for finite element simulations with LS-DYNA. If the input file is chosen, the PM can then be defined as either one tip point or a 3D shape of insertion points to be employed in the pre-processing of the FE model.

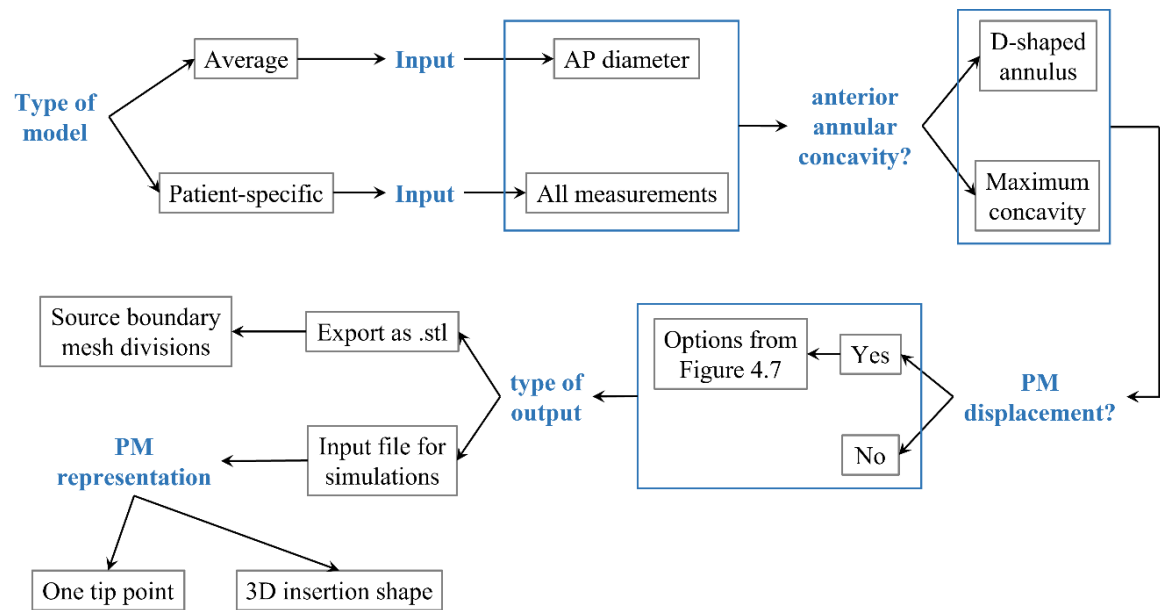


Figure 4.14: MV toolbox workflow of GUI options.

A range of average and patient-specific geometries generated by the toolbox are displayed in Figures 4.15-4.20. Figure 4.15 shows two average MV shapes obtained from different AP diameters, where a greater value (30 mm) leads to greater leading dimensions governing the annulus and the leaflets when compared with a smaller value (20 mm).

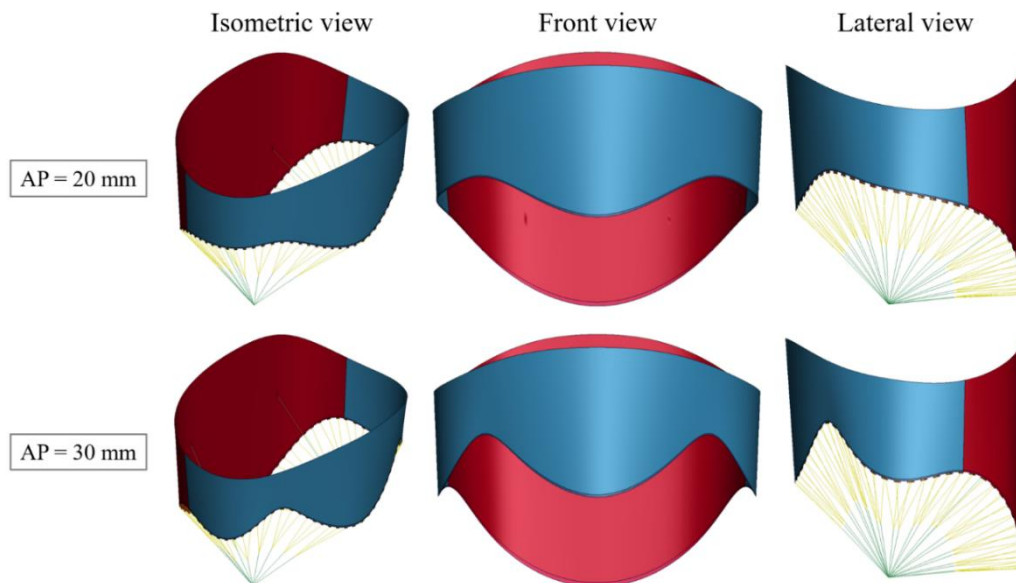


Figure 4.15: Average MV models generated with different AP diameters (20 and 30 mm).

Figures 4.16-4.20 show a range of geometries obtained with varying geometrical parameters individually while keeping others constant. An increasing CW is associated with MV diseased configurations, and potentially the presence of mitral regurgitation (Figure 4.16). While mean CW associated with disease vary with different clinical studies, values above 35 mm can be assumed as beyond the healthy anatomical range (Lee *et al.*, 2013; Jassar *et al.*, 2014). Therefore, the annular shapes in Figure 4.16 associated with CW = 25 and 30 mm are in the anatomical range, while the shape associated with CW = 35 mm may be borderline between the healthy anatomical range and a diseased configuration.

Different annular ring concavities are displayed in Figure 4.17. A healthy MV annulus has an anterior annular ring concavity, due to the aorto-mitral continuity (Timek *et al.*, 2003). A D-shape such as the one represented in Figure 4.17 (left), although not accurately representing a true annular shape, has been the base for creating annuloplasty rings; however, the native presence of an annular concavity (such as those represented by the middle and right shapes in Figure 4.17) has started to translate into novel annuloplasty ring shapes as well, associated with improved MV biomechanical performance (Choi *et al.*, 2017; Doll *et al.*, 2019; Ncho *et al.*, 2020).

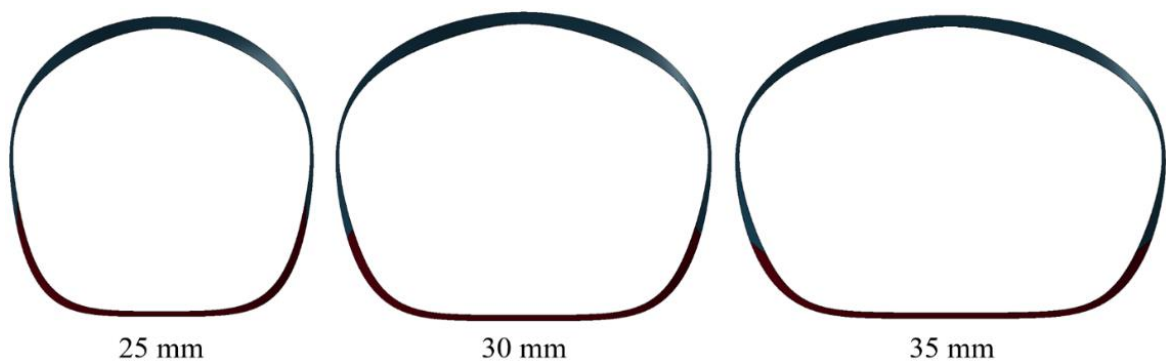


Figure 4.16: Mitral valve geometry obtained with CW varying between 25 and 35 mm.

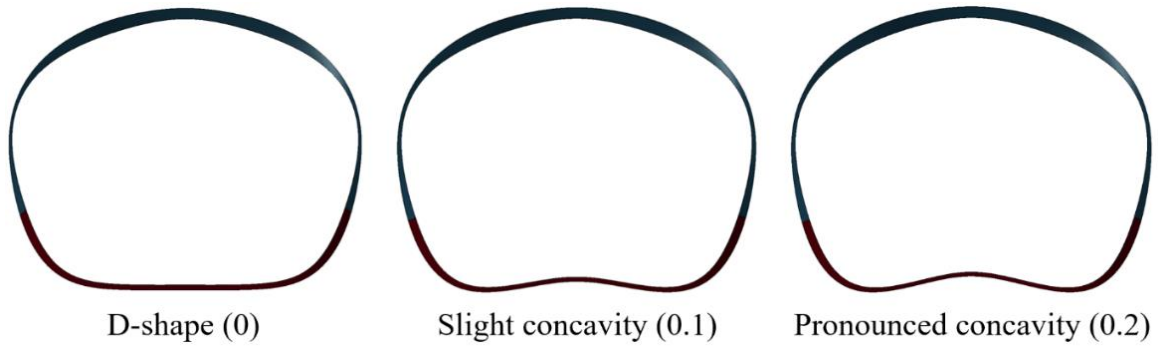


Figure 4.17: Mitral valve geometry obtained with the ring concavity varying from 0 (D-shaped annulus) to 0.2 (pronounced concavity).

Greater AL and PL heights lead to changes in the free edge profile, as displayed in Figure 4.18. Both PL heights of 15 and 20 mm are in the normal anatomical range for adult patients. By changing the PL height to a higher value, and keeping other dimensions unaltered, the height of the clefts is reduced. This can be observed when applying a PL height of 20 mm in comparison with one of 15 mm, as shown Figure 4.18.

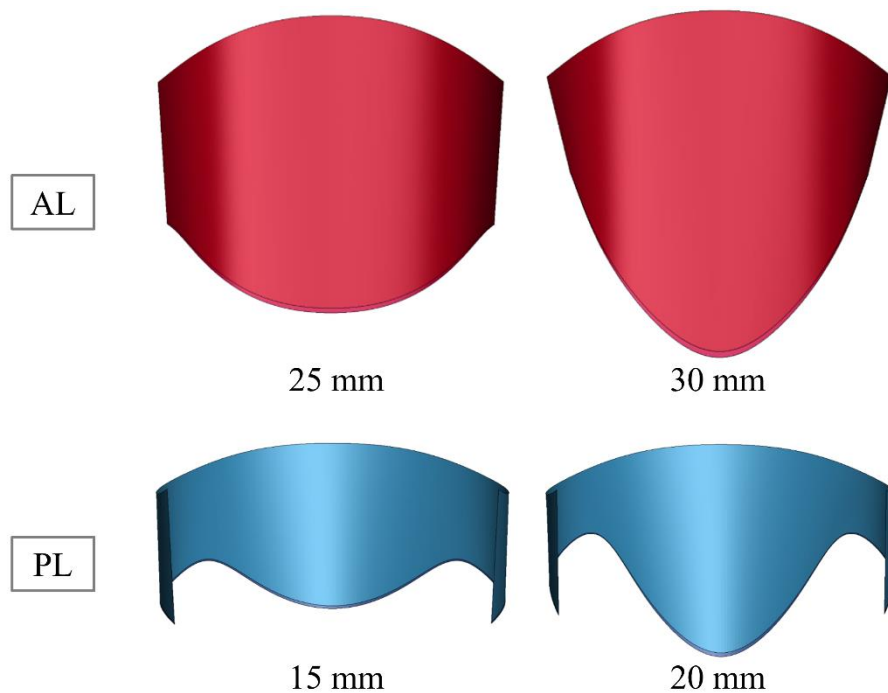


Figure 4.18: Mitral valve AL and PL geometries obtained for with different middle leaflet heights.

Examples of AL and PL shapes obtained with varying surface areas are provided in Figure 4.19. While all prescribed areas and obtained shapes are within the anatomical range, different inputted areas are associated with different final leaflet surface models. As the surface area increases while keeping other dimensions constant, and according to the framework described in the manuscript, the commissural length increases accordingly, leading to broader AL and PL shapes.

Apart from annular and leaflet dimensions, PM positions can also be prescribed. Figure 4.20 displays an example of PMPM displacement, a geometric alteration usually associated with impaired performance of the MV. Indeed, the toolbox offers flexibility to generate any desired shape.

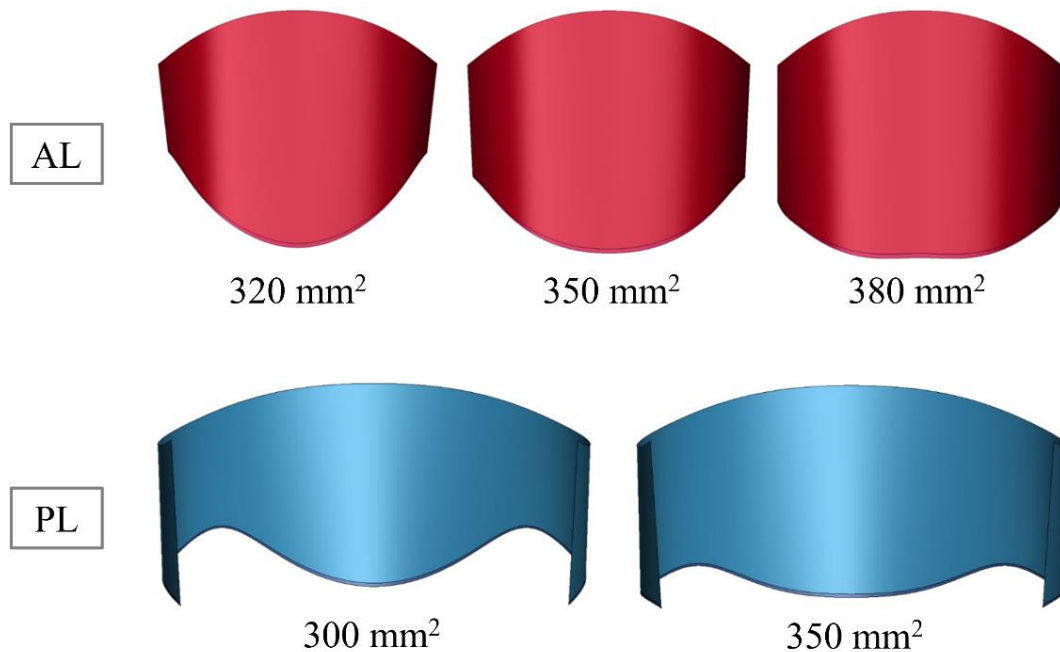


Figure 4.19: Mitral valve AL and PL geometries obtained for varying leaflet areas.

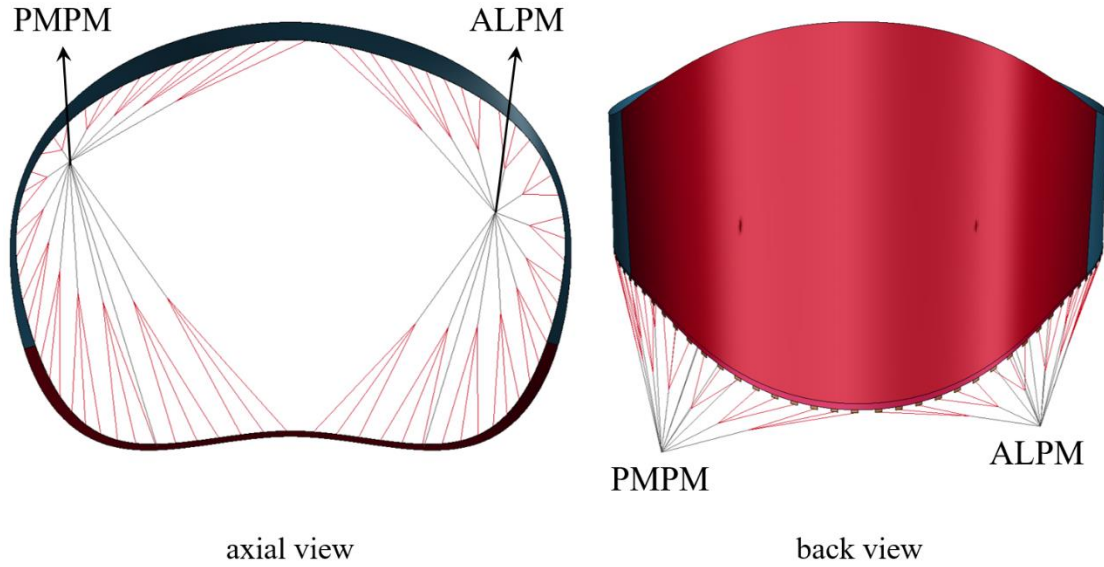


Figure 4.20: Patient-specific input of PM position, with PMPM displacement represented.

4.5. Initial assessment of prediction equations for paediatric patients

Currently, the MV toolbox can be employed in the generation of adult MV scalable geometries. In the case of paediatric patients, there are further morphometric equations which can be implemented to determine MV dimensions. Therefore, an initial assessment of the available morphometric relationships has been performed for these patients, including: 1) the determination of body surface area (BSA) from the height and mass of a patient, parameters easily obtained; 2) the prediction of the AP diameter from the BSA, to be used in the scaling of the MV geometry (Lopez *et al.*, 2017; Jolley *et al.*, 2017).

Different formulae yield the BSA from the height and mass of a paediatric patient. However, it remains unclear which provides the most accurate results, with previous studies mentioning that such formulae are not reliable (Redlarski *et al.*, 2016) or showcasing mean-BSA prediction equations depending on race (Orimadegun and Omisanjo, 2014). On the other hand, it has been reported that the Haycock formula (Haycock *et al.*, 1978) is the best

predictor of cardiovascular sizes (Lopez *et al.*, 2017; Sluysmans and Colan, 2005; Cantinotti *et al.*, 2014), as determined by previous correlation studies with Pearson coefficients > 0.99 (Lopez *et al.*, 2017). The BSA can therefore be determined from the height and mass of a patient using the Haycock formula (equation 4.4):

$$B = 0.024265 \cdot W^{0.5378} \cdot H^{0.3964}, \quad (4.4)$$

where B is the BSA (in m²) and W and H are the mass (in kg) and height (in cm) of an individual (Haycock *et al.*, 1978).

Multiple studies have also described how MV dimensions can be predicted from the BSA of an individual, most specifically the AP and AL-PM diameters (Daubeney *et al.*, 1999; Lopez *et al.*, 2017; Pettersen *et al.*, 2008; Jolley *et al.*, 2017). The type of regression model employed in these prediction equations varies. For example, Daubeney *et al.* (1999) defined a prediction equation for the AP diameter from the BSA based on a logarithmic model (124 patients, $R^2 = 0.92$, no p-value reported). Instead, Lopez *et al.* (2017) and Pettersen *et al.* (2008) employed polynomial models of different degrees, based on a larger number of patients (> 3000 and > 700 , respectively) (Lopez *et al.*, 2017; Pettersen *et al.*, 2008). Lopez *et al.* (2017), for example, obtained data from a population from different racial/ethnic backgrounds, sex and with age varying between 0 and 18 years old. In their anatomical evaluations, all obtained measurements were free from bias related to age, sex, race or ethnicity (Lopez *et al.*, 2017). However, no R^2 or p-value is reported in these studies, making the resulting predictions questionable from a statistical point of view. Jolley *et al.* (2017) also studied MV morphology and its prediction from BSA values, based on data from 100

patients and obtaining a linear regression equation correlating BSA and AP diameter ($R^2 = 0.90$ and $p\text{-value} < 0.0001$).

AP diameter predictions for BSA values varying between 0.08 and 2 m^2 are displayed in Figure 4.21, having considered the prediction equations obtained from different studies (Daubeney *et al.*, 1999; Lopez *et al.*, 2017; Pettersen *et al.*, 2008; Jolley *et al.*, 2017). AP values obtained with the equations from Jolley *et al.* (100 patients) and Daubeney *et al.* (125 patients) are very similar for $\text{BSA} > 0.7 \text{ m}^2$; However, the linear prediction from Jolley *et al.* is unable to capture nonlinear variations of the AP diameter associated with low BSA values, shown by the predictions from Daubeney *et al.* and Lopez *et al.* On the other hand, prediction equations from Daubeney *et al.* and Jolley *et al.* overestimate the AP diameter in comparison with the equations from Lopez *et al.* (3215 patients) and Pettersen *et al.* (782 patients) in the case of higher BSA values. This may be due to the analysis of a smaller population in Daubeney *et al.* and Jolley *et al.* in comparison with that of Lopez *et al.* and Pettersen *et al.*, which seem to obtain more accurate predictions due to the analysis of a larger number of individuals. These variations amongst prediction equations can have implications when determining the AP diameter and the remaining MV dimensions, potentially leading to wrong estimations of the MV geometry for a paediatric patient with specific BSA when employing different models.

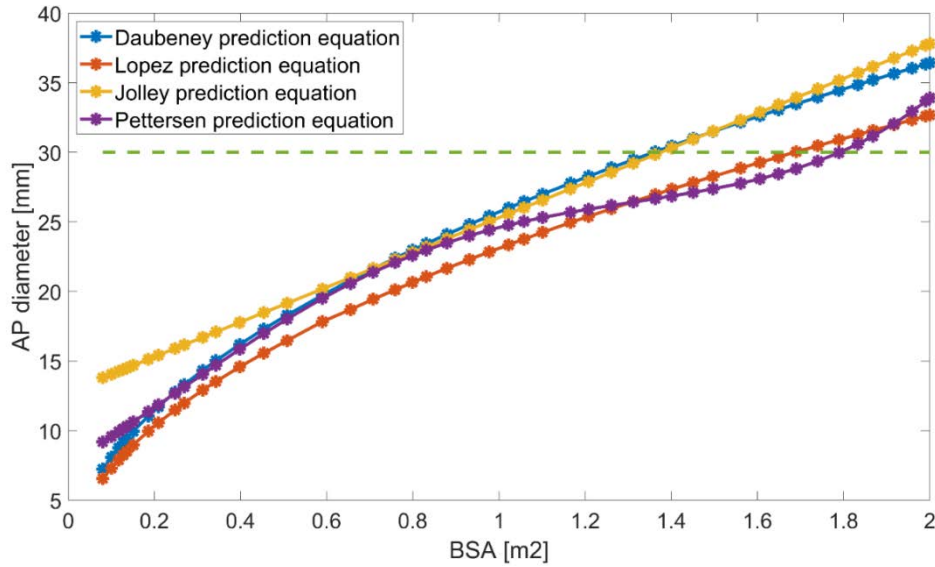


Figure 4.21: AP diameter [mm] as a function of the BSA [mm²], using prediction equations from different sources (Daubeney et al., 1999; Lopez et al., 2017; Jolley et al., 2017; Pettersen et al., 2008). An AP diameter > 30 mm may be associated with the onset of MV annular dilation.

4.6. Discussion

4.6.1. Overview

The MV toolbox allows for the automated and user-controlled generation of tailored MV geometries from patient dimensions, and the creation of finite element input files for computational biomechanical evaluation using minutes of computational time. The main novelty behind this toolbox is that it allows to: (1) obtain a geometrical model, based on dimensions from patient-specific imaging or on predicted values from Golden ratio equations; (2) create a meshed model which can be pre-processed directly in MATLAB and (3) generate an input file for computational simulations using LS-DYNA.

4.6.2. Computational approach for the average MV model and current challenges

The average healthy MV shape obtained with the toolbox is based on clinical and *ex vivo* data, and the models generated appear anatomically realistic, being comparable to average

(Choi *et al.*, 2016; Alleau *et al.*, 2019) and patient-specific (Stevanella *et al.*, 2011; Pham *et al.*, 2017) models employed in other computational studies. Despite the high average relative errors of the Golden Proportion predictions for leaflet areas against average *in vivo* data (Section 3.2.3), very good correlations ($R^2 = 0.94$, p-value = 0.01) have been found between MV leaflet lengths and the AP diameter which agreed with the Golden Proportion (Deorsola and Bellone, 2018; Deorsola and Bellone, 2019). Moreover, all annular dimensions from the literature have also shown agreement with Golden Proportion predictions (Section 3.2.1).

In reality, MV quantitative data is associated with high variability amongst a population sample, as observed in the standard deviations from clinical data. The current limitations present in clinical imaging modalities may directly impact the derived MV morphometric data, contributing towards model uncertainty (Wu and Takeuchi, 2017). In fact, the accuracy of the measurements obtained from scans (especially leaflet areas, which need to be inferred from 3D imaging parameterizations) depend on the type of modality used, their spatial and temporal resolutions, and the operator expertise, which can introduce a bias on the obtained data. Therefore, both the variability in data and the range of accuracy of the measurements present in literature studies can help explain the elevated average relative errors obtained in this study and the standard deviation of those errors. Nonetheless, further studies are required to obtain more complete datasets of morphological measurements of the MV (combining different imaging modalities, for example), which lack in the current literature. These can then be used to further validate the Golden Proportion predictions and evaluate new correlation analyses.

The main current challenge of the MV toolbox is the representation of the subvalvular apparatus: even though it is based on the literature (Yamaura, 2008; Sakai *et al.*, 1999), studies describing the PM positioning in the 3D space with greater accuracy are required.

Besides, current *in vivo* imaging modalities are unable to properly capture the chordae and the PM (Gao *et al.*, 2017b), and therefore our mathematical representation and distribution of the same is based on such assumptions. This, however, does not differ from computational studies employing average mitral leaflet geometries (Choi *et al.*, 2016; Alleau *et al.*, 2019) and even patient-specific (Gao *et al.*, 2017a; Biffi *et al.*, 2019) ones, since patient-specific chordal distributions are very difficult to obtain.

4.6.3. Comparison with other state-of-the-art methodologies

Recent studies have either 1) focused on the use of patient-specific models with valvular geometries, material properties and boundary conditions obtained from clinical data, or 2) the development of computational methodologies for the parameterization of the MV structure. While the first approach is time consuming, requiring extensive pre-processing to reconstruct the MV shape of a subject and define patient-specific modelling properties, the second approach is faster, arising as one step forward towards the clinical translation of MV models. Recent parameterization frameworks include the 2D mapping of leaflet surfaces from imaging modalities for a more intuitive detection of pathology during decision making (Lichtenberg *et al.*, 2020), the creation of 3D MV shapes from specific measurements performed in imaging modalities and their use to study the effect of transcatheter MV replacement in left ventricular outflow tract haemodynamics (Pasta *et al.*, 2020), and a heuristic generation of chordae tendineae and PM tips (Walczak *et al.*, 2021). While these frameworks are able to quickly generate clinically relevant MV shapes, they can only be applied to individual cases. The MV toolbox, on the other hand, is flexible, enabling the creation of morphological MV models, scalable to average human dimensions or patient-specific ones, within a timescale compatible with clinical use (generation of geometrical

models within minutes of computational time). In addition, the models can be directly meshed and an input file including material properties, boundary conditions and contact conditions, ready for computational simulations, can be outputted (as further explained in Chapter 5). The toolbox generates meshed models which meet criteria for numerical modelling. This means that the model pre-processing can be accelerated further, since it can be directly set up for computational simulations without other tiresome processes. As far as is known, this study is the first MV parametric model which allows the variation of its anatomy and has the flexibility to input the dimensions of a specific subject; subsequently generating an input file ready for numerical analysis (Figure 4.22). The first version of the toolbox is freely available on GitHub and Zenodo (DOI: 10.5281/zenodo.5018364).

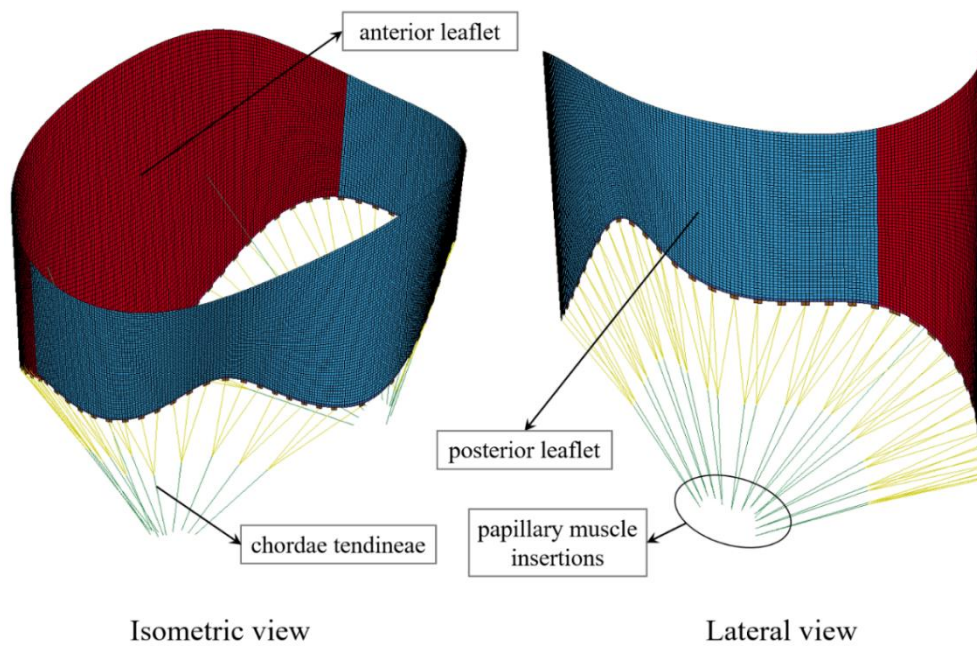


Figure 4.22: Sample 3D MV model with all components included, ready for computational simulations.

4.7. Conclusions

The MV toolbox has been developed with the aim of studying the influence of morphological MV parameters on its function, including diseased configurations, and to virtually evaluate diverse mitral interventions at a customised level. The toolbox enables an automated and user independent workflow which is compatible with a range of modelling software. Together with biomedical engineering professionals, clinicians could use this tool to simulate and understand how different MV patient-specific morphometries can impact valve biomechanics. Moreover, clinicians can choose whether to use average dimensions or provide dimensions from imaging data as an input. It can then be employed to aid clinicians when assessing MV biomechanics of their patients and improve the decision-making process behind choosing the best patient-specific clinical intervention. The setup of finite-element models within the toolbox, as well as relevant results obtained using a variety of MV cases, are described in the next chapter.

CHAPTER 5

PRE-PROCESSING OF A MITRAL VALVE MODEL FOR FINITE-ELEMENT ANALYSIS

5.1. Introduction

The MV toolbox generates accurate and scalable MV models, with the geometry being obtained from patient-specific dimensions or average dimensions based on morphometric equations (Chapter 4). This workflow is mostly automatized using MATLAB (MATLAB[®], R2019b, 9.7.0.1247435, The MathWorks Inc., Natick, MA, USA), from the geometry to mesh generation, with a GUI which guides the user through the set-up of specific options and insertion of required parameters. The final model is then ready for pre-processing for FE simulations using LS-DYNA (version 4.5.12, LSTC, Livermore CA, USA).

Current MV models from the literature are mostly based on patient-specific geometries reconstructed from medical imaging (Rim *et al.*, 2015; Kong *et al.*, 2020; Pham *et al.*, 2017). Each model pre-processing is usually done individually, including: the assignment of material properties; the definition of the number of mesh elements after a mesh sensitivity analysis; and the characterisation of relevant model surfaces and nodes for assignment of boundary conditions. The time required to set-up/solve these models has, therefore, been a major barrier for translation into clinical practice (Shinbane and Saxon, 2018).

To target this issue, frameworks which allow to automatically obtain the dynamic MV structure from medical images (Ionasec *et al.*, 2010; Voigt *et al.*, 2011; Schneider *et al.*, 2011) and

develop biomechanical models of the valvular apparatus to simulate MV function (Mansi *et al.*, 2011; Mansi *et al.*, 2012; Zhang *et al.*, 2017) have been developed. For example, in the framework specified by (Mansi *et al.*, 2012), the whole process, from obtaining the full MV geometry and adjusting chordae length, to the optimisation of parameters for material properties and simulation of leaflet coaptation, takes less than one hour, compatible with clinical timescales. Automation of the pre-processing stage is therefore crucial for a real-time biomechanical analysis of the MV and the effect of diverse surgical procedures, as previously performed for MitralClip virtual implantation in patient-specific geometries (Mansi *et al.*, 2012). This can help in the clinical decision making process, to choose the best procedure for a specific MV shape. In the present computational framework, able to generate scalable MV geometries, pre-processing of the model for FE simulations has been implemented. This can be used to virtually evaluate and optimise novel surgical devices or repair techniques through biomechanical assessment, and to evaluate the biomechanics of different MV geometries.

In addition to being sensitive to the geometry used, FE models rely on the prescription of appropriate boundary conditions (BC) and material properties, as these play a role in the predicted biomechanics. Previous computational studies of the MV have performed sensitivity analyses for BC and material parameters, unravelling dissimilar MV coaptation behaviours (e.g. non-closure with a fixed annulus) (Mansi *et al.*, 2012), different stress distributions and chordal tensions (Stevanella *et al.*, 2009; Prot *et al.*, 2009) under the application of varying conditions. In literature, there are many MV models in terms of material property assumptions and BC (Chapter 2). It is, therefore, important to assess the variability in biomechanical predictions caused by the use of different BC or material properties, especially in the case of the present framework which generates scalable MV models for FE simulations.

The aim of this chapter was to create the automatic pre-processing for the MV model, including the definition of appropriate material properties, BC and other control parameters. To demonstrate the functionalities of the toolbox, several models of the MV have been solved, with the respective biomechanical results being compared with those obtained by computational studies available in the literature. In this chapter, the steps taken to obtain a complete pre-processing of the MV model within the toolbox and assess the potential of this tool are described, including: 1) the set-up of the FE model for LS-DYNA; 2) the generation and validation of an average, healthy MV model; 3) a sensitivity analysis of annular and PM BC, PM shape, and two material constitutive models; 4) the generation and analysis of two patient-specific MV models. Figure 5.1 displays the workflow of this chapter.

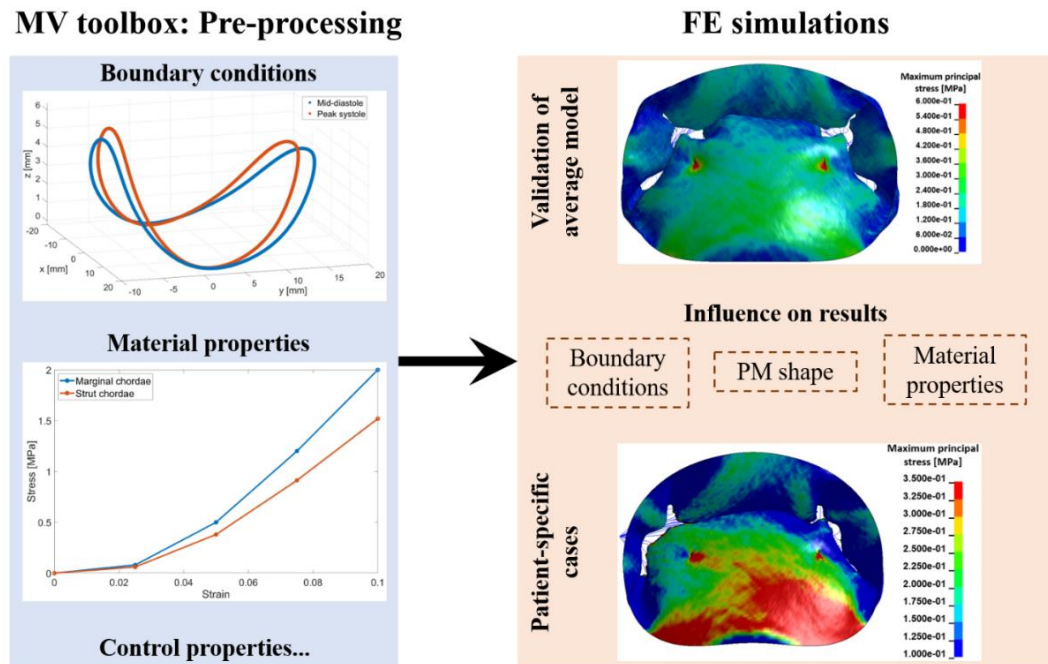


Figure 5.1: After the MV geometry generation and meshing (Chapter 4), the model is pre-processed for FE simulations, including the definition of boundary conditions, material properties and necessary control settings. Using these definitions, an average (healthy) model of the MV was generated and its computational predictions validated against the literature. Moreover, the sensitivity of computational results to different boundary conditions, material properties and PM shapes was analysed. Finally, two patient-specific cases were generated and solved.

5.2. LS-DYNA simulations and automatic FE pre-processing from MATLAB

As described in Chapter 4, the MV toolbox can pre-process all geometrical components of the MV to obtain a FE model ready for FE simulations using LS-DYNA software. If a FE model is desired, and after the generation of the baseline geometry, the toolbox user can further define:

- ❖ The type of PM representation (one tip point or a 3D insertion shape, Section 4.4, Chapter 4;
- ❖ The specific thickness of AL and PL shells (subsection 5.2.1);
- ❖ Individual material properties for AL and PL tissue (subsection 5.2.2).

Boundary and loading conditions applied to the MV model and definition of contact surfaces and conditions (subsection 5.2.3), are directly implemented in MATLAB. A simulation input file is written in MATLAB and then exported as a .k file. It can (1) be directly opened in LS-DYNA for assessment of the model and (2) be run using an appropriate LS-DYNA solver. In this section, the information required to define the model, as well as different modelling choices attempted for the definition of FE MV simulations, are described.

5.2.1. Mesh and shell element definitions

The MV toolbox can automatically generate a shell mesh representing the geometry of the leaflets and beam elements representing the chordae tendineae, ready for FE simulations with LS-DYNA (Chapter 4). Moreover, mesh sensitivity analyses were performed to ensure independency of the results from the mesh size, employing original meshes generated by MATLAB and peak systolic deformed meshes from time-dependent simulations (subsection 4.3.2). Obvious differences in mesh element quality (i.e. element aspect ratio) were observed

between models exported from MATLAB and at peak systole, as observed in Figure 5.2 for the aspect ratio.

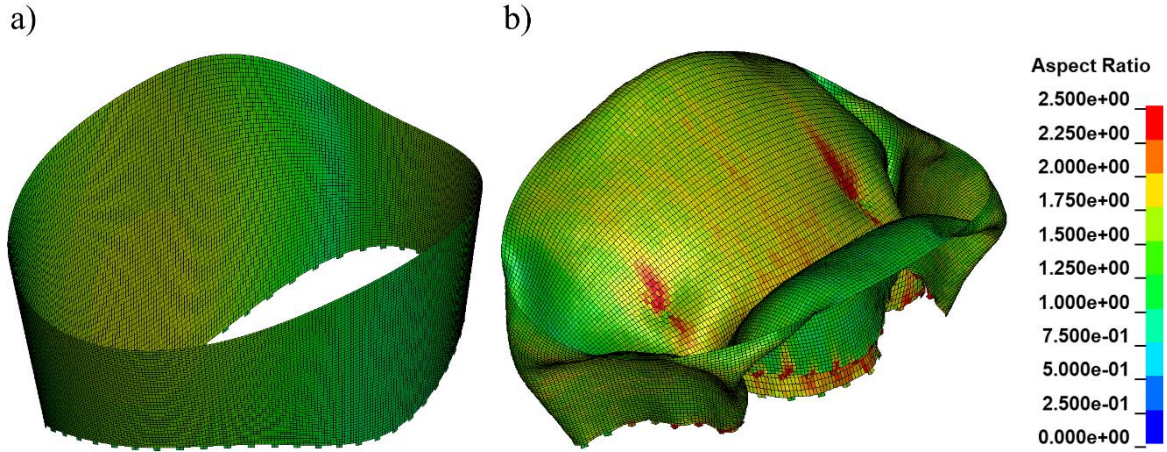


Figure 5.2: Aspect ratio of mesh elements for (a) the original MV model in a full-diastolic open state and (b) for a deformed MV model at peak systole.

Element quality decreased with MV closure, as displayed in Figure 5.2b). Increased mesh element distortion was observed near chordae insertion locations (free edge and region near strut chordae attachment) and at the coaptation area, although never beyond the predefined quality criteria threshold (aspect ratio < 4). To prevent mesh distortion and spurious element deformation, additional LS-DYNA control options were assessed and chosen for the FE simulations, as further explained in subsection 5.2.4.

The shell mesh was defined with Belytschko-Lin-Tsay (BT) finite elements, a computationally efficient option within LS-DYNA (Hallquist, 2006b). According to leaflet tissue material property implementations (subsection 5.2.2), the two shell definition approaches presented in Table 5.1 were employed.

Table 5.1: Shell definitions. Notes: NIP, number of integration points.

Type of material model	Shell layers		Shell thickness [mm]		NIP		Shear correction factor	
	AL	PL	AL	PL	AL	PL	AL	PL
Linear elastic orthotropic	1	1	1	1	3	3	5/6	5/6
Hyperelastic	2	2	layer 1: 0.7 layer 2: 0.3	layer 1: 0.55 layer 2: 0.45	1 per layer	1 per layer	-	

Shell definitions for an orthotropic material

One single shell layer, in continuity between the AL and PL, was assumed for leaflet tissue. Although the thickness of the MV leaflets is non-uniform (1 – 1.7 mm) (Kunzelman *et al.*, 2007), both AL and PL thicknesses were assumed constant and of 1 mm (Prot *et al.*, 2009) in all FE simulations presented in this chapter. A shear correction factor of 5/6 was employed to scale the transverse shear stress on the shell, since the chosen element BT formulation yields constant transverse shear strains, which violates the condition of zero traction on the top and bottom surfaces of the shell (Hallquist, 2006b; Hallquist, 2006a).

As detailed in Chapter 2, the number of integration points (NIP) in an element is key for its formulation and resultant bending stiffness (Hallquist, 2006a; Hallquist, 2006b). Although the BT element is defined with one through thickness shell integration point, a preliminary study using BT elements with varying NIP was performed to assess differences in mesh deformation and MV closure. Annular and PM motion was neglected and a physiological pressure was applied on the ventricular surface of the leaflets (Levick, 2010). BT elements with NIP of 1 and 3 were used and peak systolic maximum principal stresses and mesh element warping angles were analysed, as represented in Figures 5.3 and 5.4.

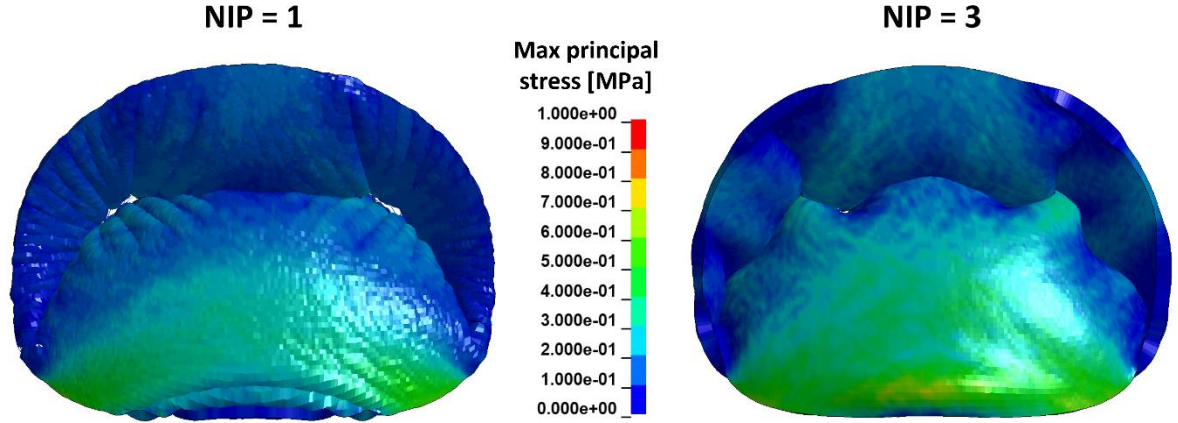


Figure 5.3: Maximum principal stress [MPa] displayed on the atrial side of the MV leaflets for 1 integration point through the thickness and 3 integration points through the thickness, respectively, at peak systole.

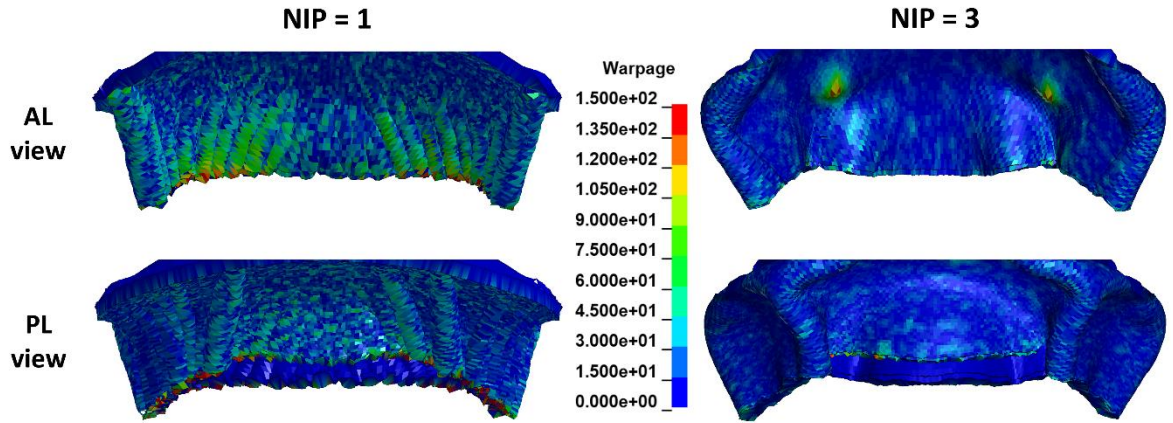


Figure 5.4: Warpage angle displayed for both the AL and PL with NIP of 1 and 3, respectively, at peak systole.

While areas of elevated stress are located at the central portion of the AL and near the anterior annulus for both NIP of 1 and 3, the use of one single integration point for shell representation seems to underestimate this stress, especially near the anterior annulus (Figure 5.3). Moreover, incomplete coaptation and inexistent bending stiffness is observed with NIP of 1, representing incorrect MV closure. One shell integration point also leads to increased element warpage throughout the whole AL and PL mesh (Figure 5.4). The model with NIP of 3, on the other

hand, shows increased element warpage at the attachment of strut chordae and near the free edge, but still demonstrates better peak systolic mesh quality when compared with a one integration point shell model. Based on this assessment, BT shell elements with three integration points in the thickness direction were employed with the use of orthotropic material properties.

Shell definitions for a hyperelastic material

In the numerical simulations using a hyperelastic material for the leaflet tissue, the leaflets were assumed as a layered structure. Similar to the strategy adopted by (Wenk *et al.*, 2012), a two-layered composite sheet was defined assuming different thickness definitions and material properties, in order to mimic the distinct biological constituents present in leaflet tissue layers *in vivo* (further detailed in subsection 5.2.2). Shell layers were assumed to act as a flexible membrane, neglecting the existence of bending stiffness and implemented using a single integration point through the thickness of the leaflet (Wenk *et al.*, 2012). A schematic of the AL and PL composites is exemplified in Figure 5.5 in comparison against the shell representation used for a linear elastic orthotropic material. Similarly to the shell definition used for an orthotropic material, the total thickness (T) was assumed uniform and as 1 mm for the hyperelastic material (Wenk *et al.*, 2012; Weinberg and Kaazempur Mofrad, 2007), with each layer representing a fraction of T (Table 5.1 and Figure 5.5b).

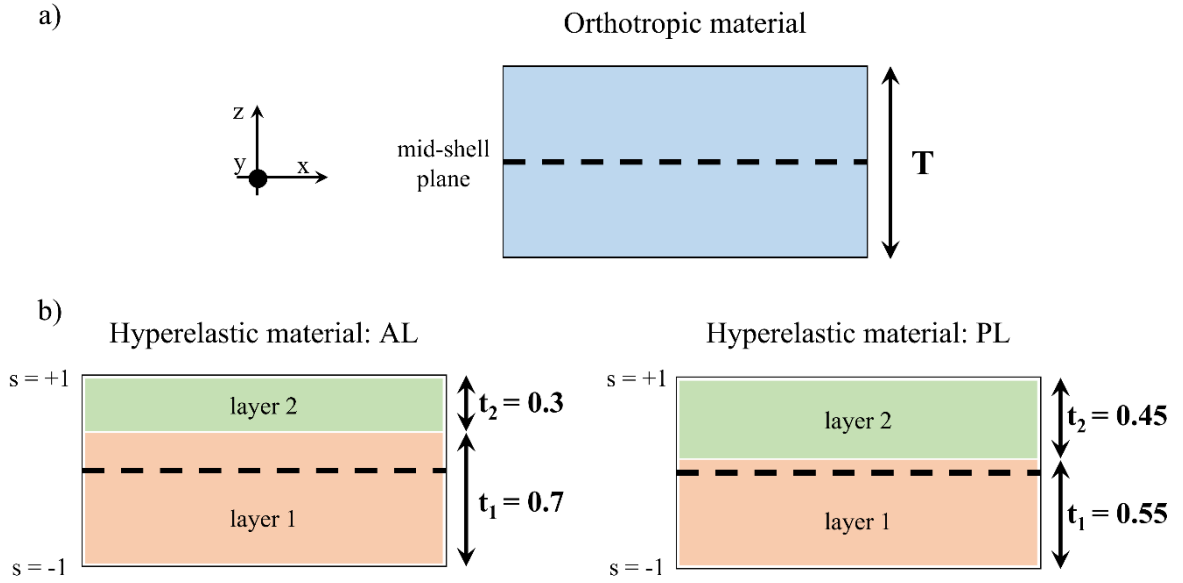


Figure 5.5: Shell representations for orthotropic and hyperelastic materials in LS-DYNA. a) The shell is characterised by a total thickness T for the orthotropic material, while b) for an hyperelastic material a composite approach is used, employing two shell layers (layer 1: fibrosa; layer 2: atrialis and ventricularis) of different thicknesses and defined with hyperelastic material properties is used, with t_1 and t_2 being the layer thicknesses.

The layers were merged together, having coincident nodes; this ensured equal in-plane strain in overlapping elements, as assumed in composite theory (Wenk *et al.*, 2012). Moreover, to obtain the correct membrane and bending stiffness for the whole composite structure, each shell layer was defined with a separate integration rule including appropriate weight factors (W) for thickness and through thickness coordinates (s). For both leaflets, and since $T = 1$ mm, the weight factors W_1 and W_2 (layers 1 and 2, respectively) were defined as:

$$W_1 = \frac{t_1}{T} \quad (5.1)$$

$$W_2 = \frac{t_2}{T} \quad (5.2)$$

where t_1 and t_2 are the thicknesses for layers 1 and 2, respectively. Based on these weight factors, the total membrane stresses in circumferential (σ_c) and radial (σ_r) directions of the layered composite can be written as

$$\sigma_c = W_1 \sigma_c^1 + W_2 \sigma_c^2, \quad (5.3)$$

$$\sigma_r = W_1 \sigma_r^1 + W_2 \sigma_r^2, \quad (5.4)$$

where σ_c^1 and σ_c^2 are the membrane Cauchy stresses in the circumferential direction (aligned with the local x-axis) for the first and second layers, respectively, and σ_r^1 and σ_r^2 are the membrane Cauchy stresses in the radial direction (aligned with the local y-axis) for the first and second layers, respectively.

5.2.2. Material properties

Here, the material properties for leaflets and chordae tendineae which are implemented in the MV toolbox are described. All tissues were assumed elastic and their density was set as 1 g/cm^3 (Choi *et al.*, 2017; Votta *et al.*, 2007; Rim *et al.*, 2013). Moreover, for leaflet tissue material property definitions, the circumferential orientation is aligned with the local x-axis of each shell element and corresponds to the direction across the leaflet, from commissure to commissure, and the radial orientation is aligned with the local y-axis of each shell element, corresponding to the direction from the annulus to the free edge.

Leaflets: orthotropic material properties

Leaflet tissue is implemented as a linear and orthotropic material within the MV toolbox, thus neglecting its nonlinear response (Barber *et al.*, 2001; Kunzelman and Cochran, 1992), but accounting for the preferential direction (circumferential) of the collagen fibers (more details are given in Appendix A - A.1). This choice is justified by the fact that, during the physiological pressure range corresponding to the systolic period, circumferential and radial stress-strain curves are linear (Krishnamurthy *et al.*, 2008; Krishnamurthy *et al.*, 2009). Individual material properties for the AL and PL can be chosen by the user, specifically Young's moduli in the circumferential (c) and radial (r) directions, respectively; nonetheless, for the numerical simulations performed, in-plane (x-y plane) coefficient values for each leaflet have been set according to the literature (Kunzelman *et al.*, 1993a; Votta *et al.*, 2007) and are reported in Table 5.2. Even though the out-of-plane material response (aligned with the local z-axis of each element) is uncoupled from the in-plane (x-y plane) response, the corresponding Young's and shear moduli are needed to set up the full material model, being employed in the calculation of the contact force for contact definitions between leaflets (Hallquist, 2006a). These values have been defined based on a previous study to allow for full coaptation of the MV (Lau, 2012).

Table 5.2: Material parameters employed in simulations with the linear orthotropic model, where x - and y - refer to circumferential and radial directions, respectively. Notes: E_c , circumferential Young's modulus; E_r , radial Young's modulus; E_o , out-of-plane Young's modulus; G_{cr} , circumferential/radial shear modulus; G_{ro} , out-of-plane shear modulus; G_{oc} , out-of-plane shear modulus; ν_{cr} , in-plane Poisson's ratio.

Coefficients	Leaflet	
	AL	PL
E_c [MPa]	6.23	2.35
E_r [MPa]	2.09	1.887
E_o [MPa]	10	10
G_{cr} [MPa]	1.37	0.69
G_{ro} [MPa]	1.37	0.69
G_{or} [MPa]	1.37	0.69
ρ [g/cm ³]	1	1
ν_{cr}	0.45	0.45

Leaflets: hyperelastic material properties

To assess differences between the orthotropic material implemented in the toolbox and the implementation of another material accounting for anisotropic leaflet response, an additional hyperelastic material has been tested. In reality, the mitral leaflets consist of three principal layers with different biomechanical properties: while the fibrosa (primary layer) is characterised by a dense collagen network preferentially oriented parallel to the annulus (circumferential orientation), the atrialis and ventricularis layers provide secondary support in the radial direction due to loosely organised collagen (Chapter 2, section 2.4.1). Leaflet tissue can then be described as a composite material. Since the atrialis and ventricularis have a similar composition, they are assumed to have the same material response (Kunzelman *et al.*, 1993b), and therefore a two-layer composite is employed: layer 1 concerns the fibrosa and layer 2 represents the atrialis and ventricularis. Each layer is modelled with a nearly incompressible, transversely isotropic, hyperelastic material model and different fiber orientations are assigned

to each layer. A soft tissue material model based on the constitutive law developed by Quapp and Weiss (Quapp and Weiss, 1998) and implemented in LS-DYNA (Hallquist, 2006a) is used to model leaflet response (further details in Appendix A – A.2). Further details on the circumferential and radial stress formulations for a 2-layer composite can be found elsewhere (Wenk *et al.*, 2012). Local shell element axis of coordinates have been defined to assign fiber angles, assumed to coincide with the collagen orientation in each layer: angles of 0° and 35° are assigned to the fibrosa and atrialis/ventricularis layers, respectively, relative to the circumferential (x-axis) direction of the element (May-Newman and Yin, 1998).

The material coefficients determined by Wenk *et al.* for this material model (Wenk *et al.*, 2012) and its implementation in LS-DYNA were further validated by simulating a biaxial tensile test of a leaflet specimen. A square sample of mitral leaflet tissue with side 10 mm and thickness 1 mm was modelled using a single element for each layer, based on previous approaches (Weinberg and Kaazempur Mofrad, 2007; Wenk *et al.*, 2012; Prot *et al.*, 2007). The model was loaded using biaxial displacement BC (Table 5.3) calculated from stress-strain data available in the literature to generate stretches comparable to experimental testing (May-Newman and Yin, 1998). The stretch ratio was set to 1000 to account for an exponential material response during fiber straightening (Sturla *et al.*, 2016). Fiber angles were assumed as previously stated and individual layer thicknesses were set to those in Table 5.3 (Kunzelman *et al.*, 1993b). Moreover, the overall strain energy defining the implemented material includes a bulk term dependent on the effective bulk modulus of the material. To ensure near-incompressible behaviour and produce the best fit between numerical and experimental results, this parameter was also adjusted in LS-DYNA (Hallquist, 2006a).

Table 5.3: Displacement conditions and shell layer thickness ratios applied in simulated biaxial tensile test. Notes: D , displacement.

Leaflet	Time [s]	D [mm]	Thickness ratio	
			<i>Fibrosa layer</i>	<i>Atrialis/ventricularis layer</i>
AL	0	0	0.7	0.3
	0.20856	2.6428		
PL	0	0	0.55	0.45
	0.2805	2.5		

The total stress in each loading direction was obtained by multiplying the Cauchy stress in overlapping elements by the thickness ratio and summed together, using the approach detailed by Wenk *et al.* A bulk modulus of 10 MPa yielded the most accurate numerical results when compared to averaged experimental data obtained from healthy tissue specimens (Figure 5.6). The stress-stretch curves obtained in LS-DYNA are in good agreement with the experimental data for both leaflets, at low and high stretches. A display of the final model with fiber directions included is presented in Figure 5.7.

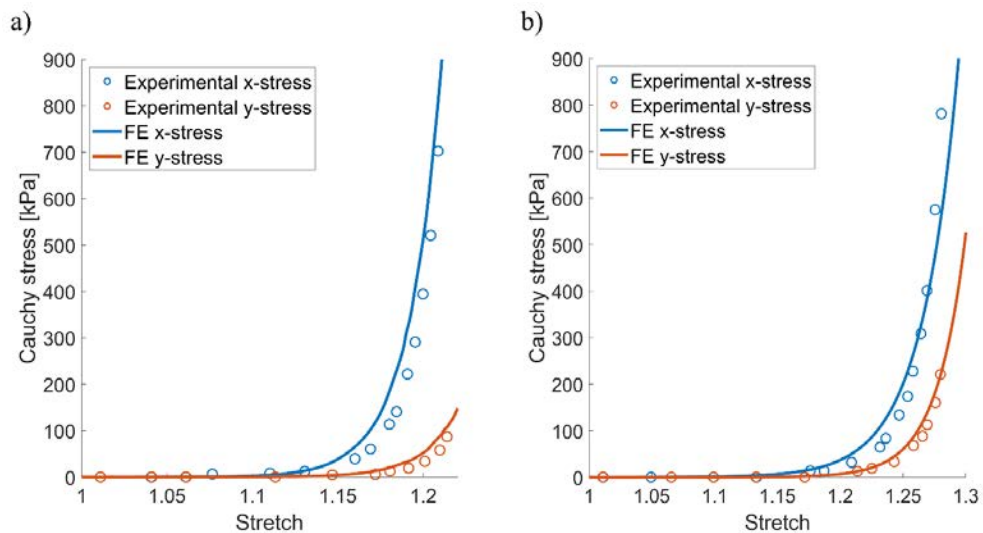


Figure 5.6: Comparison of the numerical (FE) results against experimental data (average calculated from individual specimens) for the a) anterior leaflet and the b) posterior leaflet under equibiaxial loading, with $K = 10$ MPa.

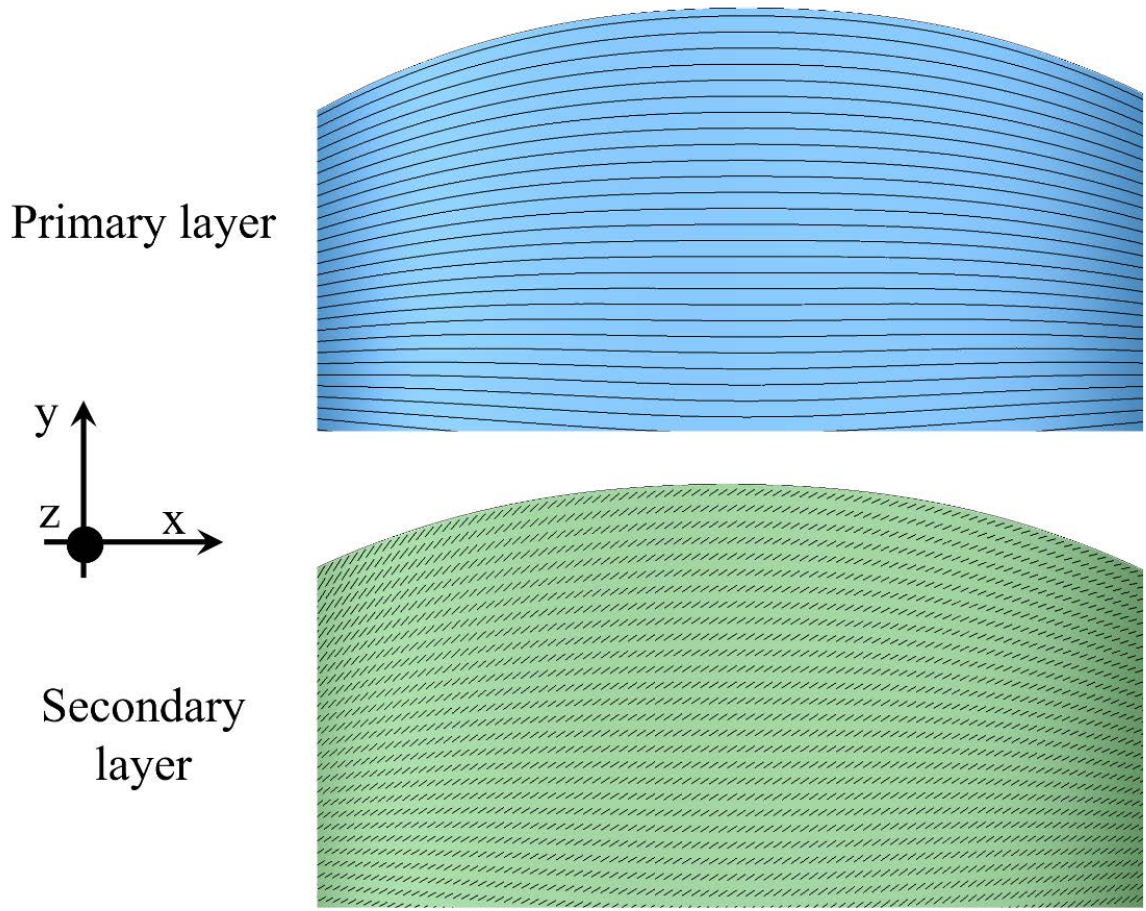


Figure 5.7: Part of the AL model with fibers embedded. The primary layer represents collagen fibers oriented preferentially in a circumferential orientation (fiber angle: 0°), while the secondary layer provides support in the radial direction (fiber angle: 35°).

The use of the material coefficients determined by (Wenk *et al.*, 2012) in the complete model led to mesh instabilities during the onset of MV closure, an issue also faced by a previous study (Wenk *et al.*, 2010). The final material values used were then manually determined and, unfortunately, it was not possible to exactly reproduce the stress-strain curves displayed in Figure 5.6. Table 5.4 represents the material properties originally determined by (Wenk *et al.*, 2012) and the ones used for all simulations employing the hyperelastic model.

Table 5.4: Material properties determined by (Wenk *et al.*, 2012) by fitting the stress equations for a 2-layer composite to experimental data from (May-Newman and Yin, 1998) and final hyperelastic material properties employed in FE simulations reported in this chapter. Notes: $C_{3,1}$, for example, represents the C_3 material constant in the first layer.

Leaflet		Material coefficients					
		C_1 [MPa]	C_2 [MPa]	$C_{3,1}$ [MPa]	$C_{4,1}$	$C_{3,2}$ [MPa]	
AL	(Wenk <i>et al.</i> , 2012)	$1.26e^{-4}$	0	$1.1e^{-5}$	52.97	$2.8e^{-5}$	48.65
	Final	0.5	0	$1.1e^{-5}$	52	$2.8e^{-5}$	48
PL	(Wenk <i>et al.</i> , 2012)	$2.33e^{-4}$	0	$7.0e^{-5}$	28.53	$7.5e^{-6}$	44.97
	Final	0.2	0	$7.0e^{-5}$	28	$7.5e^{-6}$	45

Subvalvular apparatus

No material properties were applied to the PM. As previously mentioned in Chapter 4, chordae are discretized into discrete beam elements (two nodes per element) and modelled as elastic cables which do not develop resistive force under compression. For primary chordae, and at each chordae bifurcation, the cross-sectional area is conserved over the number of branches, such that

$$A_{\text{post-branch}} = \frac{A_{\text{pre-branch}}}{N} \quad (5.5)$$

where N is the number of divisions (3 in the present implementation). Accounting for the estimated chordal sizes from literature (Lam *et al.*, 1970; Prot *et al.*, 2010; Chen *et al.*, 2020; Liao and Vesely, 2003), constant cross-sectional areas of 0.4 mm^2 and 1.05 mm^2 were chosen for marginal (pre-branching) and strut chordae, respectively. As mentioned in Chapter 2, the mechanical properties of the chordae tendineae are non-linearly elastic in nature. A discrete cable element and its non-linear material version have, therefore, been implemented in LS-

DYNA, where the behaviour of marginal chordae is defined from uniaxial test experimental measurements obtained by Kunzelman and Cochran (Kunzelman and Cochran, 1990). Strut chordae tissue is modelled as a less stiff material, implemented through a tangent elastic modulus scaled by 0.76 in comparison with the one of marginal chordae (Liao and Vesely, 2003; Stevanella *et al.*, 2009). The material responses are incorporated in the model by interpolating the stress-strain curves represented in Figure 5.8.

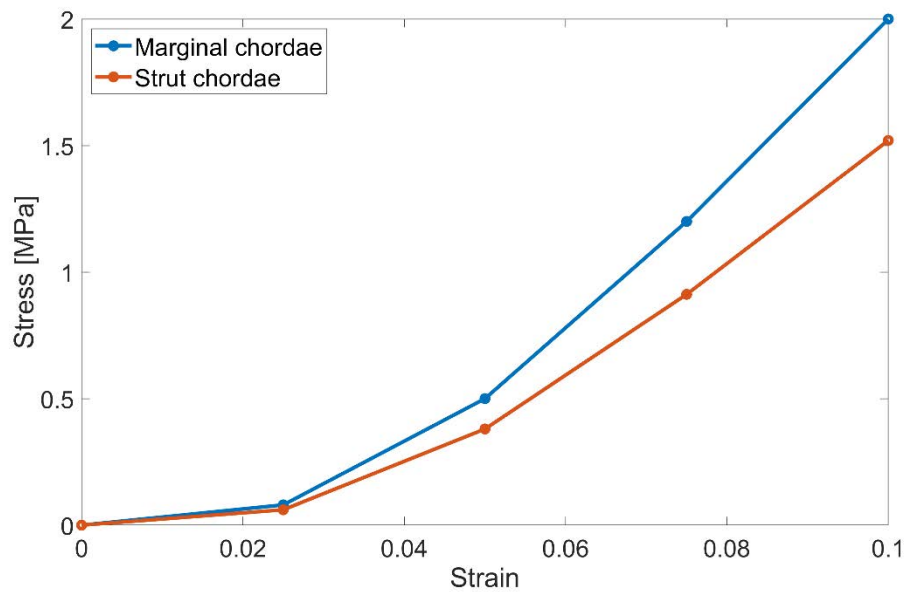


Figure 5.8: Non-linear stress-strain behaviour of marginal and strut chordae tendineae for a strain range of 0-10 %, obtained from Kunzelman and Cochran (Kunzelman and Cochran, 1990) and adapted based on information from Liao and Veseley (Liao and Vesely, 2003).

Transition elements

The transition shell elements (described in Chapter 4) are modelled as a linear elastic and isotropic material (Chen *et al.*, 2004; Stevanella *et al.*, 2009). A Young's modulus of 60 MPa and a Poisson's ratio of 0.488 are applied to represent the elevated stiffness of these mesh elements in comparison with the leaflets.

5.2.3. Boundary and loading conditions

The parts of the MV mesh to which boundary and loading conditions are applied are automatically saved as part of the toolbox script. Nodes corresponding to the mitral annular boundary and PM are saved as 3D coordinate matrices, while the leaflet mesh elements are identified through a connectivity matrix representing all element identifications and their nodes.

In the toolbox, this information is used as follows:

- ❖ The nodes associated with the mitral annulus and PM are used to apply prescribed displacements;
- ❖ The leaflet surfaces are used to define boundary conditions and to assign contact properties.

Annular displacement

Three boundary conditions were tested for mitral annular modelling:

Case 1: Fixed annulus, with suppressed annular motion prescribed through 3D nodal translation constraints;

Case 2: Moving annulus, with simplified annular contraction prescribed through equal nodal displacements towards the annular centroid;

Case 3: Moving annulus, with annular contraction prescribed through individual nodal displacements towards the annular centroid, based on literature data, which yielded more physiological annular changes during the cardiac cycle.

Concerning Case 2, an average annular diameter change of 3.5 mm was assumed (Dagum *et al.*, 2000) and a nodal displacement of 1.75 mm was applied (Figure 5.9a), acting inwards to

the annular centroid by means of prescribed direction vectors. Case 3, which is the option implemented in the toolbox, accounts for a non-homogeneous change in the annulus by incorporating the following spatial morphological alterations from mid-diastole to systole:

- ❖ A 10% increase in saddle-horn height, caused by anterior and posterior annular tilting (Itoh *et al.*, 2009);
- ❖ A 5% decrease in the CW (Topilsky *et al.*, 2013; Tang *et al.*, 2019; Maffessanti *et al.*, 2013).

Nodal changes associated with these alterations are prescribed as individual nodal displacements to obtain the desired annular shape at maximum displacement (Figure 5.9c). Moreover, these displacements are further adapted to reflect the non-homogenous temporal changes observed in clinical studies (Topilsky *et al.*, 2013; Tang *et al.*, 2019; Levack *et al.*, 2012). Average adaptations including the application of maximum displacements at early systole and annular relaxation through mid- and late-systole are implemented (Topilsky *et al.*, 2013), as represented in Figure 5.9b.

Cases 2 and 3 yielded the annular dimensional changes presented in Table 5.5. The main difference between the two implementations concerns the change in annular height from mid-diastole to mid-systole, which is present in Case 3. Moreover, Case 3 generates an overall shape and dimensions which are more in agreement with in vivo ranges for a healthy MV geometry, as observed in Table 5.5.

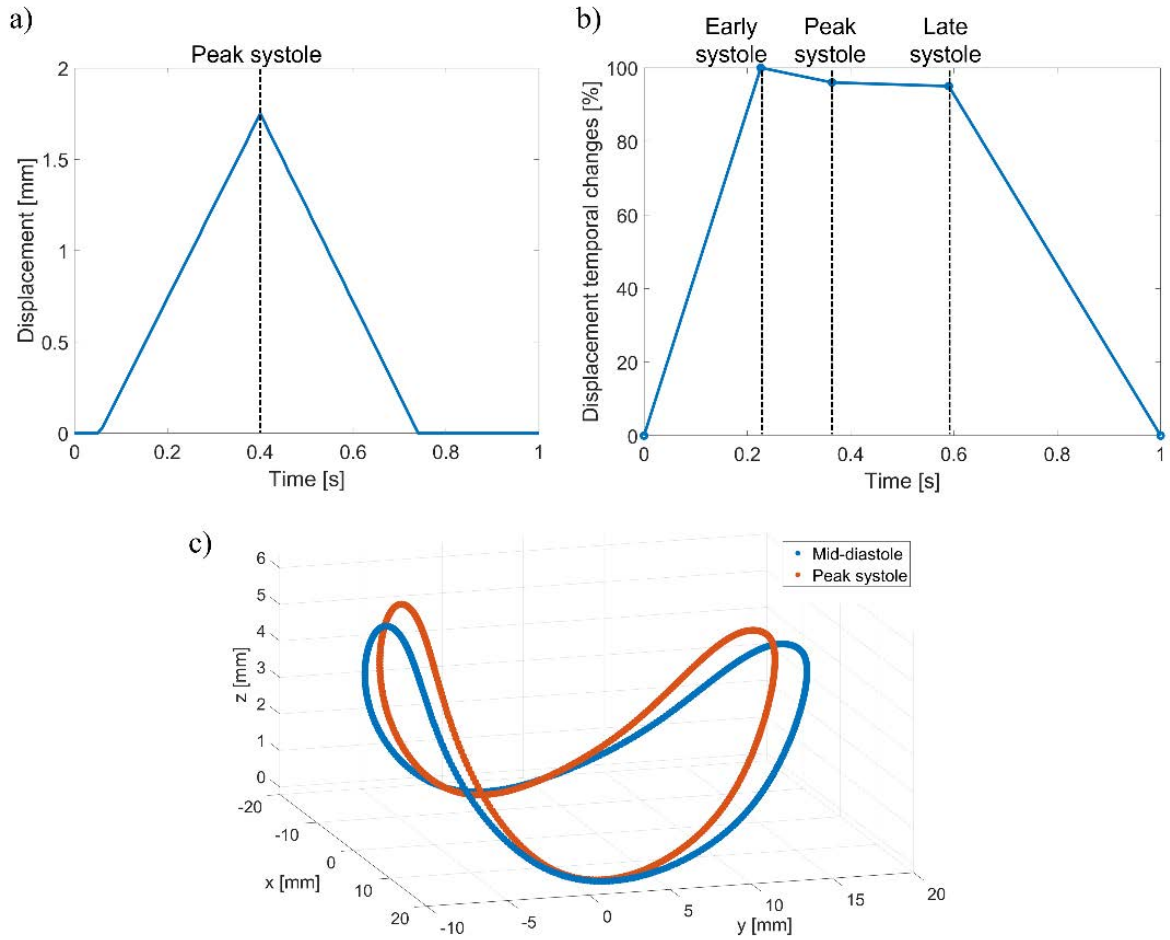


Figure 5.9: Annular displacements for cases 2 (a) and 3 (b and c). a) The magnitude of the annular displacement towards its centroid and through a cardiac cycle is displayed for case 2, with the annulus reaching a maximum displacement of 1.5 mm at peak systole; b) In case 3, all annular portions contract at the same time, but the magnitude of the annular displacement through a cardiac cycle is adapted to represent different stages of contraction, with the maximum displacement occurring at early systole; c) The three-dimensional annulus and its spatial displacement from mid-diastole to peak systole is showcased for case 3, with different annular coordinates being associated with varying displacements.

Table 5.5: Percentage changes in annular dimensions from mid-diastole to systole caused by different prescribed displacement cases. The values presented for Case 2 reflect changes from mid-diastole to peak systole, while those for Case 3 demonstrate the maximum changes obtained from mid-diastole to early-systole, compared against healthy ranges from the literature (Topilsky *et al.*, 2013; Tang *et al.*, 2019; Levack *et al.*, 2012).

	[%] Change in				
	Orifice area	Annular perimeter	AP diameter	CW	AH
Case 2	-15.40	-8.08	-11.12	-8.13	0
Case 3	-11.98	-5.88	-10.68	-5	+13.43
Literature	-8 to -15	-4 to -6	-3 to -12	-2 to -5	+7.9 to +13.5

PM displacement

PM motion is implemented through the definition of equations relating the distances from each tip to annular landmarks (trigone, AL annular midpoint and PL annular midpoint). These distances are adapted to represent a mid-systolic approximation between inter-PM tips and PM tip to anterior annulus approximation (Topilsky *et al.*, 2013). The maximum shortening of the PM is characterized by:

- ❖ A 7% decrease in the distance between each tip and the mid-anterior annulus;
- ❖ A 8% decrease in the distance between each tip and the respective fibrous trigone;
- ❖ A 5% decrease in the distance between each tip and the mid-posterior annulus;

These conditions yield a 14% decrease in the inter-PM distance, consistent with clinical studies (Topilsky *et al.*, 2013). Similarly to annular motion, PM distances to the annulus vary during the cardiac cycle (Topilsky *et al.*, 2013); therefore, displacements are adapted to reflect these temporal changes (Figure 5.10).

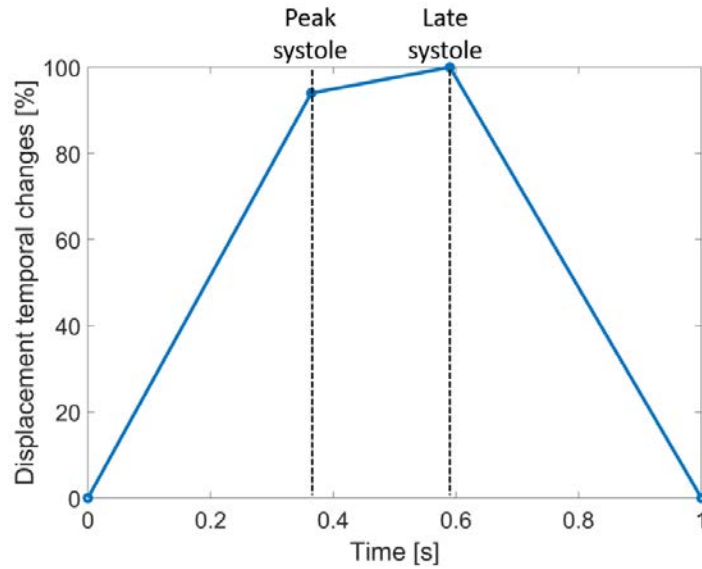


Figure 5.10: Temporal changes in PM displacement for the whole cardiac cycle.

Pressure loading

Time-dependent physiologic transvalvular pressure loadings were applied on the ventricular and atrial surfaces of valve leaflets. The pressure curves, adapted from (Herring and Paterson, 2018), represent a full cardiac cycle simulating MV closing and opening (Figure 5.11).

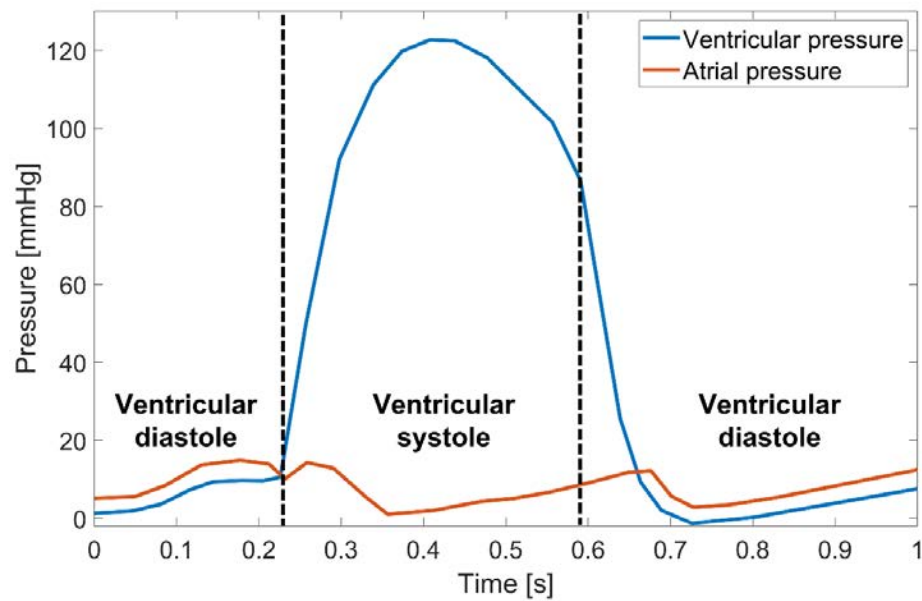


Figure 5.11: Transvalvular pressure load curves adapted from (Herring and Paterson, 2018) and applied as boundary conditions to the atrial and ventricular surfaces of the MV leaflets.

Contact properties

Contact definitions are applied to a part list defined within the toolbox containing the boundary surfaces corresponding to the leaflets and transition elements. Since self-contact can occur during MV closing, leaflet surfaces are assumed as a single surface for contact management. The 2-way automatic single surface contact formulation available in LS-DYNA is then applied to the part list defined. According to this formulation, only a slave part is defined (the entire single surface) and a master surface is not specified. When in contact, surfaces can move together and, since no frictional coefficients are defined, relative sliding between surfaces is allowed. A segment-based penalty formulation, focused on the detection of segment to segment penetration, is employed to prevent surface penetration during contact, using the approach introduced in Appendix B (Hallquist, 2006b). Additional contact parameters are specified in Table 5.6.

As the use of a single surface contact does not allow for the output of contact pressure or forces, an additional contact formulation based on a contact transducer is applied to the defined part list. This is used to record contact forces produced by the automatic single surface contact formulation, and is defined in a similar manner; however, both slave and master surfaces are defined to gather force interactions between surfaces (Table 5.6).

Table 5.6: Contact formulation options for the MV, prescribed in the toolbox.

Parameter	Contact formulation	
	Segment-based approach	Contact transducer
Slave surface	1	1
Master surface	-	1
SBOPT	2 (assumes planar segments)	-
Depth	3 (surface penetration checked at segment edges, such as the free edge)	-
Viscous damping coefficient	20% (contact damping perpendicular to contacting surfaces to prevent undesirable oscillation)	20%

5.2.4. Control properties and database outputs

The transient FE model is solved through dynamic analysis using the LS-DYNA explicit solver. Structural dynamics are solved by approximating the solution to the conservation of mass and momentum equations using the finite element method. Instead of using an iterative approach, nodal accelerations are solved directly for each time step. Once accelerations are known at a specific time step, velocities and displacements are calculated, and strain and stress quantities are obtained from displacement (Hallquist, 2006b). The transient dynamic equilibrium equation is solved through the central difference method. This method staggers the velocity with respect to the displacement in time and ensures second order accuracy in time. The numerical approaches used are described in detail in the LS-DYNA theory manual (Hallquist, 2006b).

Additional control properties are applied to the model; one of these is related to preventing hourglassing, associated with nonphysical modes of deformation associated with zero net displacements and zero-energy modes which can distort the mesh and create numerical instabilities (Hallquist, 2006b). To avoid hourglassing, hourglass control is applied to the entire leaflet mesh. This control is added at the element level in the form of numerical forces (or hourglass forces). A transient simulation of the MV representing half of a cardiac cycle was run to test the hourglass control options available in LS-DYNA: two viscosity-based formulations and one stiffness-based formulation were applied to Belytschko-Lin-Tsay shells and one formulation was applied to fully integrated shells. Internal and hourglass energies were then outputted and plotted over time, as represented in Figure 5.12.

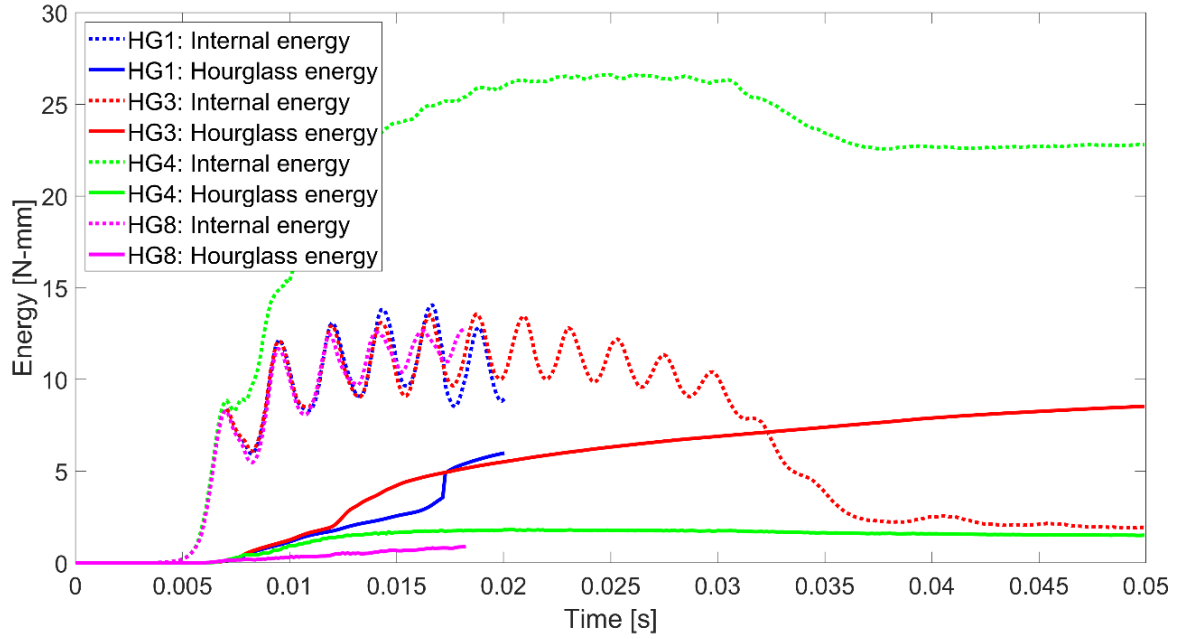


Figure 5.12: Internal and hourglass energies [N mm] over time [s] for four main hourglass control formulations. HG1 and HG3 are viscosity-based controls, HG4 is a stiffness-based control and HG8 is applied to fully integrated shell elements.

In all formulations, except HG4, the internal energy greatly oscillates for all hourglass formulations. Moreover, for HG1 and HG8, the simulation crashes at early systole (onset of closing) and, for HG3, the hourglass energy surpasses the internal energy at peak systole. Given that hour-glass energies should be much smaller ($< 10\%$) than peak internal energy and since formulation HG4 was the only one achieving this, this was the chosen formulation for hour-glass control. Details on the main options selected, values used and respective description are presented in Table 5.7.

Table 5.7: Control options included for FE simulations.

Type	Choice	Description
Time step size	Scale factor: 0.2	Control size of time step: Smaller size chosen to prevent surface penetrations during contact
Bulk viscosity	$Q_1 = 1.5$; $Q_2 = 0.06$ (default values)	Improvement of simulation stability through control of shock wave propagation by smearing shocks (Q_1) and dampening of oscillations (Q_2)
Energy	Hourglass energy: yes Rigidwall energy dissipation: no Sliding interface energy dissipation: yes Rayleigh energy dissipation: no	Control energy dissipation computing and inclusion in the energy balance output
Dynamic relaxation	Scaling factor: 0.9965 (Burriesci <i>et al.</i> , 1999)	Nodal velocity dampening to mimic immersion of MV in fluid
Accuracy of results	Second order objective stress updates: yes Invariant node numbering: yes	Invariant node numbering causes a shift in the local element system, leading to: 1) Element forces nearly independent of node sequencing; 2) Material directions not greatly affected by hourglass modes; 3) Stable calculations over a long time period.
Contact	Initial penetration check: no checking Shell thickness considered: yes Penalty stiffness: minimum of master segment and slave node (default)	Initial contact is ignored, but penetration warnings are printed; Shell thickness is considered in single-surface contact; Penalty stiffness is calculated based on equation B.1 from Appendix B
Shell	Element warpage angle threshold: 20° (default) Shell normal update: nodal fibers updated based on nodal rotation Warping stiffness: Belytschko-Wong-Chiang formulation Projection for warping stiffness: full projection	If a warpage angle greater than 20° is found, warning message is printed; Warping stiffness prevents element warping and its change into an unreasonable element shape
Hourglass	Stiffness based (type 2) Hourglass coefficient: 0.03	For shell elements using reduced integration, hourglass controls element deformation associated with zero energy deformation modes.

5.3. Cases simulated and analysis

5.3.1. Solver settings and parameters evaluated

All simulations were run for 1 s, corresponding to a full cardiac cycle, and using a desktop computer (4 cores per simulation). The solution time for each simulation ranged between 3 to 4 hours. Time-instant results were evaluated at peak systole ($t = 0.37$ s) and time-dependent results were obtained for several quantities. Leaflet stress distributions were evaluated for all cases, and stress values obtained at three different cross-sections (Figure 5.13a) were determined. Chordal elongations and tensions were determined for all chordae. PM reaction forces (F_{PM}) were calculated by performing the sum of the tension of all chordae attached to that PM. Moreover, the percentages of the force carried by the different groups of chordae relative to each total PM force were calculated using equation 5.6:

$$\text{Load proportion} = 100 \cdot \frac{\|F_{PM}\| - \|F_{PM} - F_C\|}{\|F_{PM}\|} \quad (5.6)$$

where F_C is the force vector carried by a chordal group and the load proportion is the percentage of F_{PM} carried by that group (Prot *et al.*, 2009). Functional characteristics of the MV were evaluated through quantities captured at the central cross-section of the MV (Figure 5.13a), including coaptation profiles, coaptation length, posterior billowing height and displacement distributions. The coaptation length is defined as the distance of the coapted leaflet region from the middle cross-section and posterior billowing height is calculated through the height from the anteroposterior line connecting the anterior and posterior mid-annular points to the maximum protruding point of the posterior leaflet into the left atrium (Figure 5.13b). Additional

parameters obtained only for specific cases are mentioned on the following subsections, together with geometry characteristics.

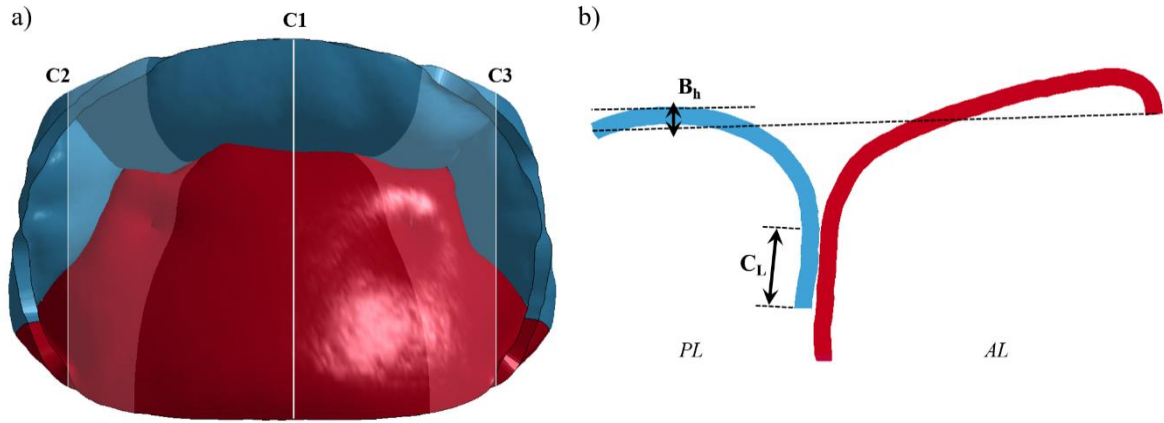


Figure 5.13: Cross-sections used for the evaluation of several results. a) Three cross-sectional planes are used for the calculation of results (C1, middle section; C2, PMPM section; C3, ALPM section); b) C1 (middle section) is used to evaluate results related to MV coaptation (C_L , coaptation length; B_h , posterior billowing height). Notes: PL, posterior leaflet; AL, anterior leaflet.

5.3.2. Mitral valve average model validation

Geometry description and generation

A healthy MV geometry, based on average dimensions (Table 5.8) and a user-inputted AP diameter of 25 mm, was created. The PM tip was assumed as a single point and leaflet surfaces were meshed with 28,054 shell elements, with the generation of the final model for FE simulations taking less than one minute. The computational simulation for a complete cardiac cycle was solved in less than five hours.

Table 5.8: MV average model dimensions.

MV part		Dimension
Annulus	d_{AP}	25 mm
	d_{CW}	5.9 mm
	h_{AH}	30.9 mm
	-	D-shape (no ring concavity)
Leaflets	A_h	25 mm
	P_{mh}	15.45 mm
	P_{ch}	9.55 mm
	A_a	397.08 mm ²
	P_a	267.53 mm ²
PM	$ALPM_0$	31.5 mm
	$ALPM_{10}$	24 mm
	$ALPM_8$	27 mm
	$PMPM_0$	31.5 mm
	$PMPM_2$	27 mm
	$PMPM_4$	24 mm

Valve closure dynamics

The FE model predicted physiological movement of the MV throughout the cardiac cycle. Figure 5.14 displays the MV shape at four time instants. Leaflet coaptation occurs before the maximum pressure load (120 mmHg) with the valve closing at a pressure drop of 80 mmHg, before peak systole ($t = 0.37$ s). The valve then opens through late systole and early diastole ($t = 0.8$ s). Through these time instants, it is also possible to see a change in the annular profile, caused by the simulation of annular contraction. Leaflet coaptation length was 4.924 mm, within the range of clinical measurements (3.2 ± 0.7 mm) (Gogoladze *et al.*, 2010) and computational predictions (Choi *et al.*, 2016; Kong *et al.*, 2018) for healthy (≈ 7 mm) and repaired (3.9 – 4.9 mm) MV geometries. Leaflet billowing (displacement of leaflet surfaces into left atrium) was not present, also consistent with clinical observations for control subjects (Lee *et al.*, 2013).

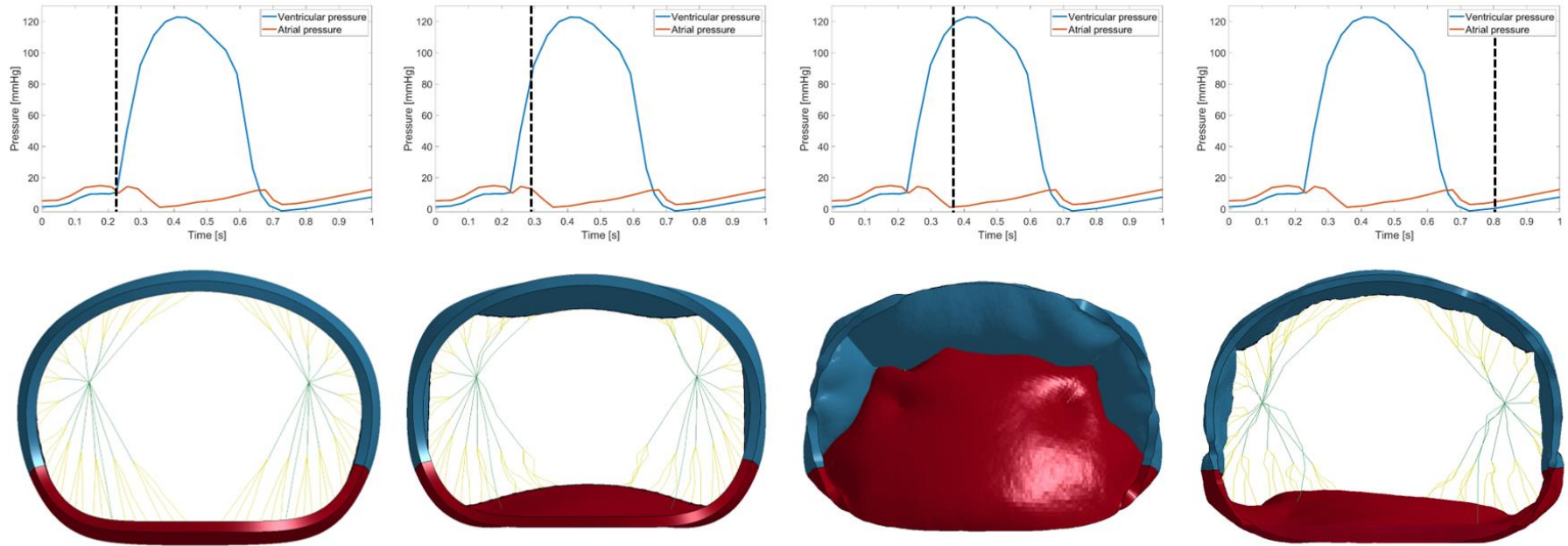


Figure 5.14: Time evolution of the average MV shape (atrial view) as predicted by the FE model at four different time instances of the cardiac cycle ($t = 0.22$ s, 0.25 s, 0.37 s, 0.8 s).

Figure 5.15 displays leaflet contact and non-contact regions in red and blue, respectively. The healthy MV geometry shows sufficient leaflet coaptation, with contact distributions similar to healthy (Rim *et al.*, 2014) and post-surgical (Choi *et al.*, 2014) models. However, and in opposition to other studies, the present model includes several contact gaps across the leaflet surfaces.

These may be caused by the use of a shell element formulation with three integration points across the leaflet thickness, which are recommended to avoid excessive softness and capture appropriate bending response (Hallquist, 2006b), but may be associated with increased bending stiffness during coaptation (Wenk *et al.*, 2010). The model has a contact area of 142.7 mm², corresponding to a coaptation to total leaflet surface area ratio of 0.215, at the extreme but still within the ranges of 0.21 to 0.36 reported for healthy and post-surgical geometries (Saito *et al.*, 2012; Guo *et al.*, 2018). Even though surface contact gaps lead to an underestimated contact area, the overall region of contact seems appropriate for a healthy model with the dimensions specified in Table 5.8.

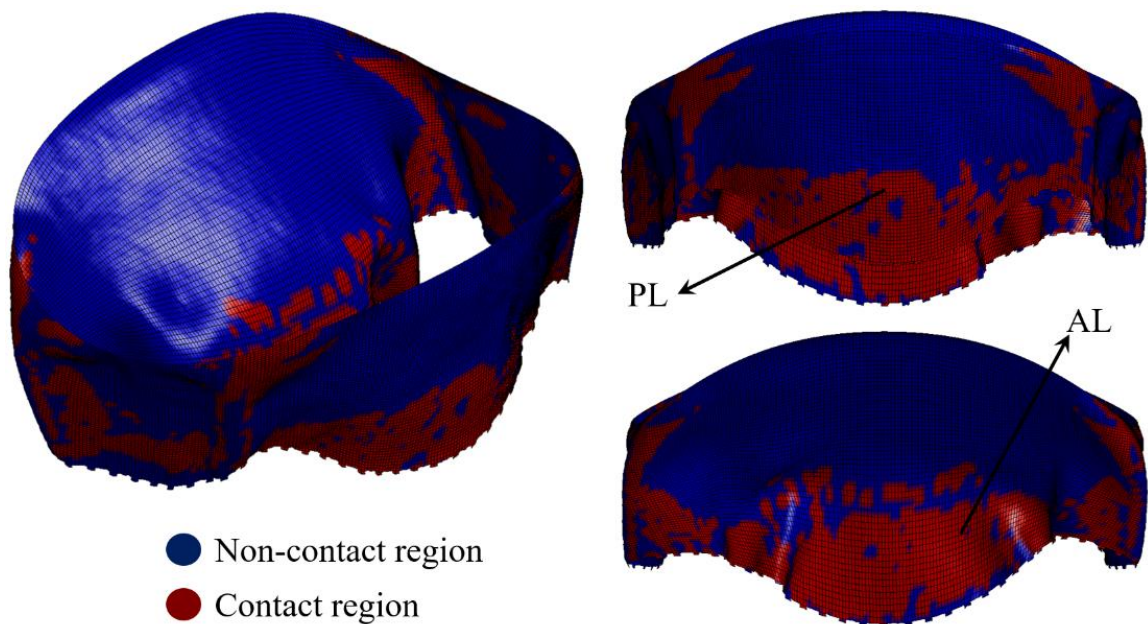


Figure 5.15: MV leaflet contact distributions.

Leaflet stresses

The maximum principal stress distributions across the mitral leaflets at peak systole are displayed in Figure 5.16. The gap present between the leaflets is a post-processing artefact, given that only the shell mid-surface is displayed. The most stressed regions correspond to marginal and strut chordae insertions (Votta *et al.*, 2008; Stevanella *et al.*, 2009). High stress values were observed near the anterior saddle horn, following the circumferential direction and connecting the trigones, as observed for patient-specific (Rim *et al.*, 2014) and idealised (Prot *et al.*, 2009) MV models. The AL undergoes larger stresses in comparison with the PL scallops, whose greatest stress distributions are mostly located near the annulus, ranging between 0.279 and 0.363 MPa (values reported in Figure 5.16). This is in agreement with previous patient-specific MV models, with reported maximum principal stresses in the AL mostly ranging from 0.2 to 0.4 MPa at peak systole (Wang and Sun, 2013; Rim *et al.*, 2014; Prot *et al.*, 2009). The PL experiences lower stresses, ranging from 0.159 to 0.247 MPa, within reported ranges of 0.05 to 0.25 MPa (Wang and Sun, 2013; Prot *et al.*, 2009; Rim *et al.*, 2014; Stevanella *et al.*, 2009).

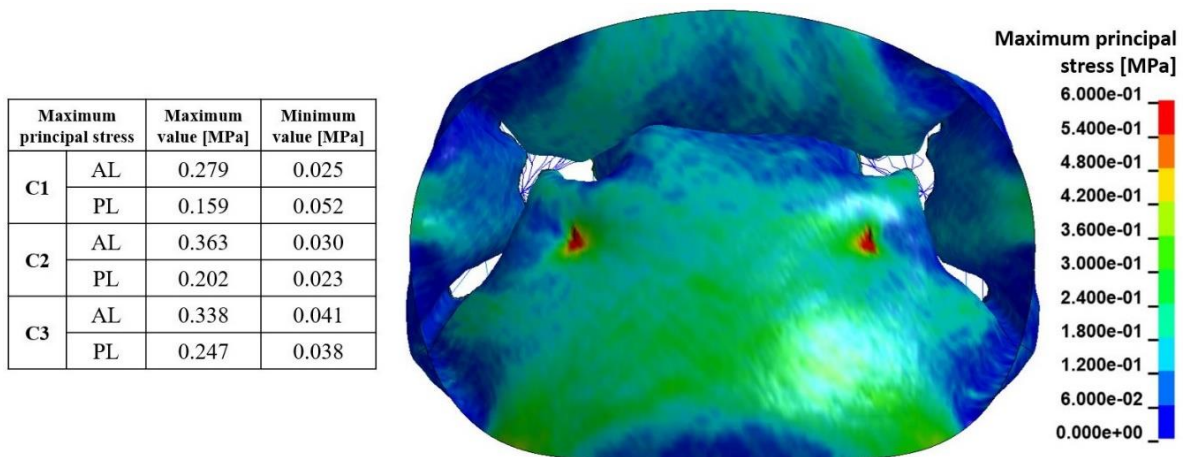


Figure 5.16: Leaflet stress distributions at peak systole and maximum and minimum stress values obtained at relevant cross-sections.

Papillary muscles and chordae forces

Time-dependent PM reaction force magnitudes follow the transvalvular pressure drop profile, as observed in Figure 5.17 for the ALPM (Stevanella *et al.*, 2009; Kunzelman *et al.*, 2007). A maximum reaction force value of 3.4 N was obtained at peak systole, comparable to values predicted by computational studies (Stevanella *et al.*, 2009; Prot *et al.*, 2009) and *in vitro* measurements (Jensen *et al.*, 2001; Jimenez *et al.*, 2003). The notch present in the PM temporal curve ($t = 0.2$ s) indicates the onset of leaflet coaptation (Kunzelman *et al.*, 2007).

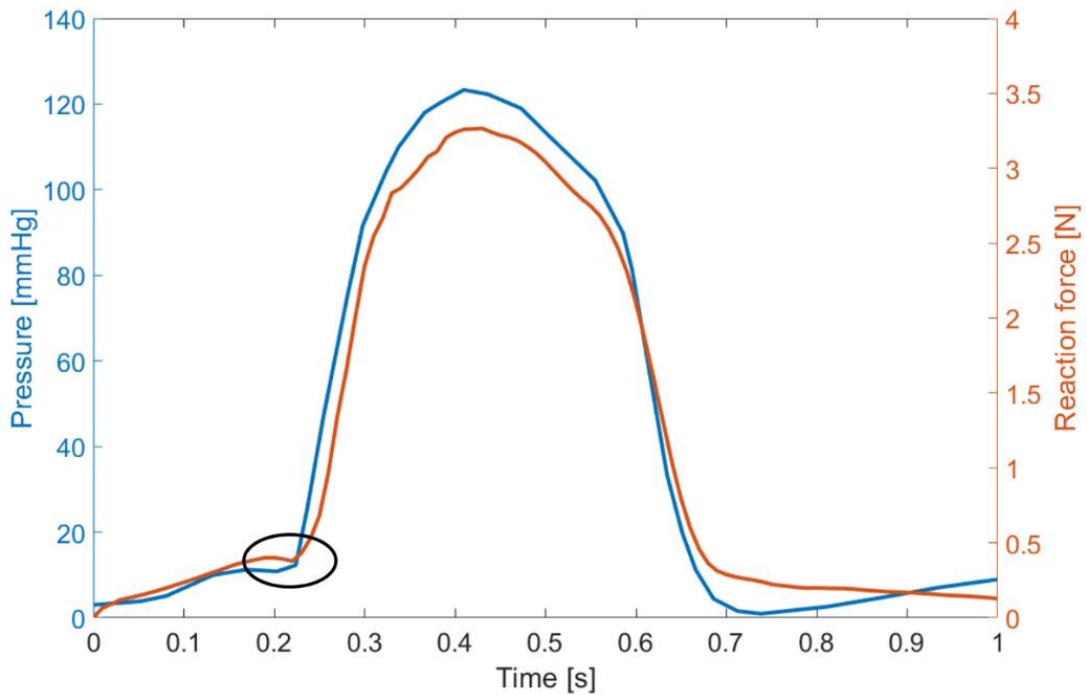


Figure 5.17: Time-dependent PMPM reaction forces.

The regional distribution of chordae tensions and elongations, as well as percentages of resultant force bore by each group, are presented in Table 5.9. Both predicted chordal elongations and tension forces are within the range of those obtained by previous computational studies (Stevanella *et al.*, 2009; Wang and Sun, 2013) and *in vitro* experiments (Jimenez *et al.*, 2003; Jimenez *et al.*, 2005; Paulsen *et al.*, 2020). Strut chordae experienced the greatest

elongation and highest load amongst all groups, bearing alone 25% of the PM total force. This demonstrates the importance of strut chordae in aiding MV proper function (Prot *et al.*, 2009; Taylor *et al.*, 2021), given that they exhibit much higher failure load than other chordal types (Sedransk *et al.*, 2002). AL and PL marginal chordae were less stressed; regardless, the load proportion bore by PL marginal chordae was the highest (47.9%), consistent with previous results (Prot *et al.*, 2009). Figure 5.18 compares the chordal tensions obtained with those from previous studies (further details on chordal tensions retrieved from the literature available in Appendix C). Despite the variability in chordal tensions amongst different studies, the tensions predicted are comparable to the range of values associated with healthy MV models. However, the average tension obtained for PL marginal chordae is higher than those obtained by experimental studies. This may derive from the fact that PL secondary chordae are not included in the model, with such chordae carrying higher tensions in comparison with marginal chordae (Paulsen *et al.*, 2019; Paulsen *et al.*, 2020). It can then be hypothesized that the PL marginal chordae carry higher tensions to compensate for the lack of secondary chordae and in an attempt to replace their function.

Table 5.9: Chordae tendineae elongation, tension and load proportion (mean \pm standard deviation) at peak systole.

Chordae	No.	Length [mm]	Elongation [mm]	Load [N]	Load proportion [%]
AL strut	1	19.33	1.33	0.817	25
AL marginal	6	14.78 \pm 1.89	0.42 \pm 0.30	0.152 \pm 0.095	27.1
PL marginal	7	14.52 \pm 1.74	0.70 \pm 0.26	0.245 \pm 0.079	47.9

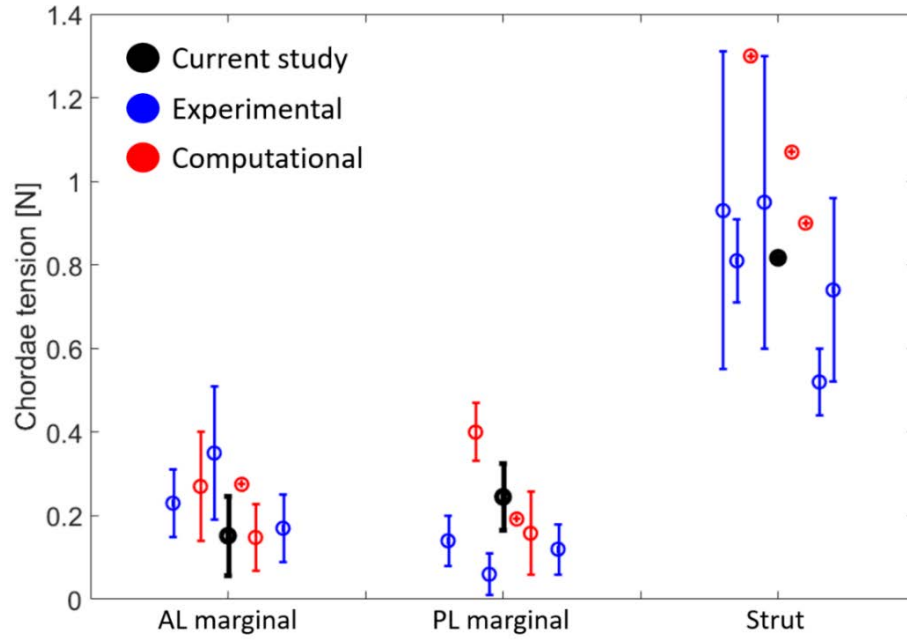


Figure 5.18: Forces carried by different groups of chordae at peak systole. Black coloured data represents the predictions of the present model, while blue and red correspond to estimations from experimental (Jimenez *et al.*, 2005; Nielsen *et al.*, 2003; Paulsen *et al.*, 2020; Paulsen *et al.*, 2019) and computational (Prot *et al.*, 2009; Stevanella *et al.*, 2009; Wang and Sun, 2013) studies, respectively.

5.3.3. Sensitivity study of material properties

Two MV models, one employing orthotropic material properties and the other hyperelastic material properties, were generated to evaluate differences in circumferential and radial strain predictions. The geometry employed was the same as in section 5.3.2 and meshes of 28,174 and 56,348 shell elements were generated for orthotropic and hyperelastic models, respectively.

Circumferential and radial strain distributions are represented in Figure 5.19 for both material models. In the AL, and similarly to (Stevanella *et al.*, 2009) circumferential tensile stretches reach peak values in the region surrounding the trigones (23 %) and gradually decrease towards the centre of the AL belly. The use of a hyperelastic material model reinforces this strain distribution, with further tensile stretches appearing in the centre of the AL belly. The orthotropic model leads to heterogeneous tensile and compressive strains on the PL. Tensile strains are observed in the belly region of the central cusp (7 %) while compressive ones (6 %)

appear near the annular region due to annular contraction. With a hyperelastic model, these compressive strains increase in percentage (10%) and distribution in the central cusp of the PL, as predicted by several studies (Rego *et al.*, 2018; Stevanella *et al.*, 2009; Stevanella *et al.*, 2011). Radial strains are greater than circumferential ones and their distribution showcases a different trend. These are mostly tensile in both leaflets: the orthotropic model leads to peak stretches of 50% in the AL belly, away from the annular boundary. They decrease towards the annulus, with lower tensile strains near the trigones (8 %) and compressive strains near the anterior saddle horn (2%) (Kunzelman *et al.*, 2007; Stevanella *et al.*, 2011). In the PL, and except for a few regions in the lateral scallops near the annulus, strains are mainly tensile, reaching peak values of 49%. With a hyperelastic model, a wider distribution of tensile strains appears in the AL belly and central cusp of the PL (both with maximum stretches of 49%). The compressive strains observed in the lateral scallops of the PL also become more evident (10%).

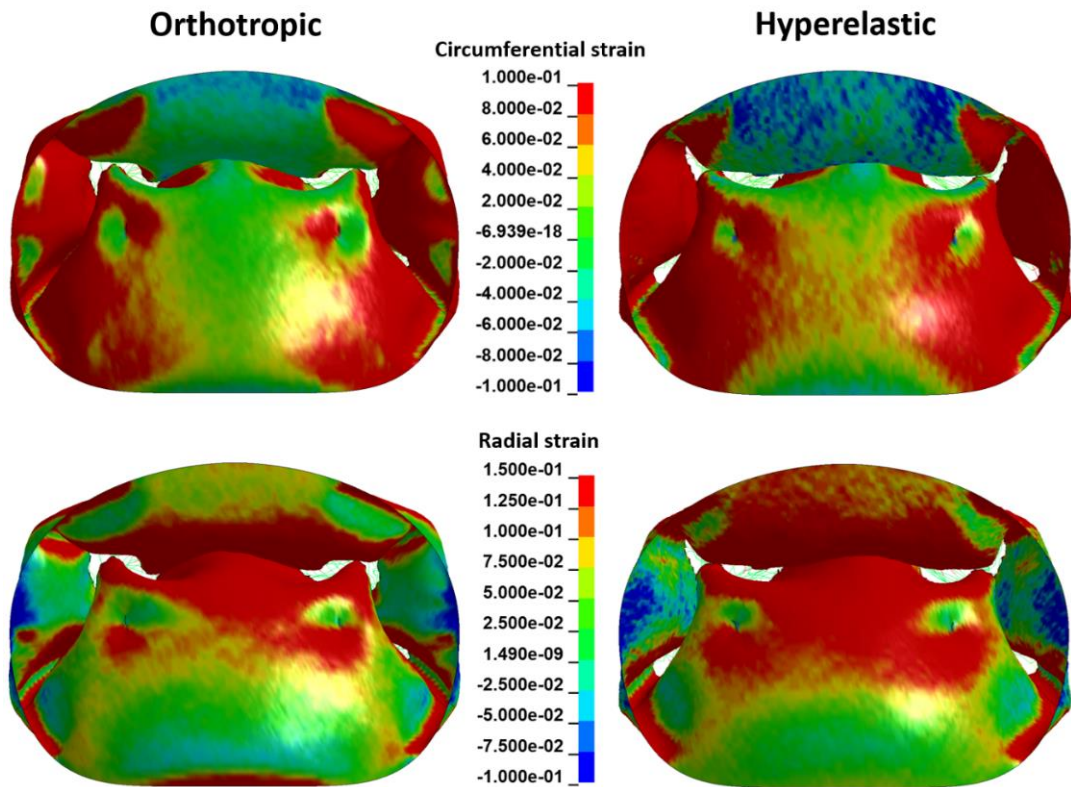


Figure 5.19: Distribution of circumferential and radial strains on mitral leaflets at peak systole for orthotropic and hyperelastic material models.

5.3.4. Sensitivity study of boundary conditions and PM shape

To evaluate the effects of boundary conditions and PM shape on MV dynamics, four models have been generated to represent: (A) fixed annulus and PM; (B) moving annulus and fixed PM, (C) moving annulus and PM; and (D) moving annulus and PM with a 3D shape. To generate these models, the three different annular displacement cases explained in section 5.2.3 have been implemented.

The influence of annular motion (and specifically the prescription of the three different displacement cases from section 5.2.3) on MV coaptation and leaflet displacement was assessed (Figure 5.20). While valve closure is achieved for all cases, the coaptation profile and length drastically changes with and without a moving annulus. A fixed annulus generated poor coaptation (length: 1.703 mm), a value usually associated with the presence of regurgitation (Gogoladze *et al.*, 2010), and excessive displacement of the PL towards the left atrium (without a billowing height). Moving annulus conditions gave rise to adequate leaflet coaptation, with coaptation lengths (4.484 and 4.924 mm) within the normal range (Choi *et al.*, 2016; Kong *et al.*, 2018; Gogoladze *et al.*, 2010), similar PL z-displacements and no billowing height.

Different stress distributions were observed for models with varying BC and PM shapes (Figure 5.21). While all models show the presence of larger stresses near the trigones and at the region of strut chordae insertions, not prescribing annular and PM motion led to elevated stresses near the anterior saddle-horn in comparison with other models. AL stress distributions in the presence of annular displacement was similar amongst models with and without PM motion. However, an increase in stress induced on the PL were observed for models with PM motion, and especially when using a 3D PM shape instead of a single tip point.

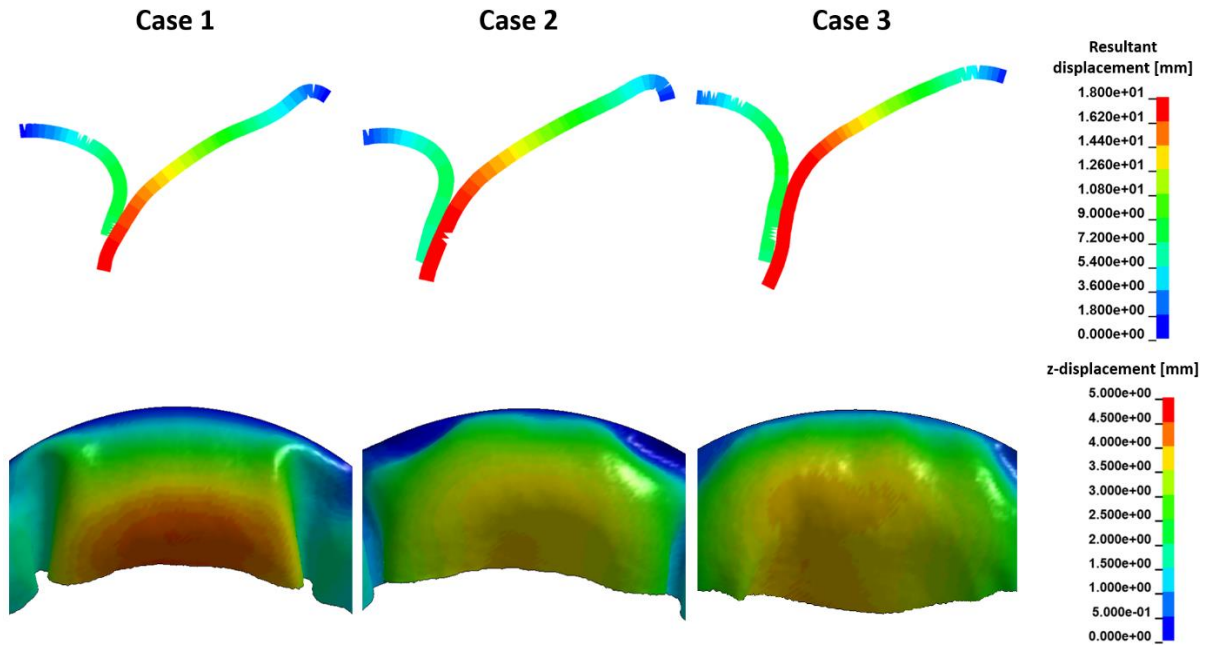


Figure 5.20: Effects of three annular boundary conditions on the leaflet coaptation profile (middle cross-section) and resultant displacement at peak systole. PL z-displacements are also displayed for each case. Coaptation lengths are 1.703 mm, 4.484 mm and 4.924 mm for cases 1, 2 and 3, respectively.

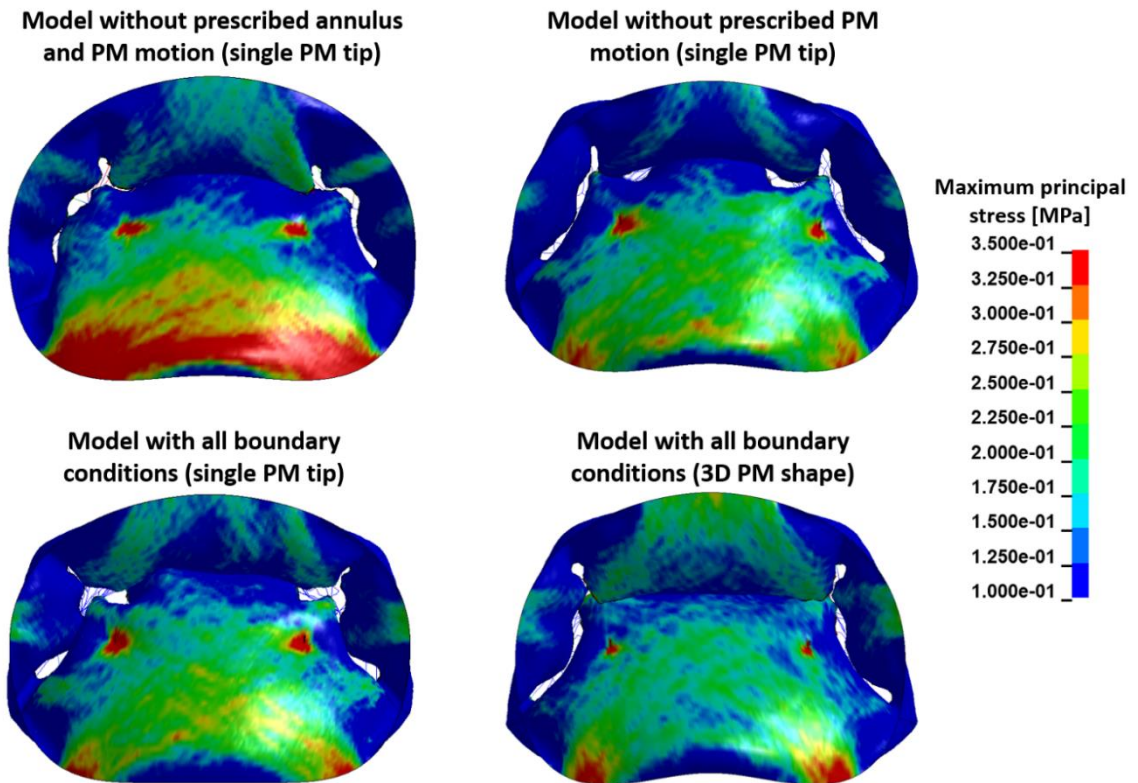


Figure 5.21: Leaflets' maximum principal stresses distribution at peak systole for four different model conditions.

Varying BC and PM shapes also induced differences on peak systolic chordal tensions and load proportions (Table 5.10). Regarding annular and PM displacements, while a fixed model induced the highest load for strut chordae, the highest load bore by AL and PL marginal chordae was associated with the presence of annular and PM motion. Regardless, no significant differences in chordal tension magnitudes were observed for conditions different BC. However, the addition of simple annular displacement (condition B from Table 5.10) increased the proportion of load carried by strut chordae and decreased the one carried by PL marginal chordae. These proportions then became similar to those of the fixed model when a more accurate annular displacement was implemented with PM motion (condition C from Table 5.10).

The greatest differences in chordal tension and proportion of load were observed with the use of a 3D PM shape (condition D from Table 5.10) instead of a single tip point. Strut chordae bore less load in comparison with the single tip model (-15.5%) and the associated proportion of load carried decreased. However, the loads bore by AL and PL marginal chordae increased by 54.6 and 53.5 %, respectively, together with the proportion of load carried.

Table 5.10: Chordae tendineae tension and load proportion at peak systole under varying boundary conditions and PM shapes. Conditions simulated correspond to (A) fixed annulus and PM (single PM tip), (B) moving annulus and fixed PM (single PM tip), (C) moving annulus and PM (single PM tip) and (D) moving annulus and PM (3D PM shape).

	A		B		C		D	
Chordae	Load [N]	Load prop. [%]	Load [N]	Load prop. [%]	Load [N]	Load prop. [%]	Load [N]	Load prop. [%]
AL strut	0.872	26	0.754	33.9	0.817	25	0.69	16.5
AL marginal	0.122 ± 0.074	25.7	0.115 ± 0.080	26.7	0.152 ± 0.095	27.1	0.235 ± 0.122	31.2
PL marginal	0.204 ± 0.107	48.3	0.125 ± 0.042	39.4	0.245 ± 0.079	47.9	0.376 ± 0.147	52.3
F_{PM}	3.32		2.36		3.4		4.17	

5.3.5. Different patient scenarios

Geometry description and generation

Two MV geometries based on inputted patient-specific dimensions (Table 5.11) and with the PM tips represented as a single points, were generated. Both models have geometrical features potentially associated with the onset of regurgitation: the first geometry (PS1) represents a diseased shape associated with annular dilation and leaflet enlargement, based on dimensions reported in the literature for diseased valves (Lee *et al.*, 2013; Mihaila, 2013). The second geometry (PS2) includes PMPM displacement caused by the implementation of LV dilation. PS1 and PS2 geometries were meshed with 27,154 and 23,314 shell elements, respectively, and the generation of the final models for FE simulations took less than five minutes. Both computational simulations were solved in less than five hours.

Table 5.11: MV patient-specific model dimensions.

MV part		Dimension	
		PS1	PS2
Annulus	d_{AP}	38 mm	22 mm
	d_{CW}	40 mm	28.5 mm
	h_{AH}	5 mm	6.1 mm
	-	D-shape (no ring concavity)	Slight ring concavity
Leaflets	A_h	30 mm	22 mm
	P_{mh}	21 mm	12 mm
	P_{ch}	12 mm	8 mm
	A_a	1200 mm ²	540 mm ²
	P_a	1200 mm ²	465 mm ²
PM	ALPM ₀	34.5 mm	27 mm
	ALPM ₁₀	27 mm	23.5 mm
	ALPM ₈	30 mm	20 mm
	PMPM ₀	34.5 mm	33.6 mm
	PMPM ₂	30 mm	29 mm
	PMPM ₄	27 mm	25 mm

Valve closure dynamics

Both patient-specific models were associated with incomplete coaptation as displayed in Figure 5.22a. The PS1 valve had a middle peak systolic coaptation length of 3.414 mm, within normal ranges (Gogoladze *et al.*, 2010), but was associated with two regurgitant areas near the paracommissures (circled on Figure 5.22). PMPM displacement led to poor coaptation in the PS2 valve represented by a much smaller peak systolic coaptation length (1.463 mm) and one regurgitant area near the closest paracommissure (circled on the figure). While the PS2 valve did not present leaflet prolapse, the PS1 valve had excessive displacement of the AL and PL (Figure 5.22b), with both leaflets bulging towards the left atrium, leading to a PL billowing height of 1.325 mm. These results reveal the importance of a healthy MV geometry for its physiological performance, demonstrating an intrinsic connection between alterations of the MV shape and the resulting coaptation length obtained during valve closure. Indeed, a previous computational study of the MV determined that annular dilation was associated with incomplete coaptation (Kunzelman *et al.*, 1997) and an *in vitro* representation of PM displacement led to uneven coaptation and the generation of coaptation gaps (He *et al.*, 2003).

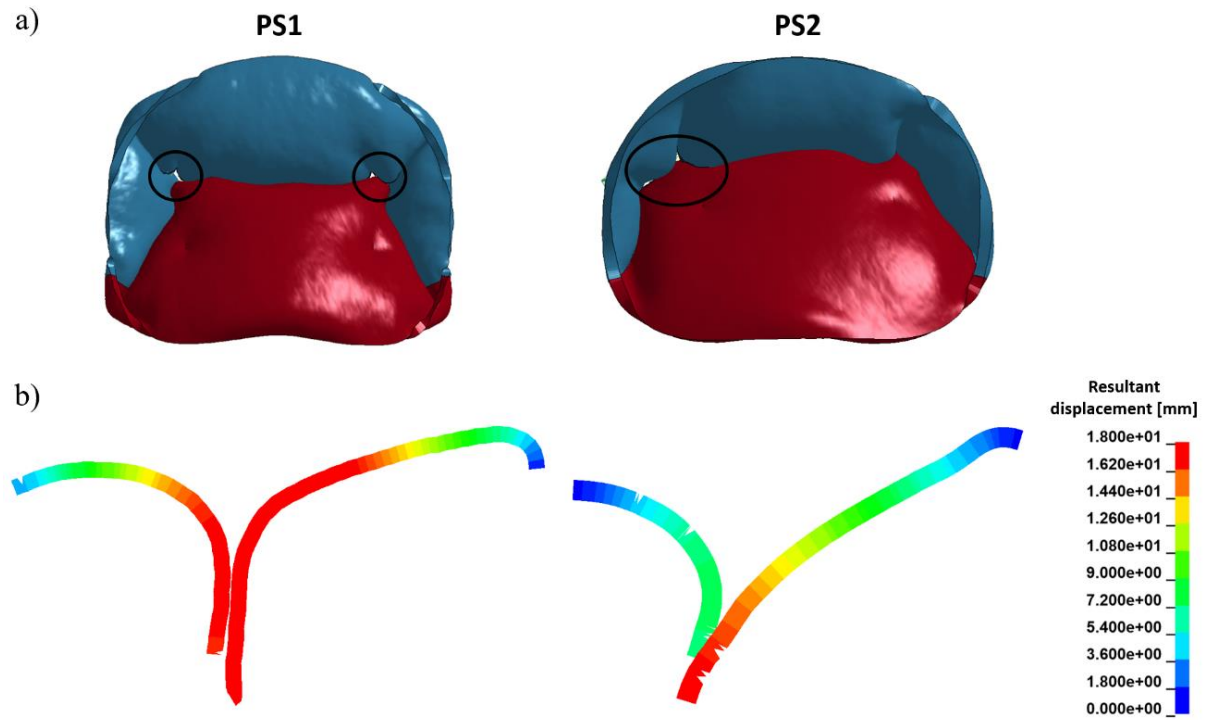


Figure 5.22: MV peak systolic closure for patient-specific shapes PS1 and PS2, (a) showcasing regurgitant areas and (b) displaying the middle coaptation cross-sectional profile and resultant displacement.

Leaflet stresses

While the maximum stress values in the healthy geometry were located near the anterior saddle horn and followed the circumferential direction (Figure 5.16), the diseased configurations presented in Figure 5.23 were associated with larger peak systolic stress distributions across the AL, spreading along the radial direction (Rim *et al.*, 2014; Stevanella *et al.*, 2011). The highest stresses were located in the AL, near the trigones and all over the belly. The PS1 valve generated a wide range of elevated stresses over the AL and middle PL scallop, associated with maximum cross-sectional stress values of 0.34 and 0.25 MPa, respectively. These represent relative increases of 23 and 54 % from the healthy model. The PS2 valve, on the other hand, had its highest stress concentration radiating from the right trigone, opposite to the displaced PM. The maximum cross-sectional stress from C3 (ALPM side) reached 0.62 MPa, equivalent to an 84

% increase from the healthy model. The PL did not present with a wide range of large stress distribution; regardless, the maximum cross-sectional value at the middle PL scallop had a 28 % increase from the one obtained for the healthy model.

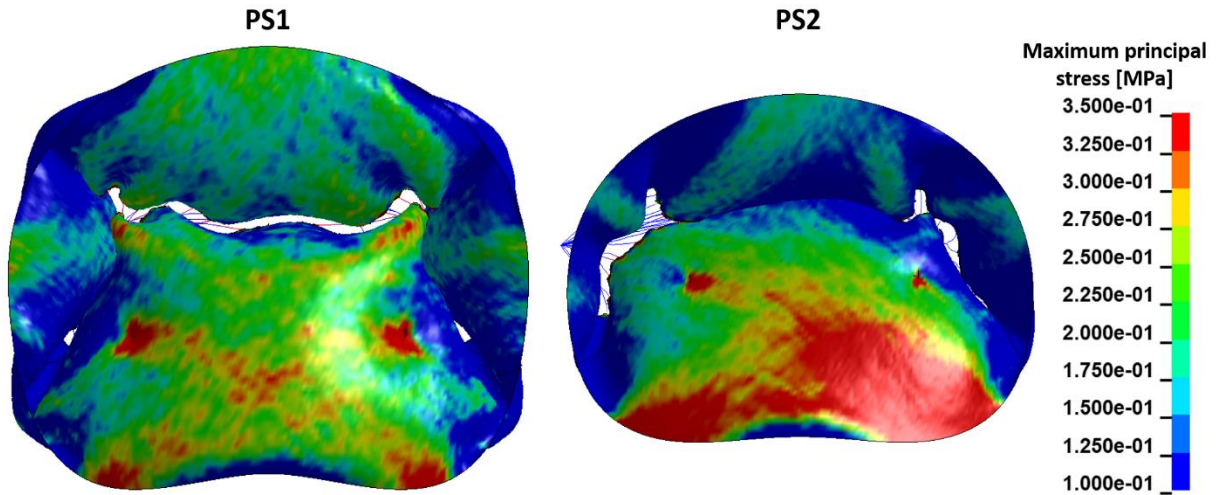


Figure 5.23: Leaflet stress distributions at peak systole for the simulated patient-specific geometries incorporating annular flattening and leaflet enlargement (PS1) and PMPM displacement due to LV dilation PS2).

Papillary muscles and chordae forces

Forces acting on the PMs differed between patient-specific scenarios (Figure 5.24). The PS1 valve yielded much higher PM reaction forces in comparison with the healthy model, with systolic peak values of 7.09 and 6.76 N on the PMPM and ALPM, respectively (+108 % and +98 % in comparison with the equivalent healthy values). These values are consistent with *in vitro* measurements obtained for pathological cases, associated with flow leakage and decreased chordae compliance (Jensen *et al.*, 2001). This is reflected on all tethering chordal forces predicted, which greatly increased in comparison with the healthy model (Table 5.12 vs Table 5.9). Moreover, and as observed in Figure 5.24, the PM reaction forces were associated with enhanced oscillations over time in comparison with the healthy model. Such a feature has been identified in a previous computational study concerning a regurgitant MV (Stevanella *et al.*,

2011) and can be due to the imbalance between tethering and closing forces in the presence of a diseased shape. In the PS2 valve, the chordal and PM force balance was disrupted. The displaced PMPM had a reaction force of 4.76 N (+ 40 % from the healthy model), a value associated with apical PM displacement in pathological MVs (Jensen *et al.*, 2001), while the force acting on the ALPM (2.44 N) decreased 28 % in relation to the healthy model. ALPM chordal tensions reflect this low PM reaction force, with all tensions decreasing relative to the healthy model. Such a low PM force can be associate with MV incapability to sustain physiological pressure, since PM forces below 2.5 N have been correlated with transmitral pressure near 80 mmHg (Jensen *et al.*, 2001), 2/3 of the normal peak systolic pressure.

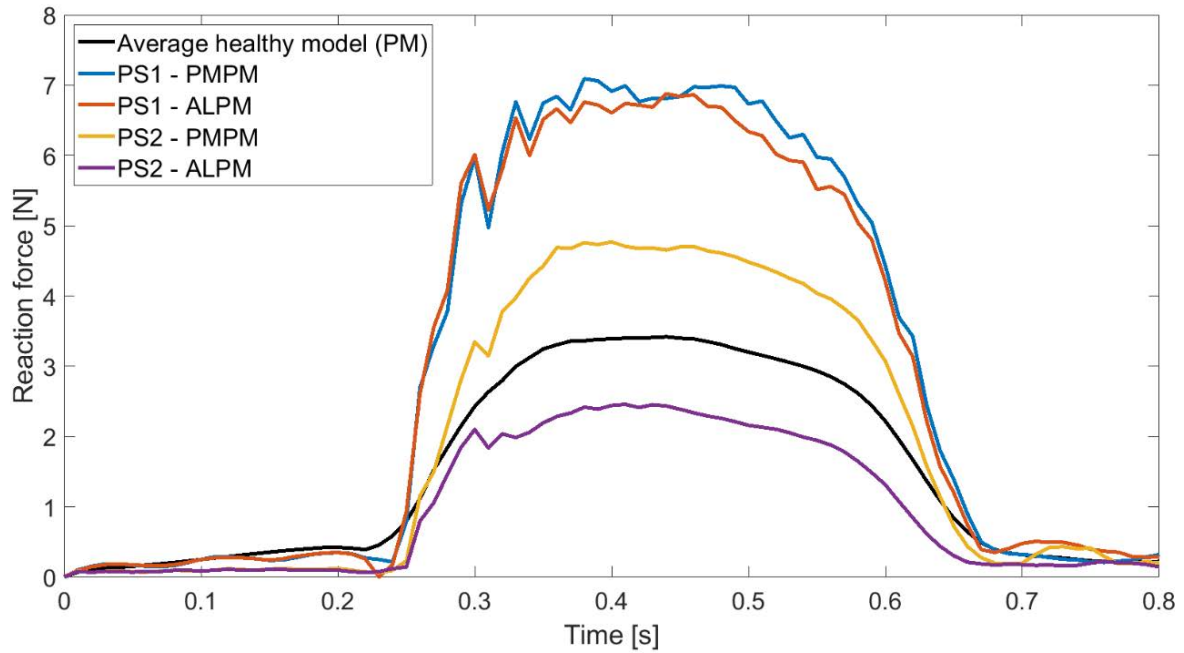


Figure 5.24: Time-dependent PM reaction forces for PS1 and PS2 valves in comparison with the prediction for the average healthy model. While the PM reaction forces for the PS1 valve are increased in comparison with the healthy model, the PS2 valve demonstrates an imbalance of PM forces, caused by PMPM displacement.

Table 5.12: Chordae tendineae tension and load proportion at peak systole for patient-specific cases.

PM		PS1		PS2	
	Chordae	Load [N]	Load proportion [%]	Load [N]	Load proportion [%]
PMPM	AL strut	1.12	21.1	0.69	13.8
	AL marginal	0.336 ± 0.174	31.7	0.392 ± 0.156	47.3
	PL marginal	0.314 ± 0.148	47.3	0.242 ± 0.124	28.9
ALPM	AL strut	0.971	17.5	0.47	19.3
	AL marginal	0.417 ± 0.243	37.7	0.108 ± 0.062	22.1
	PL marginal	0.354 ± 0.203	44.8	0.179 ± 0.104	58.6

5.4. Discussion

5.4.1. Overview and main findings

This chapter presents the automatic pre-processing of the MV available within the MV toolbox (Chapter 4), including the steps to obtain the final FE model set-up, to be run using LS-DYNA. The pre-processing of the model is completed using minutes of computational time, and the tool has the potential to assess MV function associated with a variety of geometries and can be further developed to include surgical techniques, crucial for virtual surgical planning. This study yielded the following findings:

- ❖ The average, healthy MV model has been validated against the literature, with computational predictions for valve dynamics, stress distributions, and PM and chordae tendineae forces being consistent with previous computational and experimental studies;
- ❖ The implementation of orthotropic material properties for the leaflet leads to appropriate trends in terms of circumferential and radial strain distributions. However, a leaflet anisotropic material response with fiber orientation representation (hyperelastic model) leads to more accurate circumferential and radial stretch values and distribution on mitral leaflets;

- ❖ Different annular BC lead to varying MV physiological behaviour, with a fixed annulus generating poor leaflet coaptation, excessive displacement of the PL towards the left atrium and increased stress distributions on the AL in comparison with a model with appropriate annular displacement;
- ❖ The use of 3D PM shape led to changes in chordal tension and proportions of load bore by each chordal group, with strut chordae bearing less load and marginal chordae bearing more load in comparison with a single PM tip model;
- ❖ The toolbox can successfully generate patient-specific MV geometries and pre-process those for FE simulations, as shown by the creation and analysis of two models associated with different diseased scenarios. Patient-specific diseased models were associated with incomplete leaflet coaptation (appearance of regurgitant areas), abnormally increased leaflet stresses, and unbalanced PM and chordae tendineae forces.

5.4.2. MV predicted biomechanics is sensitive to boundary conditions and material responses

The sensitivity analysis described in section 5.3.4 showed that leaflet coaptation and MV systolic shape was greatly affected by the choice of annular BC. Specifically, a fixed annulus led to poor leaflet coaptation associated with a small coaptation length and excessive displacement of the PL towards the left atrium, conditions associated with the onset of disease (Gogoladze *et al.*, 2010; Lee *et al.*, 2013). This further confirms the importance of using appropriate BC to represent physiological annular contraction and PM displacement during the cardiac cycle (Mansi *et al.*, 2012; Stevanella *et al.*, 2009). However, the absence of annular and PM motion did not greatly affect chordae tensions and PM reaction forces when compared to a model including all boundary conditions. This was expected, since the forces acting on the PM

and chordae are mainly determined by transmitral pressure and are expected to act as balancing quantities (Jimenez *et al.*, 2003; Stevanella *et al.*, 2009).

Employing a 3D PM representation instead of a single point greatly changed chordal tensions, decreasing the load carried by strut chordae and increasing the one bore by AL and PL marginal chordae, still within the ranges obtained *in vitro* for normal valves (Jimenez *et al.*, 2003). The reduction in strut chordae tension may be explained by a redistribution of the force vectors caused by the 3D distribution of insertion points into the PM, dividing the total load more evenly amongst all chordae. To balance the new force components generated, The AL and PL marginal chordae then balance the newly generated force components, possibly explaining the increase in load in these chords (Jimenez *et al.*, 2003; Jimenez *et al.*, 2005).

Both orthotropic and hyperelastic material models led to an appropriate leaflet response in terms of circumferential and radial strain distributions and values. However, the hyperelastic material implementation (also see section 5.3.4) led to more accurate stretches in the AL and PL, with peak values generally lower than *ex vivo* measurements (He *et al.*, 2005; Sacks *et al.*, 2002) and computational studies (Stevanella *et al.*, 2009; Stevanella *et al.*, 2011; Kunzelman *et al.*, 2007; Rego *et al.*, 2018), but comparable to those obtained *in vivo* (Rausch *et al.*, 2011).

A number of issues were associated with the hyperelastic material model implemented. In addition to an increase in the simulation computing time in comparison with the orthotropic material, abnormal shell deformations were present near the free edge of the leaflets, usually localised near chordal insertions and occurring at the onset of closure. This prevented the successful completion of computational simulations, perhaps due to the hyperelastic material being implemented at the local element level and depending on the quality of its shape. Increased leaflet mesh distortion near chordal insertions were minimised with the implement simulation controls mentioned in section 5.2.4, but not completely eliminated. Different

layered-shell approaches were implemented (e.g. using a unified composite definition in LS-DYNA instead of overlapping shell elements) and lower transvalvular pressures were also applied in an attempt to overcome this issue. In reality, numerical instabilities were only avoided when hyperelastic material coefficients were modified, leading to a stiffer leaflet response. This yielded higher circumferential and radial Cauchy stresses than those obtained with a square sample of tissue and represented in Figure 5.6.

The application of leaflet pre-strain and chordae pre-tension could possibly reduce the numerical instabilities observed in this case. Given that the mitral leaflets are exposed to pre-strain throughout the cardiac cycle, their constitutive response *in silico* greatly depends on the application of pre-strain (Rausch *et al.*, 2013; Rausch and Kuhl, 2013), which contributes towards peak systolic MV physiological behaviour and positioning (Prot and Skallerud, 2017). This means that higher strains than those actually computed during diastole would be expected, influencing the associated Cauchy stress predicted and the overall behaviour of the MV on the onset of leaflet closure. However, pre-tension forces in the chordae may also play a role in improving models representing MV deformation (Aguilera *et al.*, 2021). Previous studies show that chordae pre-tension is required to reproduce appropriate MV closure (Pham *et al.*, 2017; Drach *et al.*, 2018). The use of chordae pre-tension could then help minimize the abnormal shell deformations observed near chordal insertions, leading to successful replication of MV closure. Regardless, leaflet pre-strains and chordae pre-tensions are difficult to estimate *in vivo* for human MVs (Aguilera *et al.*, 2021), due to either the current limitations in medical imaging resolution (Pham *et al.*, 2017) or the use of procedures which are not applicable to clinical settings (Drach *et al.*, 2018).

Other leaflet material models have been employed in previous computational studies (Votta *et al.*, 2013). Orthotropic material properties (Mansi *et al.*, 2012; Zhang *et al.*, 2017) and isotropic

mass-spring models (Hammer *et al.*, 2008; Tenenholtz *et al.*, 2013) have been used in integrated frameworks for patient-specific MV modelling and surgical planning. In fact, previous *in vivo* animal studies focusing on inverse-problem methods found that circumferential and radial stress-strain curves are linear within the physiological pressure range (Krishnamurthy *et al.*, 2008; Krishnamurthy *et al.*, 2009). Given this, the orthotropic material response has been implemented in the toolbox and pre-processing described in this chapter. This implementation allows the FE simulations to be completed faster than with the use of a hyperelastic material (one hour vs six hours of computing time to reach peak closure of the model). This is crucial for the clinical timescales associated with the predictive end-goal of the tool, which is to simulate and compare MV biomechanics for a variety of geometries, as well as potential repair strategies.

5.4.3. Potential applications

To showcase the potential applications of the toolbox, two patient-specific MV models including different geometries associated with disease have been solved and their biomechanics analysed. Both models had incomplete coaptation associated with areas of regurgitation, elevated stress on the leaflets and unbalanced PM and chordae forces. These features are in agreement with previous *in vitro* (Taylor *et al.*, 2021) and *in vivo* (Grinberg *et al.*, 2019) studies, which mention that MV competence is compromised by geometrical alterations such as annular dilation and increased tension on the chordae.

The MV toolbox has several end-user applications. From a clinical perspective, and given its flexibility, it can be used to study the influence of morphological MV parameters on its function. The average MV shape generated assumes a healthy valve, and degenerative valve disease, for instance, leads to significant alteration in mitral valve proportions (Deorsola and

Bellone, 2019). However, inputted patient-specific parameters can be used to create a range of diseased scenarios, such as: varying annular diameters to represent different cases of annular dilation (Kim *et al.*, 2019; Lee *et al.*, 2013), which can compromise leaflet coaptation (Ito *et al.*, 2017); incorporating PM displacement, which is well correlated with increased regurgitant volume in patients with functional ischemic mitral regurgitation (Obase *et al.*, 2016; Ito *et al.*, 2017); or increasing leaflet surface area to represent myxomatous degeneration of the MV (Clavel *et al.*, 2015). Moreover, clinicians can use the toolbox to virtually evaluate current and novel mitral interventions, such as the use of extension biological patches to restore leaflet dimensions in the case of posterior leaflet congenital hypoplasia (Parato and Masia, 2018), or papillary muscle approximation as an adjunctive technique for MV regurgitation (Mihos *et al.*, 2017). The toolbox can be further edited to allow for the inclusion of medical devices (such as annuloplasty rings (Kong *et al.*, 2018)) and virtually assess their performance and influence on the biomechanics of the MV using a range of MV models through computational simulations. Ultimately, this could aid with the design optimisation and customisation of new devices.

5.5. Summary

In this chapter, the automatic pre-processing for the MV model has been described, with the implemented options validated against the literature by generating and solving a healthy MV model. Moreover, the influence of BC and PM shape, as well as choice of material constitutive models, has been assessed through a sensitivity analysis. Finally, two patient-specific MV geometries have been generated and the associated FE model solved to showcase the capabilities of the toolbox. The whole tool offers, for the first time, a flexibility in MV shape creation and automatic biomechanical evaluation, compatible with clinical timescales. In particular, this framework can be used to assess geometrical features impacting MV closure,

including leaflet coaptation profiles and coaptation lengths, and investigate how they affect leaflet stress distributions and subvalvular forces. These computational predictions can also assist clinicians determining whether a patient-specific MV geometry needs intervention, as well as improve clinical decision making by estimating the biomechanics associated with varying surgical procedures.

CHAPTER 6

COMPUTATIONAL FLUID DYNAMICS OF THE RIGHT ATRIUM: ASSESSMENT OF MODELLING CRITERIA FOR THE EVALUATION OF DIALYSIS CATHETERS

6.1. Introduction

Central venous catheters are biomedical devices widely employed in haemodialysis therapy (Chapter 2, section 2.8.3), with the catheter design chosen depending on the indication for insertion and the predicted duration of use (Smith and Nolan, 2013). These catheters can be used for short-term therapy (typically less than 21 days) or for permanent access. Temporary catheters are smaller in size in comparison with permanent catheters and can have up to three separate lumens (useful for the administration of fluids or antibiotics, for example), while permanent designs are only available with two lumens. Their placement within the human body also varies: while temporary catheters are placed directly into the vein of interest, permanent catheters possess a cuff which is tunnelled under the skin and away from the vein puncture site (Bream, 2016). Different catheter tip designs with a variety of features are currently available on the market and determining the best design is an ongoing challenge.

To assess catheter performance and give insight into how to optimise their design, both *in vitro* (Foust, 2004; Vesely and Ravenscroft, 2016) and *in silico* (Clark *et al.*, 2012; Clark *et al.*, 2015; Mareels *et al.*, 2007) studies have been performed. *In vitro* studies have used RA models to evaluate catheter performance. An idealized RA model was developed in one study with an *in*

vitro set up built for this purpose (Foust, 2004) and an *in vitro* simulator of the RA was employed to study the movement and recirculation associated with different catheter designs (Vesely and Ravenscroft, 2016). *In silico* studies have used CFD to study blood flow patterns associated with different catheter designs, as well as evaluating recirculation and thrombosis. Such studies have included a comparison of symmetric catheters (Clark *et al.*, 2015; Owen *et al.*, 2020a), the preclinical assessment of novel designs (Clark *et al.*, 2012) and the evaluation of different tip hole shapes (Mareels *et al.*, 2007); however, none included the use of a geometry representing the RA. The use of a realistic RA computational model for evaluation of catheter performance is, therefore, a current need, since it allows for: (1) A more accurate representation of the *in vivo* behaviour experienced by dialysis catheters due to the surrounding physiological flow patterns; (2) A less costly and faster prediction of the subsequent haemodynamics without the need for an *in vitro* test setup.

The aim of this chapter was to develop a physiological CFD model of the RA which enables the assessment of the performance of dialysis catheter designs. This model was used to evaluate the performance of four different catheter designs: one split tip, one symmetric tip and two step tips (with and without the presence of side-holes).

In this chapter, the development of a RA CFD model, along with validation against data in the literature, is presented (Figure 6.1). Transient physiological boundary conditions were chosen and CFD simulations were performed using ANSYS Fluent v.18.2 (Ansys Inc., Canonsburg, PA, USA). Mesh and time-convergence analyses were performed to validate the numerical approach and metrics such as blood velocity, flow rates, vorticity and pressure were compared against the literature. Four catheter geometries were then placed within the RA following medical guidelines and appropriate boundary conditions were employed. Different catheter tip placements were also used to study the impact of changing tip position on catheter performance.

Qualitative and quantitative comparisons were made between catheter designs and metrics such as flow recirculation and tip shear stress were used to evaluate their performance within the RA haemodynamic environment. These results were compared to previous clinical, *in vitro* and computational studies.

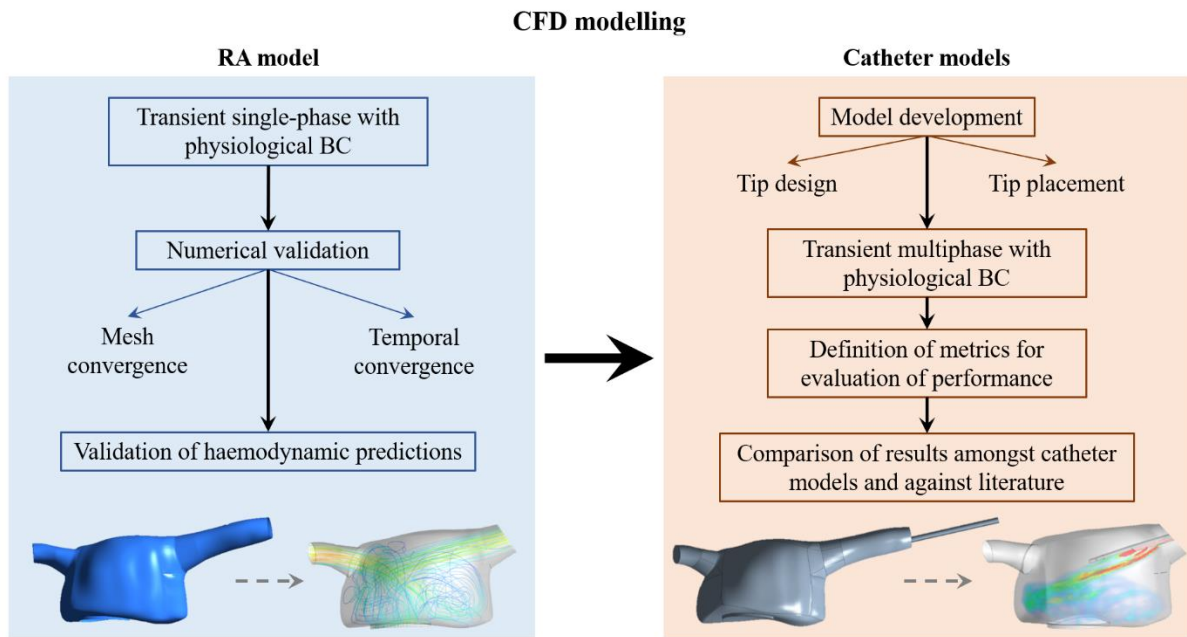


Figure 6.1: Outline of this chapter. CFD modelling was performed, first with the RA model, then with catheter models virtually placed in the RA. The RA model was validated (1) through a numerical approach, and (2) by comparing its haemodynamic predictions with the literature. After validation, the catheter models were developed, considering four different tip designs and diverse placements within the RA. Appropriate conditions were chosen for the model and relevant metrics were defined to evaluate tip performance. Lastly, the obtained results were compared amongst catheters and against literature.

6.2. Right atrium and dialysis catheter models

The 3D RA geometry (in Computer Aided Design - CAD - format) was obtained from a healthy human heart model available online and built from data in the literature (<https://grabcad.com/library/the-human-heart-1>). Pre-processing of the geometry was performed using ANSYS SpaceClaim v.18.2 (Ansys Inc., Canonsburg, PA, USA). The model

was firstly truncated at the SVC, IVC (inlets) and tricuspid valve (TV) (outlet). Then, the model had multiple geometrical flaws which needed fixing before it could be used during the remaining modelling set-up. To repair the model's surfaces, face and edge repair tools from ANSYS SpaceClaim were employed. Finally, the geometry was re-scaled to match IVC and SVC physiological mean literature diameters. Final diameters for the IVC and SVC were 16.89 mm (*in vivo* range: 16.9 ± 3.7 mm (Patil *et al.*, 2016)) and 17.06 mm (*in vivo* range: 21 ± 7 mm (Mahlon and Yoon, 2007)), respectively, and the area of the TV was 9.95 cm^2 (*in vivo* range: $9.72 \pm 2.08 \text{ cm}^2$ (Ton-Nu *et al.*, 2006)). The final RA geometry is presented in Figure 6.2.

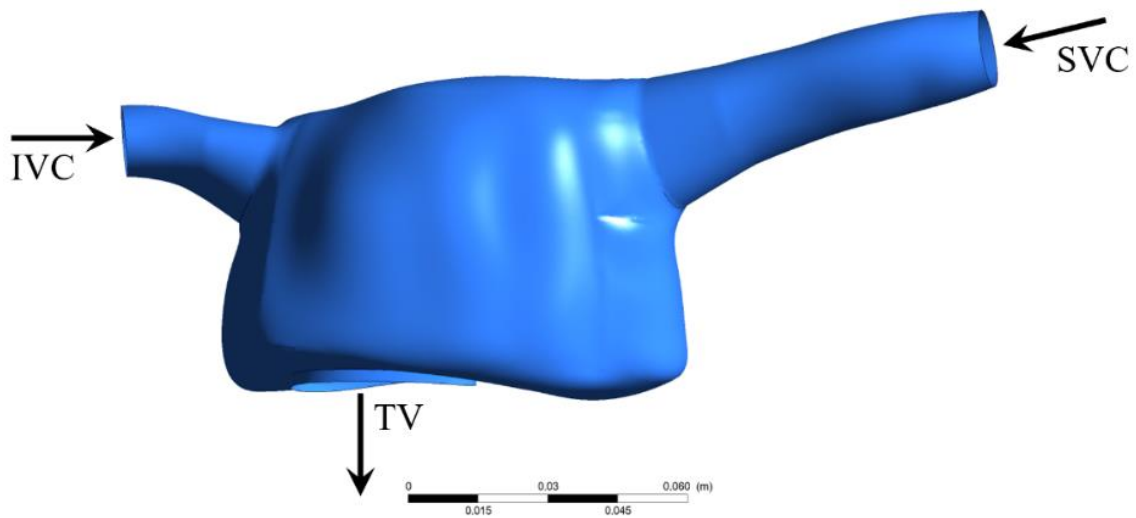


Figure 6.2: RA computational domain. Notes: IVC, inferior vena cava; SVC, superior vena cava; TV, tricuspid valve.

.CAD files representing the geometries of the four catheter designs were supplied by KIMAL Plc (Bromsgrove, Worcestershire, UK). The four designs were named A, B, C and D: catheters A and B possess a step tip with and without side-holes, respectively; catheter C has a split tip and catheter D has a symmetric tip, both without side holes. The main dimensions

characterising all designs are presented in Table 6.1 and the respective geometries are shown in Figure 6.3.

Table 6.1: Catheter dimensions. Notes: Fr, French gauge (1 Fr = 0.33 mm).

Catheter name	Tip length [mm]	Outer diameter [Fr]	Lumen area [mm ²]
A	290	15.5	7.8
B	290	15.5	7.8
C	152	15	3.5
D	240	16	7.8

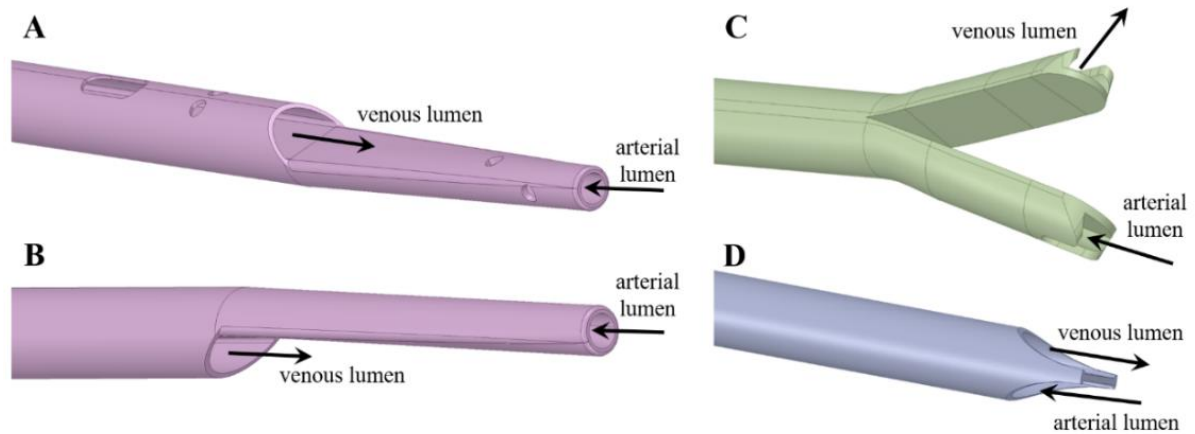


Figure 6.3: Catheter tip designs A, B, C and D, with arterial and venous lumens indicated. Note: Catheters A and B were set in reverse mode (for C and D designs, forward and reverse mode lead to the same model configuration).

All catheter designs were virtually placed within the RA geometry using ANSYS SpaceClaim: they were inserted through the SVC, with their entire functional part inside the RA and their venous tip placed well past the SVC in the central region of the RA, according to clinical guidelines (Tawk *et al.*, 2018). For each created model, the catheter structure was removed and a unified volume including the fluid within the RA and the fluid within the catheter was used for subsequent CFD simulations. An example of a unified model can be seen in Figure 6.4, including boundary conditions applied (further described in section 6.3.1).

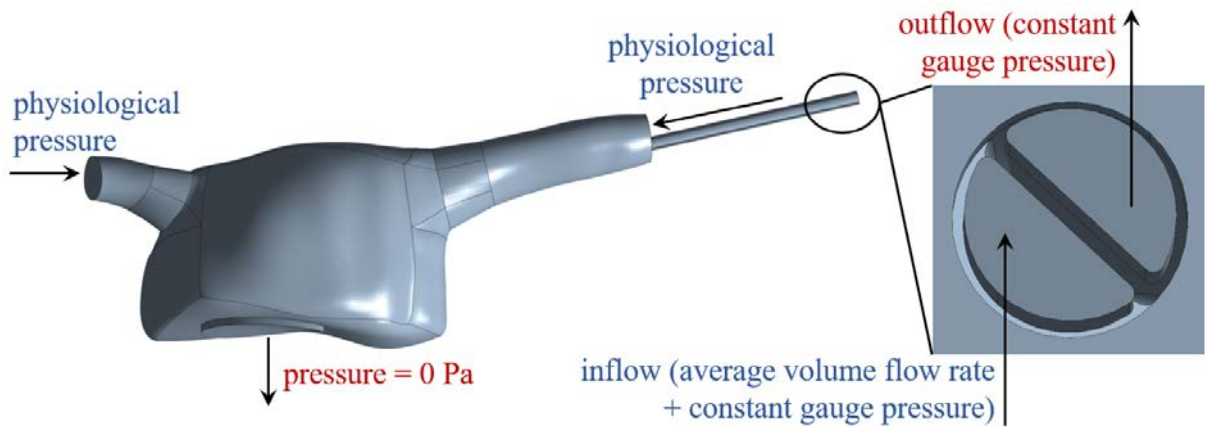


Figure 6.4: RA computational domain with example catheter inserted and set of boundary conditions defined.

6.3. CFD models

Diverse catheter placement options were considered to assess their impact on performance. More specifically, catheters A and D were virtually inserted in three and two different positions within the RA, respectively. According to this, a total of 8 computational models (including the RA model) were created, as outlined in Figure 6.5.

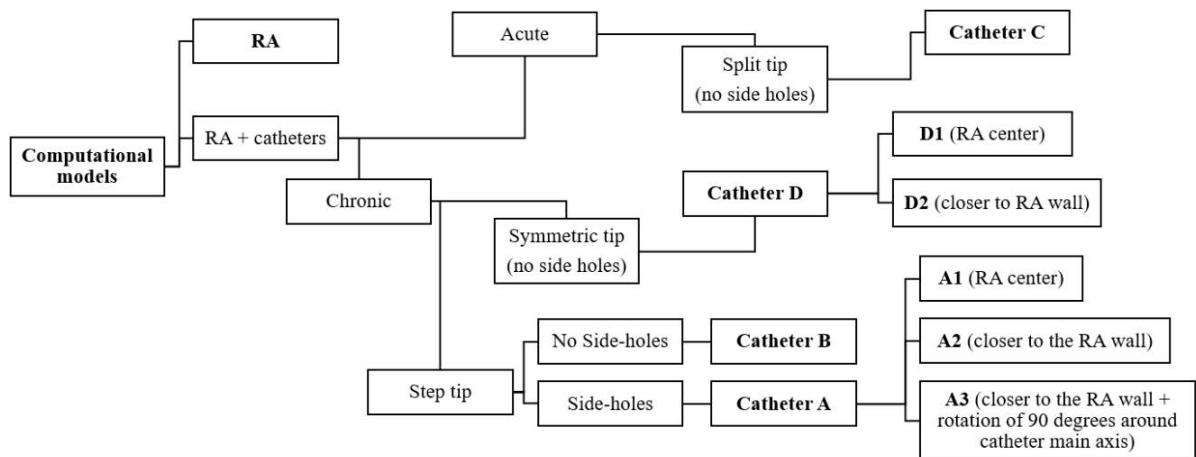


Figure 6.5: Diagrammatic overview of all computational models developed (with names written in bold). Acute refers to temporary catheter placement and chronic to permanent catheter placement, this is of relevance to the clinical use of the catheters.

6.3.1. Boundary conditions

Right atrium model

Multiple boundary conditions were tested on the RA CFD model to obtain the most physiological behaviour possible. Velocities, pressure, and flow behaviour were continuously compared against *in vivo* and *in vitro* data from the literature. Finally, and to accurately represent the pulsatile behaviour of blood flow, a time-dependent physiological pressure two-dimensional waveform was applied at the SVC and IVC inlets (Figure 6.6) (Cohen *et al.*, 1986), modelled as a spatially uniform profile. This waveform corresponds to a cardiac cycle period of 0.8 s, with diastole and systole lasting for 0.5 s and 0.3 s, respectively.

As for modelling TV function, several boundary conditions were, again, tested. Similarly to a previous study by Mareels *et al.* (2004) (Mareels *et al.*, 2004), an outflow condition (all flow reaching the boundary exits it) was attempted, but the resulting RA flow velocities were greater than the expected range. A target mass flow rate was also imposed with a constant pressure, but this yielded elevated flow velocities, as well as the loss of vortex within the chamber. Flow rate waveforms for the TV are scarce in the literature, and a study bringing together all needed conditions for the RA model (SVC, IVC and TV) is currently not available. The TV outlet was, therefore, set to a constant gauge pressure of 0 Pa, meaning that the action of the valve was not modelled and blood flow was still allowed to exit the RA during systole (when the TV is closed). Nonetheless, with this condition, physiological flow velocity results and flow patterns were predicted by the model, comparable to the literature (section 6.5.1).

The right atrial wall boundaries were assumed rigid and a no-slip condition was employed at the wall-blood interface.

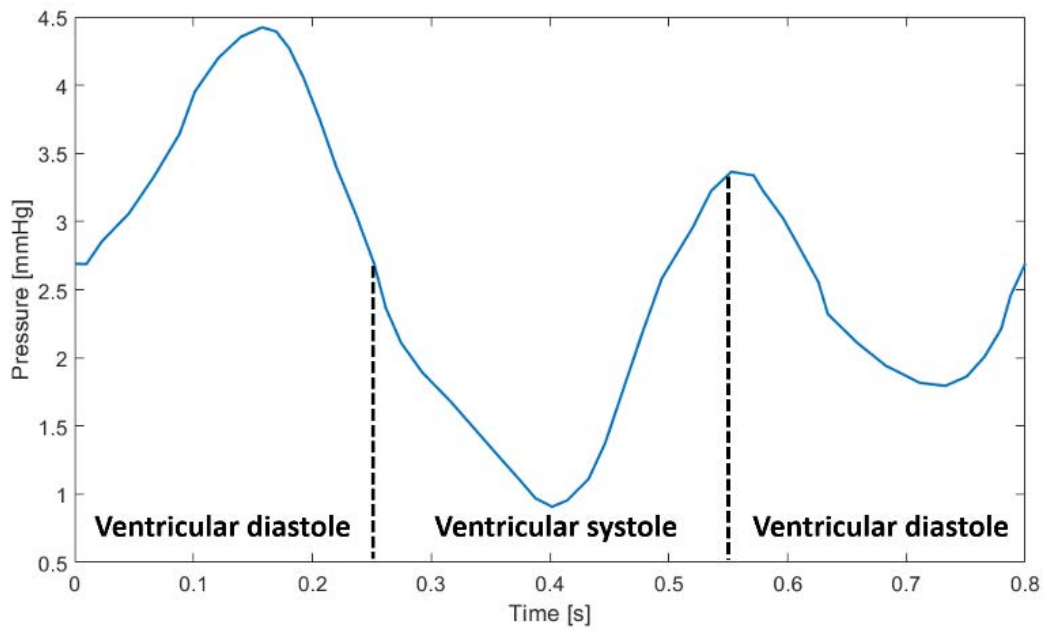


Figure 6.6: Time-dependent pressure, with diastolic and systolic periods represented, imposed at the inlets (adapted from Cohen et al. 1986).

Catheter models

All boundary conditions applied on the RA model were kept for the models with catheters inserted. The venous and arterial lumens of each catheter (represented in Figure 6.3) correspond to the placement of inlet and outlet boundary conditions, respectively. For catheters A and B, instead of employing the standard flow mode, a reverse mode (switch in venous and arterial lumens) was selected, usually associated with worse performance than the standard mode. An average volume flow rate of 400 ml/min, together with a constant gauge pressure of 248 mmHg, were applied at each catheter inlet (Depner, 2001). To yield a flow rate within the clinical range (Depner, 2001), different gauge pressures were applied at each catheter outlet (Table 6.2).

Table 6.2: Gauge pressure values applied at catheter outlets and respective flow rates achieved.

	A	B	C	D
Pressure [mmHg]	-250	-250	-250	-188
Flow rate [ml/min]	350	380	360	370

6.3.2. Flow governing equations and material properties

Blood haemodynamics have been shown to be affected by the use of non-Newtonian models (Owen *et al.*, 2020b; Carty *et al.*, 2016). To determine the fluid model to be employed, a comparison between the Newtonian and non-Newtonian Bird-Carreau models was performed using the RA model. While the Newtonian model assumes a constant viscosity, the Bird-Carreau model uses a polynomial shear thinning definition (Table 6.3). A blood density of 1060 kg/m³ was used for both rheological models.

Table 6.3: Rheological model definitions and parameters (adapted from Cho *et al.* 1991 and Johnston *et al.* 2004).

Blood model	Viscosity definition [Pa s]	Coefficient definitions	Parameters
Newtonian	$\mu = 0.004$	where μ is the blood viscosity, μ_∞ is the high shear viscosity, μ_0 is the low shear viscosity, λ is the time constant, $\dot{\gamma}$ is the shear rate and n is the Power law index	-
Bird-Carreau	$\mu = \mu_\infty + (\mu_0 - \mu_\infty)[1 + (\lambda\dot{\gamma})^2]^{(n-1)/2}$		$\mu_\infty = 0.00345$, $\mu_0 = 0.056$ $\lambda = 3.313$, $n = 0.3568$

Vorticity and wall shear stress (WSS) magnitudes were assessed over the simulation of one cardiac cycle and volume-averaged vorticity and area-averaged WSS time-dependent profiles were obtained (Figure 6.7). While the differences between the predictions yielded by both models are subtle for area-averaged WSS, these accentuate for volume-averaged vorticity. In fact, the maximum relative errors are 5.28 and 8.97 % for WSS and vorticity quantities, respectively. Therefore, to account for non-Newtonian flow effects, the Bird-Carreau model was used for the CFD simulations.

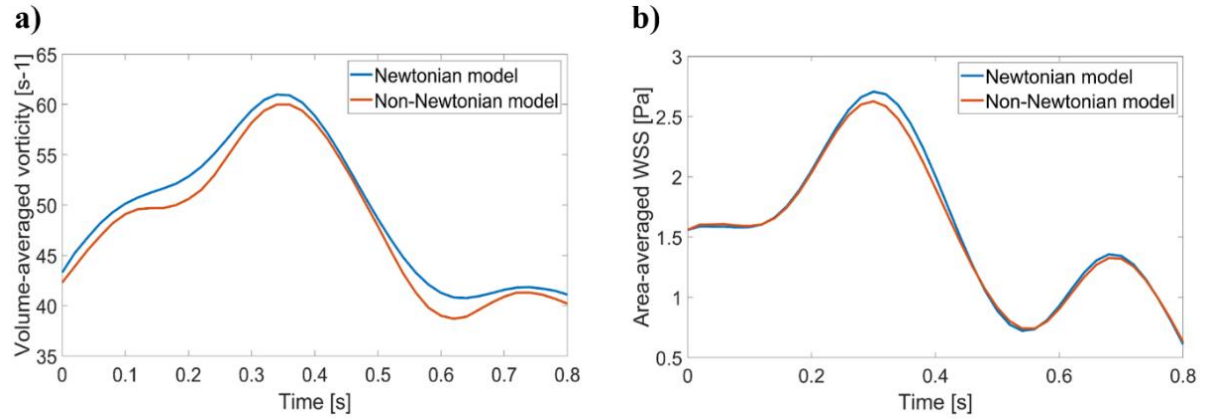


Figure 6.7: Time-dependent vorticity and WSS profiles, predicted with Newtonian and Non-Newtonian blood models.

The Reynolds number (Re) was evaluated for each boundary of the RA model (SVC, IVC and TV). This was obtained from the equation for a haemodynamic chamber (Valen-Sendstad *et al.*, 2011) and defined as:

$$Re = \frac{\rho \mathbf{U} D}{\mu}, \quad (6.1)$$

where ρ is the blood density, \mathbf{U} and μ are the velocity magnitude and viscosity at each boundary, and D is the diameter of the corresponding boundary. Averaged Reynolds numbers have been determined based on time and space-averaged values of \mathbf{U} and μ over each boundary, while the minimum and maximum Reynolds values were computed for a time-varying Reynolds number obtained using the averaged \mathbf{U} and μ over each boundary (Table 6.4). Since $Re \ll 2300$, flow was assumed to be laminar (Valen-Sendstad *et al.*, 2011).

Table 6.4: Reynolds number study performed for the RA model.

Boundary	Minimum Reynolds	Average Reynolds	Maximum Reynolds
SVC	837	1120	1270
IVC	684	1170	1400
TV	760	1140	1390

6.3.3. Computational settings

Implementation and solving of CFD simulations were performed with the commercial finite-volume ANSYS Fluent 18.2 (Ansys Inc., Canonsburg, PA, USA) under transient conditions. The RA model was solved using a fluid single-phase approach, governed by the continuity and incompressible Navier-Stokes equations without the effect of external body forces (Parker and Thiriet, 2009). A Eulerian-Eulerian multiphase model was implemented for all catheter models to monitor and quantify the blood entering the RA through each catheter from the remaining volume of fluid. More details on the multiphase flow equations can be found in Appendix E and the respective options chosen are summarized in Table 6.5.

Table 6.5: CFD set-up.

Type	Choice	Description
Solver for continuity equation	SIMPLE (ANSYS, 2017)	Coupled pressure-velocity with segregated approach Second order upwind momentum
Solver for pressure discretization	PRESTO!	
Transient solving	First order implicit	Iterative time step solving
Multiphase settings	Two Eulerian phases with equal material properties	<u>Primary phase</u> – fluid entering/exiting all boundaries except catheter inlet (unfiltered blood) <u>Recirculation phase</u> – fluid entering catheter inlet (filtered blood)
Multiphase volume fraction (ANSYS, 2017)	Explicit formulation Sharp/dispersed interface Implicit body force	
Time stepping	Single phase: 0.005 s Multiphase: 0.001 s	
Convergence criteria	Residual error $< 10^{-4}$	Residual errors for continuity and x-, y-, z- velocities

Meshing

Tetrahedral elements were used to mesh all geometries and mesh refinement was employed within the catheter volumes. Five boundary layers using a structured hexahedral mesh were created in the fluid near the right atrial wall. Mesh size was evaluated through (1) quality assessment and (2) convergence tests. The mesh convergence analysis was performed by

running one cardiac cycle with the set ups previously described, and using the RA model and a unified model of the RA and catheter D. For the RA model, mesh refinement was achieved by progressively decreasing general tetrahedral element size. After completing the convergence study for the RA model, local refinement within the catheter lumen was performed for the catheter model while keeping a constant average element size for the RA.

The velocity magnitude at a probe located at the centre of the RA and the surface averaged WSS were obtained for the RA model. Similarly, a probe was placed inside the catheter lumen in the catheter model, to capture the local velocity magnitude. The relative error between values obtained under increasing mesh density and the solution obtained when using the finest mesh was then evaluated (Figure 6.8). The relative error between the solution from each cycle and the one from the last cycle was computed using equation 6.2:

$$E = \left| \frac{v_B - v_L}{v_L} \right| \cdot 100 \%, \quad (6.2)$$

where v_B and v_L are the calculated variables for each mesh and for the finest mesh, respectively.

Given the complex flow patterns developing inside the RA, we assumed a relative error below 0.5 % as acceptable for the average WSS and below 3 % for the local probe velocity. These criteria were achieved with a mesh of 1 million elements for the RA model. Moreover, and to reduce computational time, a relative error below 5 % was deemed acceptable for the catheter model, which was associated with a mesh of more than 3 million elements. Models with a mesh density respecting these constraints were chosen for each simulation.

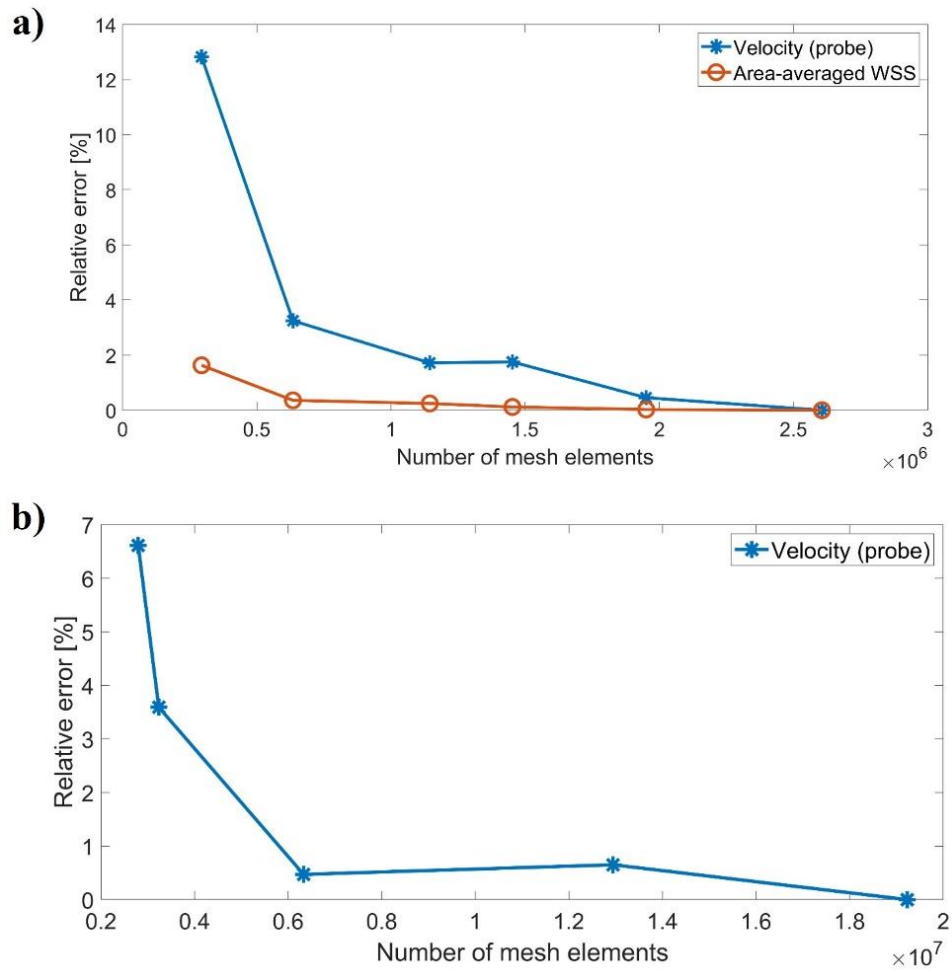


Figure 6.8: Mesh convergence results for (a) RA model and (b) catheter model.

According to quality criteria, the meshes had excellent average skewness features (between 0 and 0.25) and very good average orthogonal quality (near 0.8) (Shewchuk, 2002; Workbench, 2015). The average quality distribution of mesh elements for all catheter models is displayed in Figure 6.9, showing that most elements have a quality above 0.72. An example of a meshed model is shown in Figure 6.10 and the mesh characteristics are listed in Table 6.6. Using these settings, an average spatial resolution of 0.1 mm was achieved for the solid mesh inside each catheter while 1 mm was achieved for the remaining solid mesh, respectively.

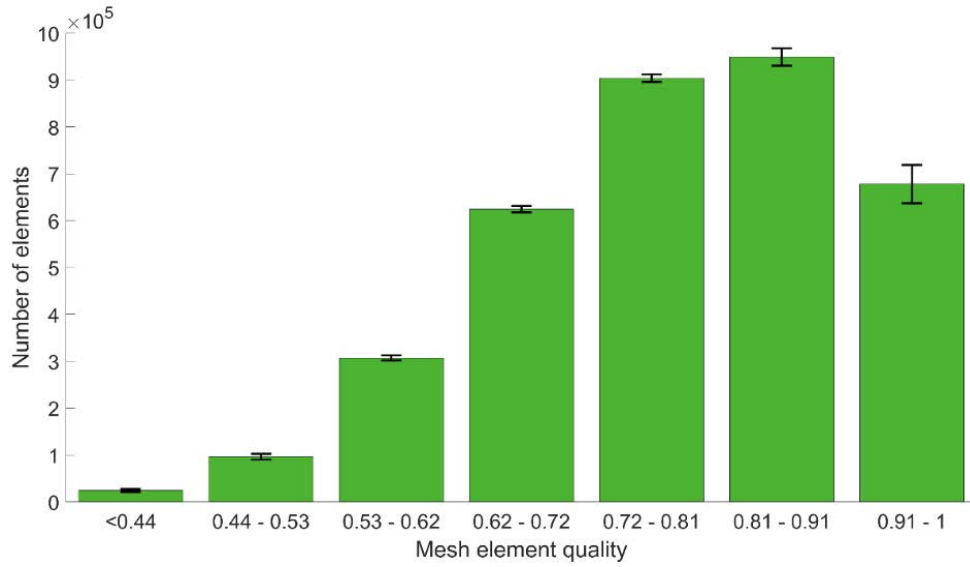


Figure 6.9: Mesh element quality, varying from 0 to 1, assessed across all catheter models. The average number of elements for each quality range is displayed, with error bars showing the standard deviation from average values.

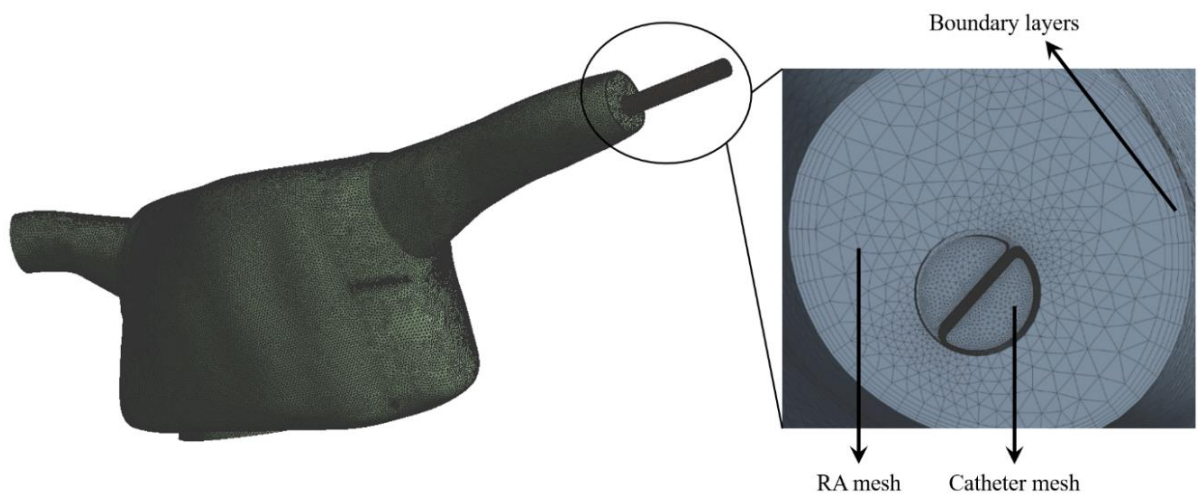


Figure 6.10: Meshed model, with a closer look at the SVC boundary. Boundary layers can be observed near the right atrial wall. A greater number of mesh elements was used to represent the catheter, in comparison with the RA.

Table 6.6: Mesh settings and quality assessment.

Model	No. mesh elements	Average orthogonal quality	Average skewness
RA	1,144,719	0.797	0.200
A1	3,325,107	0.773	0.226
A2	3,316,264	0.773	0.226
A3	3,342,044	0.773	0.226
B	3,294,202	0.773	0.226
C	3,460,285	0.787	0.212
D1	3,236,187	0.770	0.228
D2	3,237,906	0.772	0.227

Domain independence analysis

The TV outlet was not extended, similarly to previous heart modelling studies (Rigatelli *et al.*, 2018; Vedula *et al.*, 2015). In fact, doing so would give rise to incorrect computational predictions as a valve is found in that position (e.g. alteration of pressure gradients near the valve). Moreover, the SVC and IVC inlets are placed 4 and 2 diameters away from the main chamber, respectively. To assess the independence of computational predictions from the domain size, one additional transient computational simulation was solved for an altered RA model, using the same material properties and boundary conditions as the original model. In this geometry, the IVC was further extended, and the respective inlet placed at 4 diameters away from the main chamber. Volume-averaged velocity and vorticity quantities, as well as area-averaged WSS magnitudes, were evaluated and average relative errors between predictions with and without IVC extension were 4.77 %, 4.52 % and 2.09 % for velocity, vorticity and WSS, respectively. These relative errors are deemed acceptable and justify the choice of our RA domain for computational simulations.

Time convergence analysis

The RA model was run for 8 cycles to assess the temporal evolution of computational predictions. Volume-averaged velocity and pressure quantities, as well as local values obtained

at a probe placed at the centre of the RA, were obtained for all cardiac cycles and time-averaged. The relative error between the solution from each cycle and the one from the last cycle was computed using equation 6.3:

$$E = \left| \frac{v_B - v_L}{v_L} \right| \cdot 100 \%, \quad (6.3)$$

where v_B and v_L are the calculated variables for each time period before the last and for the last time period, respectively. Figure 6.11 shows that increasing the number of cardiac cycles decreased the relative errors for both volume-averaged and probe results, although localised quantities were less prone to stabilise. The 4th cardiac cycle ($E = 1.28 \%$ and $E = 4.12 \%$ for volume-averaged velocity and pressure) was chosen for result retrieval and quantifications.

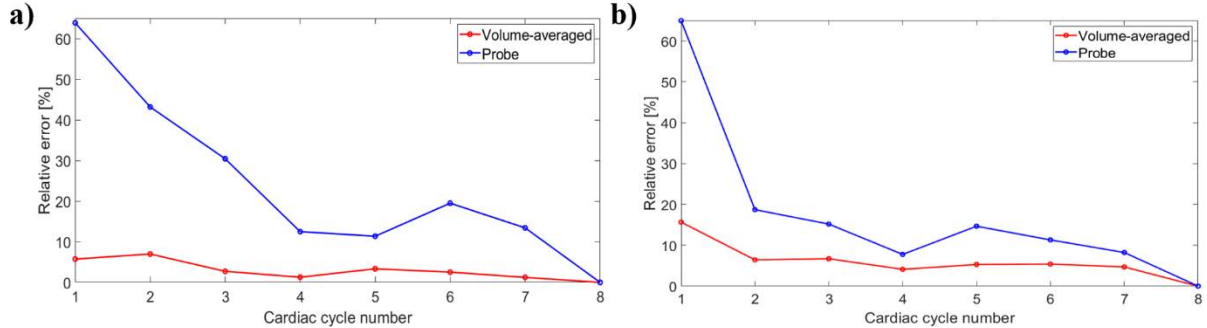


Figure 6.11: Relative percentage error for (a) velocity and (b) pressure measurements.

Solving settings

All simulations were run for a total of 3200 time steps, corresponding to 3.2 s (4 cardiac cycles), using super-computing facilities (BlueBear High Performance Computing, University of Birmingham), with 100 cores for each simulation and 5 GB RAM per core. The solution time for the simulation of the RA model was ~10 hours, and ~25 hours for the catheter models.

6.4. Haemodynamics

Right atrial haemodynamics were evaluated in terms of velocity magnitude, flow streamlines, vorticity, pressure and WSS. The obtained results were validated against the literature before using it as a model for the assessment of catheter performance (section 6.5.2). Catheter performance was evaluated using measures of vorticity, WSS, recirculation and blood shear stress. Recirculation of blood filtered through catheters was quantified through the calculation of the venous flow volume (previously labelled as the recirculation phase) returning through the arterial lumen. Key results were obtained at five time instances of the cardiac cycle, specifically late-diastole ($t = 0.1$ s), beginning of systole ($t = 0.25$ s), mid-systole ($t = 0.4$ s), late systole ($t = 0.55$ s) and mid-diastole ($t = 0.7$ s).

Regarding blood shear stress evaluation, previous studies have noted higher levels of platelet activation at the venous lumen tip in comparison with the arterial one (Clark *et al.*, 2015). To better observe any marked differences between models, the venous tip was chosen for analysis and quantification of shear stress. Rectangular volumes composed by prism elements were created at each venous tip for this purpose, including side-holes for catheter A (Mareels *et al.*, 2007) (example in Figure 6.12 and dimensions in Table 6.7). These were defined using appropriate coordinates which would yield the desired volume dimensions in order to cover the tip and side-holes. The tip volume where $\tau \geq 10$ Pa was also evaluated to identify the potential for platelet activation (Mareels *et al.*, 2007; Wang *et al.*, 2005).

All parameter definitions are listed in Table 6.8.

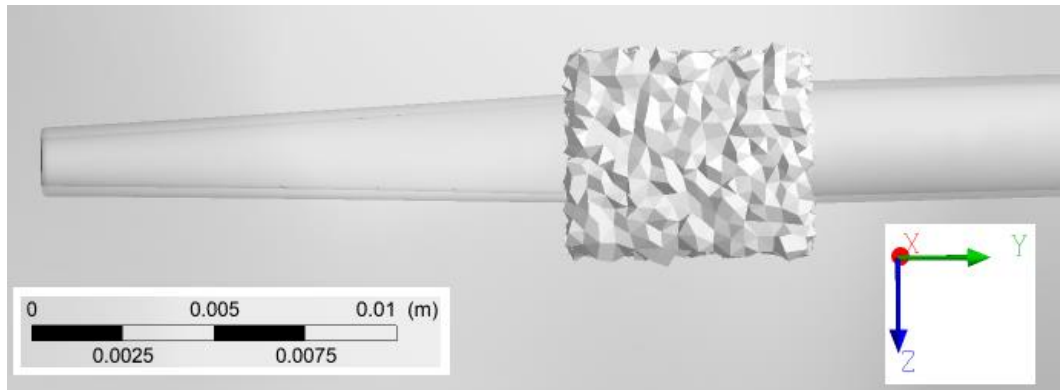


Figure 6.12: Example of volume definition to be placed at the tip.

Table 6.7: Tip volume dimensions.

	A	B	C	D
Length [mm]	4.5	8	7	13
Width [mm]	25	10	7	9
Height [mm]	6	6	7	5.5

Table 6.8: Parameter definitions for evaluation of haemodynamics.

Parameter	Definition	Variables
Volume averaged vorticity	$\boldsymbol{\omega} = \frac{1}{V} \int_{domain} \nabla \times \mathbf{u} \, dV$	where \mathbf{u} is the velocity vector and V is the fluid domain volume
Time and volume-averaged vorticity	$\bar{\boldsymbol{\omega}} = \frac{1}{T} \int_0^T \boldsymbol{\omega} \, dt$	where $\bar{\boldsymbol{\omega}}$ is the time-averaged vorticity and T is the length of the cardiac cycle (0.8 s)
WSS	$\boldsymbol{\tau}_w = \mu \left. \frac{\partial \mathbf{u}_t}{\partial \mathbf{n}} \right _{wall}$	where τ_w is the wall shear stress (WSS), μ is the blood viscosity, \mathbf{u}_t is the tangential wall velocity and \mathbf{n} is the unit vector perpendicular to the wall
TAWSS	$\bar{\tau}_w = \frac{1}{T} \int_0^T \boldsymbol{\tau}_w \, dt$	where $\bar{\tau}_w$ is the time-averaged wall shear stress (TAWSS) and T is the length of the cardiac cycle (0.8 s)
Mass-weighted recirculation fraction	$R_f = \frac{100}{\dot{m}_T} \sum_{k=1}^n \bar{\phi}_k \dot{m}_k$	where R_f is the recirculation fraction (%), \dot{m}_T and \dot{m}_k are the total mass flow rate over the catheter outlet boundary and the mass flow rate for a k^{th} facet of the catheter outlet boundary, respectively, and $\bar{\phi}_k$ is the time-averaged volume fraction of the recirculation phase for a k^{th} facet of the catheter outlet boundary ¹
Time averaged recirculation fraction	$\bar{R}_f = \frac{1}{T} \int_0^T R_f \, dt$	where \bar{R}_f is the time-averaged recirculation fraction (%) and T is the length of the cardiac cycle (0.8 s)
Strain rate magnitude	$ \boldsymbol{\epsilon}_{ij} = \sqrt{\frac{1}{2} \left(\frac{\partial u_j}{\partial x_i} + \frac{\partial u_i}{\partial x_j} \right) \left(\frac{\partial u_j}{\partial x_i} + \frac{\partial u_i}{\partial x_j} \right)}$	where u_i and u_j are the velocity vectors in the i and j directions and x_i and x_j are the spatial coordinates in the i and j directions
Volume averaged Shear stress	$\tau = \frac{1}{V} \int_{tip} (\mu \cdot \boldsymbol{\epsilon}_{ij}) \, dV$	where τ is the shear stress, V is the tip volume and $ \boldsymbol{\epsilon}_{ij} $ is the magnitude of the strain rate
Time and volume-averaged shear stress	$\bar{\tau} = \frac{1}{T} \int_0^T \tau \, dt$	where $\bar{\tau}$ is the time-averaged shear stress and T is the length of the cardiac cycle (0.8 s)

6.5. CFD results

Time-averaged results for vorticity, TAWSS magnitude (evaluation of RA haemodynamics), recirculation and shear stress (evaluation of catheter performance) are presented in Table 6.9

¹ The full mathematical derivation of this expression is described in Appendix E.

for all models.

Table 6.9: Haemodynamic predictions for all models.

	Quantity	RA	A1	A2	A3	B	C	D1	D2
RA haemodynamics	$\bar{\omega}$ [s ⁻¹]	44.1	54	55.2	55	57.2	56.1	55.8	54.9
	TAWSS [Pa]	1.89	2.01	2.04	2.05	1.93	1.97	2.15	2.14
Catheter performance	\bar{R}_f [%]	-	9.32	6.45	8.84	43.7	9.71	0.26	0.21
	$\bar{\tau}$ [Pa]	-	12.9	15.5	13.7	13.8	11.2	11.6	10.2
	Volume of $\bar{\tau} > 10$ Pa [%]	-	28.3	33.4	28.6	28.1	15.7	28.7	28.5

6.5.1. Right atrium model validation

Right atrial CFD predictions were compared against available *in vivo* and *in vitro* data for a healthy RA model without the presence of a catheter.

The predicted time- and volume-averaged pressure was 1.18 mmHg, with minimum and maximum values oscillating between 0.55 and 1.88 mmHg, respectively. Maximum pressure values reached 4.55 mmHg. These values are in agreement with clinical guidelines, which estimate a normal time- and volume-average RA pressure of 3 mmHg (with minimum and maximum values varying between 0 and 5 mmHg) for an IVC diameter < 21 mm (Rudski *et al.*, 2010), as it is the case of this model.

Blood velocity magnitudes were within the *in vivo* range: the mean time- and volume-averaged value was 0.192 m/s, with minimum and maximum velocities ranging between 0.160 m/s and 0.233 m/s, respectively. Reported clinical values are 0.174 ± 0.027 m/s (Parikh *et al.*, 2017) and *in vitro* studies also present with a similar range (Gulan *et al.*, 2017). Volume-averaged velocities kept relatively constant through most of the cardiac cycle, as shown in Figure 6.13 – left, apart from the beginning of the systolic period ($t = 0.25$ s), where a velocity increase within the RA was observed (18.2 % increase from late-diastole, $t = 0.1$ s). A similar observation can

be made for volume-averaged vorticity and area-averaged WSS, both quantities being at their highest at the beginning of systole (Figure 6.13 – middle and right). Additionally, area-averaged WSS decreases through the systolic period and up to late-diastole, where it begins increasing again (30.6 % increase from mid- to late-diastole). Interestingly, the time evolution of volume-averaged vorticity and WSS in the RA model showed similar trends (Figure 6.14), presenting a correlation with a Pearson correlation coefficient of 0.87.

The model also predicted physiological flow patterns within the RA: vortical flow patterns were present throughout the cardiac cycle, as observed in Figure 6.15. Specifically, a vortex originated from IVC flow, and SVC flow swirled around it in a helical fashion. *In vivo* studies speculate that this swirling motion optimises blood flow movement within the heart (Parikh *et al.*, 2017; Hirtler *et al.*, 2016; Gulan *et al.*, 2017; Elbaz *et al.*, 2017).

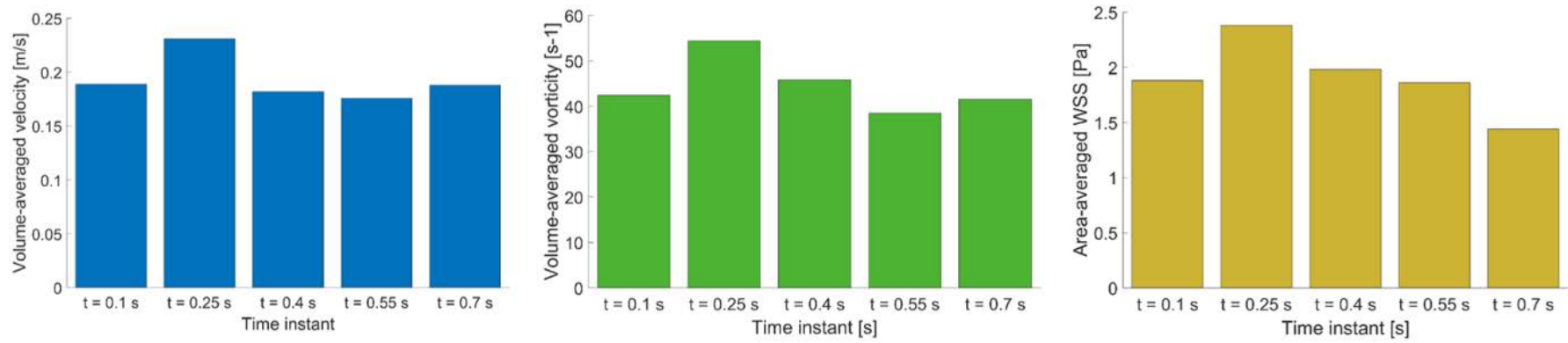


Figure 6.13: Quantitative results for volume-averaged velocity (left), volume-averaged vorticity (middle) and area-averaged WSS (right) at five time instances of the cardiac cycle.

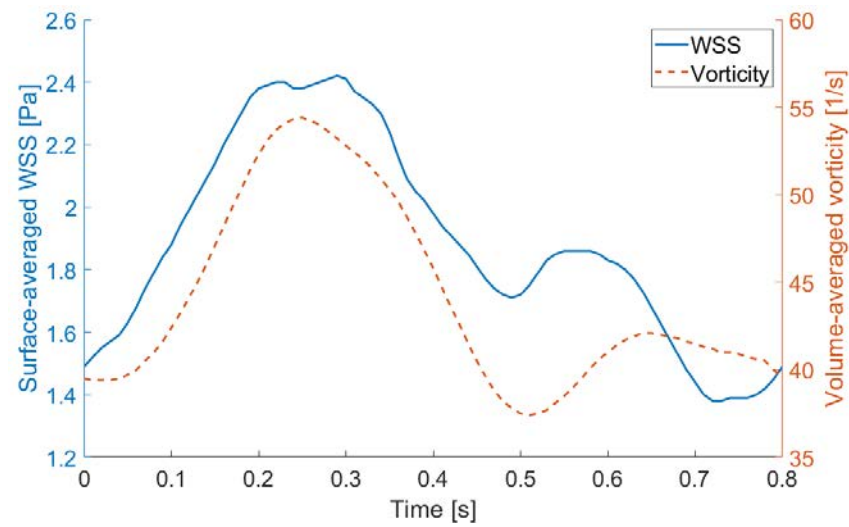


Figure 6.14: Time evolution of spatially averaged WSS and volume-averaged vorticity.

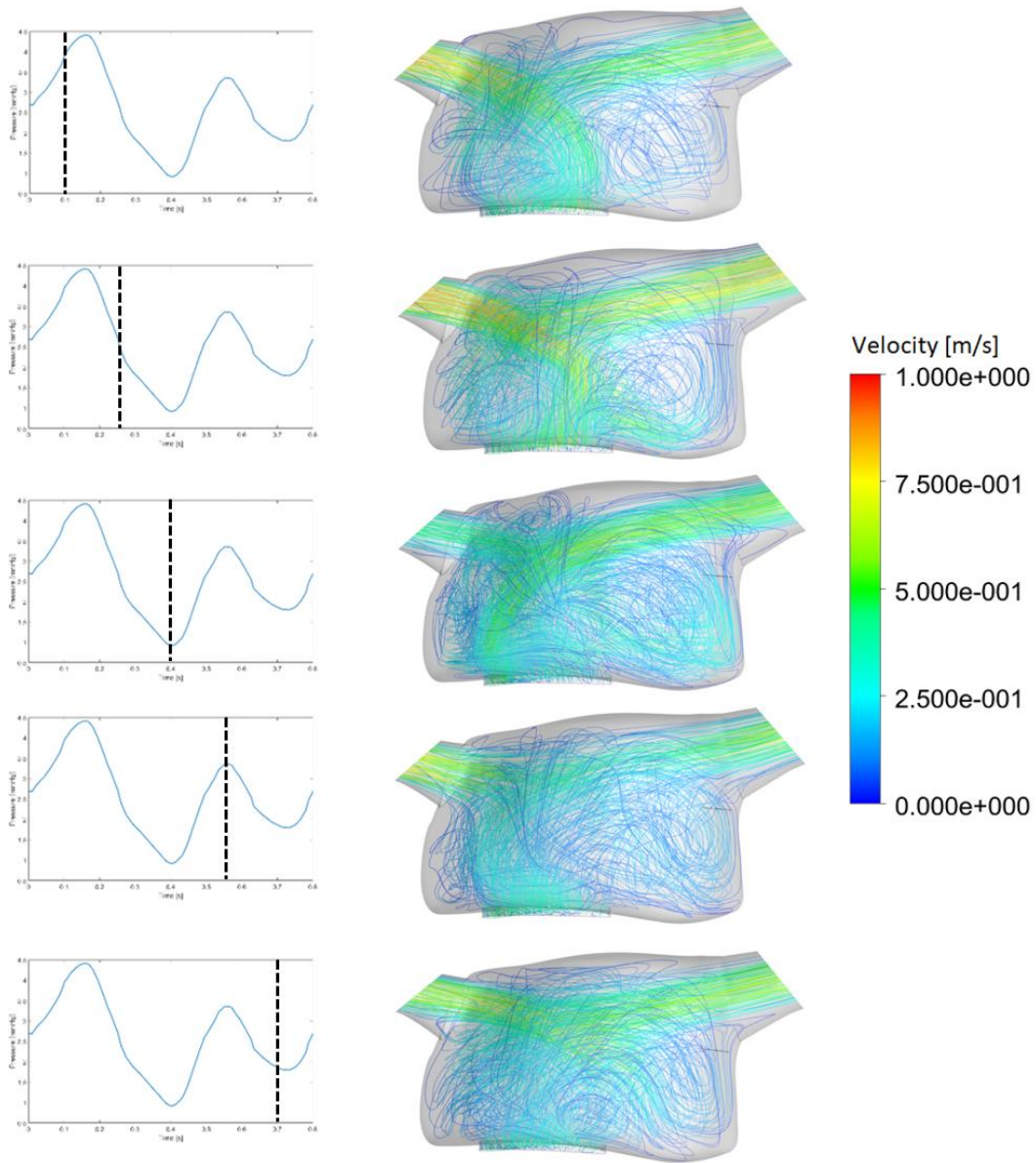


Figure 6.15: Time evolution of right atrial flow patterns: streamline fields representing velocity magnitudes are displayed at five different time instances ($t = 0.1$ s, 0.25 s, 0.4 s, 0.55 s, 0.7 s).

The predicted volume-averaged vorticity was 44.1 s^{-1} , within the range of *in vivo* predictions ($37 - 54 \text{ s}^{-1}$) (Hirtler *et al.*, 2016). Both vortical and helical features were observed, with clockwise (positive helicity) and anti-clockwise (negative helicity) rotating flow filling the RA throughout the cardiac cycle (Figure 6.16). Although the location of positive and negative helical structures changes in the RA model over one cardiac cycle, each occupies approximately

half of the RA volume. This means that none of the rotating directions is predominant. According to the literature, multiple right atrial flow patterns exist in the structurally normal heart, including vortical, helical and multiple vortical flow (Parikh *et al.*, 2017).

Figure 6.17 shows the time-evolution of blood flow rates through the SVC, IVC and TV over a cardiac cycle. Both SVC and IVC present similar flow rate waveforms, with a two-peaked shape (a peak at ventricular systole and a smaller one at ventricular diastole), in agreement with the literature (Wehrum *et al.*, 2018; Parikh *et al.*, 2017). A previous study shows that the range of these flow rate waveforms varies amongst a population sample and with age (Wehrum *et al.*, 2018). With the present model, maximum systolic flow rate values of 106 ml/s and 120 ml/s are predicted for the IVC and SVC. While the obtained waveform and maximum for the IVC are consistent with clinical estimates (maximum value of 151.1 ± 55.3 ml/s at systole for a group of healthy adults aged 20-39 years), the SVC waveform and maximum value are overestimated (maximum value increased by 22 % in comparison with the maximum standard deviation observed in the literature (Wehrum *et al.*, 2018)).

Since TV function was not modelled (section 6.3.1), the associated flow rate waveform follows a similar pattern to those of the IVC and SVC, with a peak flow rate of 225 ml/s. As previously mentioned, the current literature does not present many examples of the expected flow rate through the TV, making any comparison difficult. One study shows that there is a phase shift in the location of the TV flow rate peaks, which should appear during the ventricular diastolic period (Kroft *et al.*, 2000). This did not occur in our flow rate predictions, likely because TV function was not modelled.

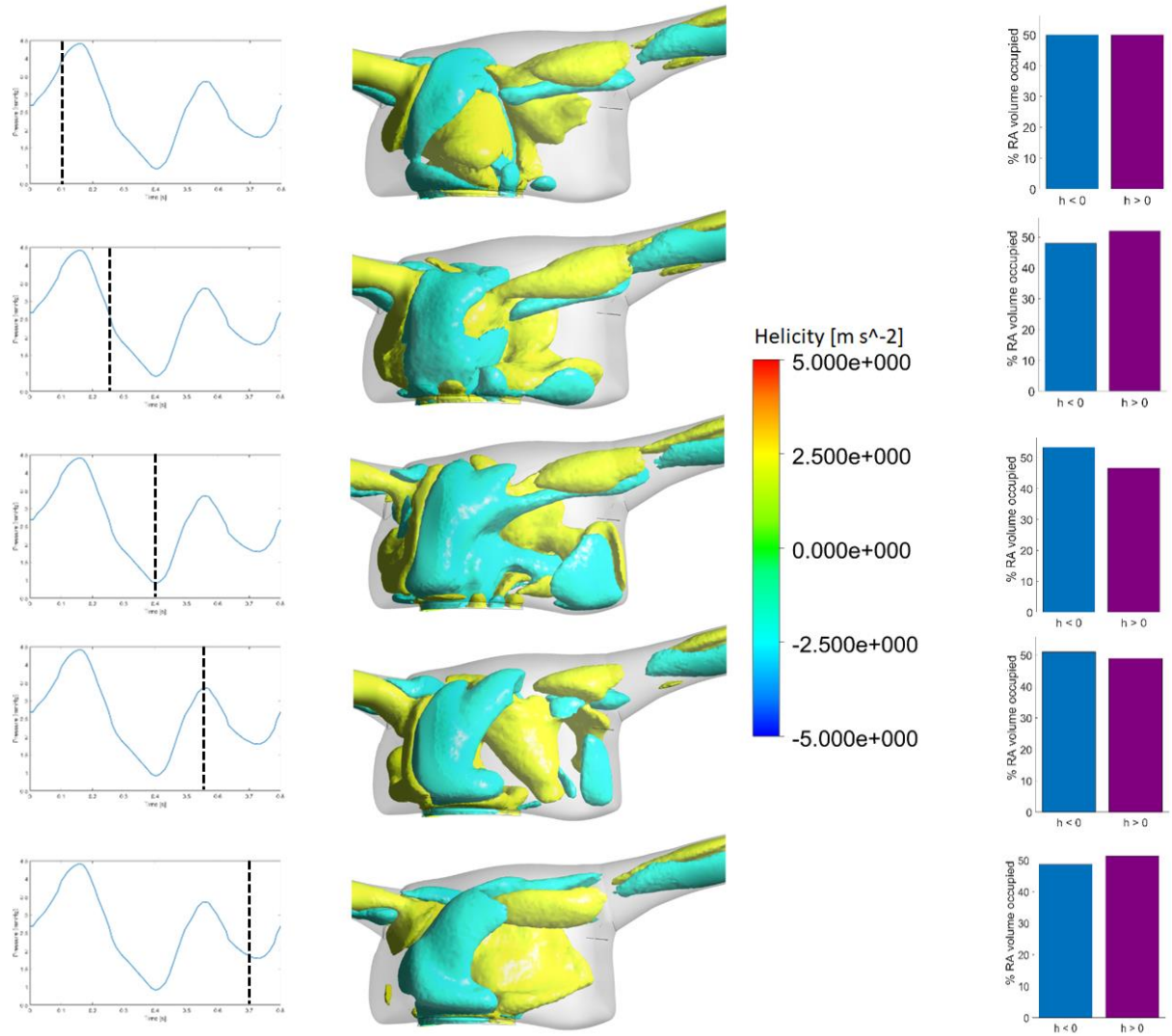


Figure 6.16: Time evolution of right atrial flow patterns: isosurfaces representing helicity (h) are displayed at five different time instances ($t = 0.1$ s, 0.25 s, 0.4 s, 0.55 s, 0.7 s), as well as the percentage of RA volume occupied by $h < 0$ and $h > 0$.

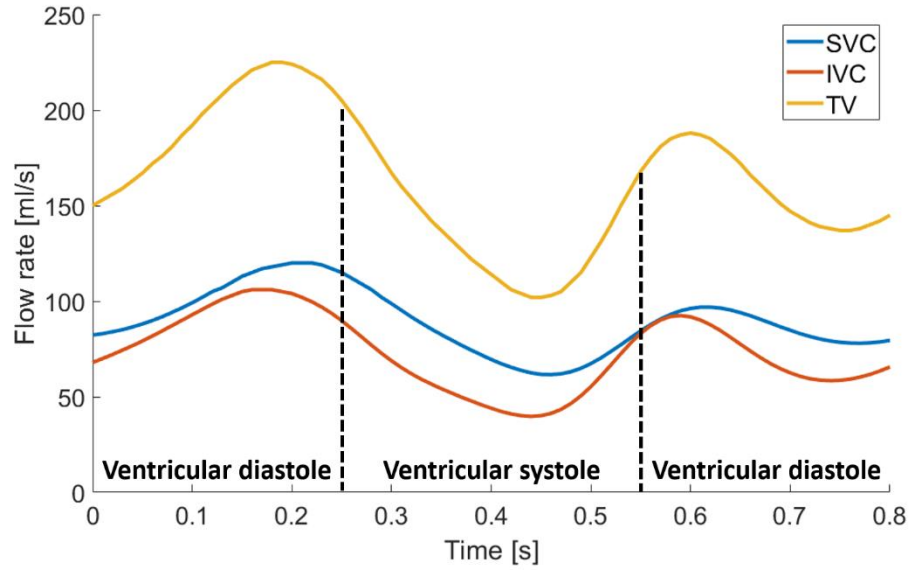


Figure 6.17: Blood flow rate profiles over one cardiac cycle at SVC, IVC and TV boundaries.

6.5.2. Catheter models

Alterations in RA haemodynamics

The insertion of catheters in the RA altered right atrial flow patterns, as can be observed in Figure 6.18 for the symmetric design. The swirling motion of flow already present in the healthy RA model intensified with the presence of a catheter, especially during the systolic period (as presented in Figure 6.18 for $t = 0.25$ s, 0.4 s and 0.55 s), where vortices are predominant within the entire chamber. Indeed, volume-averaged vorticity increased in all catheter models in comparison with the RA model (Table 6.9 and Figure 6.19a), with catheter designs yielding similar vorticity values ($54 - 57.20$ s⁻¹). Catheter B gave rise to the maximum time-averaged vorticity, characterized by increased vorticity during late systole and late diastole in comparison with other designs (Figure 6.19a). Different catheter tip placements did not greatly impact the average RA vorticity for designs A and D (Figure 6.19b), giving rise to absolute differences of 2.22 % and 1.85 %, respectively.

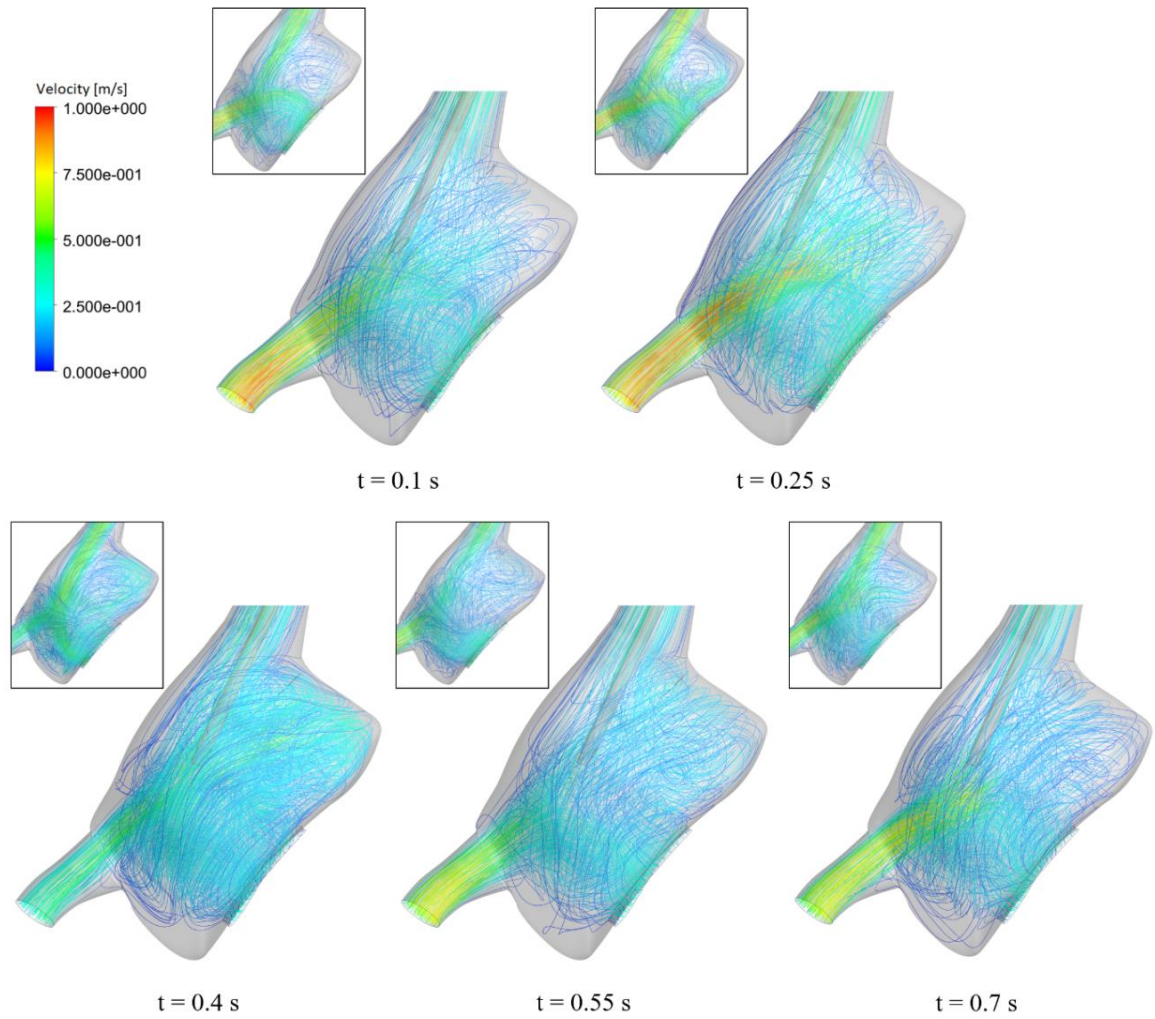


Figure 6.18: Time evolution of right atrial flow patterns after catheter insertion (symmetric design – D2): streamline fields representing velocity magnitudes are displayed at five time instances.

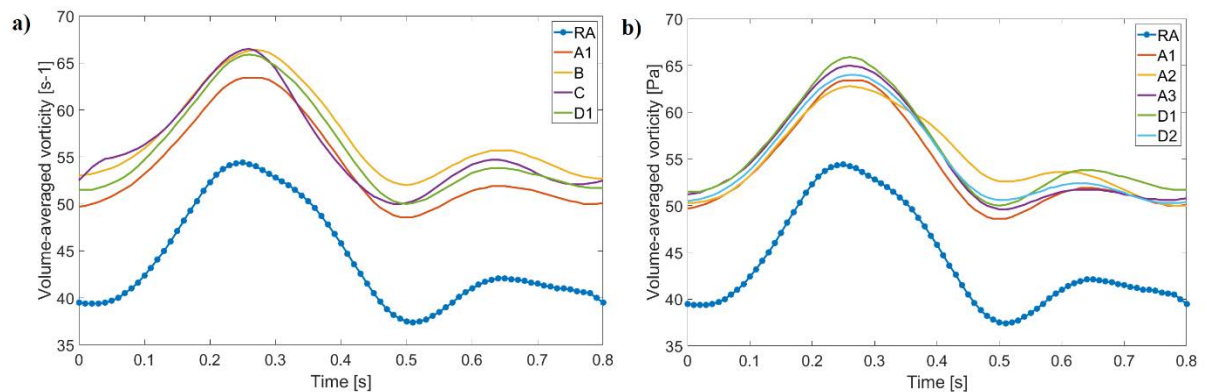


Figure 6.19: Volume-averaged vorticity profile through the cardiac cycle for all models. (a) All designs are compared with the RA; (b) A and D tip placement changes do not greatly influence overall vorticity quantifications.

TAWSS on the RA wall was not markedly affected for catheters B or C. Catheters A1, A2 and A3 suffered TAWSS percentage increases ranging between 6 and 9 %, while catheters D1 and D2 had the greatest percentage increases (13-14 %), in comparison with the value obtained for the RA model (Table 6.9). Figure 6.20 shows that, for all models, elevated WSS was located around the SVC and IVC inlets, possibly due to local diameter reductions. Concerning the RA model, sites of low and high WSS magnitudes can be observed, with the latter possibly corresponding to regions of elevated vorticity and helicity. The virtual insertion of catheter geometries in the RA led to sites of increased WSS in its central region, with surface distribution varying according to the blood flow jet pattern from each catheter tip. In addition, catheters A and D originated different sites of increased WSS, as observed below the SVC junction (circled in Figure 6.20).

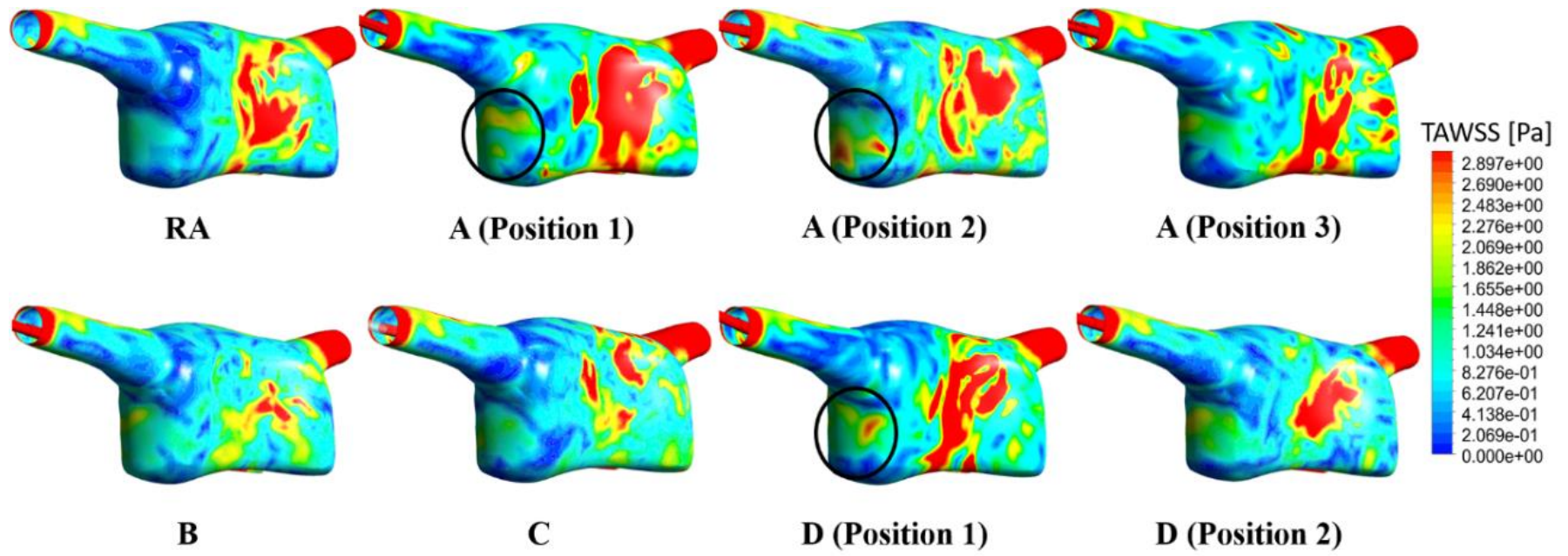


Figure 6.20: Time-averaged WSS [Pa] for the whole RA domain is displayed for all models.

Catheter performance

Flow recirculation was present in all catheter models: while B was associated with the highest recirculation percentage (43.7 %), A and C yielded recirculation > 5 %. Design D gave rise to the lowest percentages of recirculating fluid (< 0.50 %, respectively), meeting the design requirements of less than 1 % recirculation (Table 6.9).

Figure 6.21 provides a better visualisation on catheter performance. The side holes present in design A let venous lumen flow enter the RA with different trajectories, which seems to lead to better mixing of this flow with the chamber flow, preventing it from entering the arterial lumen. The lack of side holes in design B, however, seems to enhance the amount of flow returning through the catheter arterial lumen. Moreover, Figure 6.21 shows that designs C and D (Position 2) are associated with the greatest mixing of venous flow within the RA, in comparison with the other designs.

Different tip placements also impacted on recirculation outcomes: for catheter A, percentage decreases of 30.79 % and 5.15 % were observed for positions 2 and 3 in comparison with the first position. Moreover, positions 2 and 3 gave rise to a greater concentration of venous flow at the base of the RA and near the IVC junction, respectively. Concerning design D, varying tip placement did not greatly impact on recirculation percentages.

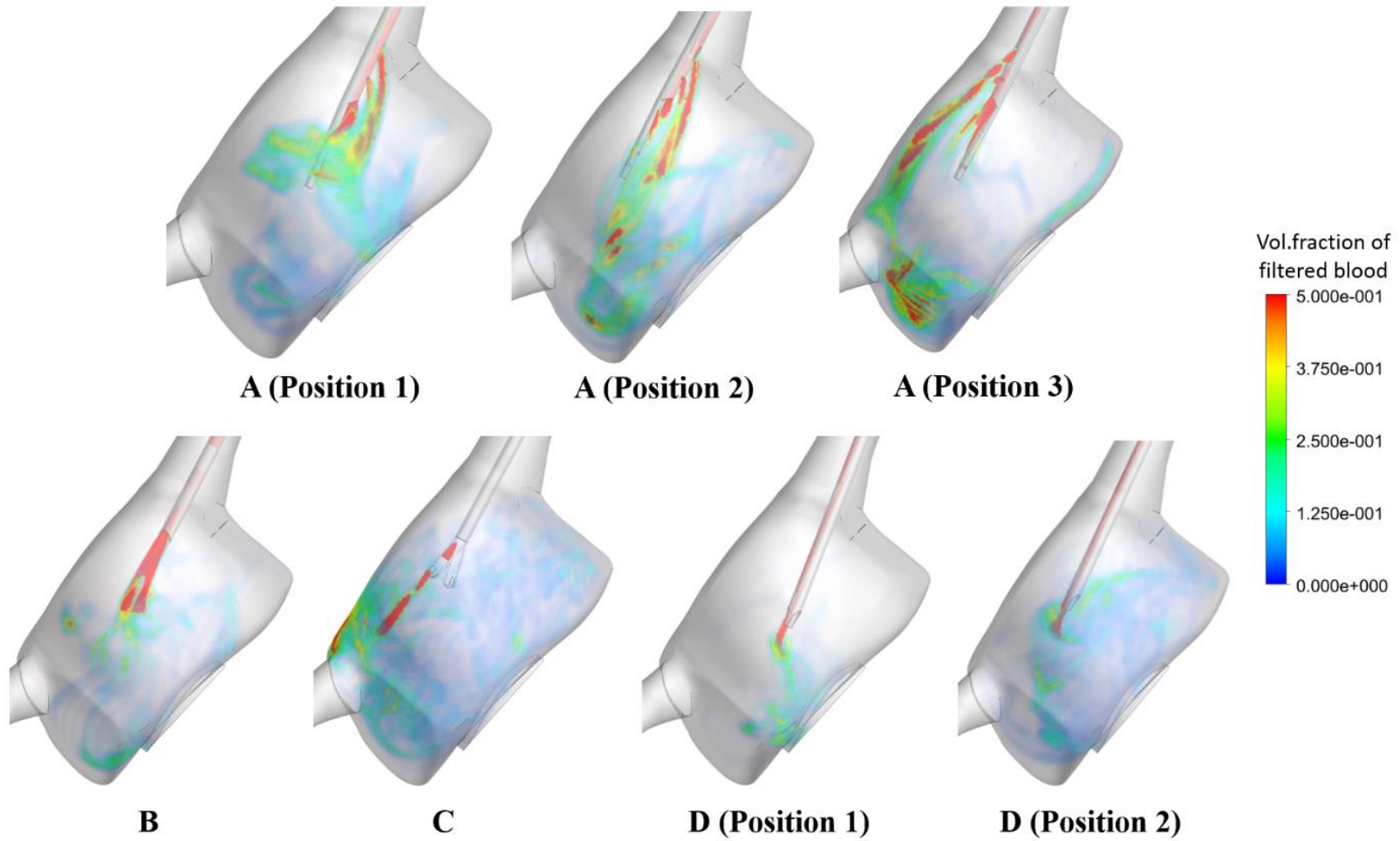


Figure 6.21: Time-averaged volume fraction of filtered blood (recirculation phase) within the RA for all catheter models. Higher volume fractions indicate larger quantities of filtered blood at one location over one cardiac cycle, while lower volume fractions indicate lower quantities of filtered blood at one location over one cardiac cycle.

Designs C and D were characterized by the lowest time-averaged shear stress at the tip, while designs A and B led to the highest ones (Table 6.9). In addition, design C had a small percentage of volume of $\bar{\tau} > 10$ Pa (15.70%), while the other designs yielded values in the same range (above 28%). Moreover, and as observed in Table 6.9 and Figure 6.22b, changing tip placement affected the predicted shear stress for catheters A and D: placing the tip closer to the atrium wall (position 2) increased the volume-averaged shear stress and percentage of volume of $\bar{\tau} > 10$ Pa for design A (20.15% and 18.02%, respectively), but decreased these quantities for design D (12.07% and 0.70%, respectively). Rotating catheter A (position 3) slightly improved these outcomes, but there was still an increase of 6.20% in the volume-averaged shear stress and of 1.06% on the percentage of volume of $\bar{\tau} > 10$ Pa in comparison with the first placement.

The shear stress profile from Figure 6.22b captures similar temporal trends, and interestingly, for design D, the first position is associated with unsteady shear stress through time (also observed on Figure 6.22a), while the second one yields smoother shear stress changes. Figure 6.22a also shows that, while designs A and B yield relatively constant temporal shear stress, for design C this stress increased near end-systole and decreased through diastole. Shear stress equal to 10 Pa were localized to both inlet and outlet boundaries, as well as side-holes (Figure 6.23). The venous lumen exit, however, had a greater proportion of shear stress equal to 10 Pa for all catheters.

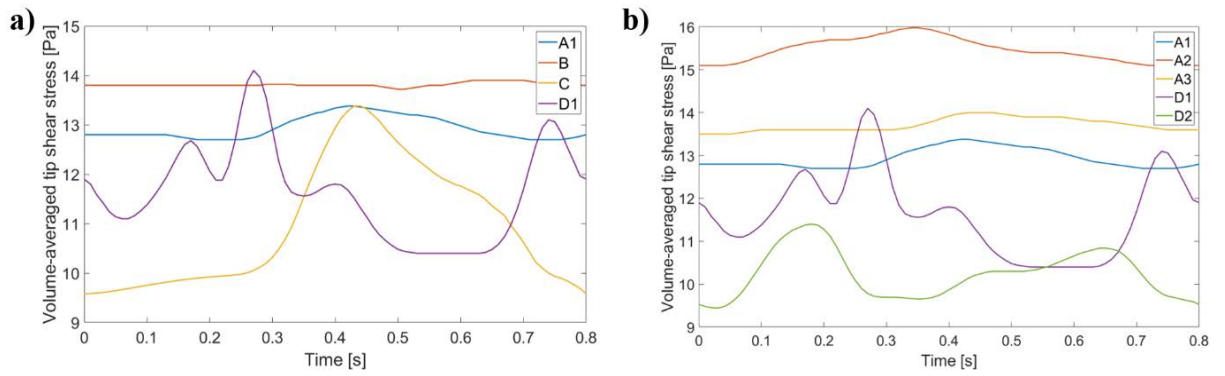


Figure 6.22: Volume-averaged shear stress profile through the cardiac cycle for all catheter venous lumen tips. (a) All designs are present; (b) A and D tip placement changes impact on tip shear stress.

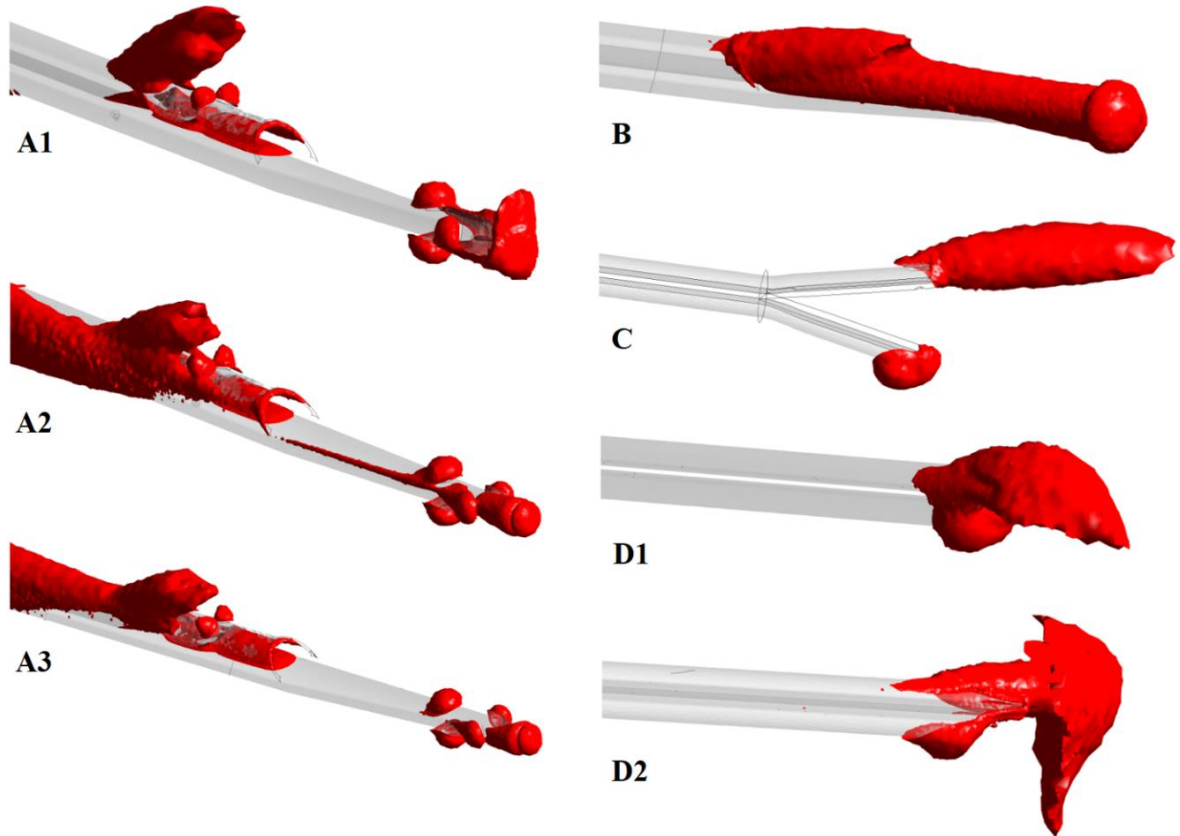


Figure 6.23: Isosurface regions near the catheter tip where blood shear stress is 10 Pa for all models at the beginning of systole ($t = 0.25$ s).

6.6. Discussion

6.6.1. Main study findings

This is the first study to develop and validate the data obtained against literature for a CFD model of the RA to assess catheter performance. Key haemodynamics have been quantified for four distinct catheter designs. The obtained results suggest the following findings:

- ❖ The CFD RA model has been validated against the literature, with haemodynamic predictions being consistent with *in vivo* data (Parikh *et al.*, 2017; Hirtler *et al.*, 2016; Francois *et al.*, 2012) and with clinical guidelines for right heart assessment (Rudski *et al.*, 2010);
- ❖ Catheter placement within the RA induces changes in its haemodynamics, including increased vorticity and alterations in TAWSS;
- ❖ Recirculation is present in all catheter designs, with only the symmetric design D complying with required specifications ($< 1\%$);
- ❖ The presence of side holes decreases the amount of recirculating flow in step designs, as given by lower recirculation percentages (6.45 – 9.32 %) in design A when compared to design B (43.7 %);
- ❖ Catheters working in reverse mode (step designs) are associated with reduced performance, having greater recirculation percentages and shear stress values;
- ❖ Elevated tip shear stress (10.2 – 15.5 Pa) is present in all catheter designs, which can induce platelet activation and aggregation and subsequently thrombosis (Kroll *et al.*, 1996);
- ❖ Different catheter tip placements impact on performance, as given by altered recirculation percentages, tip shear stress values and percentage of tip volume with $\tau > 10$ Pa;

- ❖ The symmetric catheter design has the best performance, associated with low recirculation and shear stress values.

6.6.2. Catheter insertion affects vorticity and WSS predictions in the RA

In this study, temporal WSS magnitudes were statistically correlated with vorticity in the RA model, which shows that tracking the temporal behaviour of vortex structures may provide complimentary information on the WSS (Gulan *et al.*, 2017). Similar to previous studies, it can be hypothesized that the influence of rinsing motion of increasing vortex during the systolic phase is associated with increasing WSS, thereby avoiding thrombus formation within the RA (Gulan *et al.*, 2017). Predicted TAWSS values, however, were higher than those previously obtained by a 4D cardiac magnetic resonance study (Francois *et al.*, 2012). Nonetheless, the accuracy of magnetic resonance imaging measurements is narrowed by low temporal and spatial resolutions of the order of 40 ms and 2 mm³, respectively (Rinaudo and Pasta, 2014). This causes an averaging of the *in vivo* measured velocity field, yielding spurious errors in the calculated velocity gradients at the wall-blood interface (Rinaudo and Pasta, 2014; Papathanasopoulou *et al.*, 2003). Therefore, WSS magnitudes derived from medical imaging are usually underestimated (Rinaudo and Pasta, 2014), which makes computational modelling advantageous in this matter (Papathanasopoulou *et al.*, 2003).

Increased vorticity was present in all catheter models with respect to the RA model. Prior studies have focused on understanding the connection between vorticity and cardiac function and efficiency (Hirtler *et al.*, 2016). As previously stated, the presence of vortices in the healthy RA seems to optimise blood flow and cardiac efficiency within the right heart (Hirtler *et al.*, 2016; Parikh *et al.*, 2017). However, increased right atrial vorticity has been observed in patients after repair of Tetralogy of Fallot, including the presence of additional diastolic vortex which impacted on ventricular flow (Hirtler *et al.*, 2016). Moreover, altered right atrial vorticity

has been detected in patients with right ventricular diastolic dysfunction (Fenster *et al.*, 2015). Fenster *et al.* (2015) suggested that, although premature, quantifying vorticity could be useful to: 1) correlate to right heart pathologies, and 2) serve as a non-invasive biomarker for the assessment of both haemodynamic and bioenergetics response to therapy (Fenster *et al.*, 2015). As per the results of this study and the outcomes of previous studies, it can be speculated that catheter placement within the RA may alter normal blood flow within this chamber (Francois *et al.*, 2012). This, however, requires further validation from future clinical studies.

Catheter placement within the RA also led to an increase in TAWSS magnitudes and changes in WSS distributions in the atrial wall surface: the symmetric tip (design D) was associated with the highest increase, while step tips (design A) gave rise to the creation of different high WSS sites. In fact, previous clinical (Mahadevia *et al.*, 2014) and computational (Oliveira *et al.*, 2019; Cao and Sucosky, 2017) studies have linked abnormal flow with high WSS, as well as different WSS distributions, in the ascending aorta. Abnormally high WSS has been assumed as a trigger for aortic dilation in congenital diseases by changing the wall tissue mechanical properties (Tadros *et al.*, 2009; Bissell *et al.*, 2013; Barker *et al.*, 2012). Given this, we can hypothesize that the WSS alterations predicted in this study could possibly be associated with right atrial enlargement onset and progression at specific sites, especially given the duration of use (weeks to months) of central venous catheters.

6.6.3. Different catheter designs and placements yield different performance

This study predicted time-averaged recirculation values within the same range as those obtained by previous studies (Clark *et al.*, 2015; Vesely and Ravenscroft, 2016; Clark *et al.*, 2012). Moreover, the symmetric design (catheter D) yielded negligible ($< 0.5\%$) recirculation, and the lowest of all models, which is associated with a better separation of filtered and unfiltered

blood. Step tip designs (working in reverse mode) gave rise to higher recirculation percentages, in comparison with symmetric and split designs. In fact, the literature shows the presence of up to 86% of recirculation for catheters working in reverse configuration (Vesely and Ravenscroft, 2016; Pannu *et al.*, 2006), which can explain our highest recirculation value (43.7%) for step design B. In addition, the presence of side holes in step tip design helped diminish time-average recirculating flow (catheter A vs B). This has been shown in previous studies (Clark *et al.*, 2015; Vesely and Ravenscroft, 2016) and it can be hypothesized that the presence of side holes in a step tip may improve catheter performance by allowing flow deflection from the distal tip, as suggested elsewhere (Clark *et al.*, 2015).

Shear stress characteristics were also evaluated to assess the tendency of each catheter design to cause shear-induced platelet activation and aggregation. Platelet activation has been shown to induce device thrombogenicity and they experience shear-induced activation at a larger rate than required for haemolysis of red blood cells (Klaus *et al.*, 2002). The predicted shear stresses were in the same order of magnitude as presented elsewhere, although percentages of tip volume above 10 Pa were much lower (Mareels *et al.*, 2007). This could, however, be due to the variability in tip volume definition. Nonetheless, platelet activation has been observed with $0.1 \leq \tau \leq 20$ Pa (Kroll *et al.*, 1996) and therefore, in this study, a middle value was used as a threshold (10 Pa). All catheter models yielded shear stress > 10 Pa, mostly distributed at the venous tip and side holes (step design). These high shear stress sites have been observed in a previous *in vivo* study, which showed the formation of a fibrin plaque on the catheter surface around a venous side hole (Lucas *et al.*, 2014). This suggests that all designs have a potential for shear-induced platelet activation and subsequently thrombosis (which can occur within 2 weeks after catheter insertion).

Different tip placements within the RA also yielded different performances, with a tip placement closer to the RA wall giving rise to greater recirculating flow. This is the first computational study that considers how different tip positions impact on both catheter performance and RA haemodynamics. However, the optimal positioning of an haemodialysis catheter is a continuous subject of debate and controversy, with elevated clinical variability (Vesely, 2003) and changing medical guidelines (Tawk *et al.*, 2018). It has been noted that correct tip positioning is vital to prevent/diminish recirculation (Santoro *et al.*, 2014), impacting on the efficiency of the haemodialysis treatment (Twardowski and Seger, 2002). According to the results of this study, a tip placement at the mid-level of the RA with its arterial lumen facing the mediastinum yields lower (but still significant) recirculation percentages, which is in agreement with the latest medical guidelines (Gilmore, 2006). Given this, care should be taken with catheter tip placement and orientation within the RA.

Considering all results, catheters working in reverse mode (step tip designs) yielded the highest recirculation and time-averaged shear stress values, being associated with the highest potential for shear-induced platelet activation. This implies that, in a clinical scenario, the use of standard mode should be targeted. The symmetric tip, on the other hand, was shown to have the best performance, as given by the lowest recirculation and shear stress values.

6.7. Conclusions

In this study, a model which provides realistic predictions of haemodynamics in the right atrium has been developed, subsequently aiding the assessment of haemodialysis catheter performance. This model shows that the symmetric tip design is associated with the best haemodynamic results, given by its low recirculation and shear stress values, while the step tip designs working in reverse mode gave rise to the worst haemodynamic outcomes. Moreover,

the presence of side holes at the tip helped diminish recirculating flow, suggesting that, in the design process of a step tip, this feature should be investigated to improve its performance. In addition, the use of our RA model to study catheter tip placement aids in understanding how catheter performance is affected by different tip designs perform under pulsatile conditions. Given that clinical guidelines provide generic guidance for catheter tip placement within the RA, our model and its haemodynamic predictions could potentially aid the clinical decision process.

CHAPTER 7

SYNTHESIS

7.1. Overall discussion

The aim of this thesis was to develop computational frameworks for components from both sides of the heart, including: a toolbox for the creation of parametric and scalable models of the MV (left heart), to be used in numerical simulations; and a blood flow model of the right atrium (right heart), to be used as a simulation platform for the evaluation of catheter designs for haemodialysis.

This thesis tackled the research gaps identified in Chapter 1 through:

- ❖ A mathematical evaluation of MV morphometry, performed through correlation analysis between key dimensions and evaluation of prediction equations available in the literature;
- ❖ The development of a computational toolbox enabling the quick generation of anatomically accurate and clinically useful parametric models of the MV, from the generation of the geometry to the development of the FE model;
- ❖ The creation of a CFD platform for the assessment of the performance of dialysis catheter designs, employing a physiological model of the RA which has been used to evaluate the performance of several catheter designs.

Chapter 3 focused on the assessment of mathematical definitions of MV morphometry. Correlation analyses reported in the literature have been evaluated and compared with correlation analyses performed in this thesis, using dimensions obtained from patient-specific medical images. This was performed to find a unique set of mathematical equations describing the overall shape of the MV. Moderate ($0.6 < R^2 < 0.8$) and good correlations ($R^2 > 0.8$) between MV dimensions have been found; however, the lack of consistency in MV measurements reported by clinical studies did not allow obtaining one set of equations which included all the dimensions required to represent MV geometry. Furthermore, the prediction equations available in the literature and found through correlation analysis were associated with a large range of relative errors ($< 5\%$ to $> 250\%$) when used to predict morphometric data. In addition, abnormal changes in MV dimensions, such as the increase of annular diameters, are correlated with poor valvular function. It then remains unclear whether the prediction equations described in this thesis can fit data from diseased cases or even paediatric patients. Empirical morphometric equations based on the Golden Ratio (Deorsola and Bellone, 2019; Deorsola and Bellone, 2018), on the other hand, can successfully predict MV dimensions, as given by average relative errors $< 10\%$ for annular and leaflet length dimensions, and $< 36\%$ for leaflet areas. Currently, these equations represent the best unifying method to describe MV annular and leaflet shapes and have, therefore, been implemented within the MV toolbox (Chapter 4).

The MV toolbox allows for the automated and user-controlled generation of parametric MV geometries, scaled according to pre-established parameters and user-inputted options, with the final geometry being recreated in less than 5 minutes. The current script (1) generates a scaled mitral valve geometry, compatible with a range of modelling software for virtual assessment of function, and (2) performs the pre-processing of FE model for LS-DYNA software, which can

be directly used to compute for biomechanical assessment. In reality, computational models (Ge et al., 2014; Rim et al., 2015; Wang and Sun, 2013) and integrated frameworks for biomechanical analyses of the MV (Mansi *et al.*, 2012; Zhang *et al.*, 2017) usually employ patient-specific geometries obtained from medical imaging; however, (1) such frameworks can only generate the patient-specific MV shape arising from the specific set of medical images, and (2) the time needed to set-up/solve the models is not compatible with translation into clinical practice (Shinbane and Saxon, 2018).

The MV toolbox addresses both issues mentioned above. Indeed, the tool offers flexibility in the creation of a MV geometry: a variety of user-options is available, including the customisation of PM positions based on displacement options ranging from an increase in the inter-PM distance of the application of LV dilation. Thus, this tool can capture a full range of morphological features as seen in clinical cases. Moreover, the toolbox includes the full pre-processing of a generated MV geometry for FE simulations. As discussed in Chapter 5, this includes the meshing of leaflet surfaces, definition of material properties, application of BC and contact properties and set-up of control options for numerical stability and output of results. Several aspects of model definition can be set up by the user, including the thickness of each mitral leaflet and corresponding material properties, allowing the study of pathological cases associated with altered tissue characterisations or increased leaflet thickness.

All this information is then stored as an input file for LS-DYNA. To obtain the final set-up definitions of the FE model, an average, healthy MV model was generated and validated against the literature, and different BC were assessed. The functionalities and potential of the toolbox are described in this thesis, including two applications: two patient-specific MV geometries were created and their models solved. These were associated with different diseased states which led to abnormally predicted MV function, characterised by poor coaptation, elevated

leaflet stresses and unbalanced PM and chordae forces. The toolbox has thus the potential to assess the biomechanics of varying MV geometries, associated with healthy or diseased scenarios, potentially highlighting the geometrical features which impact MV biomechanics the most.

In addition to the development of a computational framework for the generation of clinically useful parametric models of the MV and assessment of the respective biomechanics (left heart), a modelling framework for the RA (right heart) was also generated. As detailed in Chapter 6, a CFD model of the RA was developed and validated, to be used as a simulation platform to virtually assess haemodialysis catheter performance. The haemodynamics predicted for the RA model was validated against *in vivo* data (Parikh *et al.*, 2017; Hirtler *et al.*, 2016; Francois *et al.*, 2012) and clinical guidelines (Rudski *et al.*, 2010) and the model was then assumed fit for the haemodynamic evaluation of (1) four different catheter designs and (2) different catheter tip placements. It was observed, for the first time, that the insertion of a catheter within the RA alters its haemodynamics, marked by increases in flow vorticity and alterations in TAWSS. The symmetric design was associated with the best performance, complying with design requirements for recirculation ($< 1\%$), while the presence of side holes decreased the amount of recirculating flow in step designs. However, all catheters presented elevated tip shear stress (10.20 – 15.50 Pa), potentially associated with platelet activation and aggregation and subsequently thrombosis (Kroll *et al.*, 1996). In addition, different tip placements affected recirculation percentages and shear stress values and distribution, showing that correct catheter tip placement within the RA is crucial for improved performance. These results further demonstrate the potential of the developed CFD simulation platform to assess a variety of catheter designs, allowing their optimisation prior to use in a clinical environment.

7.2. Opportunities for future research

The development of improved medical imaging modalities and a larger number of morphometric studies for the MV are required to tackle some challenges associated with the assessment of its morphometry. In the present assessment of MV shape (Chapter 3), no correlation analysis could be performed for PM position or chordae insertion patterns into both the PM and the leaflets. Although human PMs spatial position has been defined accounting for their distance to the mitral annulus or to mitral coaptation (Yamaura, 2008; Sakai et al., 1999), and other measures including inter-PM distance or inter-PM angle are reported in the literature, such information is not sufficient to evaluate an association between multiple dimensions. In addition, current *in vivo* imaging modalities are unable to properly capture the chordae and the PM (Gao et al., 2017b), which makes the task of obtaining this type of measurements arduous. The capture of accurate *in vivo* chordal distribution patterns relies, therefore, on the future development of improved medical imaging modalities with higher spatial and temporal resolutions.

Most quantitative studies report mean MV morphometric data, with just a few stating measurements for each patient (Warraich et al., 2012; Duplessis and Marchand, 1964). It is crucial to provide measurements at a patient-specific level, and not averaged at a population level, which would allow to obtain correlation analyses taking into consideration a wider anatomical description of the MV. Given that the shape of the MV changes with disease (Silbiger, 2011; Lee et al., 2013) and that anatomical measurements differ from those obtained in living patients, future studies would require the collection (or reporting) of a high number of patient-specific measurements, focusing on subjects either with a healthy MV (i.e. lack of disease which would be associated with changes in shape), with a diseased MV, or both (to assess if a prediction equation could yield predictions for both healthy and diseased states).

These could then be used to 1) further validate the prediction equations found in this study, as well as evaluate new correlation analyses; 2) further assess the employability of the prediction equations based on the Golden Ratio, which have been implemented within the MV toolbox (Chapter 4).

In addition, the MV toolbox described in Chapter 4 can be further developed, especially concerning the incorporation of morphometric prediction equations for paediatric populations based on the height and mass of a patient, as well as the BSA. The tool could then account for a patient's growth (and that of their own MV), potentially improving paediatric surgical planning by enabling a virtual evaluation of pre- and post-operative scenarios over a longer time-span (Al-Atabi et al., 2012; Votta et al., 2013). The MV model itself can also be improved with respect to the representation of the subvalvular apparatus. This consists of adding more control on the addition process of the chordae tendineae, including the possibility of choosing different branching numbers and insertion into different portions of the leaflets. Moreover, the possibilities of output for computational simulations can be extended: in addition to the already implemented ready-to-use LS-DYNA mesh, the code can be expanded to allow for output of the MV model in formats compatible with other software such as gmsh or VTK.

Further pre-processing features should also be targeted, in addition to those presented in Chapter 5. Material properties can be improved by implementing a leaflet material model accounting for the anisotropic nature of this tissue and the presence of collagen fiber orientation. To obtain more accurate biomechanical predictions of MV dynamics in patient-specific cases, the option to incorporate kinematic BC based on patient-specific imaging data should be included in the toolbox (Mansi et al., 2012). Focus should also be given to the development of a fluid-structure interaction model within the toolbox, to account for the passage of blood

through the valve and its interaction with the leaflet tissue (Gao et al., 2017a; Huang et al., 2021).

In addition to the aspects afore mentioned, and for clinical planning applications, the incorporation of different surgical procedures in the toolbox is required. Combined with a more intuitive and user-friendly GUI, the automatic application of surgical procedures, simulation of a variety of cases and generation of relevant results can help clinicians decide the best treatment for a patient through the virtual evaluation of MV biomechanics pre- and post-surgery.

The CFD platform developed to assess the performance of multiple catheter designs and described in Chapter 6 can also be further improved in future research. A FSI framework can be implemented to represent the movement of the RA walls, TV opening/closing and catheter tip movement within the RA. RA wall movement has a significant effect on the blood flow patterns within the chamber, affecting catheter implementation; however, not only do very few studies provide insight on RA wall movement (Vitarelli *et al.*, 2018; Takata *et al.*, 1997), but also data on the mechanical properties of the RA wall is currently limited (Rausch and Kuhl, 2013). Future studies targeting a better understanding of the mechanical properties of the RA wall and its movement will be crucial to incorporate a non-rigid wall on the model. A compliant RA model may yield a more accurate description of pulse waves, including pressure patterns within the RA (Formaggia *et al.*, 2009), once accurate data for their elasticity is available. Incorporating the afore mentioned features in the RA model will lead to improved computational predictions of catheter design performance which can inform medical device companies regarding the design optimisation of these devices before their release on the market. Regardless, the application of FSI to such a model therefore remains a current open problem, especially given the associated increase in model complexity and computational cost.

7.3. Overall conclusions

The overall conclusions of this thesis are as follows:

- ❖ The accuracy in predictions from linear and nonlinear fittings varies with the MV dimension of interest and the type of source data (*in vivo* vs *ex vivo* or healthy vs diseased), with further studies including more complete datasets being required to perform more correlation analyses between dimensions;
- ❖ A parametric and scalable model of the MV employing prediction equations based on the Golden Ratio has been generated, with the accuracy of predicted dimensions showing good agreement with literature data;
- ❖ The MATLAB framework developed for the generation of tailored MV geometries can recreate MV anatomy based on a number of user-inputted options, allowing the flexibility to obtain a geometry from either patient-specific or predicted average dimensions and processing the model for FE simulations, within a timescale compatible with clinical use (i.e. minutes instead of weeks);
- ❖ An average, healthy MV model has been analysed and validated against previous experimental and computational studies;
- ❖ Sensitivity analyses were conducted for varying MV BC and material properties, assessing how these affect MV physiology and biomechanical predictions and highlighting the importance of appropriate BC to obtain realistic MV physiological behaviour;
- ❖ A physiological CFD model of the RA has been developed and validated against *in vivo* data from the literature, ready to be used as a simulation platform for the evaluation of HD catheter designs and the investigation of design features requiring optimisation, providing

insight on (1) the type of design associated with best and worst haemodynamic outcomes and (2) how different catheter placements within the RA impact their performance.

REFERENCES

- ABD ALAMIR, M., RADULESCU, V., GOYFMAN, M., MOHLER, E. R., 3RD, GAO, Y. L., BUDOFF, M. J. & CRIC Study Investigators. 2015. Prevalence and correlates of mitral annular calcification in adults with chronic kidney disease: Results from CRIC study. *Atherosclerosis*, 242, 117-122.
- ADHAM ESFAHANI, S., HASSANI, K. & ESPINO, D. M. 2019. Fluid-structure interaction assessment of blood flow hemodynamics and leaflet stress during mitral regurgitation. *Comput Methods Biomech Biomed Engin*, 22, 288-303.
- AGUILERA, H. M., URHEIM, S., SKALLERUD, B. & PROT, V. 2021. Influence of Annular Dynamics and Material Behavior in Finite Element Analysis of Barlow's Mitral Valve Disease. *J Elast*, 145, 163-190.
- AL-ATABI, M., ESPINO, D. M., HUKINS, D. W. & BUCHAN, K. G. 2012. Biomechanical assessment of surgical repair of the mitral valve. *Proc Inst Mech Eng H*, 226, 275-287.
- ALFIERI, O., MAISANO, F., DE BONIS, M., STEFANO, P. L., TORRACCA, L., OPPIZZI, M. & LA CANNA, G. 2001. The double-orifice technique in mitral valve repair: a simple solution for complex problems. *J Thorac Cardiovasc Surg*, 122, 674-681.
- ALLEAU, T., LANQUETIN, L. & SALSAC, A. V. 2019. Use of a parametric finite element model of the mitral valve to assess healthy and pathological valve behaviors. *Comput Methods Biomech Biomed Engin*, 22, S4-S5.
- ANSYS, I. 2013. ANSYS Fluent Theory Guide (Release 15.0). Release 15.0 ed. 275 Technology Drive Canonsburg PA 15317: ANSYS, Inc.
- ANSYS, I. 2017. ANSYS Fluent Tutorial Guide (Release 18.1). Release 18.0 ed. 275 Technology Drive Canonsburg PA 15317: ANSYS, Inc.
- BARBER, J. E., KASPER, F. K., RATLIFF, N. B., COSGROVE, D. M., GRIFFIN, B. P. & VESELY, I. 2001. Mechanical properties of myxomatous mitral valves. *J Thorac Cardiovasc Surg*, 122, 955-962.
- BARKER, A. J., MARKL, M., BURK, J., LORENZ, R., BOCK, J., BAUER, S., SCHULZ-MENGER, J. & VON KNOBELSDORFF-BRENKENHOFF, F. 2012. Bicuspid aortic valve is associated with altered wall shear stress in the ascending aorta. *Circ Cardiovasc Imaging*, 5, 457-466.

BASHORE, T. M., CABELL, C. & FOWLER, V., JR. 2006. Update on infective endocarditis. *Curr Probl Cardiol*, 31, 274-352.

BAUMGARTNER, H., FALK, V., BAX, J. J., DE BONIS, M., HAMM, C., HOLM, P. J., IUNG, B., LANCELLOTTI, P., LANSAC, E., RODRIGUEZ MUNOZ, D., ROSENHEK, R., SJOGREN, J., TORNOS MAS, P., VAHANIAN, A., WALTHER, T., WENDLER, O., WINDECKER, S., ZAMORANO, J. L. & ESC Scientific Document Group. 2017. 2017 ESC/EACTS Guidelines for the management of valvular heart disease. *Eur Heart J*, 38, 2739-2791.

BEAUDOIN, J., HANDSCHUMACHER, M. D., ZENG, X., HUNG, J., MORRIS, E. L., LEVINE, R. A. & SCHWAMMENTHAL, E. 2013a. Mitral valve enlargement in chronic aortic regurgitation as a compensatory mechanism to prevent functional mitral regurgitation in the dilated left ventricle. *J Am Coll Cardiol*, 61, 1809-1816.

BEAUDOIN, J., THAI, W. E., WAI, B., HANDSCHUMACHER, M. D., LEVINE, R. A. & TRUONG, Q. A. 2013b. Assessment of mitral valve adaptation with gated cardiac computed tomography: validation with three-dimensional echocardiography and mechanistic insight to functional mitral regurgitation. *Circ Cardiovasc Imaging*, 6, 784-789.

BIAU, D. J., KERNEIS, S. & PORCHER, R. 2008. Statistics in brief: the importance of sample size in the planning and interpretation of medical research. *Clin Orthop Relat Res*, 466, 2282-2288.

BIFFI, B., GRITTI, M., GRASSO, A., MILANO, E. G., FONTANA, M., ALKAREEF, H., DAVAR, J., JEETLEY, P., WHELAN, C., ANDERSON, S., LORUSSO, D., SAUVAGE, E., MARIA BOSI, G., SCHIEVANO, S. & CAPELLI, C. 2019. A workflow for patient-specific fluid-structure interaction analysis of the mitral valve: A proof of concept on a mitral regurgitation case. *Med Eng Phys*, 74, 153-161.

BISSELL, M. M., HESS, A. T., BIASIOLLI, L., GLAZE, S. J., LOUDON, M., PITCHER, A., DAVIS, A., PRENDERGAST, B., MARKL, M., BARKER, A. J., NEUBAUER, S. & MYERSON, S. G. 2013. Aortic dilation in bicuspid aortic valve disease: flow pattern is a major contributor and differs with valve fusion type. *Circ Cardiovasc Imaging*, 6, 499-507.

BLOODWORTH, C. H. T., PIERCE, E. L., EASLEY, T. F., DRACH, A., KHALIGHI, A. H., TOMA, M., JENSEN, M. O., SACKS, M. S. & YOGANATHAN, A. P. 2017. Ex Vivo Methods for Informing Computational Models of the Mitral Valve. *Ann Biomed Eng*, 45, 496-507.

BONOW, R. O., CARABELLO, B. A., CHATTERJEE, K., DE LEON, A. C., JR., FAXON, D. P., FREED, M. D., GAASCH, W. H., LYTLE, B. W., NISHIMURA, R. A., O'GARA, P. T., O'ROURKE, R. A., OTTO, C. M., SHAH, P. M., SHANEWISE, J. S., 2006 Writing Committee Members & American College of Cardiology/American Heart Association Task Force. 2008. 2008 focused update incorporated into the ACC/AHA 2006 guidelines for the management of patients with valvular heart disease: a report of the American College of Cardiology/American Heart Association Task Force on Practice Guidelines (Writing Committee to revise the 1998 guidelines for the management of patients with valvular heart disease). Endorsed by the Society of Cardiovascular Anesthesiologists, Society for Cardiovascular Angiography and Interventions, and Society of Thoracic Surgeons. *J Am Coll Cardiol*, 52, e1-142.

BREAM, PETER R JR. 2016. Update on Insertion and Complications of Central Venous Catheters for Hemodialysis. *Semin Interv Radiol*, 33, 31-38.

BURRIESCI, G., HOWARD, I. C. & PATTERSON, E. A. 1999. Influence of anisotropy on the mechanical behaviour of bioprosthetic heart valves. *J Med Eng Technol*, 23, 203-215.

CABALLERO, A., MAO, W. B., MCKAY, R., PRIMIANO, C., HASHIM, S. & SUN, W. 2018. New insights into mitral heart valve prolapse after chordae rupture through fluid-structure interaction computational modelling. *Sci Rep*, 9, 17306.

CABALLERO, A., MAO, W., MCKAY, R. & SUN, W. 2020. Transapical mitral valve repair with neochordae implantation: FSI analysis of neochordae number and complexity of leaflet prolapse. *Int J Numer Method Biomed Eng*, 36, e3297.

CALLEJA, A., POULIN, F., WOO, A., MEINER, M., JEDRZKIEWICZ, S., VANNAN, M. A., RAKOWSKI, H., DAVID, T., TSANG, W. & THAVENDIRANATHAN, P. 2015. Quantitative Modeling of the Mitral Valve by Three-Dimensional Transesophageal Echocardiography in Patients Undergoing Mitral Valve Repair: Correlation with Intraoperative Surgical Technique. *J Am Soc Echocardiogr*, 28, 1083-1092.

CANTINOTTI, M., SCALESE, M., MURZI, B., ASSANTA, N., SPADONI, I., FESTA, P., DE LUCIA, V., CROCETTI, M., MAROTTA, M., MOLINARO, S., LOPEZ, L. & IERVASI, G. 2014. Echocardiographic nomograms for ventricular, valvular and arterial dimensions in caucasian children with a special focus on neonates, infants and toddlers. *J Am Soc Echocardiogr*, 27, 179-191 e2.

CAO, K. & SUCOSKY, P. 2017. Computational comparison of regional stress and deformation characteristics in tricuspid and bicuspid aortic valve leaflets. *Int J Numer Method Biomed Eng*, 33.

- CARPENTIER, A. 1983. Cardiac valve surgery - the "French correction". *J Thorac Cardiovasc Surg*, 86, 323-337.
- CARPENTIER, A. F., LESSANA, A., RELAND, J. Y., BELLI, E., MIHAILEANU, S., BERREBI, A. J., PALSKEY, E. & LOULMET, D. F. 1995. The "physio-ring": an advanced concept in mitral valve annuloplasty. *Ann Thorac Surg*, 60, 1177-85; discussion 1185-1186.
- CARPENTIER, A., CHAUVAUD, S., FABIANI, J. N., DELOCHE, A., RELAND, J., LESSANA, A., D'ALLAINES, C., BLONDEAU, P., PIWNICA, A. & DUBOST, C. 1980. Reconstructive surgery of mitral valve incompetence: ten-year appraisal. *J Thorac Cardiovasc Surg*, 79, 338-348.
- CARTY, G., CHATPUN, S. & ESPINO, D. M. 2016. Modeling Blood Flow Through Intracranial Aneurysms: A Comparison of Newtonian and Non-Newtonian Viscosity. *J Med Biol Eng*, 36, 396-409.
- CASA, L. D., DEATON, D. H. & KU, D. N. 2015. Role of high shear rate in thrombosis. *J Vasc Surg*, 61, 1068-1080.
- CASTILLO, J. G., SOLIS, J., GONZALEZ-PINTO, A. & ADAMS, D. H. 2011. [Surgical echocardiography of the mitral valve]. *Rev Esp Cardiol*, 64, 1169-1181.
- CHEN, L., YIN, F. C. & MAY-NEWMAN, K. 2004. The structure and mechanical properties of the mitral valve leaflet-strut chordae transition zone. *J Biomech Eng*, 126, 244-251.
- CHEN, S., SARI, C. R., GAO, H., LEI, Y., SEGERS, P., DE BEULE, M., WANG, G. & MA, X. 2020. Mechanical and morphometric study of mitral valve chordae tendineae and related papillary muscle. *J Mech Behav Biomed Mater*, 111, 104011.
- CHOI, A., MCPHERSON, D. D. & KIM, H. 2016. Biomechanical evaluation of the pathophysiologic developmental mechanisms of mitral valve prolapse: effect of valvular morphologic alteration. *Med Biol Eng Comput*, 54, 799-809.
- CHOI, A., MCPHERSON, D. D. & KIM, H. 2017. Computational virtual evaluation of the effect of annuloplasty ring shape. *Int J Numer Method Biomed Eng*, 33, e2831.
- CHOI, A., RIM, Y., MUN, J. S. & KIM, H. 2014. A novel finite element-based patient-specific mitral valve repair: virtual ring annuloplasty. *Biomed Mater Eng*, 24, 341-347.
- CIARKA, A., BRAUN, J., DELGADO, V., VERSTEEGH, M., BOERSMA, E., KLAUTZ, R., DION, R., BAX, J. J. & VAN DE VEIRE, N. 2010. Predictors of mitral regurgitation recurrence in patients with heart failure undergoing mitral valve annuloplasty. *Am J Cardiol*, 106, 395-401.

- CLARK, T. W. I., ISU, G., GALLO, D., VERDONCK, P. & MORBIDUCCI, U. 2015. Comparison of Symmetric Hemodialysis Catheters Using Computational Fluid Dynamics. *J Vasc Interv Radiol*, 26, 252-259.
- CLARK, T. W., VAN CANNEYT, K. & VERDONCK, P. 2012. Computational flow dynamics and preclinical assessment of a novel hemodialysis catheter. *Semin Dial*, 25, 574-581.
- CLAVEL, M. A., MANTOVANI, F., MALOUF, J., MICHELENA, H. I., VATURY, O., JAIN, M. S., MANKAD, S. V., SURI, R. M. & ENRIQUEZ-SARANO, M. 2015. Dynamic phenotypes of degenerative myxomatous mitral valve disease: quantitative 3-dimensional echocardiographic study. *Circ Cardiovasc Imaging*, 8, e002989.
- COHEN, M. L., COHEN, B. S., KRONZON, I., LIGHTY, G. W. & WINER, H. E. 1986. Superior vena caval blood flow velocities in adults: a Doppler echocardiographic study. *J Appl Physiol (1985)*, 61, 215-219.
- COLLAS, C. 2021. *Mathematical Modelling of the Aorto-Mitral Valve Complex and its Implications in Surgical Valve Repair*. BSc Biomedical Science, University of Aberdeen.
- COLLI, A., MANZAN, E., RUCINSKAS, K., JANUSAUSKAS, V., ZUCCHETTA, F., ZAKARKAITE, D., AIDIETIS, A. & GEROSA, G. 2015. Acute safety and efficacy of the NeoChord procedure. *Interact Cardiovasc Thorac Surg*, 20, 575-581.
- COLLINS, A. J., FOLEY, R. N., CHAVERS, B., GILBERTSON, D., HERZOG, C., JOHANSEN, K., KASISKE, B., KUTNER, N., LIU, J., ST PETER, W., GUO, H., GUSTAFSON, S., HEUBNER, B., LAMB, K., LI, S., LI, S., PENG, Y., QIU, Y., ROBERTS, T., SKEANS, M., SNYDER, J., SOLID, C., THOMPSON, B., WANG, C., WEINHANDL, E., ZAUN, D., ARKO, C., CHEN, S. C., DANIELS, F., EBBEN, J., FRAZIER, E., HANZLIK, C., JOHNSON, R., SHEETS, D., WANG, X., FORREST, B., CONSTANTINI, E., EVERSON, S., EGGERS, P. & AGODOA, L. 2012. 'United States Renal Data System 2011 Annual Data Report: Atlas of chronic kidney disease & end-stage renal disease in the United States. *Am J Kidney Dis*, 59, A7, e1-420.
- CONG, T., GU, J., LEE, A. P., SHANG, Z., SUN, Y., SUN, Q., WEI, H., CHEN, N., SUN, S. & FU, T. 2018. Quantitative analysis of mitral valve morphology in atrial functional mitral regurgitation using real-time 3-dimensional echocardiography atrial functional mitral regurgitation. *Cardiovasc Ultrasound*, 16, 13.
- DAGUM, P., TIMEK, T. A., GREEN, G. R., LAI, D., DAUGHTERS, G. T., LIANG, D. H., HAYASE, M., INGELS, N. B., JR. & MILLER, D. C. 2000. Coordinate-free analysis of mitral valve dynamics in normal and ischemic hearts. *Circulation*, 102, III62-69.

DAGUM, P., TIMEK, T., GREEN, G. R., DAUGHTERS, G. T., LIANG, D., INGELS, N. B., JR. & MILLER, D. C. 2001. Three-dimensional geometric comparison of partial and complete flexible mitral annuloplasty rings. *J Thorac Cardiovasc Surg*, 122, 665-73.

DAL-BIANCO, J. P. & LEVINE, R. A. 2013. Anatomy of the mitral valve apparatus: role of 2D and 3D echocardiography. *Cardiol Clin*, 31, 151-64.

DAL-BIANCO, J. P., AIKAWA, E., BISCHOFF, J., GUERRERO, J. L., HANDSCHUMACHER, M. D., SULLIVAN, S., JOHNSON, B., TITUS, J. S., IWAMOTO, Y., WYLIE-SEARS, J., LEVINE, R. A. & CARPENTIER, A. 2009. Active adaptation of the tethered mitral valve: insights into a compensatory mechanism for functional mitral regurgitation. *Circulation*, 120, 334-42.

DAUBENEY, P. E., BLACKSTONE, E. H., WEINTRAUB, R. G., SLAVIK, Z., SCANLON, J. & WEBBER, S. A. 1999. Relationship of the dimension of cardiac structures to body size: an echocardiographic study in normal infants and children. *Cardiol Young*, 9, 402-10.

DEBONNAIRE, P., AL AMRI, I., LEONG, D. P., JOYCE, E., KATSANOS, S., KAMPERIDIS, V., SCHALIJ, M. J., BAX, J. J., MARSAN, N. A. & DELGADO, V. 2015. Leaflet remodelling in functional mitral valve regurgitation: characteristics, determinants, and relation to regurgitation severity. *Eur Heart J Cardiovasc Imaging*, 16, 290-9.

DEGANDT, A. A., WEBER, P. A., SABER, H. A. & DURAN, C. M. 2007. Mitral valve basal chordae: comparative anatomy and terminology. *Ann Thorac Surg*, 84, 1250-5.

DELGADO, V., TOPS, L. F., SCHUIJF, J. D., DE ROOS, A., BRUGADA, J., SCHALIJ, M. J., THOMAS, J. D. & BAX, J. J. 2009. Assessment of mitral valve anatomy and geometry with multislice computed tomography. *JACC Cardiovasc Imaging*, 2, 556-65.

DEORSOLA, L. & BELLONE, A. 2018. Coaptation Triangle and Golden Proportion in mitral valve anatomy. Does nature play with geometry? *Echocardiography*, 35, 30-38.

DEORSOLA, L. & BELLONE, A. 2019. The Golden Proportion in the scallop geometry of normal mitral valves. When nature plays with jigsaw puzzles. *Echocardiography*, 36, 1028-1034.

DEPNER, T. A. 2001. Catheter performance. *Semin Dial*, 14, 425-431.

DHINGRA, R. K., YOUNG, E. W., HULBERT-SHEARON, T. E., LEAVEY, S. F. & PORT, F. K. 2001. Type of vascular access and mortality in U.S. hemodialysis patients. *Kidney Int*, 60, 1443-1451.

- DI DONATO, M., DABIC, P., CASTELVECCHIO, S., SANTAMBROGIO, C., BRANKOVIC, J., COLLARINI, L., JOUSSEF, T., FRIGIOLA, A., BUCKBERG, G., MENICANTI, L. & RESTORE Group. 2006. Left ventricular geometry in normal and post-anterior myocardial infarction patients: sphericity index and 'new' conicity index comparisons. *Eur J Cardiothorac Surg*, 29 Suppl 1, S225-230.
- DOLL, N., SHEYTANOV, V., LABROUSSE, L., CHU, M. W. A., STEFANO, P., MOKRACEK, A., BARON, O., LI, S. & GUNZINGER, R. 2019. Clinical performance of a three-dimensional saddle-shaped, rigid ring for mitral valve repair. *Eur J Cardiothorac Surg*, 55, 217-223.
- DOMENICHINI, F. & PEDRIZZETTI, G. 2015. Asymptotic Model of Fluid-Tissue Interaction for Mitral Valve Dynamics. *Cardiovasc Eng Technol*, 6, 95-104.
- DOMENICHINI, F., PEDRIZZETTI, G. & BACCANI, B. 2005. Three-dimensional filling flow into a model left ventricle. *J Fluid Mech*, 539, 179–198.
- DOSHI, R., SHLOFMITZ, E., SHAH, J. & MERAJ, P. 2018. Comparison of Transcatheter Mitral Valve Repair Versus Surgical Mitral Valve Repair in Patients With Advanced Kidney Disease (from the National Inpatient Sample). *Am J Cardiol*, 121, 762-767.
- DRACH, A., KHALIGHI, A. H. & SACKS, M. S. 2018. A comprehensive pipeline for multi-resolution modeling of the mitral valve: Validation, computational efficiency, and predictive capability. *Int J Numer Method Biomed Eng*, 34, e2921.
- DUPLESSIS, L. A. & MARCHAND, P. 1964. The Anatomy of the Mitral Valve and Its Associated Structures. *Thorax*, 19, 221-7.
- EINSTEIN, D. R., DEL PIN, F., JIAO, X., KUPRAT, A. P., CARSON, J. P., KUNZELMAN, K. S., COCHRAN, R. P., GUCCIONE, J. M. & RATCLIFFE, M. B. 2010. Fluid-Structure Interactions of the Mitral Valve and Left Heart: Comprehensive Strategies, Past, Present and Future. *Int J Numer Methods Eng*, 26, 348-380.
- EL SABBAGH, A., REDDY, Y. N. V. & NISHIMURA, R. A. 2018. Mitral Valve Regurgitation in the Contemporary Era: Insights Into Diagnosis, Management, and Future Directions. *JACC Cardiovasc Imaging*, 11, 628-643.
- ELBAZ, M. S., VAN DER GEEST, R. J., CALKOEN, E. E., DE ROOS, A., LELIEVELDT, B. P., ROEST, A. A. & WESTENBERG, J. J. 2017. Assessment of viscous energy loss and the association with three-dimensional vortex ring formation in left ventricular inflow: In vivo evaluation using four-dimensional flow MRI. *Magn Reson Med*, 77, 794-805.

- ERRTHUM, R., CABALLERO, A., MCKAY, R. & SUN, W. 2021. Comparative computational analysis of PASCAL and MitraClip implantation in a patient-specific functional mitral regurgitation model. *Comput Biol Med*, 136, 104767.
- ESPINO, D. M., SHEPHERD, D. E. & BUCHAN, K. G. 2007. Effect of mitral valve geometry on valve competence. *Heart Vessels*, 22, 109-115.
- ESPINO, D. M., SHEPHERD, D. E., HUKINS, D. W. & BUCHAN, K. G. 2005. The role of Chordae tendineae in mitral valve competence. *J Heart Valve Dis*, 14, 603-609.
- FALETRA, F. F. & NARULA, J. 2017. Imaging of Cardiac Anatomy. In: ELLENBOGEN, K. A., WILKOFF, B. L., KAY, G. N., LAU, C. & AURICCHIO, A. (eds.) *Clinical Cardiac Pacing, Defibrillation and Resynchronization Therapy*. 5 ed. Philadelphia, USA: Elsevier Inc.
- FEDAK, P. W., MCCARTHY, P. M. & BONOW, R. O. 2008. Evolving concepts and technologies in mitral valve repair. *Circulation*, 117, 963-974.
- FEINDEL, C. M., TUFAIL, Z., DAVID, T. E., IVANOV, J. & ARMSTRONG, S. 2003. Mitral valve surgery in patients with extensive calcification of the mitral annulus. *J Thorac Cardiovasc Surg*, 126, 777-782.
- FENSTER, B. E., BROWNING, J., SCHROEDER, J. D., SCHAFER, M., PODGORSKI, C. A., SMYSER, J., SILVEIRA, L. J., BUCKNER, J. K. & HERTZBERG, J. R. 2015. Vorticity is a marker of right ventricular diastolic dysfunction. *Am J Physiol Heart Circ Physiol*, 309, H1087-H1093.
- FERRING, V. & PANCHERZ, H. 2008. Divine proportions in the growing face. *Am J Orthod Dentofacial Orthop*, 134, 472-9.
- FORMAGGIA, L., PERKTOLD, K. & QUARTERONI, A. 2009. Basic mathematical models and motivations. In: FORMAGGIA, L., QUARTERONI, A. & VENEZIANI, A. (eds.) *Cardiovascular Mathematics: Modeling and simulation of the circulatory system*. Milano: Springer.
- FOUST, J. 2004. *Blood flow simulation past a catheter positioned in the SVC-IVC-RA junction : steady and unsteady flow considerations*. Master of Science, Lehigh University.
- FRANCOIS, C. J., SRINIVASAN, S., SCHIEBLER, M. L., REEDER, S. B., NIESPODZANY, E., LANDGRAF, B. R., WIEBEN, O. & FRYDRYCHOWICZ, A. 2012. 4D cardiovascular magnetic resonance velocity mapping of alterations of right heart flow patterns and main pulmonary artery hemodynamics in tetralogy of Fallot. *J Cardiovasc Magn Reson*, 14, 16.

GAO, H., FENG, L., QI, N., BERRY, C., GRIFFITH, B. E. & LUO, X. 2017a. A coupled mitral valve-left ventricle model with fluid-structure interaction. *Med Eng Phys*, 47, 128-136.

GAO, H., QI, N., FENG, L., MA, X., DANTON, M., BERRY, C. & LUO, X. 2017b. Modelling mitral valvular dynamics-current trend and future directions. *Int J Numer Method Biomed Eng*, 33, e2858.

GARBI, M. & MONAGHAN, M. J. 2015. Quantitative mitral valve anatomy and pathology. *Echo Res Pract*, 2, R63-72.

GE, L., MORREL, W. G., WARD, A., MISHRA, R., ZHANG, Z., GUCCIONE, J. M., GROSSI, E. A. & RATCLIFFE, M. B. 2014. Measurement of mitral leaflet and annular geometry and stress after repair of posterior leaflet prolapse: virtual repair using a patient-specific finite element simulation. *Ann Thorac Surg*, 97, 1496-503.

GELMAN, S. 2008. Venous function and central venous pressure: a physiologic story. *Anesthesiology*, 108, 735-48.

GILMORE, J. 2006. KDOQI clinical practice guidelines and clinical practice recommendations - 2006 updates. *Nephrology Nursing Journal*, 33, 487-488.

GO, A. S., CHERTOW, G. M., FAN, D., MCCULLOCH, C. E. & HSU, C. Y. 2004. Chronic kidney disease and the risks of death, cardiovascular events, and hospitalization. *N Engl J Med*, 351, 1296-305.

GOGOLADZE, G., DELLIS, S. L., DONNINO, R., RIBAKOVE, G., GREENHOUSE, D. G., GALLOWAY, A. & GROSSI, E. 2010. Analysis of the mitral coaptation zone in normal and functional regurgitant valves. *Ann Thorac Surg*, 89, 1158-61.

GOODMAN, A. A. 2004. Lectures 1 and 2: Cardiovascular System. In: COMPANY, T. T. (ed.) *Understanding the Human Body: An Introduction to Anatomy and Physiology*. Virginia, USA: The Great Courses.

GOODMAN, W. G., GOLDIN, J., KUIZON, B. D., YOON, C., GALES, B., SIDER, D., WANG, Y., CHUNG, J., EMERICK, A., GREASER, L., ELASHOFF, R. M. & SALUSKY, I. B. 2000. Coronary-artery calcification in young adults with end-stage renal disease who are undergoing dialysis. *N Engl J Med*, 342, 1478-83.

GRINBERG, D., COTTINET, P. J., THIVOLET, S., AUDIGIER, D., CAPSAL, J. F., LE, M. Q. & OBADIA, J. F. 2019. Measuring chordae tension during transapical neochordae implantation: Toward understanding objective consequences of mitral valve repair. *J Thorac Cardiovasc Surg*, 158, 746-755.

- KDIGO CKD Work Group. 2013. KDIGO 2012 Clinical Practice Guideline for the Evaluation and Management of Chronic Kidney Disease. *Kidney Int Suppl*, 3, 1-150.
- GULAN, U., SAGUNER, A., AKDIS, D., GOTSCHY, A., MANKA, R., BRUNCKHORST, C., HOLZNER, M. & DURU, F. 2017. Investigation of Atrial Vortices Using a Novel Right Heart Model and Possible Implications for Atrial Thrombus Formation. *Scientific Reports*, 7, 16772.
- GUMPANGSETH, T., LEKAWANVIJIT, S. & MAHAKKANUKRAUH, P. 2020. Histological assessment of the human heart valves and its relationship with age. *Anat Cell Biol*, 53, 261-271.
- GUO, Y., HE, Y., ZHANG, Y., GE, S., SUN, L., LIU, W., HAN, J. & GU, X. 2018. Assessment of the mitral valve coaptation zone with 2D and 3D transesophageal echocardiography before and after mitral valve repair. *J Thorac Dis*, 10, 283-290.
- HADIAN, M., CORCORAN, B. M., HAN, R. I., GROSSMANN, J. G. & BRADSHAW, J. P. 2007. Collagen organization in canine myxomatous mitral valve disease: an x-ray diffraction study. *Biophys J*, 93, 2472-2476.
- HALLQUIST, J. 2006a. LS-DYNA Keyword User's Manual. Livermore Software Technology Corporation: LSTC, USA.
- HALLQUIST, J. 2006b. LS-DYNA Theory Manual. Livermore Software Technology Corporation: LSTC, USA.
- HAMMER, P. E., VASILYEV, N. V., PERRIN, D. P., NIDO, P. J. D. & HOWE, R. D. Fast Image-based Model of Mitral Valve Closure for Surgical Planning. 2008. MIDAS Journal, Computational Biomechanics for Medicine (MICCAI 2008 Workshop), 15-26.
- HARMEL, E. K., REICHENSPURNER, H. & GIRDAUSKAS, E. 2018. Subannular reconstruction in secondary mitral regurgitation: a meta-analysis. *Heart*, 104, 1783-1790.
- HASSANI, K., KARIMI, A., DEHGHANI, A., TAVAKOLI GOLPAYGANI, A., ABDI, H. & ESPINO, D. M. 2019. Development of a fluid-structure interaction model to simulate mitral valve malcoaptation. *Perfusion*, 34, 225-230.
- HAYCOCK, G. B., SCHWARTZ, G. J. & WISOTSKY, D. H. 1978. Geometric method for measuring body surface area: a height-weight formula validated in infants, children, and adults. *J Pediatr*, 93, 62-66.
- HE, S., JIMENEZ, J., HE, Z. & YOGANATHAN, A. P. 2003. Mitral leaflet geometry perturbations with papillary muscle displacement and annular dilatation: an in-vitro study of ischemic mitral regurgitation. *J Heart Valve Dis*, 12, 300-307.

- HE, Z., RITCHIE, J., GRASHOW, J. S., SACKS, M. S. & YOGANATHAN, A. P. 2005. In vitro dynamic strain behavior of the mitral valve posterior leaflet. *J Biomech Eng*, 127, 504-511.
- HENEIN, M. Y., GOLDEN RATIO, C., ZHAO, Y., NICOLL, R., SUN, L., KHIR, A. W., FRANKLIN, K. & LINDQVIST, P. 2011. The human heart: application of the golden ratio and angle. *Int J Cardiol*, 150, 239-242.
- HERRING, N. & PATERSON, D. J. 2018. The cardiac cycle. *Levick's Introduction to Cardiovascular Physiology*. 6 ed.: CRC Press - Taylor & Francis Group.
- HIRTLE, D., GARCIA, J., BARKER, A. J. & GEIGER, J. 2016. Assessment of intracardiac flow and vorticity in the right heart of patients after repair of tetralogy of Fallot by flow-sensitive 4D MRI. *Eur Radiol*, 26, 3598-3607.
- HUANG, X. Y., DENG, L., ZUO, H., YANG, C., SONG, Y. H., LESPERANCE, M. & TANG, D. L. 2021. Comparisons of simulation results between passive and active fluid structure interaction models for left ventricle in hypertrophic obstructive cardiomyopathy. *Biomed Eng Online*, 20, 9.
- HWANG, H. S., KANG, S. H., CHOI, S. R., SUN, I. O., PARK, H. S. & KIM, Y. 2012. Comparison of the palindrome vs. step-tip tunneled hemodialysis catheter: a prospective randomized trial. *Semin Dial*, 25, 587-591.
- IONASEC, R. I., VOIGT, I., GEORGESCU, B., WANG, Y., HOULE, H., VEGA-HIGUERA, F., NAVAB, N. & COMANICIU, D. 2010. Patient-specific modeling and quantification of the aortic and mitral valves from 4-D cardiac CT and TEE. *IEEE Trans Med Imaging*, 29, 1636-1651.
- IOSA, M., FUSCO, A., MARCHETTI, F., MORONE, G., CALTAGIRONE, C., PAOLUCCI, S. & PEPPE, A. 2013. The golden ratio of gait harmony: repetitive proportions of repetitive gait phases. *Biomed Res Int*, 2013, 918642.
- ITO, K., ABE, Y., TAKAHASHI, Y., SHIMADA, Y., FUKUMOTO, H., MATSUMURA, Y., NARUKO, T., SHIBATA, T., YOSHIYAMA, M. & YOSHIKAWA, J. 2017. Mechanism of atrial functional mitral regurgitation in patients with atrial fibrillation: A study using three-dimensional transesophageal echocardiography. *J Cardiol*, 70, 584-590.
- ITOH, A., ENNIS, D. B., BOTHE, W., SWANSON, J. C., KRISHNAMURTHY, G., NGUYEN, T. C., INGELS, N. B., JR. & MILLER, D. C. 2009. Mitral annular hinge motion contribution to changes in mitral septal-lateral dimension and annular area. *J Thorac Cardiovasc Surg*, 138, 1090-1099.

- JASSAR, A. S., VERGNAT, M., JACKSON, B. M., MCGARVEY, J. R., CHEUNG, A. T., FERRARI, G., WOO, Y. J., ACKER, M. A., GORMAN, R. C. & GORMAN, J. H. 2014. Regional Annular Geometry in Patients With Mitral Regurgitation: Implications for Annuloplasty Ring Selection. *Ann Thorac Surg*, 97, 64-70.
- JENSEN, H., JENSEN, M. O., SMERUP, M. H., RINGGAARD, S., SORENSEN, T. S., ANDERSEN, N. T., WIERUP, P., HASENKAM, J. M. & NIELSEN, S. L. 2010. Three-dimensional assessment of papillary muscle displacement in a porcine model of ischemic mitral regurgitation. *J Thorac Cardiovasc Surg*, 140, 1312-1318.
- JENSEN, M. O., FONTAINE, A. A. & YOGANATHAN, A. P. 2001. Improved in vitro quantification of the force exerted by the papillary muscle on the left ventricular wall: three-dimensional force vector measurement system. *Ann Biomed Eng*, 29, 406-413.
- JHA, V., GARCIA-GARCIA, G., ISEKI, K., LI, Z., NAICKER, S., PLATTNER, B., SARAN, R., WANG, A. Y. & YANG, C. W. 2013. Chronic kidney disease: global dimension and perspectives. *Lancet*, 382, 260-272.
- JIANG, L., OWAIS, K., MATYAL, R., KHABBAZ, K. R., LIU, D. C., MONTEALEGRE-GALLEGOS, M., HESS, P. E. & MAHMOOD, F. 2014. Dynamism of the mitral annulus: a spatial and temporal analysis. *J Cardiothorac Vasc Anesth*, 28, 1191-1197.
- JIMENEZ, J. H., SOERENSEN, D. D., HE, Z., HE, S. & YOGANATHAN, A. P. 2003. Effects of a saddle shaped annulus on mitral valve function and chordal force distribution: an in vitro study. *Ann Biomed Eng*, 31, 1171-1181.
- JIMENEZ, J. H., SOERENSEN, D. D., HE, Z., RITCHIE, J. & YOGANATHAN, A. P. 2005. Mitral valve function and chordal force distribution using a flexible annulus model: an in vitro study. *Ann Biomed Eng*, 33, 557-566.
- JOLLEY, M. A., GHELANI, S. J., ADAR, A. & HARRILD, D. M. 2017. Three-Dimensional Mitral Valve Morphology and Age-Related Trends in Children and Young Adults with Structurally Normal Hearts Using Transthoracic Echocardiography. *J Am Soc Echocardiogr*, 30, 561-571.
- KAISER, A. D., MCQUEEN, D. M. & PESKIN, C. S. 2019. Modeling the mitral valve. *Int J Numer Method Biomed Eng*, e3240.
- KAKKOS, S. K., HADDAD, G. K., HADDAD, R. K. & SCULLY, M. M. 2008. Effectiveness of a new tunneled catheter in preventing catheter malfunction: a comparative study. *J Vasc Interv Radiol*, 19, 1018-1026.
- KHODAEI, S., FATOURAEE, N. & NABAEI, M. 2017. Numerical simulation of mitral valve prolapse considering the effect of left ventricle. *Math Biosci*, 285, 75-80.

- KIM, D. H., HEO, R., HANDSCHUMACHER, M. D., LEE, S., CHOI, Y. S., KIM, K. R., SHIN, Y., PARK, H. K., BISCHOFF, J., AIKAWA, E., SONG, J. M., KANG, D. H., LEVINE, R. A. & SONG, J. K. 2019. Mitral Valve Adaptation to Isolated Annular Dilation: Insights Into the Mechanism of Atrial Functional Mitral Regurgitation. *JACC Cardiovasc Imaging*, 12, 665-677.
- KIM, K., KAJI, S., AN, Y., NISHINO, T., TANI, T., KITAI, T. & FURUKAWA, Y. 2014. Interpapillary muscle distance independently affects severity of functional mitral regurgitation in patients with systolic left ventricular dysfunction. *J Thorac Cardiovasc Surg*, 148, 434-440 e1.
- KIM, K., KAJI, S., AN, Y., YOSHITANI, H., TAKEUCHI, M., LEVINE, R. A., OTSUJI, Y. & FURUKAWA, Y. 2012. Mechanism of asymmetric leaflet tethering in ischemic mitral regurgitation: 3D analysis with multislice CT. *JACC Cardiovasc Imaging*, 5, 230-232.
- KLAUS, S., KORFER, S., MOTTAGHY, K., REUL, H. & GLASMACHER, B. 2002. In vitro blood damage by high shear flow: human versus porcine blood. *Int J Artif Organs*, 25, 306-312.
- KNUTTINEN, M. G., BOBRA, S., HARDMAN, J., GABA, R. C., BUI, J. T. & OWENS, C. A. 2009. A review of evolving dialysis catheter technologies. *Semin Intervent Radiol*, 26, 106-114.
- KOHLI, K., WEI, Z. A., SADRI, V., NETTO, T., LISKO, J. C., GREENBAUM, A. B., BABALIAROS, V., OSHINSKI, J. N. & YOGANATHAN, A. P. 2021. A Simplified In Silico Model of Left Ventricular Outflow in Patients After Transcatheter Mitral Valve Replacement with Anterior Leaflet Laceration. *Ann Biomed Eng*, 49, 1449-1461.
- KONG, F., CABALLERO, A., MCKAY, R. & SUN, W. 2020. Finite element analysis of MitraClip procedure on a patient-specific model with functional mitral regurgitation. *J Biomech*, 104, 109730.
- KONG, F., PHAM, T., MARTIN, C., ELEFTERIADES, J., MCKAY, R., PRIMIANO, C. & SUN, W. 2018. Finite element analysis of annuloplasty and papillary muscle relocation on a patient-specific mitral regurgitation model. *PLoS One*, 13, e0198331.
- KRAMER, K. E., ROSS, C. J., LAURENCE, D. W., BABU, A. R., WU, Y., TOWNER, R. A., MIR, A., BURKHART, H. M., HOLZAPFEL, G. A. & LEE, C. H. 2019. An investigation of layer-specific tissue biomechanics of porcine atrioventricular valve anterior leaflets. *Acta Biomater*, 96, 368-384.

- KRAWCZYK-OZOG, A., HOLDA, M. K., SORYSZ, D., KOZIEJ, M., SIUDAK, Z., DUDEK, D. & KLIMEK-PIOTROWSKA, W. 2017. Morphologic variability of the mitral valve leaflets. *J Thorac Cardiovasc Surg*, 154, 1927-1935.
- KRISHNAMURTHY, G., ENNIS, D. B., ITOH, A., BOTHE, W., SWANSON, J. C., KARLSSON, M., KUHL, E., MILLER, D. C. & INGELS, N. B., JR. 2008. Material properties of the ovine mitral valve anterior leaflet in vivo from inverse finite element analysis. *Am J Physiol Heart Circ Physiol*, 295, H1141-H1149.
- KRISHNAMURTHY, G., ITOH, A., BOTHE, W., SWANSON, J. C., KUHL, E., KARLSSON, M., CRAIG MILLER, D. & INGELS, N. B., JR. 2009. Stress-strain behavior of mitral valve leaflets in the beating ovine heart. *J Biomech*, 42, 1909-1916.
- KROFT, L. J., SIMONS, P., VAN LAAR, J. M. & DE ROOS, A. 2000. Patients with pulmonary fibrosis: cardiac function assessed with MR imaging. *Radiology*, 216, 464-471.
- KROLL, M. H., HELLUMS, J. D., MCINTIRE, L. V., SCHAFER, A. I. & MOAKE, J. L. 1996. Platelets and shear stress. *Blood*, 88, 1525-1541.
- KUNKEL, M. E., SCHMIDT, H. & WILKE, H. J. 2010. Prediction equations for human thoracic and lumbar vertebral morphometry. *J Anat*, 216, 320-328.
- KUNZELMAN, K. S. & COCHRAN, R. P. 1990. Mechanical properties of basal and marginal mitral valve chordae tendineae. *ASAIO Trans*, 36, M405-408.
- KUNZELMAN, K. S. & COCHRAN, R. P. 1992. Stress/strain characteristics of porcine mitral valve tissue: parallel versus perpendicular collagen orientation. *J Card Surg*, 7, 71-78.
- KUNZELMAN, K. S., COCHRAN, R. P., CHUONG, C., RING, W. S., VERRIER, E. D. & EBERHART, R. D. 1993a. Finite element analysis of the mitral valve. *J Heart Valve Dis*, 2, 326-340.
- KUNZELMAN, K. S., COCHRAN, R. P., MURPHREE, S. S., RING, W. S., VERRIER, E. D. & EBERHART, R. C. 1993b. Differential collagen distribution in the mitral valve and its influence on biomechanical behaviour. *J Heart Valve Dis*, 2, 236-244.
- KUNZELMAN, K. S., EINSTEIN, D. R. & COCHRAN, R. P. 2007. Fluid-structure interaction models of the mitral valve: function in normal and pathological states. *Philos Trans R Soc Lond B Biol Sci*, 362, 1393-1406.
- KUNZELMAN, K. S., REIMINK, M. S. & COCHRAN, R. P. 1997. Annular dilatation increases stress in the mitral valve and delays coaptation: a finite element computer model. *Cardiovasc Surg*, 5, 427-434.

LAM, J. H., RANGANATHAN, N., WIGLE, E. D. & SILVER, M. D. 1970. Morphology of the human mitral valve. I. Chordae tendineae: a new classification. *Circulation*, 41, 449-458.

LAU, K. D. 2012. *Numerical Simulation of Mitral Valve Function*. Doctor of Philosophy in Mechanical Engineering, University College London.

LAZAM, S., VANOVERSCHDELDE, J. L., TRIBOUILLOY, C., GRIGIONI, F., SURI, R. M., AVIERINOS, J. F., DE MEESTER, C., BARBIERI, A., RUSINARU, D., RUSSO, A., PASQUET, A., MICHELENA, H. I., HUEBNER, M., MAALOUF, J., CLAVEL, M. A., SZYMANSKI, C., ENRIQUEZ-SARANO, M. & MIDA Investigators. 2017. Twenty-Year Outcome After Mitral Repair Versus Replacement for Severe Degenerative Mitral Regurgitation: Analysis of a Large, Prospective, Multicenter, International Registry. *Circulation*, 135, 410-422.

LEE, A. P., HSIUNG, M. C., SALGO, I. S., FANG, F., XIE, J. M., ZHANG, Y. C., LIN, Q. S., LOOI, J. L., WAN, S., WONG, R. H., UNDERWOOD, M. J., SUN, J. P., YIN, W. H., WEI, J., TSAI, S. K. & YU, C. M. 2013. Quantitative analysis of mitral valve morphology in mitral valve prolapse with real-time 3-dimensional echocardiography: importance of annular saddle shape in the pathogenesis of mitral regurgitation. *Circulation*, 127, 832-841.

LEE, C. H., RABBAH, J. P., YOGANATHAN, A. P., GORMAN, R. C., GORMAN, J. H., 3RD & SACKS, M. S. 2015. On the effects of leaflet microstructure and constitutive model on the closing behavior of the mitral valve. *Biomech Model Mechanobiol*, 14, 1281-302.

LEVACK, M. M., JASSAR, A. S., SHANG, E. K., VERGNAT, M., WOO, Y. J., ACKER, M. A., JACKSON, B. M., GORMAN, J. H., 3RD & GORMAN, R. C. 2012. Three-dimensional echocardiographic analysis of mitral annular dynamics: implication for annuloplasty selection. *Circulation*, 126, S183-188.

LEVICK, J. R. 2010. *An introduction to cardiovascular physiology*, 5th ed. London: Hodder Arnold.

LIAO, J. & VESELY, I. 2003. A structural basis for the size-related mechanical properties of mitral valve chordae tendineae. *J Biomech*, 36, 1125-1133.

LICHTENBERG, N., EULZER, P., ROMANO, G., BRCIC, A., KARCK, M., LAWONN, K., DE SIMONE, R. & ENGELHARDT, S. 2020. Mitral valve flattening and parameter mapping for patient-specific valve diagnosis. *Int J Comput Assist Radiol Surg*, 15, 617-627.

LIU, G. R. & QUEK, S. S. 2014. *The finite element method: a practical course*, 2nd ed. Butterworth-Heinemann.

LOK, C. E. & FOLEY, R. 2013. Vascular access morbidity and mortality: trends of the last decade. *Clin J Am Soc Nephrol*, 8, 1213-1219.

LOMHOLT, M., NIELSEN, S. L., HANSEN, S. B., ANDERSEN, N. T. & HASENKAM, J. M. 2002. Differential tension between secondary and primary mitral chordae in an acute in-vivo porcine model. *J Heart Valve Dis*, 11, 337-345.

LOPEZ, L., COLAN, S., STYLIANOU, M., GRANGER, S., TRACHTENBERG, F., FROMMELT, P., PEARSON, G., CAMARDA, J., CNOTA, J., COHEN, M., DRAGULESCU, A., FROMMELT, M., GARUBA, O., JOHNSON, T., LAI, W., MAHGEREFTEH, J., PIGNATELLI, R., PRAKASH, A., SACHDEVA, R., SORIANO, B., SOSLOW, J., SPURNEY, C., SRIVASTAVA, S., TAYLOR, C., THANKAVEL, P., VAN DER VELDE, M., MINICH, L. & Pediatric Heart Network Investigators. 2017. Relationship of Echocardiographic Z Scores Adjusted for Body Surface Area to Age, Sex, Race, and Ethnicity: The Pediatric Heart Network Normal Echocardiogram Database. *Circ Cardiovasc Imaging*, 10, e006979.

LUCAS, T. C., TESSAROLO, F., JAKITSCH, V., CAOLA, I., BRUNORI, G., NOLLO, G. & HUEBNER, R. 2014. Blood flow in hemodialysis catheters: a numerical simulation and microscopic analysis of in vivo-formed fibrin. *Artif Organs*, 38, 556-565.

MAFFESENTI, F., GRIPARI, P., PONTONE, G., ANDREINI, D., BERTELLA, E., MUSHTAQ, S., TAMBORINI, G., FUSINI, L., PEPI, M. & CAIANI, E. G. 2013. Three-dimensional dynamic assessment of tricuspid and mitral annuli using cardiovascular magnetic resonance. *Eur Heart J Cardiovasc Imaging*, 14, 986-995.

MAGANTI, K., RIGOLIN, V. H., SARANO, M. E. & BONOW, R. O. 2010. Valvular heart disease: diagnosis and management. *Mayo Clin Proc*, 85, 483-500.

MAHADEVIA, R., BARKER, A. J., SCHNELL, S., ENTEZARI, P., KANSAL, P., FEDAK, P. W., MALAISRIE, S. C., MCCARTHY, P., COLLINS, J., CARR, J. & MARKL, M. 2014. Bicuspid aortic cusp fusion morphology alters aortic three-dimensional outflow patterns, wall shear stress, and expression of aortopathy. *Circulation*, 129, 673-682.

MAHLON, M. A. & YOON, H. C. 2007. CT angiography of the superior vena cava: normative values and implications for central venous catheter position. *J Vasc Interv Radiol*, 18, 1106-1110.

MALAS, M. B., CANNER, J. K., HICKS, C. W., ARHUIDESE, I. J., ZARKOWSKY, D. S., QAZI, U., SCHNEIDER, E. B., BLACK, J. H., 3RD, SEGEV, D. L. & FREISCHLAG, J. A. 2015. Trends in incident hemodialysis access and mortality. *JAMA Surg*, 150, 441-448.

MANSI, T., VOIGT, I., ASSOUMOU MENGUE, E., IONASEC, R., GEORGESCU, B., NOACK, T., SEEBURGER, J. & COMANICIU, D. 2011. Towards patient-specific finite-element simulation of MitralClip procedure. *Med Image Comput Comput Assist Interv*, 14, 452-459.

- MANSI, T., VOIGT, I., GEORGESCU, B., ZHENG, X., MENGUE, E. A., HACKL, M., IONASEC, R. I., NOACK, T., SEEBURGER, J. & COMANICIU, D. 2012. An integrated framework for finite-element modeling of mitral valve biomechanics from medical images: application to MitralClip intervention planning. *Med Image Anal*, 16, 1330-1346.
- MAO, W., CABALLERO, A., MCKAY, R., PRIMIANO, C. & SUN, W. 2017. Fully-coupled fluid-structure interaction simulation of the aortic and mitral valves in a realistic 3D left ventricle model. *PLoS One*, 12, e0184729.
- MAREELS, G., DE WACHTER, D. S. & VERDONCK, P. R. 2004. Computational fluid dynamics-analysis of the Niagara hemodialysis catheter in a right heart model. *Artif Organs*, 28, 639-648.
- MAREELS, G., KAMINSKY, R., ELOOT, S. & VERDONCK, P. R. 2007. Particle image velocimetry-validated, computational fluid dynamics-based design to reduce shear stress and residence time in central venous hemodialysis catheters. *ASAIO J*, 53, 438-446.
- MASON, J. W., RAMSETH, D. J., CHANTER, D. O., MOON, T. E., GOODMAN, D. B. & MENDZELEVSKI, B. 2007. Electrocardiographic reference ranges derived from 79,743 ambulatory subjects. *J Electrocardiol*, 40, 228-234.
- MATHEW, E., DOMINGUEZ-ROBLES, J., STEWART, S. A., MANCUSO, E., O'DONNELL, K., LARRANETA, E. & LAMPROU, D. A. 2019. Fused Deposition Modeling as an Effective Tool for Anti-Infective Dialysis Catheter Fabrication. *Acs Biomater Sci Eng*, 5, 6300-6310.
- MAY-NEWMAN, K. & YIN, F. C. 1998. A constitutive law for mitral valve tissue. *J Biomech Eng*, 120, 38-47.
- MCCARTHY, K. P., RING, L. & RANA, B. S. 2010. Anatomy of the mitral valve: understanding the mitral valve complex in mitral regurgitation. *Eur J Echocardiogr*, 11, i3-9.
- MIHAILA, S., MURARU, D., CASABLANA, S., PELUSO, D., CUCCHINI, U., DEL BIANCO, L., VINEREANU, D., ILICETO, S., BADANO, L. 2013. Three-dimensional changes in mitral valve annulus geometry in organic and functional mitral regurgitation: insights for mitral valve repair. *Eur. Heart J.*, 34, 4751.
- MIHAILA, S., MURARU, D., PIASENTINI, E., MIGLIORANZA, M. H., PELUSO, D., CUCCHINI, U., ILICETO, S., VINEREANU, D. & BADANO, L. P. 2014. Quantitative analysis of mitral annular geometry and function in healthy volunteers using transthoracic three-dimensional echocardiography. *J Am Soc Echocardiogr*, 27, 846-857.

MIHOS, C. G., YUCEL, E. & SANTANA, O. 2017. The role of papillary muscle approximation in mitral valve repair for the treatment of secondary mitral regurgitation. *Eur J Cardiothorac Surg*, 51, 1023-1030.

MILLINGTON-SANDERS, C., MEIR, A., LAWRENCE, L. & STOLINSKI, C. 1998. Structure of chordae tendineae in the left ventricle of the human heart. *J Anat*, 192 (Pt 4), 573-581.

MISFELD, M. & SIEVERS, H. H. 2007. Heart valve macro- and microstructure. *Philos Trans R Soc Lond B Biol Sci*, 362, 1421-1436.

MOERMAN, K. M. 2018. GIBBON: The Geometry and Image-Based Bioengineering add-On. *JOSS*, 3, 506.

MORRIS, P. D., NARRACOTT, A., VON TENGG-KOBLIGK, H., SILVA SOTO, D. A., HSIAO, S., LUNGU, A., EVANS, P., BRESSLOFF, N. W., LAWFORD, P. V., HOSE, D. R. & GUNN, J. P. 2016. Computational fluid dynamics modelling in cardiovascular medicine. *Heart*, 102, 18-28.

MUNIN, M. A., THIERER, J., RAGGIO, I. M., GOERNER, M. S., LOMBARDERO, M., GODIA, J., SÁNCHEZ, G. A., SPERNANZONI, F., ORTEGA, J. & TORRES, V. 2014. Three Dimensional Echocardiographic Analysis of Mitral Valve Characteristics. *Rev Argent Cardiol*, 82, 279-284.

NCHO, B. E., PIERCE, E. L., BLOODWORTH, C. H. T., IMAI, A., OKAMOTO, K., SAITO, Y., GORMAN, R. C., GORMAN, J. H., 3RD & YOGANATHAN, A. P. 2020. Optimized mitral annuloplasty ring design reduces loading in the posterior annulus. *J Thorac Cardiovasc Surg*, 159, 1766-1774 e2.

NHS. 2016. NHS Digital Health Survey for England [Online]. <https://digital.nhs.uk/data-and-information/publications/statistical/health-survey-for-england/health-survey-for-england-2016>. [Accessed 1 Oct 2021].

NIEDERER, S. A., LUMENS, J. & TRAYANOVA, N. A. 2019. Computational models in cardiology. *Nat Rev Cardiol*, 16, 100-111.

NIELSEN, S. L., TIMEK, T. A., GREEN, G. R., DAGUM, P., DAUGHTERS, G. T., HASENKAM, J. M., BOLGER, A. F., INGELS, N. B. & MILLER, D. C. 2003. Influence of anterior mitral leaflet second-order chordae tendineae on left ventricular systolic function. *Circulation*, 108, 486-491.

NIELSEN, S. L., TIMEK, T. A., LAI, D. T., DAUGHTERS, G. T., LIANG, D., HASENKAM, J. M., INGELS, N. B. & MILLER, D. C. 2001. Edge-to-edge mitral repair: tension on the approximating suture and leaflet deformation during acute ischemic mitral regurgitation in the ovine heart. *Circulation*, 104, 129-35.

NOMURA, K., AJIRO, Y., NAKANO, S., MATSUSHIMA, M., YAMAGUCHI, Y., HATAKEYAMA, N., OHATA, M., SAKUMA, M., NONAKA, T., HARII, M., UTSUMI, M., SAKAMOTO, K., IWADE, K. & KUNINAKA, N. 2019. Characteristics of mitral valve leaflet length in patients with pectus excavatum: A single center cross-sectional study. *PLoS One*, 14, e0212165.

OBADIA, J. F., CASALI, C., CHASSIGNOLLE, J. F. & JANIER, M. 1997. Mitral subvalvular apparatus: different functions of primary and secondary chordae. *Circulation*, 96, 3124-3128.

OBADIA, J. F., MESSIKA-ZEITOUN, D., LEURENT, G., IUNG, B., BONNET, G., PIRIOU, N., LEFEVRE, T., PIOT, C., ROULEAU, F., CARRIE, D., NEJJARI, M., OHLMANN, P., LECLERCQ, F., SAINT ETIENNE, C., TEIGER, E., LEROUX, L., KARAM, N., MICHEL, N., GILARD, M., DONAL, E., TROCHU, J. N., CORMIER, B., ARMOIRY, X., BOUTITIE, F., MAUCORT-BOULCH, D., BARNEL, C., SAMSON, G., GUERIN, P., VAHANIAN, A., MEWTON, N. & MITRA-FR Investigators. 2018. Percutaneous Repair or Medical Treatment for Secondary Mitral Regurgitation. *N Engl J Med*, 379, 2297-2306.

OBASE, K., JEEVANANDAM, V., SAITO, K., KESNER, K., BARRY, A., HOLLATZ, A., FAROOQUI, F., ADDETIA, K., ROBERTS, J. D., OTA, T., BALKHY, H. H., YOSHIDA, K., MOR-AVI, V. & LANG, R. M. 2015. Visualization and measurement of mitral valve chordae tendineae using three-dimensional transesophageal echocardiography from the transgastric approach. *J Am Soc Echocardiogr*, 28, 449-454.

OBASE, K., WEINERT, L., HOLLATZ, A., FAROOQUI, F., ROBERTS, J. D., MINHAI, M. M., TUNG, A., CHANEY, M., OTA, T., JEEVANANDAM, V., YOSHIDA, K., MOR-AVI, V. & LANG, R. M. 2016. Elongation of chordae tendineae as an adaptive process to reduce mitral regurgitation in functional mitral regurgitation. *Eur Heart J Cardiovasc Imaging*, 17, 500-509.

OKAMOTO, H., ITOH, Y. & NARA, Y. 2007. Geometric analysis of the anterior mitral leaflet and mitral valve orifice in cadaveric hearts. *Circ J*, 71, 1794-1799.

OLIVEIRA, D., ROSA, S. A., TIAGO, J., FERREIRA, R. C., AGAPITO, A. F. & SEQUEIRA, A. 2019. Bicuspid aortic valve aortopathies: An hemodynamics characterization in dilated aortas. *Comput Methods Biomech Biomed Engin*, 22, 815-826.

- ORIMADEGUN, A. & OMISANJO, A. 2014. Evaluation of five formulae for estimating body surface area of nigerian children. *Ann Med Health Sci Res*, 4, 889-898.
- OTTO, C. M. 2001. Clinical practice. Evaluation and management of chronic mitral regurgitation. *N Engl J Med*, 345, 740-746.
- OWEN, B., BOJDO, N., JIVKOV, A., KEAVNEY, B. & REVELL, A. 2018. Structural modelling of the cardiovascular system. *Biomech Model Mechanobiol*, 17, 1217-1242.
- OWEN, D. G., DE OLIVEIRA, D. C., QIAN, S., GREEN, N. C., SHEPHERD, D. E. T. & ESPINO, D. M. 2020a. Impact of side-hole geometry on the performance of hemodialysis catheter tips: A computational fluid dynamics assessment. *PLoS One*, 15, e0236946.
- OWEN, D. G., SCHENKEL, T., SHEPHERD, D. E. T. & ESPINO, D. M. 2020b. Assessment of surface roughness and blood rheology on local coronary haemodynamics: a multi-scale computational fluid dynamics study. *J R Soc Interface*, 17, 20200327.
- PADALA, M., SACKS, M. S., LIOU, S. W., BALACHANDRAN, K., HE, Z. & YOGANATHAN, A. P. 2010. Mechanics of the mitral valve strut chordae insertion region. *J Biomech Eng*, 132, 081004.
- PANNU, N., JHANGRI, G. S. & TONELLI, M. 2006. Optimizing dialysis delivery in tunneled dialysis catheters. *Asaio J*, 52, 157-162.
- PAPATHANASOPOULOU, P., ZHAO, S., KOHLER, U., ROBERTSON, M. B., LONG, Q., HOSKINS, P., XU, X. Y. & MARSHALL, I. 2003. MRI measurement of time-resolved wall shear stress vectors in a carotid bifurcation model, and comparison with CFD predictions. *J Magn Reson Imaging*, 17, 153-62.
- PARATO, V. M. & MASIA, S. L. 2018. Hypoplasia or Absence of Posterior Leaflet: A Rare Congenital Anomaly of The Mitral Valve in Adulthood - Case Series. *J Cardiovasc Echogr*, 28, 45-47.
- PARIKH, J. D., KAKARLA, J., KEAVNEY, B., O'SULLIVAN, J. J., FORD, G. A., BLAMIRE, A. M., HOLLINGSWORTH, K. G. & COATS, L. 2017. 4D flow MRI assessment of right atrial flow patterns in the normal heart - influence of caval vein arrangement and implications for the patent foramen ovale. *PLoS One*, 12, e0173046.
- PARK, J., GEIRSSON, A. & BONDE, P. N. 2019. Mathematical Blueprint of a Mitral Valve. *Semin Thorac Cardiovasc Surg*. 31, 399-411.

- PARKER, K. & THIRIET, M. 2009. Physiology and pathology of the cardiovascular system: a physical perspective. *In*: FORMAGGIA, L., QUARTERONI, A. & VENEZIANI, A. (eds.) *Cardiovascular Mathematics. Modeling and simulation of the circulatory system*. Milano: Springer.
- PASTA, S., CANNATA, S., GENTILE, G., AGNESE, V., PILATO, M. & GANDOLFO, C. 2020. Simulation of left ventricular outflow tract (LVOT) obstruction in transcatheter mitral valve-in-ring replacement. *Med Eng Phys*, 82, 40-48.
- PATIL, S., JADHAV, S., SHETTY, N., KHARGE, J., PUTTEGOWDA, B., RAMALINGAM, R. & CHOLENAHALLY, M. N. 2016. Assessment of inferior vena cava diameter by echocardiography in normal Indian population: A prospective observational study. *Indian Heart J*, 68 Suppl 3, S26-S30.
- PAULSEN, M. J., BAE, J. H., IMBRIE-MOORE, A. M., WANG, H., HIRONAKA, C. E., FARRY, J. M., LUCIAN, H., THAKORE, A. D., CUTKOSKY, M. R. & JOSEPH WOO, Y. 2020. Development and Ex Vivo Validation of Novel Force-Sensing Neochordae for Measuring Chordae Tendineae Tension in the Mitral Valve Apparatus Using Optical Fibers With Embedded Bragg Gratings. *J Biomech Eng*, 142, 0145011-9.
- PAULSEN, M. J., IMBRIE-MOORE, A. M., WANG, H., BAE, J. H., HIRONAKA, C. E., FARRY, J. M., LUCIAN, H. J., THAKORE, A. D., MACARTHUR, J. W., CUTKOSKY, M. R. & WOO, Y. J. 2019. Mitral chordae tendineae force profile characterization using a posterior ventricular anchoring neochordal repair model for mitral regurgitation in a three-dimensional-printed ex vivo left heart simulator. *Eur J Cardiothorac Surg*, 57, 535-544.
- PETTERSEN, M. D., DU, W., SKEENS, M. E. & HUMES, R. A. 2008. Regression equations for calculation of z scores of cardiac structures in a large cohort of healthy infants, children, and adolescents: an echocardiographic study. *J Am Soc Echocardiogr*, 21, 922-934.
- PHAM, T., KONG, F., MARTIN, C., WANG, Q., PRIMIANO, C., MCKAY, R., ELEFTERIADES, J. & SUN, W. 2017. Finite Element Analysis of Patient-Specific Mitral Valve with Mitral Regurgitation. *Cardiovasc Eng Technol*, 8, 3-16.
- PIBAROT, P., DELGADO, V. & BAX, J. J. 2019. MITRA-FR vs. COAPT: lessons from two trials with diametrically opposed results. *Eur Heart J Cardiovasc Imaging*, 20, 620-624.
- POUCH, A. M., VERGNAT, M., MCGARVEY, J. R., FERRARI, G., JACKSON, B. M., SEHGAL, C. M., YUSHKEVICH, P. A., GORMAN, R. C. & GORMAN, J. H. 2014. Statistical Assessment of Normal Mitral Annular Geometry Using Automated Three-Dimensional Echocardiographic Analysis. *Ann Thorac Surg*, 97, 71-77.

- PROT, V. & SKALLERUD, B. 2017. Contributions of prestrains, hyperelasticity, and muscle fiber activation on mitral valve systolic performance. *Int J Numer Method Biomed Eng*, 33, e2806.
- PROT, V., HAAVERSTAD, R. & SKALLERUD, B. 2009. Finite element analysis of the mitral apparatus: annulus shape effect and chordal force distribution. *Biomech Model Mechanobiol*, 8, 43-55.
- PROT, V., SKALLERUD, B. & HOLZAPFEL, G. A. 2007. Transversely isotropic membrane shells with application to mitral valve mechanics. Constitutive modelling and finite element implementation. *Int J Numer Methods Eng*, 71, 987-1008.
- PROT, V., SKALLERUD, B., SOMMER, G. & HOLZAPFEL, G. A. 2010. On modelling and analysis of healthy and pathological human mitral valves: two case studies. *J Mech Behav Biomed Mater*, 3, 167-177.
- QUAPP, K. M. & WEISS, J. A. 1998. Material characterization of human medial collateral ligament. *J Biomech Eng*, 120, 757-763.
- RABBAH, J. P., CHISM, B., SIEFERT, A., SAIKRISHNAN, N., VELEDAR, E., THOURANI, V. H. & YOGANATHAN, A. P. 2013. Effects of targeted papillary muscle relocation on mitral leaflet tenting and coaptation. *Ann Thorac Surg*, 95, 621-628.
- RANGANATHAN, N., LAM, J. H., WIGLE, E. D. & SILVER, M. D. 1970. Morphology of the human mitral valve. II. The valve leaflets. *Circulation*, 41, 459-467.
- RAPP, B. E. 2017. Chapter 31 - Finite Volume Method. In: RAPP, B. E. (ed.) *Microfluidics: Modeling, Mechanics and Mathematics*. Elsevier.
- RAUSCH, M. K. & KUHL, E. 2013. On the effect of prestrain and residual stress in thin biological membranes. *J Mech Phys Solids*, 61, 1955-1969.
- RAUSCH, M. K., BOTHE, W., KVITTING, J. P., SWANSON, J. C., INGELS, N. B., JR., MILLER, D. C. & KUHL, E. 2011. Characterization of mitral valve annular dynamics in the beating heart. *Ann Biomed Eng*, 39, 1690-1702.
- RAUSCH, M. K., FAMAHEY, N., SHULTZ, T. O., BOTHE, W., MILLER, D. C. & KUHL, E. 2013. Mechanics of the mitral valve: a critical review, an in vivo parameter identification, and the effect of prestrain. *Biomech Model Mechanobiol*, 12, 1053-1071.
- REDLARSKI, G., PALKOWSKI, A. & KRAWCZUK, M. 2016. Body surface area formulae: an alarming ambiguity. *Sci Rep*, 6, 27966.

- Reference Values for Arterial Stiffness' Collaboration. 2010. Determinants of pulse wave velocity in healthy people and in the presence of cardiovascular risk factors: 'establishing normal and reference values'. *Eur Heart J*, 31, 2338-2350.
- REGO, B. V., KHALIGHI, A. H., DRACH, A., LAI, E. K., POUCH, A. M., GORMAN, R. C., GORMAN, J. H., 3RD & SACKS, M. S. 2018. A noninvasive method for the determination of in vivo mitral valve leaflet strains. *Int J Numer Method Biomed Eng*, 34, e3142.
- RIGATELLI, G., ZUIN, M. & FONG, A. 2018. Computational Flow Dynamic Analysis of Right and Left Atria in Patent Foramen Ovale: Potential Links with Atrial Fibrillation. *J Atr Fibrillation*, 10, 1852.
- RIM, Y., CHOI, A., MCPHERSON, D. D. & KIM, H. 2015. Personalized Computational Modeling of Mitral Valve Prolapse: Virtual Leaflet Resection. *PLoS One*, 10, e0130906.
- RIM, Y., MCPHERSON, D. D. & KIM, H. 2014. Effect of leaflet-to-chordae contact interaction on computational mitral valve evaluation. *Biomed Eng Online*, 13, 31.
- RIM, Y., MCPHERSON, D. D., CHANDRAN, K. B. & KIM, H. 2013. The effect of patient-specific annular motion on dynamic simulation of mitral valve function. *J Biomech*, 46, 1104-1112.
- RINAUDO, A. & PASTA, S. 2014. Regional variation of wall shear stress in ascending thoracic aortic aneurysms. *Proc Inst Mech Eng H*, 228, 627-638.
- RITCHIE, J., WARNOCK, J. N. & YOGANATHAN, A. P. 2005. Structural characterization of the chordae tendineae in native porcine mitral valves. *Ann Thorac Surg*, 80, 189-197.
- ROSS, C. J., HSU, M. C., BAUMWART, R., MIR, A., BURKHART, H. M., HOLZAPFEL, G. A., WU, Y. & LEE, C. H. 2021. Quantification of load-dependent changes in the collagen fiber architecture for the strut chordae tendineae-leaflet insertion of porcine atrioventricular heart valves. *Biomech Model Mechanobiol*, 20, 223-241.

ROTH, G. A., MENSAH, G. A., JOHNSON, C. O., ADDOLORATO, G., AMMIRATI, E., BADDOUR, L. M., BARENGO, N. C., BEATON, A. Z., BENJAMIN, E. J., BENZIGER, C. P., BONNY, A., BRAUER, M., BRODMANN, M., CAHILL, T. J., CARAPETIS, J., CATAPANO, A. L., CHUGH, S. S., COOPER, L. T., CORESH, J., CRIQUI, M., DECLEENE, N., EAGLE, K. A., EMMONS-BELL, S., FEIGIN, V. L., FERNANDEZ-SOLA, J., FOWKES, G., GAKIDOU, E., GRUNDY, S. M., HE, F. J., HOWARD, G., HU, F., INKER, L., KARTHIKEYAN, G., KASSEBAUM, N., KOROSHETZ, W., LAVIE, C., LLOYD-JONES, D., LU, H. S., MIRIJELLO, A., TEMESGEN, A. M., MOKDAD, A., MORAN, A. E., MUNTNER, P., NARULA, J., NEAL, B., NTSEKHE, M., MORAES DE OLIVEIRA, G., OTTO, C., OWOLABI, M., PRATT, M., RAJAGOPALAN, S., REITSMA, M., RIBEIRO, A. L. P., RIGOTTI, N., RODGERS, A., SABLE, C., SHAKIL, S., SLIWA-HAHNLE, K., STARK, B., SUNDSTROM, J., TIMPEL, P., TLEYJEH, I. M., VALGIMIGLI, M., VOS, T., WHELTON, P. K., YACoub, M., ZUHLKE, L., MURRAY, C., FUSTER, V. & GROUP, G.-N.-J. G. B. O. C. D. W. 2020. Global Burden of Cardiovascular Diseases and Risk Factors, 1990-2019: Update From the GBD 2019 Study. *J Am Coll Cardiol*, 76, 2982-3021.

RUDSKI, L. G., LAI, W. W., AFILALO, J., HUA, L., HANDSCHUMACHER, M. D., CHANDRASEKARAN, K., SOLOMON, S. D., LOUIE, E. K. & SCHILLER, N. B. 2010. Guidelines for the echocardiographic assessment of the right heart in adults: a report from the American Society of Echocardiography endorsed by the European Association of Echocardiography, a registered branch of the European Society of Cardiology, and the Canadian Society of Echocardiography. *J Am Soc Echocardiogr*, 23, 685-713; quiz 786-8.

SACKS, M. S. & YOGANATHAN, A. P. 2007. Heart valve function: a biomechanical perspective. *Philos Trans R Soc Lond B Biol Sci*, 362, 1369-1391.

SACKS, M. S., DAVID MERRYMAN, W. & SCHMIDT, D. E. 2009. On the biomechanics of heart valve function. *J Biomech*, 42, 1804-1824.

SACKS, M. S., HE, Z., BAIJENS, L., WANANT, S., SHAH, P., SUGIMOTO, H. & YOGANATHAN, A. P. 2002. Surface strains in the anterior leaflet of the functioning mitral valve. *Ann Biomed Eng*, 30, 1281-1290.

SAHA, A. & ROY, S. 2018. Papillary muscles of left ventricle-Morphological variations and it's clinical relevance. *Indian Heart J*, 70, 894-900.

SAITO, K., OKURA, H., WATANABE, N., OBASE, K., TAMADA, T., KOYAMA, T., HAYASHIDA, A., NEISHI, Y., KAWAMOTO, T. & YOSHIDA, K. 2012. Influence of chronic tethering of the mitral valve on mitral leaflet size and coaptation in functional mitral regurgitation. *JACC Cardiovasc Imaging*, 5, 337-345.

- SAKAI, T., OKITA, Y., UEDA, Y., TAHATA, T., OGINO, H., MATSUYAMA, K. & MIKI, S. 1999. Distance between mitral annulus and papillary muscles: anatomic study in normal human hearts. *J Thorac Cardiovasc Surg*, 118, 636-641.
- SALGO, I. S., GORMAN, J. H., 3RD, GORMAN, R. C., JACKSON, B. M., BOWEN, F. W., PLAPPERT, T., ST JOHN SUTTON, M. G. & EDMUNDS, L. H., JR. 2002. Effect of annular shape on leaflet curvature in reducing mitral leaflet stress. *Circulation*, 106, 711-717.
- SANTORO, D., BENEDETTO, F., MONDELLO, P., PIPITO, N., BARILLA, D., SPINELLI, F., RICCIARDI, C. A., CERNARO, V. & BUEMI, M. 2014. Vascular access for hemodialysis: current perspectives. *Int J Nephrol Renovasc Dis*, 7, 281-294.
- SCHINDELIN, J., ARGANDA-CARRERAS, I., FRISE, E., KAYNIG, V., LONGAIR, M., PIETZSCH, T., PREIBISCH, S., RUEDEN, C., SAALFELD, S., SCHMID, B., TINEVEZ, J. Y., WHITE, D. J., HARTENSTEIN, V., ELICEIRI, K., TOMANCAK, P. & CARDONA, A. 2012. Fiji: an open-source platform for biological-image analysis. *Nat Methods*, 9, 676-682.
- SCHNEIDER, R. J., TENENHOLTZ, N. A., PERRIN, D. P., MARX, G. R., DEL NIDO, P. J. & HOWE, R. D. 2011. Patient-specific mitral leaflet segmentation from 4D ultrasound. *Med Image Comput Comput Assist Interv*, 14, 520-527.
- SCHULTS, J. A., KLEIDON, T., PETSKY, H. L., STONE, R., SCHOUTROP, J. & ULLMAN, A. J. 2019. Peripherally inserted central catheter design and material for reducing catheter failure and complications. *Cochrane Database Syst Rev*, 7, CD013366.
- SEDRANSK, K. L., GRANDE-ALLEN, K. J. & VESELY, I. 2002. Failure mechanics of mitral valve chordae tendineae. *J Heart Valve Dis*, 11, 644-650.
- SENECHAL, M., MICHAUD, N., MACHAALANY, J., BERNIER, M., DUBOIS, M., MAGNE, J., COUTURE, C., MATHIEU, P., BERTRAND, O. F. & VOISINE, P. 2012. Relation of mitral valve morphology and motion to mitral regurgitation severity in patients with mitral valve prolapse. *Cardiovasc Ultrasound*, 10, 3.
- SHAH, B., VILLABLANCA, P. A., VEMULAPALLI, S., MANANDHAR, P., AMOROSO, N. S., SARIC, M., STANILOAE, C. & WILLIAMS, M. R. 2019. Outcomes After Transcatheter Mitral Valve Repair in Patients With Renal Disease. *Circ Cardiovasc Interv*, 12, e007552.
- SHEN, X., WANG, T., CAO, X. & CAI, L. 2017. The geometric model of the human mitral valve. *PLoS One*, 12, e0183362.
- SHEWCHUK, J. R. 2002. What is a Good Linear Element? Interpolation, Conditioning, and Quality Measures. Eleventh International Meshing Roundtable. 115-126.

- SHINBANE, J. S. & SAXON, L. A. 2018. Virtual medicine: Utilization of the advanced cardiac imaging patient avatar for procedural planning and facilitation. *J Cardiovasc Comput Tomogr*, 12, 16-27.
- SILBIGER, J. J. 2011. Mechanistic insights into ischemic mitral regurgitation: echocardiographic and surgical implications. *J Am Soc Echocardiogr*, 24, 707-19.
- SLUYSMANS, T. & COLAN, S. D. 2005. Theoretical and empirical derivation of cardiovascular allometric relationships in children. *J Appl Physiol* (1985), 99, 445-457.
- SMITH, R. N. & NOLAN, J. P. 2013. Central venous catheters. *BMJ*, 347, f6570.
- SONNE, C., SUGENG, L., WATANABE, N., WEINERT, L., SAITO, K., TSUKIJI, M., YOSHIDA, K., TAKEUCHI, M., MOR-AVI, V. & LANG, R. M. 2009. Age and body surface area dependency of mitral valve and papillary apparatus parameters: assessment by real-time three-dimensional echocardiography. *Eur J Echocardiogr*, 10, 287-294.
- SOUSA UVA, M., GRARE, P., JEBARA, V., FUZELIER, J. F., PORTOGHESE, M., ACAR, C., RELLAND, J., MIHAILEANU, S., FABIANI, J. N. & CARPENTIER, A. 1993. Transposition of chordae in mitral valve repair. Mid-term results. *Circulation*, 88, II35-38.
- STEVANELLA, M., MAFFESSANTI, F., CONTI, C. A., VOTTA, E., ARNOLDI, A., LOMBARDI, M., PARODI, O., CAIANI, E. G. & REDAELLI, A. 2011. Mitral Valve Patient-Specific Finite Element Modeling from Cardiac MRI: Application to an Annuloplasty Procedure. *Cardiovascular Engineering and Technology*, 2, 66-76.
- STEVANELLA, M., VOTTA, E. & REDAELLI, A. 2009. Mitral valve finite element modeling: implications of tissues' nonlinear response and annular motion. *J Biomech Eng*, 131, 121010.
- STEVENS, P. E., O'DONOGHUE, D. J., DE LUSIGNAN, S., VAN VLYMEN, J., KLEBE, B., MIDDLETON, R., HAGUE, N., NEW, J. & FARMER, C. K. 2007. Chronic kidney disease management in the United Kingdom: NEOERICA project results. *Kidney Int*, 72, 92-99.
- STONE, G. W., LINDENFELD, J., ABRAHAM, W. T., KAR, S., LIM, D. S., MISHELL, J. M., WHISENANT, B., GRAYBURN, P. A., RINALDI, M., KAPADIA, S. R., RAJAGOPAL, V., SAREMBOCK, I. J., BRIEKE, A., MARX, S. O., COHEN, D. J., WEISSMAN, N. J., MACK, M. J. & COAPT Investigators. 2018. Transcatheter Mitral-Valve Repair in Patients with Heart Failure. *N Engl J Med*, 379, 2307-2318.
- STONE, G. W., VAHANIAN, A. S., ADAMS, D. H., ABRAHAM, W. T., BORER, J. S., BAX, J. J., SCHOFER, J., CUTLIP, D. E., KRUCOFF, M. W., BLACKSTONE, E. H., GENEREUX, P., MACK, M. J., SIEGEL, R. J., GRAYBURN, P. A., ENRIQUEZ-

SARANO, M., LANCELLOTTI, P., FILIPPATOS, G., KAPPETEIN, A. P. & Mitral Valve Research Consortium (MVARC). 2015. Clinical Trial Design Principles and Endpoint Definitions for Transcatheter Mitral Valve Repair and Replacement: Part 1: Clinical Trial Design Principles: A Consensus Document From the Mitral Valve Academic Research Consortium. *J Am Coll Cardiol*, 66, 278-307.

STURLA, F., RONZONI, M., VITALI, M., DIMASI, A., VISMARA, R., PRESTON-MAHER, G., BURRIESCI, G., VOTTA, E. & REDAELLI, A. 2016. Impact of different aortic valve calcification patterns on the outcome of transcatheter aortic valve implantation: A finite element study. *J Biomech*, 49, 2520-2530.

TABATA, M., KASEGAWA, H., FUKUI, T., SHIMIZU, A., SATO, Y. & TAKANASHI, S. 2014. Long-term outcomes of artificial chordal replacement with tourniquet technique in mitral valve repair: a single-center experience of 700 cases. *J Thorac Cardiovasc Surg*, 148, 2033-2038 e1.

TADROS, T. M., KLEIN, M. D. & SHAPIRA, O. M. 2009. Ascending aortic dilatation associated with bicuspid aortic valve: pathophysiology, molecular biology, and clinical implications. *Circulation*, 119, 880-890.

TAKATA, M., HARASAWA, Y., BELOUCIF, S. & ROBOTHAM, J. L. 1997. Coupled vs. uncoupled pericardial constraint: effects on cardiac chamber interactions. *J Appl Physiol* (1985), 83, 1799-1813.

TAL, M. G. 2005. Comparison of recirculation percentage of the palindrome catheter and standard hemodialysis catheters in a swine model. *J Vasc Interv Radiol*, 16, 1237-1240.

TANG, Z., FAN, Y. T., WANG, Y., JIN, C. N., KWOK, K. W. & LEE, A. P. 2019. Mitral Annular and Left Ventricular Dynamics in Atrial Functional Mitral Regurgitation: A Three-Dimensional and Speckle-Tracking Echocardiographic Study. *J Am Soc Echocardiogr*, 32, 503-513.

TAWK, S., BARAKAT, E. & HAMMER, F. 2018. A Proposed Simple and Accurate Technique for Optimal Long-Term Hemodialysis Catheter Tip Placement. *J Belg Soc Radiol*, 102, 21.

TAYLOR, S., BUCHAN, K. G. & ESPINO, D. M. 2021. The role of strut chordae in mitral valve competence during annular dilation. *Perfusion*, 36, 253-260.

TENENHOLTZ, N. A., HAMMER, P. E., FABOZZO, A., FEINS, E. N., DEL NIDO, P. J. & HOWE, R. D. 2013. Fast Simulation of Mitral Annuloplasty for Surgical Planning. *Funct Imaging Model Heart*, 7945, 106-113.

- THOMPSON, S., JAMES, M., WIEBE, N., HEMMELGARN, B., MANNS, B., KLARENBACH, S., TONELLI, M. & Alberta Kidney Disease Network. 2015. Cause of Death in Patients with Reduced Kidney Function. *J Am Soc Nephrol*, 26, 2504-2511.
- TIMEK, T. A., GREEN, G. R., TIBAYAN, F. A., LAI, D. T., RODRIGUEZ, F., LIANG, D., DAUGHTERS, G. T., INGELS, N. B., JR. & MILLER, D. C. 2003. Aorto-mitral annular dynamics. *Ann Thorac Surg*, 76, 1944-1950.
- TIMEK, T. A., NIELSEN, S. L., GREEN, G. R., DAGUM, P., BOLGER, A. F., DAUGHTERS, G. T., HASENKAM, J. M., INGELS, N. B. & MILLER, D. C. 2001. Influence of anterior mitral leaflet second-order chordae on leaflet dynamics and valve competence. *Ann Thorac Surg*, 72, 535-540.
- TOMA, M., EINSTEIN, D. R., BLOODWORTH, C. H. T., COCHRAN, R. P., YOGANATHAN, A. P. & KUNZELMAN, K. S. 2017. Fluid-structure interaction and structural analyses using a comprehensive mitral valve model with 3D chordal structure. *Int J Numer Method Biomed Eng*, 33, e02815.
- TOMA, M., JENSEN, M. O., EINSTEIN, D. R., YOGANATHAN, A. P., COCHRAN, R. P. & KUNZELMAN, K. S. 2016. Fluid-Structure Interaction Analysis of Papillary Muscle Forces Using a Comprehensive Mitral Valve Model with 3D Chordal Structure. *Ann Biomed Eng*, 44, 942-953.
- TON-NU, T. T., LEVINE, R. A., HANDSCHUMACHER, M. D., DORER, D. J., YOSEFY, C., FAN, D., HUA, L., JIANG, L. & HUNG, J. 2006. Geometric determinants of functional tricuspid regurgitation: insights from 3-dimensional echocardiography. *Circulation*, 114, 143-149.
- TOPILSKY, Y. 2020. Mitral Regurgitation: Anatomy, Physiology, and Pathophysiology-Lessons Learned From Surgery and Cardiac Imaging. *Front Cardiovasc Med*, 7, 84.
- TOPILSKY, Y., VATURI, O., WATANABE, N., BICHARA, V., NKOMO, V. T., MICHELENA, H., LE TOURNEAU, T., MANKAD, S. V., PARK, S., CAPPS, M. A., SURI, R., PISLARU, S. V., MAALOUF, J., YOSHIDA, K. & ENRIQUEZ-SARANO, M. 2013. Real-time 3-dimensional dynamics of functional mitral regurgitation: a prospective quantitative and mechanistic study. *J Am Heart Assoc*, 2, e000039.
- TORTORA, G. J. & DERRICKSON, B. H. 2014. *Introduction to the Human Body*. 10th edition. John Wiley & Sons.
- TWARDOWSKI, Z. J. & SEGER, R. M. 2002. Measuring central venous structures in humans: implications for central-vein catheter dimensions. *J Vasc Access*, 3, 21-37.

- UEMURA, T., OTSUJI, Y., NAKASHIKI, K., YOSHIFUKU, S., MAKI, Y., YU, B., MIZUKAMI, N., KUWAHARA, E., HAMASAKI, S., BIRO, S., KISANUKI, A., MINAGOE, S., LEVINE, R. A. & TEI, C. 2005. Papillary muscle dysfunction attenuates ischemic mitral regurgitation in patients with localized basal inferior left ventricular remodeling: insights from tissue Doppler strain imaging. *J Am Coll Cardiol*, 46, 113-119.
- VALEN-SENDSTAD, K., MARDAL, K. A., MORTENSEN, M., REIF, B. A. & LANGTANGEN, H. P. 2011. Direct numerical simulation of transitional flow in a patient-specific intracranial aneurysm. *J Biomech*, 44, 2826-2832.
- Vascular Access Work Group. 2006. Clinical practice guidelines for vascular access. *Am J Kidney Dis*, 48 Suppl 1, S248-273.
- VEDULA, V., GEORGE, R., YOUNES, L. & MITTAL, R. 2015. Hemodynamics in the Left Atrium and Its Effect on Ventricular Flow Patterns. *J Biomech Eng*, 137, 111003.
- VERONESI, F., CORSI, C., SUGENG, L., MOR-AVI, V., CAIANI, E. G., WEINERT, L., LAMBERTI, C. & LANG, R. M. 2009. A study of functional anatomy of aortic-mitral valve coupling using 3D matrix transesophageal echocardiography. *Circ Cardiovasc Imaging*, 2, 24-31.
- VESELY, T. M. & RAVENSCROFT, A. 2016. Hemodialysis catheter tip design: observations on fluid flow and recirculation. *J Vasc Access*, 17, 29-39.
- VESELY, T. M. 2003. Central venous catheter tip position: a continuing controversy. *J Vasc Interv Radiol*, 14, 527-534.
- VICECONTI, M., OLSEN, S., NOLTE, L. P. & BURTON, K. 2005. Extracting clinically relevant data from finite element simulations. *Clin Biomech (Bristol, Avon)*, 20, 451-454.
- VITARELLI, A., MANGIERI, E., GAUDIO, C., TANZILLI, G., MIRALDI, F. & CAPOTOSTO, L. 2018. Right atrial function by speckle tracking echocardiography in atrial septal defect: Prediction of atrial fibrillation. *Clin Cardiol*, 41, 1341-1347.
- VOIGT, I., MANSI, T., MIHALEF, V., IONASEC, R. I., CALLEJA, A., MENGUE, E. A., SHARMA, P., HOULE, H., GEORGESCU, B., HORNEGGER, J. & COMANICIU, D. 2011. Patient-specific model of left heart anatomy, dynamics and hemodynamics from 4d tee: a first validation study. *Functional Imaging and Modeling of the Heart-FIMH 2011*. Springer.
- VOTTA, E., CAIANI, E., VERONESI, F., SONCINI, M., MONTEVECCHI, F. M. & REDAELLI, A. 2008. Mitral valve finite-element modelling from ultrasound data: a pilot study for a new approach to understand mitral function and clinical scenarios. *Philos Trans A Math Phys Eng Sci*, 366, 3411-3434.

VOTTA, E., LE, T. B., STEVANELLA, M., FUSINI, L., CAIANI, E. G., REDAELLI, A. & SOTIROPOULOS, F. 2013. Toward patient-specific simulations of cardiac valves: state-of-the-art and future directions. *J Biomech*, 46, 217-228.

VOTTA, E., MAISANO, F., BOLLING, S. F., ALFIERI, O., MONTEVECCHI, F. M. & REDAELLI, A. 2007. The Geoform disease-specific annuloplasty system: a finite element study. *Ann Thorac Surg*, 84, 92-101.

WALCZAK, L., TAUTZ, L., NEUGEBAUER, M., GEORGII, J., WAMALA, I., SUNDERMANN, S., FALK, V. & HENNEMUTH, A. 2021. Interactive editing of virtual chordae tendineae for the simulation of the mitral valve in a decision support system. *Int J Comput Assist Radiol Surg*, 16, 125-132.

WANG, J. S., LI, Y. S., CHEN, J. C. & CHEN, Y. W. 2005. Effects of exercise training and deconditioning on platelet aggregation induced by alternating shear stress in men. *Arterioscler Thromb Vasc Biol*, 25, 454-460.

WANG, Q. & SUN, W. 2013. Finite element modeling of mitral valve dynamic deformation using patient-specific multi-slices computed tomography scans. *Ann Biomed Eng*, 41, 142-153.

WARRAICH, H. J., CHAUDARY, B., MASLOW, A., PANZICA, P. J., PUGSLEY, J. & MAHMOOD, F. 2012. Mitral annular nonplanarity: correlation between annular height/commissural width ratio and the nonplanarity angle. *J Cardiothorac Vasc Anesth*, 26, 186-190.

WEBSTER, A. C., NAGLER, E. V., MORTON, R. L. & MASSON, P. 2017. Chronic Kidney Disease. *Lancet*, 389, 1238-1252.

WEHRUM, T., LODEMANN, T., HAGENLOCHER, P., STUPLICH, J., NGO, B. T. T., GRUNDMANN, S., HENNEMUTH, A., HENNIG, J. & HARLOFF, A. 2018. Age-related changes of right atrial morphology and inflow pattern assessed using 4D flow cardiovascular magnetic resonance: results of a population-based study. *J Cardiovasc Magn Reson*, 20, 38.

WEINBERG, E. J. & KAAZEMPUR MOFRAD, M. R. 2007. A finite shell element for heart mitral valve leaflet mechanics, with large deformations and 3D constitutive material model. *J Biomech*, 40, 705-711.

WENK, J. F., RATCLIFFE, M. B. & GUCCIONE, J. M. 2012. Finite element modeling of mitral leaflet tissue using a layered shell approximation. *Med Biol Eng Comput*, 50, 1071-1079.

- WENK, J. F., ZHANG, Z., CHENG, G., MALHOTRA, D., ACEVEDO-BOLTON, G., BURGER, M., SUZUKI, T., SALONER, D. A., WALLACE, A. W., GUCCIONE, J. M. & RATCLIFFE, M. B. 2010. First finite element model of the left ventricle with mitral valve: insights into ischemic mitral regurgitation. *Ann Thorac Surg*, 89, 1546-1553.
- WILCOX, A. G., BUCHAN, K. G. & ESPINO, D. M. 2014. Frequency and diameter dependent viscoelastic properties of mitral valve chordae tendineae. *J Mech Behav Biomed Mater*, 30, 186-195.
- WORKBENCH, A. 2015. ANSYS Meshing User's Guide 16.0. Ansys Inc, USA.
- WU, V. C. & TAKEUCHI, M. 2017. Three-Dimensional Echocardiography: Current Status and Real-Life Applications. *Acta Cardiol Sin*, 33, 107-118.
- XU, F., JOHNSON, E. L., WANG, C., JAFARI, A., YANG, C., SACKS, M. S., KRISHNAMURTHY, A. & HSU, M. 2021. Computational investigation of left ventricular hemodynamics following bioprosthetic aortic and mitral valve replacement. *Mech Res Commun*, 112, 103604.
- YAMAURA, Y., ET AL. 2008. Three-Dimensional Echocardiographic Measurements of Distance Between Papillary Muscles and Mitral Annulus: Assessment With Three-Dimensional Quantification Software System. *J Echocardiogr*, 6, 67-73.
- YIU, S. F., ENRIQUEZ-SARANO, M., TRIBOUILLOY, C., SEWARD, J. B. & TAJIK, A. J. 2000. Determinants of the degree of functional mitral regurgitation in patients with systolic left ventricular dysfunction: A quantitative clinical study. *Circulation*, 102, 1400-1406.
- ZAJEC, B. 2020. *Collagen fibre network architecture in the porcine mitral valve*. BSc Biomedical Science, University of Aberdeen.
- ZHANG, F., KANIK, J., MANSI, T., VOIGT, I., SHARMA, P., IONASEC, R. I., SUBRAHMANYAN, L., LIN, B. A., SUGENG, L., YUH, D., COMANICIU, D. & DUNCAN, J. 2017. Towards patient-specific modeling of mitral valve repair: 3D transesophageal echocardiography-derived parameter estimation. *Med Image Anal*, 35, 599-609.
- ZHANG, L. W., ADEMILOYE, A. S. & LIEW, K. M. 2019. Meshfree and Particle Methods in Biomechanics: Prospects and Challenges. *Archives of Computational Methods in Engineering*, 26, 1547-1576.
- ZHANG, W., AYOUB, S., LIAO, J. & SACKS, M. S. 2016. A meso-scale layer-specific structural constitutive model of the mitral heart valve leaflets. *Acta Biomater*, 32, 238-255.

ZUO, K., PHAM, T., LI, K., MARTIN, C., HE, Z. & SUN, W. 2016. Characterization of biomechanical properties of aged human and ovine mitral valve chordae tendineae. *J Mech Behav Biomed Mater*, 62, 607-618.

APPENDIX A

DESCRIPTION OF MATERIAL PROPERTIES

A.1. Orthotropic material

The orthotropic material is defined by 9 elastic constants: 3 Young's moduli (E_x , E_y , E_z), 3 Poisson's ratios (ν_{xy} , ν_{yz} , ν_{zx}) and 3 shear moduli (G_{xy} , G_{yz} , G_{zx}). Stresses and strains are related through the following equation:

$$\boldsymbol{\varepsilon} = \mathbf{C} \cdot \boldsymbol{\sigma}, \quad (\text{A.1})$$

where $\boldsymbol{\varepsilon}$ is the strain, $\boldsymbol{\sigma}$ is the Cauchy stress and \mathbf{C} is a compliance matrix in terms of the material constants of the material in the x, y and z directions, defined as

$$\mathbf{C} = \begin{bmatrix} \frac{1}{E_x} & -\frac{\nu_{yx}}{E_y} & -\frac{\nu_{zx}}{E_z} & 0 & 0 & 0 \\ -\frac{\nu_{xy}}{E_x} & \frac{1}{E_y} & -\frac{\nu_{zy}}{E_z} & 0 & 0 & 0 \\ -\frac{\nu_{xz}}{E_x} & -\frac{\nu_{yz}}{E_y} & \frac{1}{E_z} & 0 & 0 & 0 \\ 0 & 0 & 0 & \frac{1}{2G_{yz}} & 0 & 0 \\ 0 & 0 & 0 & 0 & \frac{1}{2G_{zx}} & 0 \\ 0 & 0 & 0 & 0 & 0 & \frac{1}{2G_{xy}} \end{bmatrix}, \quad (\text{A.2})$$

where $\frac{\nu_{yz}}{E_y} = \frac{\nu_{zy}}{E_z}$, $\frac{\nu_{zx}}{E_z} = \frac{\nu_{xz}}{E_x}$, $\frac{\nu_{xy}}{E_x} = \frac{\nu_{yx}}{E_y}$.

A.2. Hyperelastic material

The stress tensor of the hyperelastic material implemented in this thesis can be obtained by writing its strain energy (W) in terms of the two invariants of the right Cauchy deformation tensor (I_1, I_2), defined as:

$$I_1 = \lambda_{xx}^2 + \lambda_{yy}^2 + \lambda_{zz}^2 \quad (A.3)$$

$$I_2 = \lambda_{xx}^2 \lambda_{yy}^2 + \lambda_{yy}^2 \lambda_{zz}^2 + \lambda_{zz}^2 \lambda_{xx}^2 - \lambda_{xy}^4 - \lambda_{yz}^4 - \lambda_{zx}^4 \quad (A.4)$$

where λ is the deviatoric part of the stretch along the respective fiber direction. The representation of this transversely isotropic hyperelastic model yields the following strain energy (W):

$$W = F_1(I_1) + F_2(\lambda) = C_1(I_1 - 3) + F_2(\lambda) \quad (A.5)$$

where F_1 and $F_2(\lambda)$ represent the behaviour of the matrix component (Neo-Hookean) and the contribution from the fibers (Fung-type exponential), respectively. The Cauchy stress can be obtained by differentiating the components of W . In the case of $F_1(I_1)$, this becomes:

$$\frac{\partial F_1(I_1)}{\partial I_1} = \frac{C_1}{2}, \quad (A.6)$$

where C_1 is a material constant, representing a dependence of the ground matrix on the three principal stretches of deformation.

The fiber term F_2 is meant to capture the behavior of crimped collagen fibers, which are implemented as unable to resist compression (isotropy for $\lambda < 1$). Fiber straightening is assumed exponential, and a linear function describes the behaviour of the fibers after straightening past a critical stretch ($\lambda \geq \lambda^*$). In the present implementation, this last stage of fiber behaviour is neglected by assuming a critical stretch much larger than the observed one. The function describing the derivatives of $F_2(\lambda)$ is, therefore, written as:

$$\frac{\partial F}{\partial \lambda} = \begin{cases} 0 & \lambda < 1 \\ \frac{C_3}{\lambda} [e^{C_4(\lambda-1)} - 1] & \lambda < \lambda^* \end{cases}, \quad (\text{A.7})$$

where coefficients C_3 and C_4 are material constants which scale the exponential stresses (C_3) and control the collagen fiber straightening rate (C_4), respectively (Quapp and Weiss, 1998).

The derivation of stress components in x- and y- directions for a 2-layer composite is detailed elsewhere (Wenk *et al.*, 2012).

APPENDIX B

SURFACE CONTACT FORMULATION

The segment-based penalty formulation uses segment masses (equal to element masses in the case of shell-to-shell contact) instead of nodal ones to calculate the contact stiffness (c_s). The contact stiffness is calculated through Equation B.1,

$$c_s(t) = 0.5 \cdot \alpha \cdot \left\{ \begin{matrix} \beta \\ \text{or} \\ \gamma \end{matrix} \right\} \left(\frac{m_A m_B}{m_A + m_B} \right) \left(\frac{1}{\Delta t_c(t)} \right)^2, \quad (\text{B.1})$$

where α , β and γ are scale factors (LS-DYNA parameters SLSFAC, SFS and SFM, respectively), m_A and m_B are the segment masses from the shells in contact and Δt_c is the time step factor. This time step factor is set to the initial solution time step, being updated to prevent instabilities if the time step becomes too large (i.e. $> 5\%$ increase) (Hallquist, 2006a).

APPENDIX C

CHORDAE TENDINEAE TENSIONS RETRIEVED FROM THE LITERATURE

Table C.1: Chordae tendineae tensions obtained from the literature. Notes: ALPM, anterolateral papillary muscle; PMPM, posteromedial papillary muscle.

Author	No. specimens/models	Type of study	Load [N]		
			AL strut	AL marginal	PL marginal
(Jimenez <i>et al.</i> , 2005)	6 (human)	Experimental	0.95 ± 0.35	0.35 ± 0.16	0.06 ± 0.05
(Nielsen <i>et al.</i> , 2003)	8 (ovine)	Experimental	(ALPM) 0.52 ± 0.08 (PMPM) 0.81 ± 0.1	-	-
(Paulsen <i>et al.</i> , 2019)	8 (porcine)	Experimental	0.93 ± 0.38	0.23 ± 0.08	0.14 ± 0.06
(Paulsen <i>et al.</i> , 2020)	5 (porcine)	Experimental	0.74 ± 0.22	0.17 ± 0.08	0.12 ± 0.06
(Prot <i>et al.</i> , 2009)	1	Computational	1.3	0.27 ± 0.13	0.4 ± 0.069
(Stevanella <i>et al.</i> , 2009)	1	Computational	0.9	0.148 ± 0.079	0.158 ± 0.1
(Wang and Sun, 2013)	1	Computational	1.07	0.275	0.192

APPENDIX D

FINITE VOLUME METHOD FUNDAMENTALS

To discretise the system of equations, it is necessary to first integrate independently each term of the Navier-Stokes momentum equation across a cell volume. Since the unsteady term does not change across the volume, its integral can be easily computed:

$$\int_V \frac{\partial \mathbf{u}}{\partial t} dV = \frac{\partial \mathbf{u}}{\partial t} V. \quad (\text{D.1})$$

The divergence theorem (Equation C.2) needs to be applied to the convection, diffusion and pressure terms in order to find a solution:

$$\int_V \nabla \cdot \mathbf{F} dV = \int_S \mathbf{F} \cdot \hat{\mathbf{n}} dS, \quad (\text{D.2})$$

where \mathbf{F} is a vector, S is the area of each face of the volume and $\hat{\mathbf{n}}$ is the normal vector between the cell centroid and the respective face. By applying Equation C.2 to the convective term, we obtain a surface integral which can be further simplified (Equation C.3):

$$\int_V (\mathbf{u} \cdot \nabla) \mathbf{u} dV = \int_S \mathbf{u} (\mathbf{u} \cdot \hat{\mathbf{n}}) dS = \sum_{i=1}^N \int_S \mathbf{u}_i (\mathbf{u}_i \cdot \hat{\mathbf{n}}_i) dS_i, \quad (\text{D.3})$$

where $(\mathbf{u} \cdot \widehat{\mathbf{n}})$ represents the volume flow rate through a face and, since one cell has a finite number of faces (N), the expression can be further simplified as presented on the right side of Equation C.3.

Since it is assumed that the flow variables are calculated at the centroid of the face, Equation C.3 can be rewritten to include the assumption that only the velocity at the centroid of the face is calculated (i.e. linear variation of velocity across the face):

$$\sum_{i=1}^N \int_S \mathbf{u}_i (\mathbf{u}_i \cdot \widehat{\mathbf{n}}_i) dS_i \approx \sum_{i=1}^N \mathbf{u}_{fi} (\mathbf{u}_{fi} \cdot \widehat{\mathbf{n}}_{fi}) S_{fi}, \quad (\text{D.4})$$

where \mathbf{u}_{fi} is the unknown centred velocity vector on each face of the cell. By using the divergence theorem, a simplified expression for the advection term can also be found:

$$\int_V \chi \nabla^2 \mathbf{u} dV \approx \sum_{i=1}^N \chi (\nabla \mathbf{u}_{fi} \cdot \widehat{\mathbf{n}}_{fi}) S_{fi}. \quad (\text{D.5})$$

APPENDIX E

MULTIPHASE FLOW FORMULATIONS

The selected multiphase model consists of two phases with equal material properties, where the primary (q) phase corresponds to the fluid entering/exiting all boundaries except the catheter inlet (unfiltered blood) and the recirculation (p) phase corresponds to the fluid entering the catheter inlet (filtered blood). It employs a volume of fluid (VOF) model, where the volume fraction of each phase in a computational cell is tracked throughout the domain (ANSYS, 2013). The fundamental laws governing phase volume fraction, continuity of mass and continuity of momentum for primary and recirculation phases are given, respectively, in equations (D.1 – D.3).

The primary-phase volume fraction is computed based on the following constraint:

$$\sum_{n=1}^2 \alpha_n = 1, \quad (\text{E.1})$$

where α_n denotes the volume fraction of fluid phase n . The conservation of mass and momentum equations are given by:

$$\frac{\partial}{\partial t}(\alpha_q \rho_q) + \nabla \cdot (\alpha_q \rho_q \mathbf{u}_q) = 0, \quad (\text{E.2})$$

$$\begin{aligned}
& \frac{\partial}{\partial t} (\alpha_q \rho_q \mathbf{u}_q) + \nabla \cdot (\alpha_q \rho_q \mathbf{u}_q \mathbf{u}_q) \\
& = -\alpha_q \nabla P + \nabla \cdot \bar{\bar{\tau}}_q + \sum_{p,q=1}^2 K_{pq} (\mathbf{u}_p - \mathbf{u}_q) + \mathbf{F},
\end{aligned} \tag{E.3}$$

where \mathbf{u} is the velocity vector, ρ is the density of the fluid phase, $\bar{\bar{\tau}}$ is the stress-strain tensor, K_{pq} is the interphase momentum exchange coefficient and \mathbf{F} are the external forces. Since the purpose of using a multiphase model was to quantify the volume fraction of the recirculation phase, K_{pq} was assumed equal to zero and the only interaction between fluid phases was provided as their complementary volume fractions within each computational cell.

Based on the chosen multiphase flow model, and to calculate recirculation of blood through catheters, the volume fraction (0 – 1) of the recirculation phase (ϕ_r) is considered; for multiphase catheter models, any measure in a mesh element is weighted between the primary and the recirculation phases. The time-averaged volume fraction of the recirculation phase at the catheter outlet is then defined as:

$$\overline{\phi_r} = \frac{1}{T} \int_0^T \phi_r \, dt, \tag{E.4}$$

where T is the length of the cardiac cycle. For a k^{th} facet of the catheter outlet boundary, the magnitude of the recirculation fraction can then be defined as a mass-weighted average of $\overline{\phi_k}$ through the catheter outlet,

$$R_f = \frac{1}{\dot{m}_T} \sum_{k=1}^n \overline{\phi}_k \dot{m}_k, \quad (\text{E.5})$$

where \dot{m}_T and \dot{m}_k are the total mass flow rate over the catheter outlet boundary and the mass flow rate for a k^{th} facet, respectively. The latter is defined by:

$$\dot{m}_k = \rho(\mathbf{u}_k \cdot \mathbf{A}_k), \quad (\text{E.6})$$

where \mathbf{u}_k and \mathbf{A}_k are the k^{th} facet velocity and area vectors, respectively (ANSYS, 2013).